The Dissertation Committee for Elyes Balti
certifies that this is the approved version of the following dissertation:

Advanced Signal Processing Techniques For Full-Duplex Systems

Committee:

Prof. Brian L. Evans, Supervisor

Prof. Haris Vikalo

Prof. Ahmed Tewfik

Prof. Lili Qiu

Prof. Murat Torlak

Advanced Signal Processing Techniques For Full-Duplex Systems

by

Elyes Balti

Dissertation

Presented to the Faculty of the Graduate School of

The University of Texas at Austin

in Partial Fulfillment

of the Requirements

for the Degree of

Doctor of Philosophy

The University of Texas at Austin

December 2024

Dedicated to my family.

Epigraph

What starts here changes the world.

—The University of Texas at Austin

Acknowledgments

This dissertation represents the culmination of a journey filled with learning, growth, and the unwavering support of many remarkable individuals to whom I owe immense gratitude.

First and foremost, I extend my deepest appreciation to my advisor, Prof. Brian L. Evans, for his exceptional mentorship, insightful guidance, and steadfast encouragement throughout my Ph.D. journey. His dedication to research excellence and his belief in my potential have profoundly shaped my academic and personal growth.

I am also deeply grateful to my dissertation committee members, Prof. Haris Vikalo, Prof. Ahmed Tewfik, Prof. Lili Qiu, and Prof. Murat Torlak, for their invaluable feedback, thoughtful insights, and generous commitment of time and expertise. Their contributions have been instrumental in refining this work and pushing the boundaries of my research.

I would like to express my special thanks to my collaborators: Dr. Salam Akoum and Dr. Iyad Alfallujah from AT&T Research Lab, Dr. Chriss Dick from Nvidia, Dr. Keith Tinsley from Tektronix, and Dr. Neji Mensi, from Florida Institute of Technology. Their expertise, guidance, and collaboration have significantly enriched this work and broadened its impact.

I wish to express my heartfelt gratitude to the administrative staff: Ms. Melanie Gulick, Dr. Verónica Vera-Vasquez, and Ms. Karen Little, for their unwavering support, guidance, and dedication to ensuring a smooth and enriching graduate experience. Their efforts have gone above and beyond, and their kindness and professionalism have been invaluable throughout my time at UT Austin.

A special note of thanks goes to my dear friends, Pooja Nuti, Alice Liu, Vignesh Nandakumar, and Faraz Barati, whose companionship, advice, and unwavering

support have made this journey less daunting and infinitely more enjoyable. Their friendship has been a pillar of strength through both challenges and triumphs.

To my family, words cannot capture the depth of my gratitude. To my parents, Mahmoud and Monia, for their unconditional love, sacrifices, and belief in my dreams. To my brother, Oussama, for his constant encouragement and support. And to my wife, Arij, whose love, patience, and unwavering belief in me have been my anchor. Her sacrifices and understanding during the most demanding times of this journey are beyond measure, and I owe this accomplishment as much to her as to myself.

Lastly, I would like to acknowledge the University of Texas at Austin for providing the resources, community, and platform that have enabled me to pursue my research ambitions.

To everyone who has been a part of this journey, I express my heartfelt gratitude. This work is a testament to your influence, inspiration, and unwavering belief in me.

Abstract

Advanced Signal Processing Techniques For Full-Duplex Systems

Elyes Balti, PhD
The University of Texas at Austin, 2024

SUPERVISOR: Prof. Brian L. Evans

The evolution of cellular communications has seen each generation achieve a tenfold increase in data rates and a reduction in latency by a factor of 1/10, alongside more complex infrastructure and use cases. As the industry progresses toward sixth generation (6G), emerging services such as high-fidelity mobile holograms, digital twins that replicate and interact with physical entities in real-time, and truly immersive extended reality (XR) are becoming increasingly prominent. These services demand exceptionally high data rates and low latency, which current outdoor cellular networks such as long term evolution (LTE) and fifth generation (5G) struggle to support. While virtual and augmented reality applications are currently limited to indoor environments powered by wireless-fidelity (Wi-Fi), cellular networks must evolve to accommodate these advanced applications. Full-duplex (FD) communication, which can double data rates and reduce latency, is identified as a key enabler for delivering these next-generation services over cellular networks. This research examines FD technology and its potential to overcome the limitations of current cellular systems, paving the way for seamless, high-performance 6G services.

FD systems enable bidirectional transmission over the same resource block, with the potential to significantly reduce latency and double spectral efficiency. How-

ever, self-interference (SI) remains a key challenge, as the power of the SI signal can be several orders of magnitude higher than the desired signal, potentially saturating the analog-to-digital converters (ADCs) and degrading system performance. Massive antenna arrays offer the necessary degrees of freedom for spatial multiplexing and effective SI suppression. Current FD solutions, primarily implemented for sub-6 GHz radios, provide a valuable foundation for extending FD capabilities to the millimeter wave (mmWave) spectrum. Nevertheless, this extension requires more than just a frequency shift—it necessitates a reevaluation of the underlying assumptions in signal processing developed for the sub-6 GHz band. Adapting FD solutions to the mmWave band thus demands the development of advanced signal processing techniques that account for the specific challenges of mmWave communication. Recently, the combination of FD and mmWave communication has been proposed in 3GPP Releases 17 and 18, where FD is being considered for integrated access and backhaul (IAB) systems. Throughout the literature, various SI cancellation techniques have been explored, typically classified into passive and active methods. Passive techniques include antenna array directionality, strategic antenna placement, and isolation, while active cancellation involves suppression through analog and digital circuitry. In this research, I leverage the available degrees of freedom provided by massive antenna arrays to design robust hybrid analog and digital beamformers capable of suppressing SI and enabling FD operation in mmWave systems. The design of these hybrid beamformers is subject to several constraints, including the unit modulus constraint imposed by mmWave hardware, which necessitates phased-array implementation for beam direction tuning. Additionally, significant SI power must be mitigated in the analog domain to prevent ADC saturation, while residual interference is eliminated in the digital domain.

First, I focused on a point-to-point system where two FD nodes communicate over bidirectional links. I formulated the problem of maximizing the sum spectral efficiency under the constraints imposed by hybrid analog/digital beamformers. Directly maximizing the sum spectral efficiency or signal-to-interference-plus-noise ratio

(SINR) involves jointly addressing both the signal power and the self-interference (SI) components of the SINR. Consequently, the problem was reformulated as minimizing the SI power, a key step toward enhancing the overall sum spectral efficiency. Specifically, I formulated the SI power minimization problem under the constraints of the analog beamformers, including the unit modulus constraint and maintaining the rank of the effective channel, i.e., optimizing the beamformed received channel. To address this, I relaxed the unit modulus constraint to preserve the convexity of the minimization problem and derived a closed-form solution for the analog beamformers at both FD nodes. Following this, I proposed a digital beamforming design aimed at maximizing the sum spectral efficiency. Simulations confirmed the efficacy of the proposed algorithm, demonstrating significant improvements in spectral efficiency and SI power reduction. Furthermore, I developed a practical design framework, analyzing trade-offs in terms of the number of antennas, RF chains, system complexity, and power consumption necessary to enable full-duplex operation. In this context, I established that a minimum of 50 dB of self-interference must be mitigated through analog beamforming to achieve effective FD performance.

Second, I examined a single-cell, single-user scenario where both uplink and downlink communications are handled by a FD base station (BS). In this setup, the uplink user is affected by self-interference, while the downlink user experiences inter-user interference (IUI) caused by the uplink transmission. I formulated the problem of maximizing the sum of uplink and downlink spectral efficiency, subject to minimizing SI, inter-user interference, and adhering to unit modulus and semi-unitary constraints. The objective was to design low-complexity hybrid analog/digital beamformers that require few iterations to converge. I further investigated factors influencing the algorithm's convergence, such as the regularization of the interference covariance matrix and the normalization of beamforming both before and after convergence. The performance of the algorithm was assessed based on key metrics, including self-interference reduction, computational cost, rate of convergence, and convergence stability. Simulation results demonstrate the robustness of the proposed approach, achieving signif-

icant improvements in interference suppression and spectral efficiency compared to existing methods.

Third, I investigated an IAB system, where the IAB node receives data from the gNB donor via the backhaul link and transmits to the user through the access channel. Operating in full-duplex mode, the IAB node experiences self-interference (SI), which degrades the performance of the backhaul channel. To address this, I formulated an SI power minimization problem and applied a similar approach as in my previous work to design the analog beamformers at the IAB node. For the gNB donor and user, I derived regularized zero-forcing (RZF) and minimum mean square error (MMSE) beamforming designs, respectively. The computational complexity of designing the hybrid beamformers was found to be relatively low compared to existing solutions. By using SI reduction as the objective in both the analog and digital domains, the proposed algorithm demonstrated rapid convergence, typically requiring only $3 - 5$ iterations to efficiently suppress SI. Additionally, simulation results confirmed that the proposed hybrid analog/digital beamforming design outperforms half-duplex systems and other state-of-the-art approaches in terms of spectral efficiency.

Fourth, I extended the second contribution to a wideband multiuser uplink and downlink communication system. In this scenario, the users employ a fully digital architecture, while the BS utilizes a hybrid analog/digital architecture. To reduce power consumption, the phase shifters at the BS are quantized, and the transmission/reception arrays at the BS implement a partially connected structure. I formulated the problem of maximizing the per-subcarrier sum spectral efficiency for both uplink and downlink users, subject to minimizing self-interference, inter-user interference (uplink users interfering with downlink users), and multiuser interference (among uplink or downlink users), while also satisfying unit modulus and semi-unitary constraints. To address these challenges, I designed hybrid analog/digital beamformers that meet the imposed requirements. Simulation results demonstrate the optimization of beampatterns at both the BS and user devices. Furthermore, I tracked interference

reduction across different stages of the receiver chain and over the entire bandwidth. The findings also highlight the advantages of using a partially connected architecture, showing improvements in both energy efficiency and spectral efficiency when compared to existing methods.

In the fifth contribution, I extended the previous contribution to a massive multiple-input-multiple-output (MIMO) multicell, multi-user scenario, where BSs operate in FD mode and are equipped with a large number of antennas. I developed a unified analytical framework for both uplink (reverse) and downlink (forward) links, applicable to both LTE and mmWave bands, while incorporating the use of low-resolution data converters. The analysis accounted for various system imperfections, including low-resolution quantization noise, pilot contamination, network irregularities, imperfect channel state information (CSI), user mobility, cellular interference, and self-interference. I derived the signal-to-quantization-to-interference-to-noise ratio (SQINR) as a key performance metric, and based on this, I investigated the effective spectral and energy efficiency of the system. In addition, I derived the special cases, asymptotic results and power scaling laws to unpack several engineering insights of the proposed model. This comprehensive analysis provides insights into the challenges and trade-offs involved in implementing FD massive MIMO systems in real-world scenarios.

These five contributions offer significant advancements in the feasibility and development of power-efficient FD systems by addressing the communication requirements of modern wireless networks. They effectively mitigate interference below the noise floor, optimize spectral and energy efficiency, reduce latency, and maximize the utilization of available resources and degrees of freedom. These enhancements are critical for improving the performance and scalability of next-generation wireless systems, particularly in the context of FD communication.

Table of Contents

List of Tables

List of Figures

Notation

$\mathbf{x}$ column vector

$\mathbf{X}$ matrix

X, x scalar

$\mathcal{X}$ set

$\|\mathbf{X}\|_F$ Frobenius norm

$|x|$ absolute value

$\sigma_\ell(\mathbf{X})$ ℓ-th singular value of $\mathbf{X}$ in descending order

$\lambda_\ell(\mathbf{X})$ ℓ-th eigenvalue of $\mathbf{X}$ in descending order

$\mathrm{Tr}(\mathbf{X})$ trace

$\det(\mathbf{X})$ determinant

$\mathbf{X}^*$ Hermitian operator

$\mathbf{X}^T$ Transpose operator

$\mathbf{X}^{-1}$ Inverse of a non-singular square matrix

$\mathbf{X}^\dagger$ Moore-Penrose pseudo-inverse

$\mathbf{x}_n$ n-th entry of the column vector $\mathbf{x}$

$\mathbf{X}_{mn}$ element located in the m-th row and n-th column in matrix $\mathbf{X}$

$\mathcal{CN}(\mathbf{m}, \mathbf{\Sigma})$ circularly complex symmetric Gaussian random vector with mean $\mathbf{m}$ and covariance $\mathbf{\Sigma}$

$\mathbf{I}_N$ identity matrix of size $N \times N$

$\mathbb{E}(\cdot)$ expectation operator

$\mathbb{P}(\cdot)$ probability measure

Glossary

1G First Generation

2G Second Generation

3G Third Generation

4G Fourth Generation

5G Fifth Generation

6G Sixth Generation

3GPP Third Generation Partnership Protocol

ADC Analog-to-Digital Converter

AI Artificial Intelligence

AMPS Advanced Mobile Phone Service

AoA Angle of Arrival

AoD Angle of Departure

AQNM Additive Quantization Noise Model

AR Augmented Reality

AWGN Additive White Gaussian Noise

BDMA Beam Division Multiple Access

BFC Beamforming Cancellation

BER Bit Error Rate

BS Base Station

CAQP Constant Amplitude Quantized Phase

CDF Cumulative Distribution Function

CDMA Code Division Multiple Access

CLI Cross-Link Interference

CSI Imperfect Channel State Information

DAC Digital-to-Analog Converter

DoF Degree of Freedom

DFT Discrete Fourrier Transform

DSP Digital Signal Processing

E2E End-to-End

eMBB Enhanced Mobile Broadband

FBMC Filter Bank Multi-Carrier

FD Full-Duplex

FDD Frequency Division Duplex

FDMA Frequency Division Multiple Access

FLOP Floating Point Operation

FWA Fixed Wireless Access

GPRS General Packet Radio Service

GBSCM Geometry-Based Statistical Channel Model

GSM Global Systems for Mobile Communication

HARQ Hybrid Automatic Repeat Request

HD Half-Duplex

HPADC High Power Analog-to-Digital Converter

HSPA High Speed Packet Access

IAB Integrated Access and Backhaul

IID Independent and Identically Distributed

INR Interference-to-Noise Ratio

IoT Internet of Thing

IQ In-phase and Quadrature

IPADC Intermediate Power Analog-to-Digital Converter

ISAC Integrated Sensing and Communication

IUI Inter-User Interference

LMMSE Linear Minimum Mean Square Error

LNA Low Noise Amplifier

LOS Line-Of-Sight

LPADC Low Power Analog-to-Digital Converter

LS Least Squares

MIMO Multiple-Input-Multiple-Output

MMSE Minimum Mean Square Error

MSE Mean Square Error

MU-MIMO Multiuser MIMO

MUI Multiuser Interference

mMTC Massive Machine-Type Communication

mmWave Millimeter Wave

MR Mixed Reality

MS Mobile Station

NLOS Non-Line-Of-Sight

NR New Radio

NSP Null Space Projection

OFDM Orthogonal Frequency Division Multiplexing

OFDMA Orthogonal Frequency Division Multiple Access

OMP Orthogonal Matching Pursuit

PDP Power Delay Profile

PPP Poisson Point Process

PS Phase Shifter

QCQP Quadratically-Constrained Quadratic Programming

QoS Quality of Service

RF Radio Frequency

RSI Residual Self-Interference

RX Receive/Receiver

RZF Regularized Zero-Forcing

SC-FDE Single-Carrier Frequency Domain Equalization

SC-FDMA Single-Carrier Frequency Division Multiple Access

SI Self-Interference

SIC Self-Interference Cancellation

SINR Signal-to-Interference-plus-Noise Ratio

SIR Signal-to-Interference Ratio

SNR Signal-to-Noise Ratio

SISO Single-Input-Single-Output

SQNR Signal-to-Quantization-plus-Noise Ratio

SQINR Signal-to-Quantization-plus-Interference-plus-Noise Ratio

SVD Singular Value Decomposition

TACS Total Access Communication System

TDD Time Division Duplexing

TDMA Time Division Multiple Access

TX Transmit/Transmitter

UE User Equipment

UHD Ultra High Definition

UMTS Universal Mobile Telecommunications Systems

URLLC Ultra Reliable Low Latency Communication

VR Virtual Reality

WCDMA Wideband Code Division Multiple Access

WIMAX Worldwide Interoperability for Microwave Access

XDD Cross-Division Duplex

XR Extended Reality

ZF Zero-Forcing

Chapter 1: Introduction

1.1 Background

1.1.1 Evolution of Cellular Communications

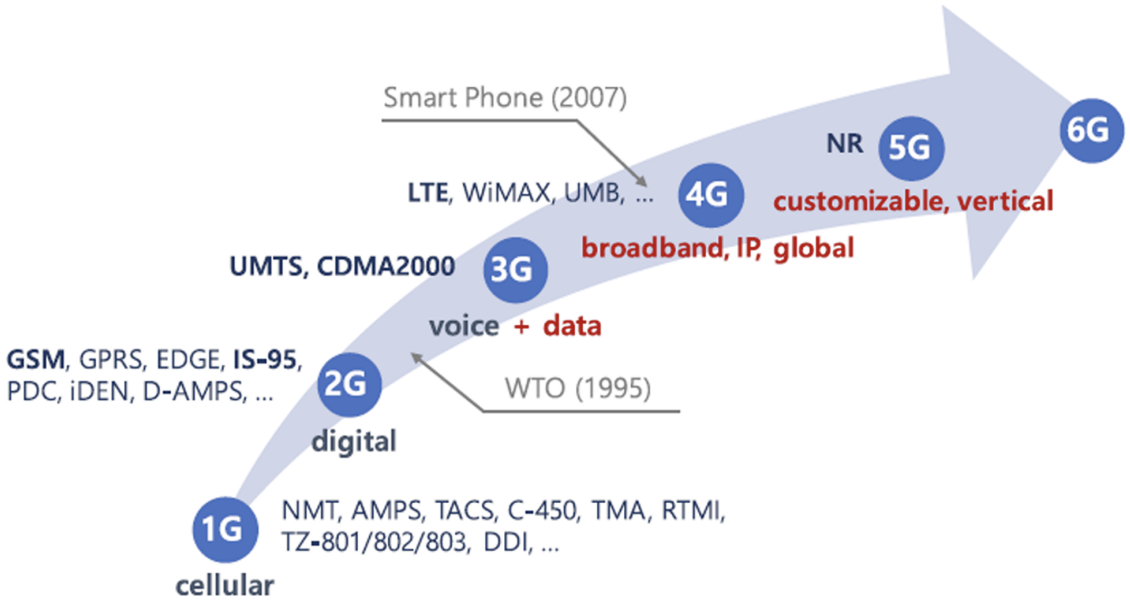

Figure 1.1: Evolution of cellular networks generations.

The evolution of cellular communications has unfolded over several decades, marked by successive generations of technology, each bringing significant advancements in data rates, network capacity, latency, and connectivity. The journey began with the first generation (1G) in the 1980s, which utilized analog technology and Frequency Division Multiple Access (FDMA) to facilitate basic voice communication. These early systems, such as the Advanced Mobile Phone System (AMPS) and Total Access Communication System (TACS), were limited by poor voice quality, lack of data services, and minimal security.

The second generation (2G), introduced in the 1990s, transitioned to digital technology with the adoption of Time Division Multiple Access (TDMA) and Code

Division Multiple Access (CDMA). This shift brought improved voice quality, enhanced security, and the introduction of SMS and basic data services. Prominent examples include the Global System for Mobile Communications (GSM) and IS-95 (CDMA ONE). The evolution continued with the advent of General Packet Radio Service (GPRS) and Enhanced Data rates for GSM Evolution, which enabled rudimentary internet access on mobile devices.

The third generation (3G), which emerged in the 2000s, significantly enhanced mobile data capabilities. Utilizing Wideband CDMA (WCDMA) and CDMA2000, 3G systems supported higher data rates and mobile internet access, making services like video calling and multimedia messaging possible. Universal Mobile Telecommunications System (UMTS) and CDMA2000 became the standards of this era, providing mobile broadband with peak data rates up to 2 Mbps, later improved by High-Speed Packet Access (HSPA) technologies.

The fourth generation (4G), launched in the 2010s, marked a major leap forward with the introduction of LTE and LTE-Advanced. These technologies employed Orthogonal Frequency Division Multiple Access (OFDMA) and MIMO techniques to deliver high-speed data transmission, significantly improving data rates, latency, and network capacity. 4G enabled seamless HD video streaming, VoIP, and online gaming, with peak data rates reaching up to 1 Gbps. The increased spectral efficiency and reduced latency set new standards for mobile communication.

In the 2020s, the 5G brought transformative advancements, including Enhanced Mobile Broadband (eMBB), Ultra-Reliable Low-Latency Communication (URLLC), and Massive Machine-Type Communication (mMTC) to support the growing Internet of Things (IoT). Leveraging New Radio (NR) technology, including mmWave frequencies, massive MIMO, and beamforming, 5G achieved peak data rates of up to 20 Gbps and sub-millisecond latency. These advancements have enabled new applications such as autonomous vehicles, smart cities, and augmented reality, with 5G networks deployed globally by major Telecom operators.

Looking ahead, the 6G is envisioned for the 2030s and beyond, promising even greater capabilities. 6G is expected to explore terahertz (THz) frequencies, advanced artificial intelligence (AI)-driven networks, reconfigurable intelligent surfaces, and quantum communication. It aims to achieve data rates up to 1 Tbps, microsecond-level latency, and extreme connectivity for immersive experiences like holographic communication and digital twins. However, 6G faces challenges, including spectrum allocation, energy efficiency, security, and the need for global standardization.

In summary, the evolution of cellular communications has been driven by the increasing demand for faster, more reliable, and more connected mobile services and fixed wireless access (FWA) as shown by Fig. 1.2. From the analog voice services of first generation (1G) to the high-speed, low-latency networks of 5G, each generation has built upon the advancements of its predecessors. As we move towards 6G, the focus will be on integrating cutting-edge technologies to create even faster, more efficient, and more intelligent networks that bridge the gap between the physical and digital worlds.

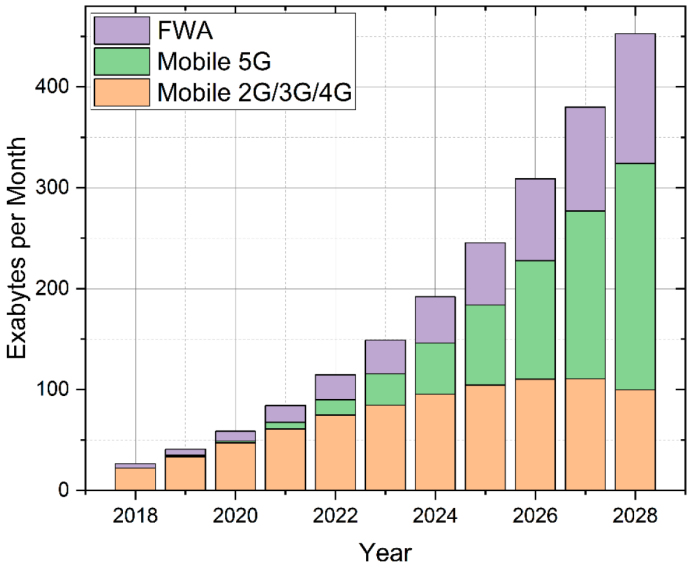

Figure 1.2: Global mobile traffic forecast [58].

Figure 1.3: Truly immersive XR.

1.1.2 Road to 6G Cellular

The road to 6G cellular technology is driven by the need for higher data rates, lower latency, massive connectivity, and the integration of advanced technologies to support new and transformative applications. It will involve overcoming significant technical challenges, developing new standards, and ensuring that the next generation of wireless networks meets the growing demands of a hyper-connected world. The journey to 6G is expected to shape the future of communication, bringing about unprecedented changes in how we interact with the digital and physical world.

1.1.2.1 6G Services

The representative categories of 5G services—eMBB, URLLC, and mMTC are expected to continue evolving and improving as we transition toward 6G. This section focuses on emerging 6G services that will arise from advancements in communications and other technologies such as sensing, imaging, display, and AI. These new services will leverage hyper-connectivity to integrate humans and a wide range of devices, delivering an unparalleled multimedia experience. Specifically, we highlight three key 6G services: truly immersive XR, high-fidelity mobile holograms, and digital replicas.

Truly Immersive XR: XR is an emerging term that encompasses Virtual Reality (VR), Augmented Reality (AR), and Mixed Reality (MR). XR has garnered

significant attention and is expanding opportunities across various sectors, including entertainment, healthcare, science, education, and manufacturing. While technical advancements in XR are ongoing, and new innovations continue to emerge, the primary barrier between XR's potential and its practical application is hardware. XR technologies require sophisticated device form factors, such as handheld components, to support mobile and dynamic software content. However, current mobile devices lack the standalone computing capabilities needed to meet these demands. The progress in hardware performance, particularly in mobile computing power and battery capacity, is lagging behind the rapid growth of XR, posing a significant threat to market expansion. We believe that these challenges can be addressed by offloading computational tasks to more powerful devices or servers.

Another critical challenge is ensuring sufficient wireless capacity. For example, current AR technology requires 55.3 Mbps to support 8K displays with one million points, which is adequate for a mobile display experience. However, achieving truly immersive AR will require substantially increased density and a throughput of 0.44 Gbps for 16 million points. Additionally, XR media streaming may demand bandwidth similar to 16K Ultra High Definition (UHD) quality video, where 16K VR, for instance, requires 0.9 Gbps throughput with a compression ratio of 1:400. The current data rates provided by 5G are insufficient for seamless streaming experiences. The market sizes for VR and AR are projected to reach $44.7 billion [103] and $87 billion, respectively, by 2030 [43].

High-Fidelity Mobile Hologram: With rapid advancements in high-resolution rendering, wearable displays, and wireless networks, mobile devices will soon be capable of rendering media for 3D hologram displays. Holography represents a next-generation media technology that can depict gestures and facial expressions through holographic displays. The content for these displays is generated using real-time capture, transmission, and 3D rendering techniques. To offer hologram displays as part of real-time services, exceptionally high data transmission rates—hundreds of times greater than those supported by current 5G systems—will be required. For instance,

Figure 1.4: 3D hologram display over mobile devices.

Figure 1.5: Digital replica: bridge the real and virtual worlds.

a 19.1 Gigapixel hologram display demands a data rate of 1 Tbps [159]. A hologram display on a mobile device with a 6.7-inch form factor and one micrometer pixel size (equating to 11.1 Gigapixels) would require at least 0.58 Tbps. Additionally, supporting human-sized holograms would necessitate an even larger number of pixels, requiring several Tbps [27]. Given that the peak data rate of 5G is 20 Gbps, it is inadequate for supporting the substantial data volume needed for real-time hologram media. To reduce the data transmission requirements for hologram displays and make them feasible in the 6G era, AI technologies can be employed to enable efficient compression, extraction, and rendering of hologram data. The market for hologram displays is projected to reach $7.6 billion by 2023 [66].

Digital Replica: Leveraging advanced sensors, AI, and communication tech-

nologies, it will become feasible to replicate physical entities—including individuals, devices, objects, systems, and locations—in a virtual environment. This virtual representation of a physical entity is known as a digital twin. In a 6G environment, digital twins will enable users to explore and monitor the physical world within a virtual space, free from temporal or spatial limitations. Through digital twins, users can remotely observe changes, detect issues, and even interact with these virtual representations using VR devices or holographic displays. Digital twins can represent a network of sensors and actuators that are remotely controlled, allowing interactions with digital twins to trigger actions in the physical world. For example, a user could navigate a remote site by controlling a robot through real-time interactions with a digital twin of that site.

AI enhances digital replication, enabling efficient management, problem detection, and mitigation in the real world without the need for human presence or detailed supervision. If an issue is identified within the digital twin, AI can automatically initiate the necessary actions in the physical environment. However, the technical challenges are considerable. For instance, replicating a $1m \times 1m$ area would require a Tera-pixel, necessitating a data throughput of 0.8 Tbps, assuming periodic synchronization every 100 milliseconds and a compression ratio of 1:300. The market for digital replicas is projected to reach $26 billion by 2025 [54].

1.1.2.2 6G Spectrum

As an initial step to design the 6G spectrum concept, three groups of bands, i.e., low, mid and high bands are defined as shown in Fig. 1.6

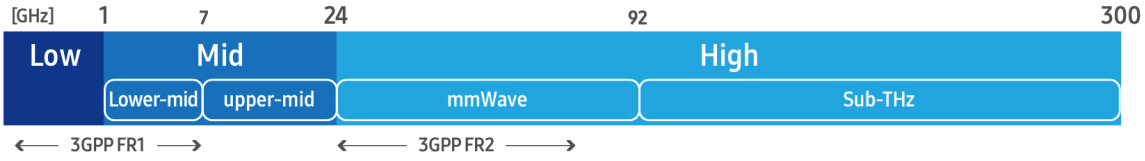

Figure 1.6: 6G spectrum grouping.

- **Low-Band**: Frequency range below 1 GHz is to emphasize the spectrum requirement for extremely large area and deep indoor coverage of the network.
- **Mid-Band**: Frequency range from 1 GHz to 24 GHz taking into account the following.
    1. the band from 1 GHz to 7 GHz, generally called mid-band today,
    2. the need for extension of mid-band up to 24 GHz,
    3. various rulemaking processes,
    4. discussion progress in mobile industry-based organizations such as 3GPP and GSA, and
    5. International Mobile Telecommunication (IMT) bands identification and candidate bands being studied in ITU-R.
- **High-Band**: The upper boundary needs to be extended beyond that for 5G, so that the frequency range 24-300 GHz is grouped as high-band. In addition, this frequency range can consist of two sub-frequency ranges, i.e., the mmWave band (24-92 GHz) to be used as an important band not only for 5G but also for 6G and the sub-THz band (92-300 GHz) as a new frontier band for 6G. It is noted that this white paper focuses on the sub-THz band up to 300 GHz at this stage, while we expect that the full range of terahertz spectrum up to 3 THz could be considered in future.

To achieve the 6G vision, securing the appropriate spectrum is crucial. When considering spectrum allocation for 6G, several key factors must be addressed, including coverage, the requirements of new services, high throughput, and Quality of Service (QoS), among others.

The low-band spectrum (below 1 GHz), though offering limited bandwidth compared to higher frequency bands, provides extensive area coverage and excellent indoor penetration due to its superior propagation characteristics.

The mid-band spectrum (1-24 GHz) offers the advantage of relatively large contiguous bandwidth (hundreds of MHz), providing a balance between coverage and capacity. However, this bandwidth remains insufficient to support high-throughput environments, such as hotspots with dense connection demands.

The high-band spectrum, specifically the 24-92 GHz range, also known as the mmWave band, allows for high-capacity services with wide contiguous bandwidth, though it faces coverage limitations. The sub-THz range within 92-300 GHz of the high-band is well-suited for both existing and emerging services that demand an ultimate user experience, such as holograms and XR, which require ultra-high capacity and ultra-low latency.

To explore the 6G spectrum in depth, we analyze these three band groups across three key dimensions: coverage, contiguous bandwidth, and frequency. These dimensions are essential for determining service usage scenarios. Our initial approach to examining potential 6G spectrum candidates is depicted in Fig. 1.7.

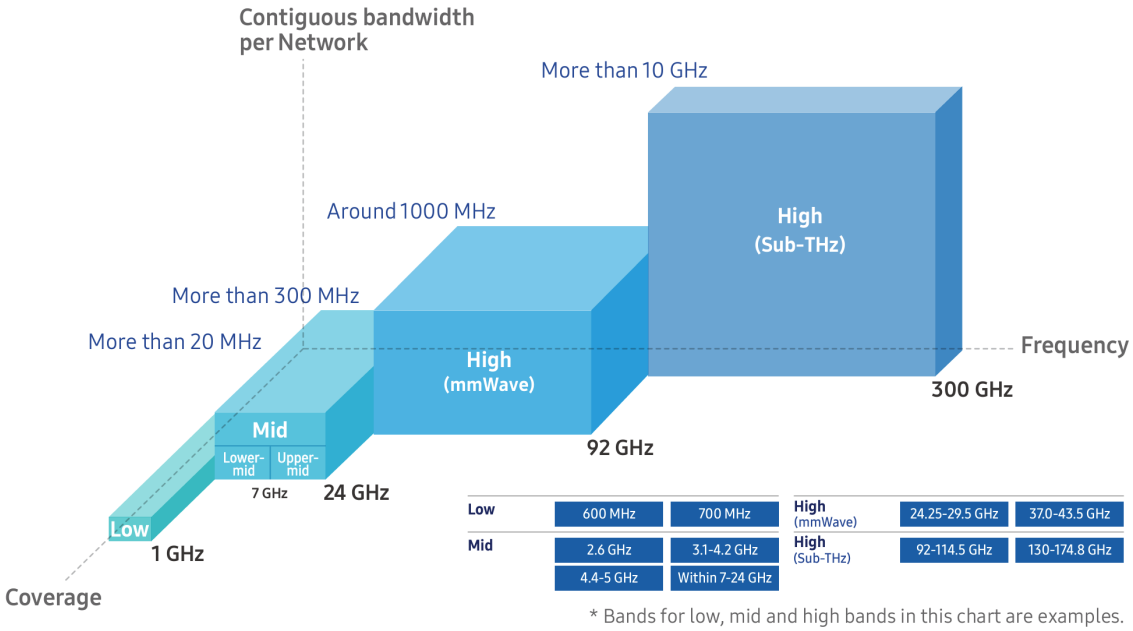

Figure 1.7: Three dimensions of 6G spectrum grouping.

1.1.2.3 Requirements

To enable advanced multimedia services such as truly immersive XR, mobile holograms, and digital replicas, 6G must deliver significantly higher data rates than 5G. While 5G was designed to achieve a peak data rate of 20 Gbps, the target for 6G is a peak data rate of 1,000 Gbps, along with a user-experienced data rate of 1 Gbps.

To provide these advanced services to a large number of users, the overall network performance must be enhanced, aiming for a spectral efficiency that is twice that of 5G. For delay-sensitive, real-time applications such as interactive tactile internet, substantial improvements in latency-related performance are essential. The performance targets include air latency of less than 100 microseconds, end-to-end (E2E) latency of less than 1 millisecond, and extremely low delay jitter on the order of microseconds. Meeting these requirements would result in a user-experienced latency of less than 10 milliseconds, aligning with the motion-to-photon latency needs of XR services. This latency requirement encompasses all latency components, including wireless and wireline links, as well as computational delays on both client and server sides.

For latency-sensitive services that demand extreme reliability, such as industrial automation, emergency response, and remote surgery, 6G aims to improve reliability by a factor of 100 compared to 5G, targeting an error rate of 10^{-7}.

Network coverage has been a crucial aspect of past generations and will continue to be vital in 6G. We aim to support broader coverage than 5G. The maximum supported speed for mobile devices has increased from 350 km/h in 4G to 500 km/h in 5G, and further improvements may be necessary in 6G to accommodate advances in transportation systems. The anticipated surge in connected devices will require 6G to support approximately 10^7 devices per square kilometer, which is ten times the connection density requirement of 5G.

In the 6G era, users will expect seamless, high-end services in their daily lives, ideally with extended battery life. Given the increasing emphasis on environmental

sustainability, minimizing the energy consumption of 6G networks is a priority. The goal is to enhance the energy efficiency of both devices and networks by at least two-fold.

Fig. 1.8 illustrates the enhancement of key requirements from 5G to 6G.

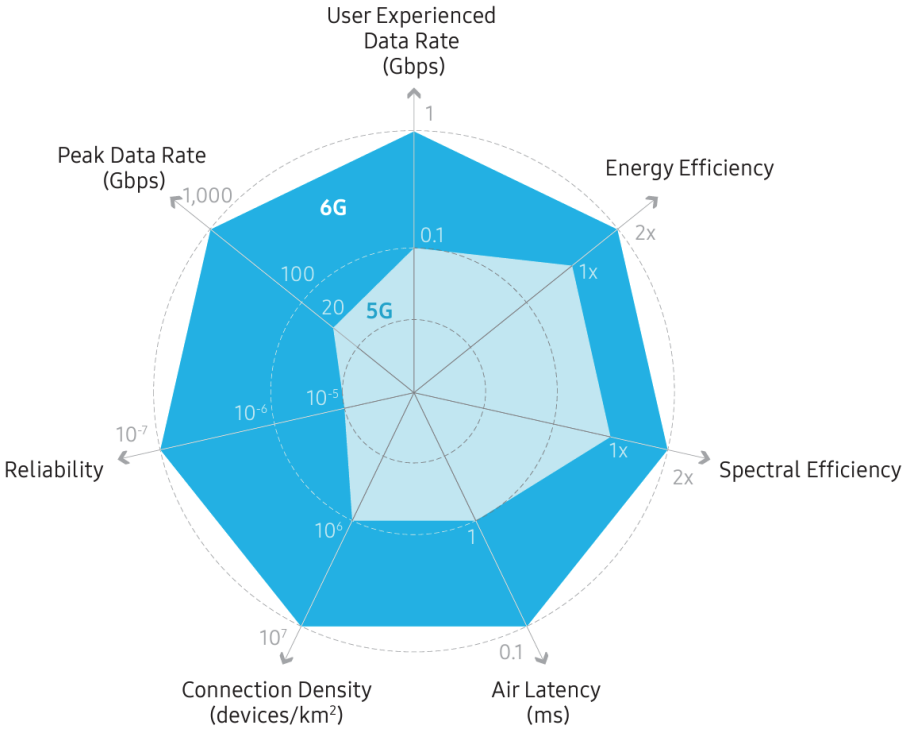

Figure 1.8: Comparison of key performance requirements between 5G and 6G.

1.1.3 Low Resolution Data Converters

Low-resolution data converters are valuable in applications where speed, power efficiency, and cost are prioritized over high precision. They are widely used in wireless communications, portable devices, and high-speed digital systems. While they offer advantages in terms of simplicity and performance, careful consideration of their limitations, such as increased quantization noise and limited dynamic range, is necessary to ensure optimal system performance.

For infinite resolution, a typical received signal is given by

$$\mathbf{y} = \mathbf{H}\mathbf{x} + \mathbf{n} \tag{1.1}$$

where $\mathbf{H}$, $\mathbf{x}$, and $\mathbf{n}$ are the channel matrix, precoded symbols, and additive white Gaussian noise (AWGN), respectively. The landscape of wireless communications literature is rich with various proposals for nonlinear quantization models. However, when it comes to a more significant number of Analog-to-Digital Converter (ADC) bits, the analysis of such models escalates in complexity. The realm of quantized systems has seen the derivation of a lower bound on spectral efficiency, achieved by interpreting the quantization as additive Gaussian noise. This noise exhibits a variance inversely proportional to the quantizer's resolution, namely $2^{-\mathsf{Bits}}$ multiplied by the received input power.

Intriguingly, more recent research endeavors, as illustrated in [85, 5], have employed the additive quantization noise model (AQNM) for mmWave signals that feature arbitrary numbers of ADC bits. This area of work aligns closely with other studies [115, 51], which have derived Gaussian approximations via Bussgang Theory, aiming to linearize the nonlinear quantization distortion. The similarities between these studies and AQNM modeling are noteworthy.

Following this line of reasoning, the received signal, as expressed in (1.1), is subjected to processing through the Radio Frequency (RF) chains. Subsequently, the ADC converts it into the digital domain. The AQNM provides a representation for the quantized version of (1.1), as follows

$$\mathbf{y}_{\mathsf{q}} = \alpha\mathbf{y} + \mathbf{q} \tag{1.2}$$

where $\mathbf{q}$ is the additive quantization noise, $\alpha = 1-\eta$, and η is the inverse of the signal-to-quantization-plus-noise ratio (SQNR), which is inversely proportional to the square of the resolution of an ADC, i.e., $\eta = \frac{\pi\sqrt{3}}{2} \cdot 2^{-2\mathsf{Bits}}$. See Table 1.1.

To examine the robustness and validity of the AQNM, we contemplate a uniform quantizer defined by a specific step size Δ. This step size is given by the formula

Table 1.1: η for different numbers of bits [170].

Bits	1	2	3	4	5
$\boldsymbol{\eta}$	0.3634	0.1175	0.03454	0.009497	0.002499

$\Delta = \frac{b-a}{2^{\mathsf{Bits}}-1}$, wherein a and b represent the lower and upper bounds of the quantizer respectively.

We introduce $\mathbf{y}_{\mathsf{e}}$ as the output generated by the uniform quantizer. Additionally, we denote $\mathbf{y}_{\mathsf{q}}$ as the signal quantized via the AQNM, defined by $\mathbf{y}_{\mathsf{q}} = \alpha\mathbf{y} + \mathbf{q}$. In this equation, $\mathbf{y}$ symbolizes the input of the quantizer, which follows a uniform distribution in the range $[a, b]$.

It is worth noting that $\mathbf{q}$ is characterized as the AQNM, following a Gaussian distribution with a zero mean and a variance as per the guidelines outlined in [8]. This theoretical model and its underpinnings serve as the foundation for further investigation into the behavior of AQNM in the domain of wireless communication.

$$\sigma_{\mathsf{q}}^2 = \frac{\Delta^2}{12} \tag{1.3}$$

The mean square error (MSE) is defined by

$$\mathsf{MSE} = \sum_{n} \mathbb{E}\left[|\mathbf{y}_{\mathsf{e}}[n] - \mathbf{y}_{\mathsf{q}}[n]|^2\right] \tag{1.4}$$

To show the tightness, let's consider an example of a quantizer with $a = -15V$ and $b = 15V$, $\mathbf{y} \sim \mathcal{U}[-15, 15]$.

As shown by Fig. 1.9, as the number of quantization bits gets increased the MSE is decreasing, i.e., the precision of the AQNM is accurate and the model gets closer to the output of the quantizer.

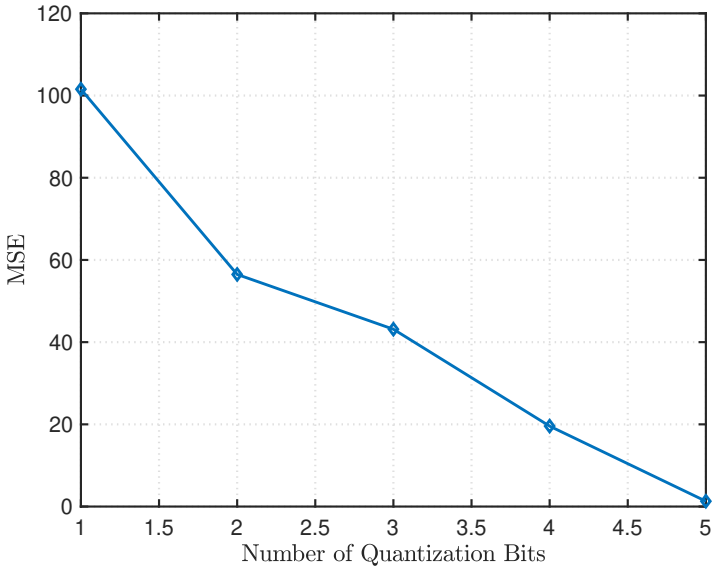

Figure 1.9: Mean square error between the output of the quantizer and the quantized signal through AQNM.

1.1.4 Evolution of Duplex Technology

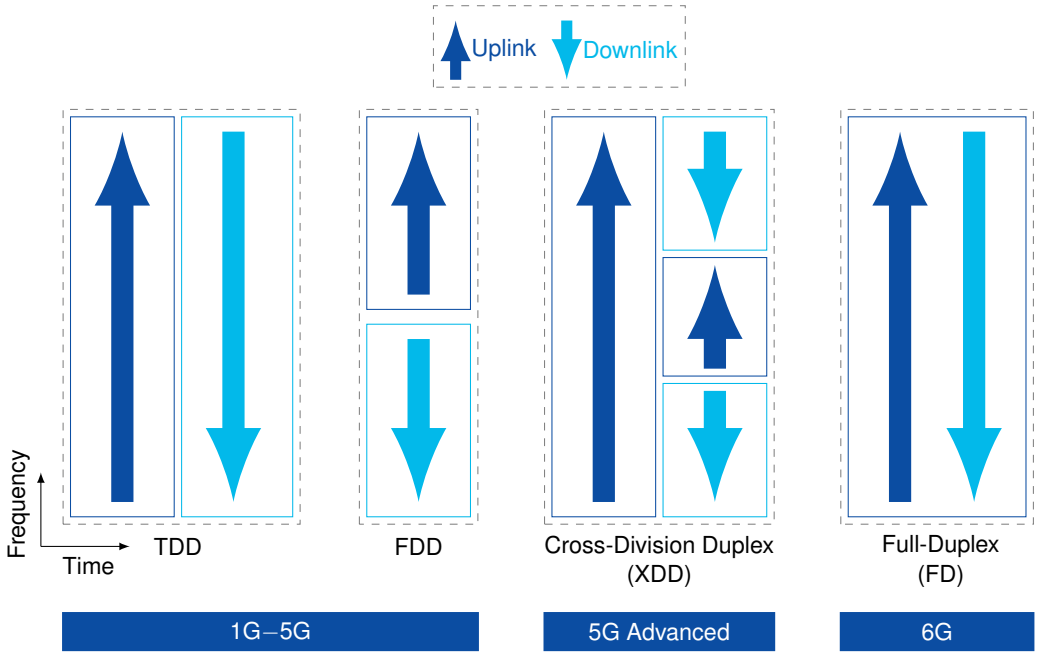

Figure 1.10: Evolution of duplex technology.

In early cellular systems such as 3G, Frequency Division Duplexing (FDD) was commonly used due to the narrowband characteristics of wireless signals and the symmetrical nature of downlink and uplink traffic, particularly for voice telephony, which was the predominant application at the time. In FDD, downlink and uplink utilize separate, non-overlapping frequency resources, as illustrated in the Fig. 1.10, with substantial separation between the frequencies to prevent interference between the signals. A key advantage of FDD is that it allows both downlink and uplink to fully utilize time resources, thereby enhancing coverage. However, a limitation of FDD is its inflexibility in reallocating frequency resources between downlink and uplink, as these resources are fixed for each direction.

Unlike FDD, Time Division Duplexing (TDD) utilizes the same frequency resources for both downlink and uplink. Rather than separating downlink and uplink through distinct frequency bands, TDD allocates dedicated and non-overlapping time resources for each, as shown in Fig. 1.10. As a result, in TDD, neither downlink nor uplink can fully access the time resources, leading to reduced coverage compared to FDD.

Although TDD was initially introduced in 3G to complement FDD, it was not as widely adopted. However, as wireless traffic has grown exponentially, driven by downlink-heavy applications such as video streaming and wireless internet, the advantages of TDD have become more apparent. TDD allows the allocation of additional time resources to either downlink or uplink, depending on network demands, a flexibility not possible with FDD. This limitation of FDD often results in under utilization of uplink frequency resources while downlink resources are heavily used in many commercial 4G networks. In 5G, most newly assigned spectrum bands are TDD carriers, which better accommodate the asymmetric nature of downlink and uplink traffic. However, TDD still faces the inherent challenge of limited coverage compared to FDD.

Cross-Division Duplex (XDD) was developed to address the limitations of

TDD while preserving its key advantages. XDD enables simultaneous downlink and uplink operations within a TDD carrier by utilizing non-overlapping downlink and uplink frequency resources within the same carrier. This flexible allocation of frequency resources allows XDD to effectively manage the asymmetric downlink and uplink traffic ratios typical of modern cellular systems. Additionally, XDD can allocate non-overlapping downlink and uplink resources in both the frequency and time domains. In essence, duplexing can be achieved through time, frequency, or a combination of both within a TDD carrier, depending on the specific requirements of the deployment scenario.

In XDD, a base station can allocate non-overlapping frequency resources to terminals, allowing downlink and uplink transmissions to occur simultaneously within the same time slot, as illustrated in Fig. 1.10. For instance, cell-edge terminals can be assigned to continuously transmit uplink while the base station simultaneously transmits downlink to other terminals. Consequently, the accumulated received energy on the uplink at the base station is higher in XDD than in TDD, resulting in enhanced coverage, as depicted in Fig. 1.11. It is important to note that simultaneous downlink and uplink operations occur only at the base station. For terminals, they can either transmit uplink or receive downlink at any given time, but not both. Although enabling simultaneous uplink reception and downlink transmission at the terminal level would offer additional benefits, the implementation challenges, particularly for devices with small form factors such as smartphones, would be prohibitive.

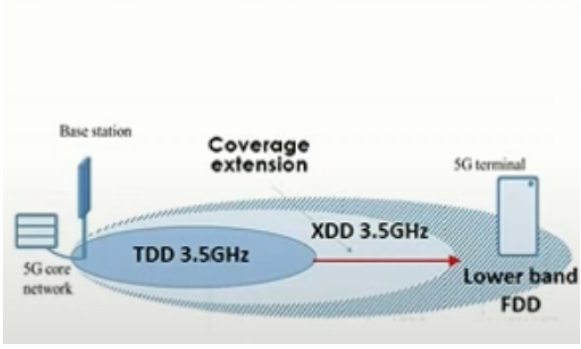

Figure 1.11: Extending 5G TDD coverage with XDD.

Unlike XDD which allows the uplink to borrow a portion of the frequency resources from the downlink, FD allows overlap between downlink and uplink over the entire time-frequency resource as illustrated by Fig. 1.10.

Following benefits can be expected for XDD/FD compared to conventional TDD:

- **Coverage enhancement**: One of the most straightforward ways to improve coverage is by increasing the total energy delivered to the receiver. In TDD, the received energy at the base station is limited because only about 20% to 25% of the time resources are typically allocated to uplink in commercial networks. In contrast, FDD does not face this issue, as the uplink has full access to all time resources. XDD/FD addresses this limitation by enabling simultaneous downlink and uplink operations within a single TDD carrier, allowing uplink coverage to be extended to levels comparable to FDD. Unlike TDD, where uplink access is restricted, XDD/FD enables the uplink to utilize 100% of the time resources, significantly enhancing coverage.

- **Latency reduction**: A notable drawback of TDD compared to FDD is the increased latency caused by the intermittent availability of uplink transmission times. Due to the limited allocation of uplink transmission slots, the hybrid automatic repeat request (HARQ) responses for downlink and other feedback information transmitted on the uplink experience greater latency than in FDD. When the latency of HARQ responses for downlink increases, it prolongs the time required to clear data packets from the base station buffers, leading to reduced user-perceived throughput. In contrast, XDD/FD can minimize this latency because uplink transmission time is continuously available, allowing for more timely HARQ responses and feedback.

- **Throughput enhancement**: Extending the uplink transmission time in XDD/FD enhances not only coverage and latency but also throughput. For terminals lo-

cated closer to the cell center, the additional uplink resources can be utilized to increase the uplink data rate, thereby improving overall performance.

1.1.5 Challenges

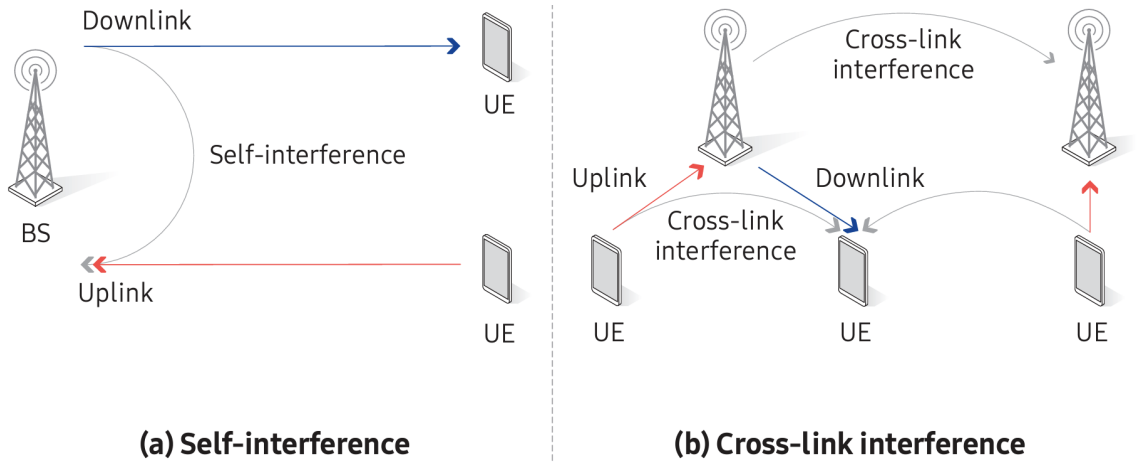

Figure 1.12: Main obstacles in deploying (XDD/FD).

Deviating from the "mutually exclusive" (FDD/TDD) principle in duplex communication introduces challenges such as SI and cross-link interference. SI, as depicted in Figures 1.12 and 1.13, occurs at the base station (BS) receiver when it transmits downlink signals on the same time-frequency resources used by uplink signals from user equipment (UE). Due to the proximity of the BS's transmit and receive antennas, the SI is significantly stronger than the desired signals from the UEs. To advance duplex technology beyond the "mutually exclusive" approach, effectively mitigating SI is essential. Research in SI cancellation (SIC) has shown that effective solutions often involve both analog and digital domain cancellation techniques [141, 84]. The following requirements need to be met for the SIC implementation of an XDD base station.

- The power of the downlink signal received on the uplink receiver should be sufficiently suppressed to prevent ADC saturation.

- Residual interference after SIC must not rise above the base station receiver's noise level to provide sufficient demodulation and decoding performance.
- Frequency separation between the uplink and downlink within the TDD carrier which acts as a guardband should be minimized to achieve XDD without sacrificing resource efficiency.

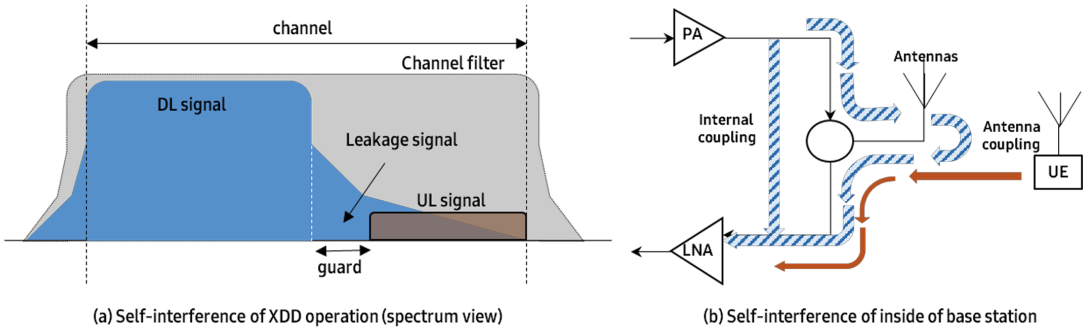

Figure 1.13: SI scenario in XDD.

Table 1.2 summarizes the amount of SI to be canceled to enable FD operation for various network generations.

Table 1.2: Amount of SI Suppressed to Enable FD Operation [35, 48, 89, 138, 144, 101, 13, 128, 112].

Generation	Technology/Medium Access	Channel Bandwidth	Transmit Power	Noise Power	SI Cancellation
1G	AMPS/FDMA	30 KHz	up to 60 dBm	-129 dBm	189 dB
2G	GSM/TDMA	200 KHz	36 dBm	-121 dBm	157 dB
3G	WCDMA/UMTS	5 MHz	43 dBm	-107 dBm	150 dB
	CDMA 2000	1.25 MHz	43 dBm	-113 dBm	156 dB
4G/LTE	LTE-Advanced (OFDMA/SC-FDMA)	20 MHz	46 dBm	-101 dBm	147 dB
	WIMAX/ Scalable OFDMA	10 MHz	43 dBm	-104 dBm	150 dB
5G	BDMA/ FBMC	60 GHz	20 dBm	-96 dBm	116 dB
	802.11ac - Gigabit Wi-Fi (taunted as 5G Wi-Fi)	20, 40, 80, 160 MHz	20 dBm	-91 dBm	112 dB
	802.11ad - Wireless Gigabit (Microwave Wi-Fi)	2 GHz	20 dBm	-81 dBm	101 dB
	802.11af - White-Fi	5, 10, 20, 40 MHz	20 dBm	-98 dBm	118 dB

† Advanced Mobile Phone Service (AMPS), Frequency Division Multiple Multiple Access (FDMA), Global Systems for Mobile Communications (GSM), Time Division Multiple Access (TDMA), Code Division Multiple Access (CDMA), Wideband CDMA (WCDMA), Universal Mobile Telecommunications Systems (UMTS), Long Term Evolution (LTE), Orthogonal/Single Carrier Frequency Division Multiple Access (OFDMA/SC-FDMA), Worldwide Interoperability for Microwave Access (WIMAX), Beam Division Multiple Access (BDMA), Filter Bank Multi-Carrier (FBMC).

Cross-link interference (CLI) refers to the interference that occurs between UEs or between BSs. Fig. 1.12 provides an example where UEs adhere to the "mutually exclusive" principle between their uplink transmissions and downlink receptions, while the BS does not. CLI between UEs arises when the same time-frequency resource is allocated for uplink transmission from one UE and downlink transmission to another UE. This UE-to-UE CLI can be mitigated if the BS selects a group of UEs that do not cause significant interference to each other. CLI between BSs occurs when the downlink transmission from one BS (the aggressor) uses the same time-frequency resource as the uplink of another BS (the victim). Mitigating BS-to-BS CLI requires close coordination between BSs to manage resource allocation effectively.

Another challenge is managing adjacent channel CLI, known as inter-operator cross-carrier CLI. This issue arises when the spectrum allocated to one operator is positioned directly adjacent to the spectrum of another operator within the same cellular band. For instance, in a region with nationwide 5G coverage, three Mobile Network Operators (MNOs) have their 5G spectrum allocations situated next to each other (as shown in Fig. 1.14).

- MNO#1: 3.42 GHz - 3.6GHz (3GPP band n78)
- MNO#2: 3.5 GHz - 3.6 GHz (3GPP band n78)
- MNO#3: 3.6 GHz - 3.7 GHz (3GPP band n78)

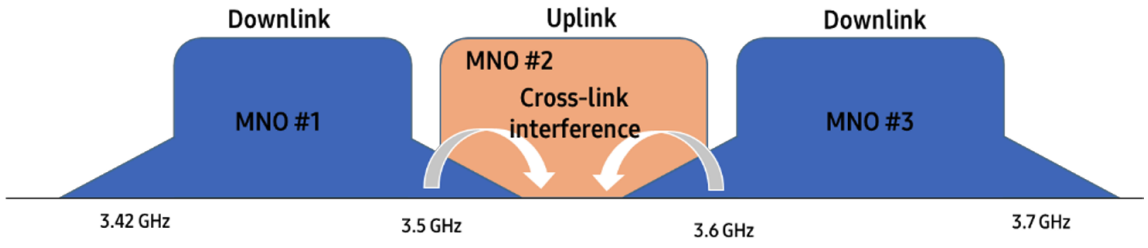

Figure 1.14: CLI from adjacent carriers from multi-operator scenario.

Assume that MNO#2 is deploying XDD in its network. In this scenario, MNO#2 must address not only co-channel CLI (such as inter-base station and inter-terminal CLI) within its own spectrum but also adjacent channel CLI caused by the downlink transmissions of the other two MNOs due to insufficient filtering. In a conventional TDD system, this adjacent channel CLI would not pose a problem, as all three operators would use the same uplink-downlink time resource configuration, effectively eliminating adjacent channel CLI. However, managing adjacent channel CLI is significantly more challenging than dealing with SI, as there is no prior knowledge of the interference characteristics.

1.1.6 SI Mitigation Techniques

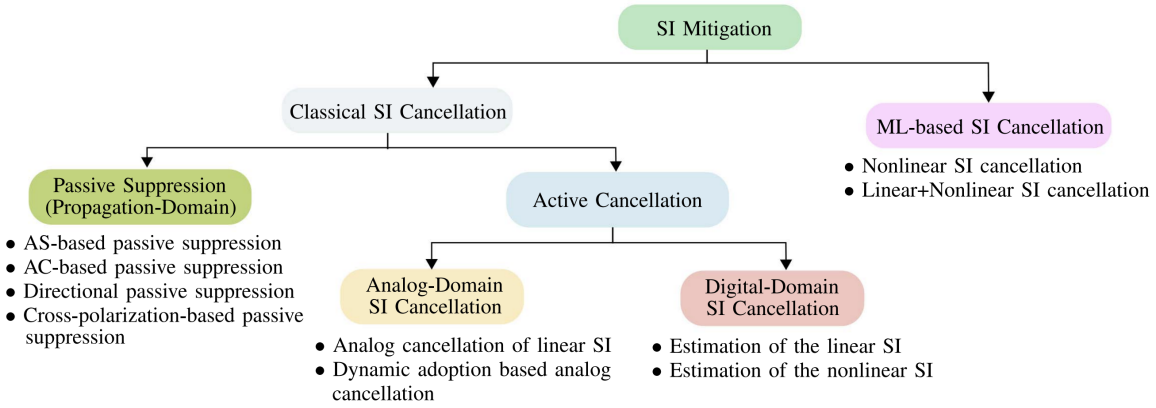

Figure 1.15: SI mitigation techniques [104].

In FD transceivers, SI power suppression is typically achieved through a synergistic application of both active and passive techniques. Passive cancellation leverages the enhancement of path loss for the loopback SI signal, utilizing strategies such as array directivity, physical separation of antennas (antenna isolation), polarization, and the incorporation of RF absorbing materials. For instance, improvements in array directivity and strategic antenna placement have been shown to attenuate SI power by 30 dB and 47 dB, respectively, while cross-polarization techniques can facilitate up to 50 dB of SI reduction [81].

Conversely, active cancellation techniques are predicated on the precise knowledge of the transmitted signal and are typically executed in three distinct stages: RF suppression, antenna suppression, and digital suppression. RF suppression uses the known transmitted signal as a reference within the RF chain to reconstruct and subsequently subtract the SI. Antenna cancellation is achieved by generating two antiphase replicas of the transmitted signal through multiple transmit (TX) and receive (RX) antennas, thereby nullifying the SI through the superposition of these antiphase replicas. Digital cancellation complements RF or antenna suppression methods by further attenuating the SI in the baseband, which, when combined with either RF or antenna suppression techniques, can result in approximately 60 dB of SI reduction, as both SI and noise are concurrently mitigated [81]. However, these techniques may encounter performance degradation due to nonlinearities introduced by data converters, power amplifiers, in-phase and quadrature (IQ) imbalance, and phase noise, leading to significant residual SI [156]. This highlights the complex interplay between various suppression methods and the inherent challenges in achieving optimal SI mitigation in FD communication systems. Table 1.2 summarizes the amount of SI to be canceled to enable FD operation for various network generations.

Machine learning (ML)-based SI cancellation (SIC) is an advanced approach used in FD wireless communication systems to address the complex and dynamic nature of SI, where traditional analog and digital methods often fall short. By leveraging models such as neural networks, reinforcement learning, and support vector machines, ML-based SIC can adaptively learn and mitigate interference in real time, enhancing signal quality and overall system performance. Key benefits include the ability to handle nonlinear interference patterns and dynamically adjust to varying channel conditions. However, challenges such as high computational complexity, significant data requirements, latency issues, and the need for robust model generalization must be managed. Additionally, integrating ML-based SIC with existing systems can be complex and resource-intensive, posing limitations in resource-constrained environments. Despite these challenges, ML-based SIC holds significant potential to improve

FD communication in 5G and future wireless networks by providing more effective interference management and enhancing spectral efficiency.

Table 1.3 summarizes the SI mitigation techniques along with the advantages and limitations.

1.1.7 Beamforming

Beamforming is a signal processing technique used in wireless communication systems to direct the transmission or reception of signals in specific directions using an array of antennas. By controlling the phase and amplitude of the signals at each antenna in the array, beamforming creates constructive interference in desired directions and destructive interference in others. This effectively forms a focused beam that can be steered dynamically toward a target, such as a user or device, enhancing signal strength, reducing interference, and improving overall communication efficiency.

Beamforming works by using an array of antennas where each antenna element contributes to the overall signal in a controlled manner. By adjusting the phase and amplitude of the signals sent from or received by each antenna element, beamforming shapes the overall radiation pattern of the antenna array. Constructive interference occurs in the desired direction, where the signals from each antenna combine to strengthen the signal, while destructive interference reduces signals in unwanted directions. Beamforming can be implemented in various ways, including analog, digital, and hybrid beamforming, each offering different balances of complexity, flexibility, and performance.

Table 1.3: Performance comparison among variant SI cancellation techniques [171].

Category	Technique	$N_{\mathsf{TX}} \times N_{\mathsf{RX}}$	Advantages	Disadvantages
Passive Cancellation	• Directional • Diversity • Antennas • Isolation		• SI mitigated due to pathloss • Minimizes inter-device interference • Improves power efficiency • More isolation results in a better mitigation of SI signal	• Performance depends highly on AS and beam pattern • AS is restricted by variant factors such as device size and interference channel estimation accuracy • Restricted application to SISO
Analog Cancellation (Active)	• Antenna cancellation	2×1	• Easy to implement • High cancellation capability • Robust in narrowband systems	• Broadband-induced loss • Degrades the received signal • Limited transmit power • Requires fixed AS
	• Pre-nulling	$N_{\mathsf{TX}} \times 1$	• Simple to implement • No influence on receiver BER • Stringent requirements on antenna isolation are required	• SI Channel estimation is required • Designed specifically for flat-fading channels
	• AFC	$1 \times N_{\mathsf{RX}}$	• Low complexity • Needs no training sequence • No delay insertion in the relay • Compensates for multipath propagation	• The second order statistical information of the source signal is required to be exploited by the filter design
	• Precoding/Decoding	$N_{\mathsf{TX}} \times N_{\mathsf{RX}}$	• Better than pre-nuling • Enables advanced optimization • Capacity optimization	• Requires SI estimation • Requires SVD of SI channel matrix
	• Block diagonalization	$N_{\mathsf{TX}} \times N_{\mathsf{RX}}$	• Outpeforms ZF beamforming • Precoding with adaptive power allocation to optimize the sum rate	• CSI is required by the base station • SVD is required • Power allocation satisfies KKT conditions
	• ZF filters	$N_{\mathsf{TX}} \times N_{\mathsf{RX}}$	• High capacity for a high SNR • Multiple spatial streams are supported in the MIMO relay	• Performance loss in low-SNR regions • SVD is required
	• Optimal Eigenbeamforming	$N_{\mathsf{TX}} \times N_{\mathsf{RX}}$	• Power of the residual SI is minimized	• Beam selection matrices are calculated • SVD is required
	• Maximum SIR	$N_{\mathsf{TX}} \times N_{\mathsf{RX}}$	• Improves the useful signal • Suppresses both SI and noise	• High complexity in deriving the optimum matrices • Channel attenuation highly impacts the performance
	• MMSE filtering	$N_{\mathsf{TX}} \times N_{\mathsf{RX}}$	• Improves the useful signal • Suppresses both SI and noise	• High complexity
	• TAS	$N_{\mathsf{TX}} \times N_{\mathsf{RX}}$	• Has a low complexity • Avoids losses in low-SNR regions • Adaptivity to varying SIRs	• High dimensional MIMO complicates the best subset selection • Unique solution for the best subset selection is not always achievable
Digital Cancellation (Active)			• Residual SI after analog cancellation can be eliminated in digital domain • Modulation independence • Addresses hidden terminal problem • High collision-combating capability	• Quantization noise cannot be reduced • Becomes unneccessary if preceded by a powerful analog cancellation • Limited cancellation capability

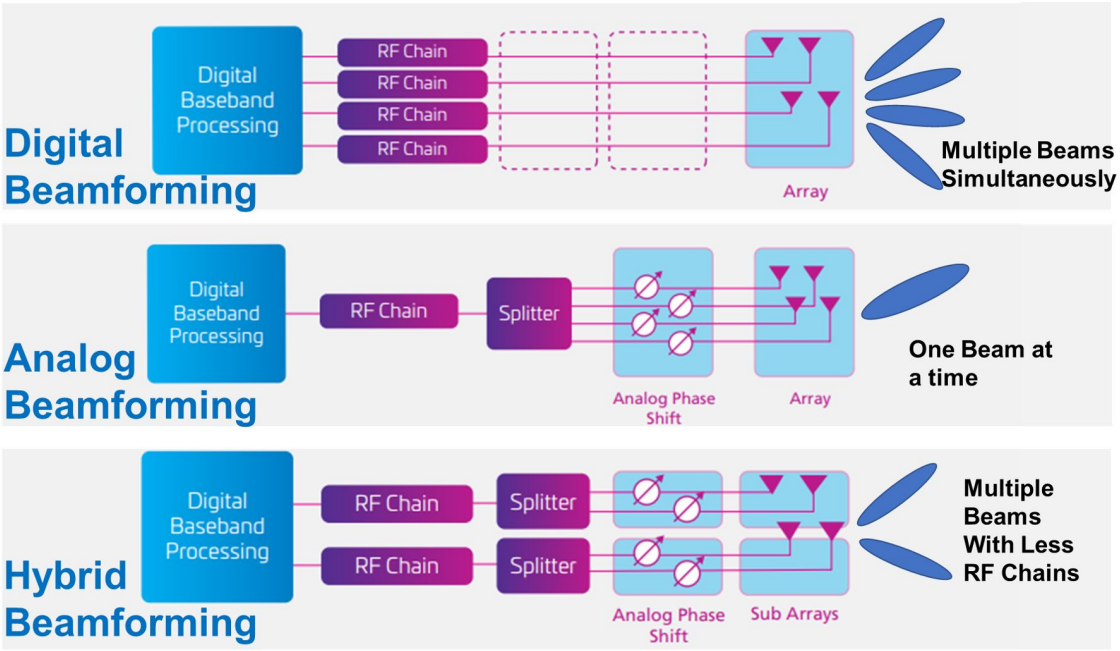

Figure 1.16: Different types of beamforming.

1. **Digital Beamforming**: Utilizes digital signal processing (DSP) to control the phase and amplitude of the signals, offering greater flexibility and precision in shaping the beam. Multiple beams are simultaneously synthesized to serve multiple users. Since each antenna has its own dedicated RF chain, this architecture consumes prohibitively large amount of power, in particular, for massive MIMO.

2. **Analog Beamforming**: Adjusts the phase of the signals in the analog domain using phase shifters (PSs). It is simpler but less flexible compared to digital beamforming. It consists of a single RF chain and serves only one user at a time.

3. **Hybrid Beamforming**: Combines analog and digital beamforming to balance performance and complexity, often used in systems with a large number of antennas, such as massive MIMO in 5G. In this architecture, reduced number

of RF chains, fewer than the number of antennas, are considered while multiple beams are created to serve multiple users. Reducing the number of RF chains is beneficial to save the power, however, it penalizes fraction of the spectral efficiency.

1.1.8 SI Channels Models

SI channel models are essential for designing and evaluating SIC techniques in FD communication systems. These models characterize how the transmitted signal from a device, such as a BS or UE, interferes with its own receiver, which operates on the same frequency simultaneously. Understanding and accurately modeling the SI channel is crucial for developing effective SIC strategies. Here's an overview of some SI channel models.

1.1.8.1 Rician Model

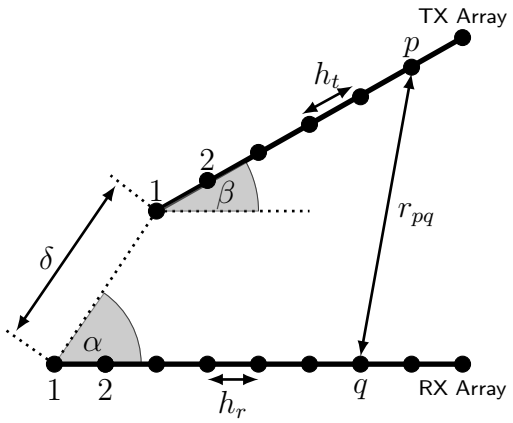

Figure 1.17: Relative position of TX and RX arrays at BS. Given that the TX and RX arrays are collocated, the far-field assumption that the signal impinges on the antenna array as a planar wave does not hold. Instead, for FD transceivers, it is more suitable to assume that the signal impinges on the array as a spherical wave for the near-field LOS channel.

As illustrated in Fig. 1.17, the SI leakage at the BS is modeled by the channel matrix $\mathbf{H}_{\mathsf{SI}}$. Note that the SI channel is decomposed into a static line-of-sight (LOS) channel modeled by $\mathbf{H}_{\mathsf{LOS}}$, which is derived from the geometry of the transceiver, and a non-line-of-sight (NLOS) channel described by $\mathbf{H}_{\mathsf{NLOS}}$. Considering a wideband fading for the purpose of generality, the ℓ-th tap of the aggregate SI channel matrix can be expressed by

$$\mathbf{H}_{\mathsf{SI}}[\ell] = \underbrace{\sqrt{\frac{\kappa}{\kappa+1}}\mathbf{H}_{\mathsf{LOS}}}_{\text{Near-Field}} + \underbrace{\sqrt{\frac{1}{\kappa+1}}\mathbf{H}_{\mathsf{NLOS}}[\ell]}_{\text{Far-Field}} \tag{1.5}$$

where κ is the Rician factor.

$$r_{pq} = \sqrt{(\delta\cos\beta + (p-1)h_t\cos\alpha - (q-1)h_r)^2 + (\delta\sin\beta + (p-1)h_t\sin\alpha)^2} \tag{1.6}$$

LOS Channel: The (q,p)-th entry of the LOS SI leakage matrix can be written as

$$[\mathbf{H}_{\mathsf{LOS}}]_{qp} = \frac{1}{r_{pq}}\mathsf{e}^{-i2\pi\frac{r_{pq}}{\lambda}} \tag{1.7}$$

where r_{pq} is the distance between the p-th antenna in the TX array and q-th antenna in the RX array at BS given by (1.6).

NLOS Channel: It is often useful to represent the channel in the frequency domain. In general, the channel response is time-varying [61]

$$\mathbf{H}(t,f) = \sum_{\ell=0}^{N_{\mathsf{p}}-1} \alpha_\ell \mathsf{e}^{i2\pi(\nu_\ell t - \tau_\ell f)}\mathbf{a}_{\mathsf{R}}(\phi_{\mathsf{R},\ell},\theta_{\mathsf{R},\ell})\mathbf{a}_{\mathsf{T}}^*(\phi_{\mathsf{T},\ell},\theta_{\mathsf{T},\ell}) \tag{1.8}$$

where $\phi_{\mathsf{R},\ell},\theta_{\mathsf{R},\ell}$ are the azimuth and elevation angles of arrival (AoA) of the ℓ-th ray, $\phi_{\mathsf{T},\ell},\theta_{\mathsf{T},\ell}$ are the angles of departure (AoD) of the ℓ-th ray. We denote by $\mathbf{a}(\phi,\theta)$ the array response of the uniform rectangular array defined by

$$\mathbf{a}(\phi,\theta) = \frac{1}{\sqrt{NM}}\left[1,\ldots,\mathsf{e}^{i\frac{2\pi}{\lambda}(d_h p\sin\phi\sin\theta + d_v q\cos\theta)},\ldots,\mathsf{e}^{i\frac{2\pi}{\lambda}(d_h(M-1)\sin\phi\sin\theta + d_v(N-1)\cos\theta)}\right]^T \tag{1.9}$$

where N and M are the vertical and horizontal dimensions of the array panel, respectively. λ is the signal wavelength, d_h and d_v are the antenna spacing in horizontal and vertical dimensions, respectively, $0 \leq p \leq M-1$, and $0 \leq q \leq N-1$ are the antennas indices in the 2D plane.

Assuming that the channel is sufficiently slowly varying over the signal period T, the Doppler shifts of all the paths are small, $\nu_\ell T \ll 1$, $\forall \ell, \ell = 1, \ldots, N_{\mathsf{p}}$. Therefore, (1.8) can be reduced to

$$\mathbf{H}(f) = \sum_{\ell=0}^{N_{\mathsf{p}}-1} \alpha_\ell \mathsf{e}^{-i2\pi\tau_\ell f} \mathbf{a}_{\mathsf{R}}(\phi_{\mathsf{R},\ell}, \theta_{\mathsf{R},\ell}) \mathbf{a}_{\mathsf{T}}^*(\phi_{\mathsf{T},\ell}, \theta_{\mathsf{T},\ell}) \tag{1.10}$$

Besides, if the channel bandwidth W is sufficiently small so that $W\tau_\ell \ll 1$, $\forall \ell, \ell = 1, \ldots, N_{\mathsf{p}}$, then the channel fading becomes narrowband and (1.10) can be simplified into

$$\mathbf{H} = \sum_{\ell=0}^{N_{\mathsf{p}}-1} \alpha_\ell \mathbf{a}_{\mathsf{R}}(\phi_{\mathsf{R},\ell}, \theta_{\mathsf{R},\ell}) \mathbf{a}_{\mathsf{T}}^*(\phi_{\mathsf{T},\ell}, \theta_{\mathsf{T},\ell}) \tag{1.11}$$

1.1.8.2 Empirical Model

Improving the performance of current SIC schemes relies on exact model of SI channels [4]. A number of measurement based studies have been done to present empirical models of SI channels.

Power delay profiles (PDPs) of SI channels at 2.6 GHz in indoor environments were measured in studies [154] and [149]. In [154], the PDP was decomposed into three components: the leakage path, the antenna reflection path, and space multipath. The space multipath was further modeled using a power-law decay with a noise-like variation following a Lognormal distribution. In contrast, the PDP in [149] was represented as an exponentially decaying function with specular components modeled by delta functions. Additionally, the SI channel at 2.45 GHz was characterized using a 2×2 MIMO FD transceiver with dual-polarized antennas, as reported in [31]. This study indicated that the SI channel could be represented by a multipath model

consisting of a quasi-static internal subchannel and a time-varying external subchannel, modeled by a modified Saleh-Valenzuela model. Furthermore, the dispersive behaviors of the SI channel in both direction and delay domains were investigated at millimeter-wave frequency bands within a meeting room environment, as explored in [60].

While previous studies primarily focused on indoor environments, Wang et al. [150] conducted measurement campaigns in a dense urban environment. Their observations revealed that the power of multipath components within a cluster decayed exponentially, whereas the most significant path in each cluster remained unaffected. Additionally, residual SI (RSI) channel measurements were performed in a mmWave beamformed FD system for both indoor and outdoor settings, as reported in [82]. The study found that RSI exhibited long propagation delays that could not be effectively mitigated by conventional analog-circuit-domain cancellation techniques. To the best of our knowledge, this study is unique in investigating the characteristics of RSI independently from direct SI.

AT&T Labs: constructs an empirical SI channel model elaborated in an anechoic chamber [36, 135]. In this study, the authors present a comprehensive analysis and series of measurements pertaining to SI in a multi-panel mmWave FD communication system operating at 28 GHz. Utilizing an anechoic chamber, the authors perform the measurements of the SI power between the input of a transmitting phased array and the output of a co-located receiving phased array. Both arrays were electronically steered across a range of directions in azimuth and elevation. Figures 1.18, 1.19 and 1.20 illustrate the block diagram explaining the steps of measurement collections as well as the layout of the anechoic chamber wherein the experiments are carried out.

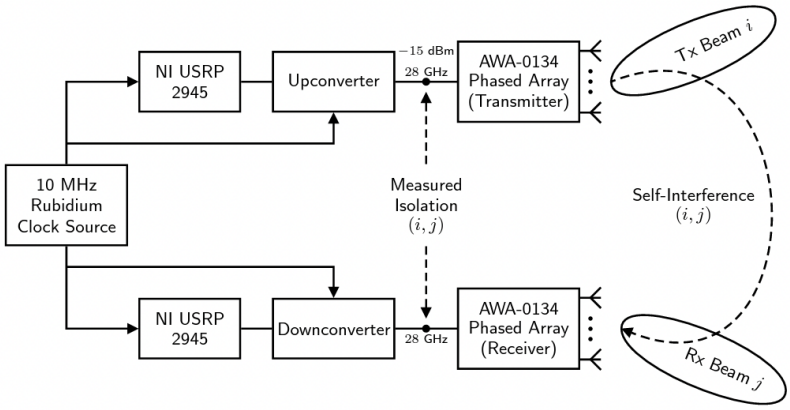

Figure 1.18: A block diagram explaining the way the measurements are carried out by AT&T Labs.

The power measurements of SI provide invaluable insights into the feasibility of a FD communication system receiving a target signal while simultaneously transmitting in-band. Our study, comprising nearly 6.5 million measurements, demonstrated that increased SI is typically coupled when the transmitting and receiving phased arrays direct their beams toward each other. However, slight shifts in the steering direction, on the order of a single degree, can lead to considerable fluctuations in SI power.

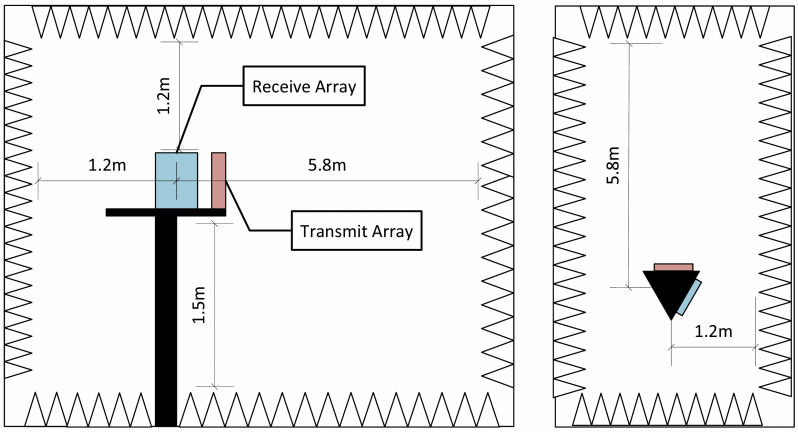

Figure 1.19: A side-view (left) and top-view (right) of the phased array measurement platform in the anechoic chamber.

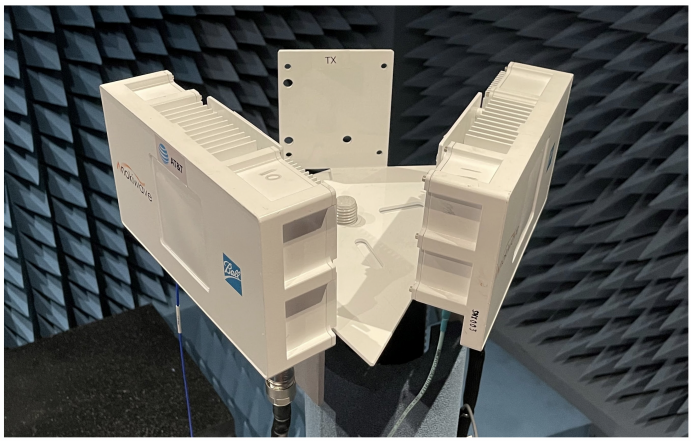

Figure 1.20: 28 GHz Phased array measurement platform inside an anechoic chamber; receive array on left and transmit array on right

These measurements were meticulously analyzed to characterize the spatial variability of SI, enabling to better quantify and create a statistical model of this sensitivity. The analysis and the resulting statistical findings serve as useful references when developing and evaluating mmWave FD systems. Furthermore, this study motivates a myriad of future topics including beam selection, beamforming codebook design, and SI channel modeling.

Following the empirical model, a statistical geometric channel model is elaborated based on the parameters fitting from the collected data, depicted by Fig. 1.21.

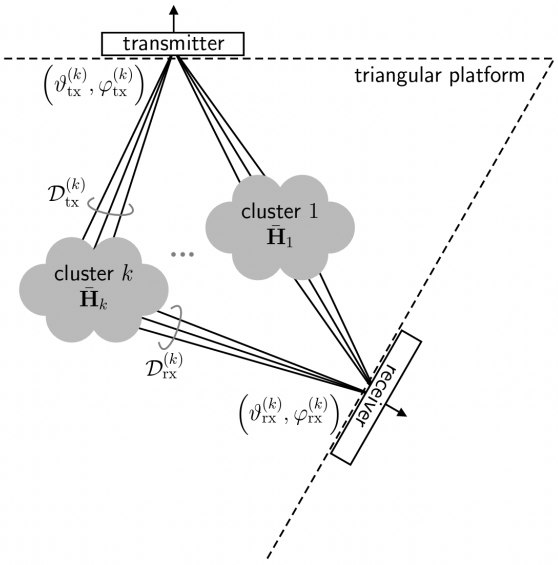

Figure 1.21: An illustration of coupling clusters comprising the coarse geometric model of the SI channel between the transmit and receive arrays.

The channel matrix produced by the k-th cluster (in Fig. 1.21) is given by

$$\mathbf{H}_k = \sum_{(\theta_{\mathsf{tx}},\phi_{\mathsf{tx}})\in\mathcal{D}_{\mathsf{tx}}^{(k)}} \sum_{(\theta_{\mathsf{rx}},\phi_{\mathsf{rx}})\in\mathcal{D}_{\mathsf{rx}}^{(k)}} \mathbf{a}_{\mathsf{rx}}(\theta_{\mathsf{rx}},\phi_{\mathsf{rx}})\mathbf{a}_{\mathsf{tx}}(\theta_{\mathsf{tx}},\phi_{\mathsf{tx}})^* \tag{1.12}$$

Note that $\mathcal{D}_{\mathsf{rx}}^{(k)}$ and $\mathcal{D}_{\mathsf{rx}}^{(k)}$ are the beamforming codebooks at the receiver and transmitter, respectively. The resulting channel matrix comprising all the $\mathcal{N}_{\mathsf{clust}}$ is $\mathbf{H} = \sum_{k=1}^{\mathcal{N}_{\mathsf{clust}}} \mathbf{H}_k \frac{\sqrt{N_{\mathsf{rx}}N_{\mathsf{tx}}}}{\|\sum_{k=1}^{\mathcal{N}_{\mathsf{clust}}} \mathbf{H}_k\|_F}$.

1.1.8.3 Geometry-Based Statistical Channel Model

Analytical channel models are generally more appealing than empirical models for representing channel behavior in diverse environments. One of the most widely used analytical models is the geometry-based statistical channel model (GBSCM) [33]. GBSCMs are defined by the spatial locations of the transmitter, receiver, and scatterers, which are characterized by their spatial distribution and density within a specified area [174].

The literature features numerous studies on foundational GBSCMs for propagation channels in half-duplex (HD) systems. Liberti and Rappaport [87] introduced a geometrical model for microcell propagation channels, where scatterers are uniformly distributed within an ellipse with the base station and mobile receiver located at the foci. Additionally, a circular model for macrocell channels was developed in [121], assuming scatterers uniformly distributed within a circle centered on the mobile receiver, with the base station positioned outside this area. Subsequent models have utilized ellipses [47, 72] or circles [113, 120, 68] to define scattering areas as illustrated by Fig. 1.22.

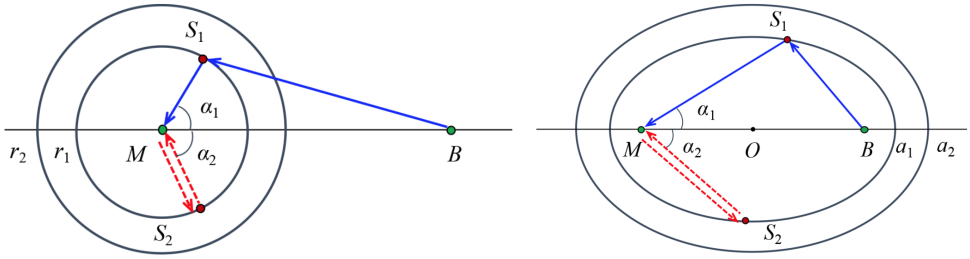

(a) Concentric ellipses model. (b) Concentric ellipses model.

Figure 1.22: The BS and mobile station (MS) are denoted by green circles and the reflectors by red circles. The blue solid and red dash arrows denote the propagation paths of DS from S_1 and RSI from S_2, respectively. Note that the propagation paths of RSI from S_1 and DS from S_2 are omitted.

A multi-elliptical model for single scattering path geometry was proposed by Parsons and Bajwa [119], with an extension in [174] that links the Doppler effect to the spatial positions of objects. Other forms such as rings and semi-ellipses have also been employed as scattering areas [114, 164]. Beyond these 2-D scattering models, 3-D scattering models have been developed as well, as seen in [109, 127, 57].

1.2 Dissertation Summary

In summary, I have dedicated my research to the development of advanced signal processing techniques aimed at effectively mitigating interference and optimiz-

ing data rates, thereby demonstrating the feasibility of FD technology in real-world applications. These contributions lay the foundation for integrating FD systems into current and emerging communication networks, showcasing their potential to enhance performance in both existing and future applications, such as 5G, 6G, IoT, and beyond. Through rigorous analysis and innovative solutions, this work proves that FD technology can play a pivotal role in overcoming the challenges of next-generation wireless communication systems.

1.2.1 Thesis Statement

In this dissertation, I define the following statement:

FD systems have the potential to double data rates and significantly reduce latency, thereby meeting the stringent demands of current and future applications. Although the inherent SI, particularly arising from the near-far problem, presents a substantial challenge, advanced signal processing techniques can effectively mitigate this interference. By preventing receiver chain saturation, these techniques enable the practical implementation of FD systems, ensuring their viability for real-world applications.

1.2.2 Overview of Contributions

The main contributions of this dissertation are summarized as follows:

- **Chapter 2: Point-to-Point Systems**

  1. The methodology presented in [137] focuses on designing all-digital beamforming and derives a hybrid analog/digital (A/D) decomposition utilizing the Least Squares (LS) method. This approach has two major shortcomings. First, the technique seeks to attenuate SI at baseband. In practical applications, however, this suppression should occur in the analog domain to circumvent saturation in the analog front end. Second, such hybrid LS

approximations are not guaranteed to effectively neutralize SI [172], leading to performance degradation at elevated SI levels. I proposed design explicitly addresses these two issues.

2. I design the hybrid A/D beamformers at the two-FD nodes wherein the analog beamformers substantially minimize the SI power (of around 67 dB reduction on average per Table 2.5)) to avoid ADC saturation and preserve the rank of the effective channel, i.e., sustain the maximum admissible spatial streams/layers. In other terms, we introduced a constraint into the optimization problem to balance the use of the Degree of Freedom (DoF) between suppressing the SI and avoiding rank deficiency of the effective channel. This contribution is in TX and RX beamforming cancellation BFC as illustrated by Fig. 2.2.

3. I design all-digital beamformers, which use a prohibitively consume a large amount of power, to serve as a benchmark. The results show the proposed all-digital solution is very tight to the upper bound.

4. I provide computational complexity analysis of the proposed hybrid A/D and all-digital beamforming design in the number of floating-point operations (FLOPS).

5. I analyze the effects of the number of antennas, number of RF chains, channel estimation error, number of PS resolution bits on spectral efficiency, energy efficiency, SINR per RF chain, and the residual and suppressed analog effective SI reduction.

6. I conduct a comprehensive comparison and discussion to establish a practical design in terms how many number of antennas and RF chains are required to achieve the best tradeoff in terms of spectral efficiency, amount of analog effective SI suppression (to enable FD operation and avoid the ADC saturation), complexity (how many FLOPS required) and the total power consumption at the RX.

- **Chapter 3: Single-Cell Single User MIMO**

    1. I design the all-digital beamformers to not only serve as a performance benchmark due to their higher power consumption but also to provide a SE upper bound. Our findings reveal that the proposed all-digital solution closely approximates this upper bound.
    2. I develop robust hybrid A/D beamforming techniques for both users and the BS, aimed at minimizing SI and Inter-User Interference (IUI) while ensuring the preservation of the rank of the effective channels in uplink/downlink communications.
    3. For the hybrid A/D design, I adopt a strategic approach to manage unit modulus and interference suppression constraints concurrently in the analog domain, ensuring the unit modulus constraint does not violate interference suppression. This methodology is pivotal for minimizing ADC saturation risks. Our findings, as shown in Fig. 2.2, confirm the effectiveness of this strategy, with more than 50 dB of SI reduction achieved in the analog domain, thus facilitating FD operation.
    4. I compare and analyze our beamforming design in computational cost and performance (SE and SI reduction). Since the hybrid A/D beamforming design problem is not convex, we investigate the stability and rate of the convergence under different scenarios.
    5. I present a comprehensive comparative analysis, benchmarking our hybrid A/D beamforming design against prior methods. This evaluation highlights the enhanced robustness and superior performance of the proposed method, effectively illustrating its advancements in SE and interference suppression over related work.

- **Chapter 4: Integrated Access and backhaul**

    1. I propose low complexity hybrid A/D beamforming algorithm to suppress the SI, avoid the ADC saturation and maximize the sum spectral efficiency of the access and backhaul links.
    2. I derive the all-digital solution and upper bound on the spectral efficiency.
    3. I present complexity analysis of the proposed hybrid A/D as well as all-digital beamforming in the number of FLOPS.
    4. I conduct a comprehensive comparison against HD, all-digital beamforming, conventional SI cancellation techniques and upper bound.

- **Chapter 5: Single-Cell Multiuser MIMO**

    1. I propose a novel design for all-digital beamformers aimed at enhancing spectral efficiency. This design extends existing literature from a narrowband single-user scenario to a wideband multiuser context, applicable to both uplink and downlink FD BS mmWave transceivers supporting multiple streams. The proposed all-digital framework demonstrates near-optimal efficacy and provides a foundational reference and benchmark for subsequent hybrid A/D designs.
    2. I introduce a methodology to derive hybrid precoders and combiners for the FD BS, predicated on a partially-connected PS-based framework for the analog stage, while meticulously considering the quantization effects of PSs. This design is readily adaptable to accommodate a fully-connected array configuration.
    3. While minimizing the interference in the analog domain to avoid the ADC saturation, I developed a method for the design of the analog beamformers to circumvent the losses incurred by the constant amplitude quantized phase-shifters (CAQP) constraint, as it violates the interference suppression constraint as shown in the literature.

4. I propose a method to compute the baseband beamformers at the FD BS trading-off interference suppression and maximizing uplink/downlink beamformed powers.

- **Chapter 6: Massive MIMO Cellular Networks**

1. I derive expressions for the received signals as well as the relative SQINR for reverse and forward links under channel hardening, LMMSE channel estimation, low-resolution ADCs/digital-analog-converters (DACs), and pilot contamination.
2. I derive closed-form and approximate analytical expressions for spectral efficiency in the reverse and forward links. We adopt the additive quantization noise model (AQNM[1]) to model ADC and DAC quantization error. We show that the spectral efficiency is substantially affected by the use of low-resolution ADCs/DACs which cannot be compensated only by employing a massive number of BS antennas; each UE should adopt high resolution ADCs/DACs to ensure good performance. Since each UE only requires two ADCs for in-phase and quadrature (IQ) sampling in the reverse link and two DACs for IQ sampling in the forward link, using high-resolution data converters in the UEs is a viable solution.
3. I analyze the effects of network imperfections and irregularities such as the cell shape, shadowing, noise and cellular interference on the reverse and forward links. Cellular interference includes includes pilot contamination as well as inter-cell and intra-cell interference. We further investigate the impact of pilot overhead, number of users per cell, and frequency reuse factor on both the cumulative distribution function (CDF) and spectral efficiency.

[1]To facilitate analytical performance of systems with low resolution ADCs/DACs, we adopt the common AQNM proposed in the literature.

4. I gauge the effects of full-duplexing such as SI channel power, SI signal power, and IUI on the reverse and forward link users, respectively.

5. Derive asymptotic results as well as power scaling laws for reverse and forward links in order to unpack engineering insights into the proposed system model.

6. I demonstrate the generality of the proposed work by showing the results match those in related work for several special cases. Although some of the special cases such as single-user, single-cell, and high-resolution cases, are less common, the analysis of these cases is useful for gaining insight.

7. I assess the numerical results in terms of CDF, spectral and energy efficiency for hexagonal lattice, square grid and Poisson point process (PPP) tessellation.

Chapter 2: Point-to-Point Systems

Enabling simultaneous transmission and reception on the same resource block known as FD communication necessitates significant suppression of SI. In this chapter[1], we focus on design of hybrid A/D beamformers (precoders and combiners) in an FD millimeter-wave point-to-point bidirectional link to enable spatial suppression of SI. The proposed beamforming design aims to cancel SI at the analog combiner output, mitigating risk of saturation in the ADC in the RX. Each analog beamformer, which reduces the number of RF chains to lower power consumption, imposes a unit modulus constraint, which causes loss of convexity in the optimization problem. For practical consideration, we evaluate tradeoffs for our proposed hybrid beamformer design in spectral efficiency, computational complexity, total power consumption, and analog SI suppression vs. numbers of antennas and RF chains. At least 50 dB of analog SI reduction is needed for FD communication per Fig. 2.2. We further investigate tradeoffs for our proposed hybrid beamformer design in SINR, spectral efficiency, energy efficiency and residual and suppressed effective SI reduction vs. number of PS quantization bits, channel estimation error, number of antennas, and number of RF chains. The results show our proposed design not only achieves analog SI reduction of 67 dB on average (Table 2.5) but also outperforms HD mode in spectral efficiency, supporting feasibility of FD in practical mmWave systems. We also design all-digital beamformers, which consume prohibitively large amounts of power, to serve as benchmark.

[1]This chapter is based on the following journal paper: E. Balti, and B. L. Evans, "Millimeter Wave Full-Duplex Massive MIMO: Beamforming and System Design Tradeoffs". It is an extension version of the conference paper: E. Balti and N. Mensi, "Zero-Forcing Max-Power Beamforming for Hybrid mmWave Full-Duplex MIMO Systems," *2020 4th International Conference on Advanced Systems and Emergent Technologies (IC_ASET)*, Hammamet, Tunisia, 2020, pp. 344-349. These works were supported by AT&T Labs, NVIDIA and Tektronix through their industrial affiliation with the 6G@UT research center at UT Austin.

2.1 Introduction

Mobile networks are incorporating mmWave bands (30-300 GHz)[2]. The current 5G NR standards extend mmWave FR2 bands up to 52.6 GHz. Future standards are anticipated to extend the FR2 bands beyond 52.6 GHz, possibly into sub-THz bands for 6G.

The vast bandwidths inherent in mmWave offer a significant opportunity for elevated data rates. However, crafting communication systems at mmWave frequencies poses significant challenges. To counteract pronounced path losses and maintain a robust link margin, mmWave communication leans heavily on beamforming advantages offered by large antenna arrays, typically comprising dozens or even hundreds of elements.

FD is an emerging physical layer technology garnering significant attention in research. This mode allows simultaneous TX and RX on the same resource block. This stands in stark contrast to the conventional HD mode, which utilizes either separate time intervals or bandwidths to maintain TX-RX orthogonality [172, 146]. Beyond potentially doubling spectral efficiency, FD can enhance point-to-point handshaking, advance multiple access schemes, and curtail HD latencies [143].

2.1.1 Prior Work

A primary challenge impeding the widespread adoption of FD is SI. SI arises when an FD node's transmission inadvertently feeds into its own receiver, overshadowing the more subdued incoming signal from a distant node. Consequently, extensive research efforts have concentrated on SI mitigation techniques tailored for FD. Encouraging outcomes have been documented for single-antenna FD nodes functioning at microwave frequencies [24, 64, 37] via an amalgamation of strategies [74]. Initially, passive methods in the propagation domain emphasize optimized antenna design and

[2]While a precise definition places mmWave frequencies between 30 and 300 GHz, the industry more broadly defines them from 10 to 300 GHz.

strategic placement [25, 49]. Subsequently, analog circuit techniques actively fashion an analog counterpart of the SI, which is then subtracted from the incoming signal to avert RX front-end saturation [69]. Finally, digital domain strategies discern and deduct any remaining SI at baseband [78]. This approach necessitates the remaining SI intensities remain low to ensure ADCs operate at their maximum dynamic range.

In recent advances, the integration of FD capabilities into mmWave systems has garnered significant attention [156, 133]. Yet, the cancellation of SI in these systems presents unique challenges not encountered at microwave frequencies. Particularly, RF impairments become more pronounced, necessitating SI addressal in the analog domain due to the inherent difficulties in baseband cancellation [156]. Moreover, traditional analog-circuit domain techniques aren't easily scalable with an increasing number of antennas, complicating their application to MIMO FD systems [146]. However, the silver lining resides in leveraging the plethora of antennas inherent to MIMO FD for SI mitigation through BFC. While BFC's adoption in microwave-band systems typically results in a tradeoff of spectral efficiency as some spatial DoF are expended in SI mitigation [41, 65, 50, 67] — the expansive arrays in mmWave offer substantially greater DoF. Consequently, BFC strategies for SI mitigation emerge as a highly attractive solution in the mmWave context.

Initial research into FD mmWave prioritized assessing the effectiveness of propagation domain methods for SI mitigation [124, 44, 42]. Within this context, BFC was first introduced in [92], utilized a singular data stream in each direction, and applied a zero-forcing (ZF) constraint related to the SI. The methodology in [92] presumed all-digital beamforming, limiting its applicability in mmWave scenarios; nonetheless, it demonstrated minimal loss compared to an SI-free benchmark. This suggests that the DoF utilized by ZF constraints marginally affected the final performance.

Regarding analog beamforming, [156] elucidated that directly projecting optimal all-digital beamforming weights to the feasible set drastically reduced performance, even with infinite-resolution phase shifters. This degradation can be at-

tributed to the fact ZF constraints may not remain intact post-projection, leading to SI leakage. This challenge was addressed in [21] by refining the design from [156], subsequently broadening its scope to incorporate multiple data streams via hybrid beamforming [21]. Other FD methodologies for hybrid beamformers in similar contexts are discussed in [137, 6, 131, 73, 134].

The technique in [137] hinges on hybrid factorization using a least squares (LS) approximation of all-digital beamformers. LS approximation inaccuracies lead to significant SI leakage. Additionally, it tackles SI at baseband instead of the analog domain, much like [131]. In contrast, other designs [117, 73, 134] curb SI in the analog domain. To conceptualize hybrid beamformers, [117] harnesses a principle from [145] that posits any beamforming matrix can be decomposed into analog (presuming unquantized PSs) and digital components without discrepancies, provided the number of RF chains is double the number of data streams. However, this condition is not always feasible. Meanwhile, [73] offers a design premised on the angular data of the pertinent far-field channel reactions, but assumes the LOS proximal-field component of SI channels can be impeccably curtailed through antenna isolation strategies. In [6] and [134], RF phases are found by exhaustive search, solving an optimization dilemma for each potential candidate. Specifically, [6] advocates for a combined design incorporating active analog cancellation, whereas [145] presupposes residual SI is precisely known, facilitating its cancellation through subtraction in the digital domain.

MmWave FD has been recently introduced into integrated access and backhaul in 3GPP Rel. 17 wherein [22] proposed hybrid A/D beamforming to suppress analog SI power to avoid ADC saturation and maximize sum spectral efficiency across backhaul and access links. In subsequent work, [20, 18, 19, 17] introduced FD into multicell and multiuser networks for LTE and mmWave bands. For BSs operating in FD mode with low-resolution data converters, they derived asymptotic analysis as well as power scaling laws.

2.1.2 Contributions

In this chapter, the main contributions can be summarized as

- The methodology presented in [137] focuses on designing all-digital beamforming and derives a hybrid A/D decomposition using the Least Squares (LS) method. However, this approach has two significant limitations. First, it targets SI attenuation at baseband, whereas in practical systems, suppression should occur in the analog domain to prevent saturation in the analog front end. Second, the hybrid LS approximations are not guaranteed to neutralize SI effectively, as highlighted in [172], leading to performance degradation, especially at high SI levels. I proposed design addresses these two issues directly.

- I design hybrid A/D beamformers for the two FD nodes, where the analog beamformers significantly reduce SI power, achieving an average reduction of 67 dB (as shown in Table 2.5), thereby preventing ADC saturation and preserving the rank of the effective channel. This ensures that the maximum allowable number of spatial streams or layers is maintained. In essence, we introduced a constraint in the optimization problem to balance the degrees of freedom between SI suppression and maintaining the full rank of the effective channel. This contribution is evident in both the transmit and receive beamforming chains, as illustrated in Fig. 2.2.

- I design all-digital beamformers, which, although highly effective, consume an impractically large amount of power, serving primarily as a benchmark for comparison. The results demonstrate that the proposed all-digital solution closely approaches the theoretical upper bound in terms of performance.

- I provide a detailed computational complexity analysis of both the proposed hybrid A/D and all-digital beamforming designs, expressed in terms of the number of FLOPS.

- I investigate the impact of key factors such as the number of antennas, RF chains, channel estimation errors, and the resolution of phase shifters on spectral efficiency, energy efficiency, SINR per RF chain, as well as the residual and suppressed SI in the analog domain.

- I conduct a comprehensive comparison and analysis are performed to establish an optimal design, identifying the required number of antennas and RF chains to achieve the best tradeoff between spectral efficiency, the extent of analog SI suppression (to enable FD operation and prevent ADC saturation), computational complexity (measured in FLOPS), and overall power consumption at the receiver.

2.1.3 Structure

I organize the rest of this chapter as follows: Section 2.2 presents the system model. In Section 2.3, I formulate the optimization of the beamforming design while in Section 2.4, I discuss the target metrics. In Section 2.5, I discussed the numerical results while the concluding remarks are reported in Section 2.6.

2.2 System Model

We consider a bidirectional FD system depicted in Fig. 2.1, where both nodes possess FD functionalities. With each node indexed as $n \in \{1, 2\}$, node n is equipped with $N_{\mathsf{TX}}^{(n)}$ TX antennas, enabling transmission of $N_{\mathsf{s}}^{(n)}$ data streams to the counterpart node $m \in \{1, 2\}, m \neq n$. This counterpart node is outfitted with $N_{\mathsf{RX}}^{(m)}$ RX antennas. The data vectors $\mathbf{s}_n \in \mathbb{C}^{N_{\mathsf{s}}^{(n)}}, n \in \{1, 2\}$, are zero-mean Gaussian distributed with covariance $\mathbb{E}\left[\mathbf{s}_n \mathbf{s}_n^*\right] = \mathbf{I}_{N_{\mathsf{s}}^{(n)}}$. Node n's TX and RX interfaces consist of $N_{\mathsf{RF}}^{\mathsf{TX}(n)}$ and $N_{\mathsf{RF}}^{\mathsf{RX}(n)}$ RF chains, respectively. In a purely digital system that allocates a single RF chain to each antenna, it is derived that $N_{\mathsf{RF}}^{\mathsf{TX}(n)} = N_{\mathsf{TX}}^{(n)}$ and $N_{\mathsf{RF}}^{\mathsf{RX}(n)} = N_{\mathsf{RX}}^{(n)}, n \in \{1, 2\}$. Transitioning to a hybrid A/D framework results in a reduced RF chain count to reduce cost and improve power efficiency. Thus, it typically follows that

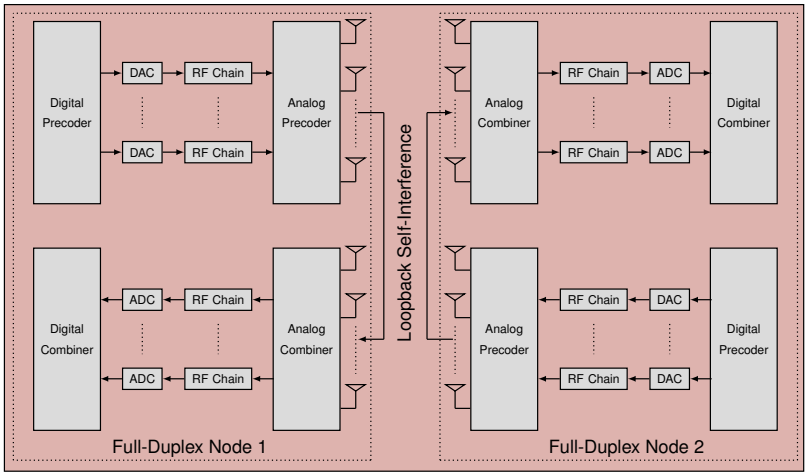

Figure 2.1: Basic abstraction of a hybrid A/D architecture of a bidirectional two-node FD system. The two nodes are simultaneously communicating with each other at the same resource block. This incurs a loopback SI between the TX and RX arrays at each node.

$N_{\mathsf{s}}^{(n)} \leq N_{\mathsf{RF}}^{\mathsf{TX}(n)} \leq N_{\mathsf{TX}}^{(n)}$ and $N_{\mathsf{s}}^{(m)} \leq N_{\mathsf{RF}}^{\mathsf{RX}(m)} \leq N_{\mathsf{RX}}^{(m)}, n, m \in \{1, 2\}, m \neq n.$

It is presumed that channel characteristics can be viewed as frequency-flat, signifying narrowband transmission, and their attributes are precisely known. Such assumptions align with prior studies on the subject [92, 137, 117, 39]. Channel estimation can be carried out during an initial training stage in HD mode leveraging renowned sparsity-driven methods for mmWave, as per [7]. Nevertheless, it is recognized that FD channel modeling and estimation at mmWave remain active research topics [156, 133, 39]. Accepting that contemporary mmWave systems are likely to be wideband, and acknowledging the significance of channel estimation in practice, we defer the extension to frequency-selective channels and channel uncertainty as a future direction. Consequently, we represent by $\mathbf{H}_{nm} \in \mathbb{C}^{N_{\mathsf{RX}}^{(n)} \times N_{\mathsf{TX}}^{(m)}}$ the channel matrix bridging the TX array of node m to the RX array of node n. For $n \neq m$, $\mathbf{H}_{nm}$ represents the inter-node channel, while $\mathbf{H}_{nn}$ corresponds to the SI channel affecting node n. Channel matrices are presumed normalized, hence $\|\mathbf{H}_{nm}\|_F^2 = N_{\mathsf{RX}}^{(n)} N_{\mathsf{TX}}^{(m)}$.

2.2.1 Received Signal Model

Before transmission, node m applies a digital precoder $\mathbf{F}_m^{\mathsf{BB}}$ to the data stream vector $\mathbf{s}_m$, followed by the analog precoder $\mathbf{F}_m^{\mathsf{RF}}$. Since the analog beamformers are implemented using phased arrays, they are subject to the unit modulus constraint. To process the received signal, the node n applies the analog combiner $\mathbf{W}_n^{\mathsf{RF}}$ followed by the digital combiner $\mathbf{W}_n^{\mathsf{BB}}$ in order to extract the data streams. Accordingly, the received signal at node n transmitted from node $m \neq n$ is given by

$$\mathbf{y}_n = \underbrace{\mathbf{W}_n^{\mathsf{BB}*}\mathbf{W}_n^{\mathsf{RF}*}\mathbf{H}_{nm}\mathbf{F}_m^{\mathsf{RF}}\mathbf{F}_m^{\mathsf{BB}}\mathbf{x}_m}_{\text{Desired Signal}} + \underbrace{\mathbf{W}_n^{\mathsf{BB}*}\mathbf{W}_n^{\mathsf{RF}*}\mathbf{H}_{nn}\mathbf{F}_n^{\mathsf{RF}}\mathbf{F}_n^{\mathsf{BB}}\mathbf{x}_n}_{\text{Self-Interference Signal}} + \underbrace{\mathbf{W}_n^{\mathsf{BB}*}\mathbf{W}_n^{\mathsf{RF}*}\mathbf{n}_n}_{\text{Filtered Noise}} \tag{2.1}$$

where $\mathbf{H}_{nn}$ and $\mathbf{n}_n \sim \mathcal{CN}(\mathbf{0}, \mathbf{I})$ are the SI channel and additive white Gaussian noise (AWGN) at node n. The goal is to come up with a practical design of the analog and digital beamformers in order to enable FD systems operation, i.e., suppressing at least 50 dB of effective SI in the analog domain per Fig. 2.2 and maximizing the spectral efficiency, thus, outperforming the HD mode, the case of actual cellular systems.

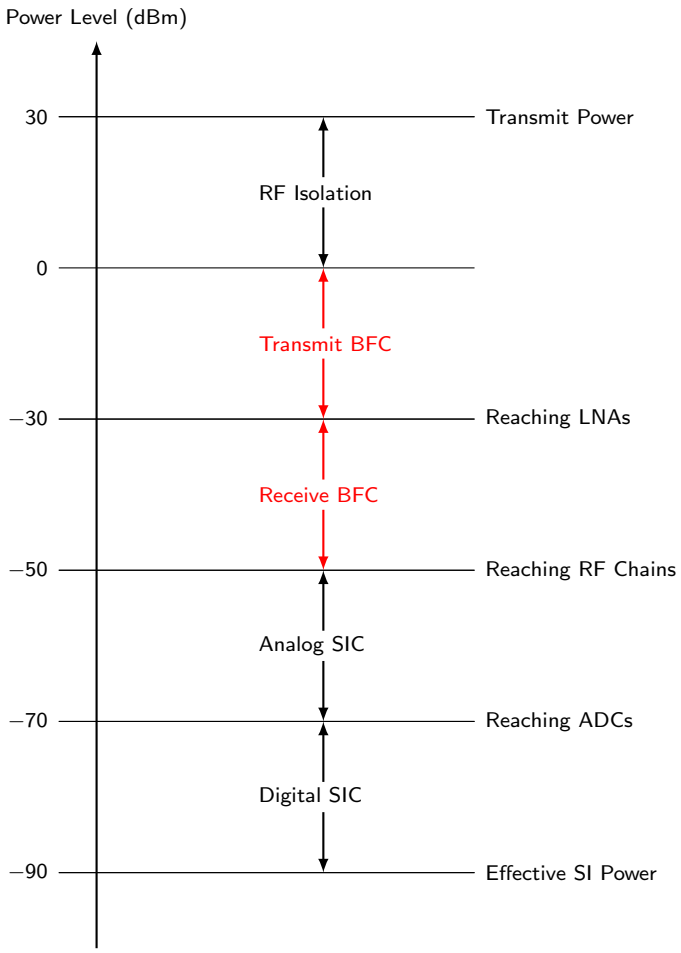

Figure 2.2: Example breakdown of SIC power levels at various points in a FD mmWave transceiver employing beamforming cancellation (BFC), analog and digital (A/D) cancellation [133]. My work focuses on transmit and receive BFC range (50 dB) shown in red.

2.3 Problem Formulation and Beamforming Design

The main objective of this work is to design optimal beamformers to maximize spectral efficiency and reject a large amount of interference in the analog domain to

Table 2.1: System Model Notations and Variables.

Variable	Definition	Size
N_{TX}	Number of antennas at TX	–
N_{RX}	Number of antennas at RX	–
$N_{\mathsf{RF}}^{\mathsf{TX}}$	Number of RF chains at TX	–
$N_{\mathsf{RF}}^{\mathsf{RX}}$	Number of RF chains at RX	–
N_{s}	Number of spatial streams	–
$\mathbf{W}_n$	All-digital combiner at node n	$N_{\mathsf{RX}} \times N_{\mathsf{s}}$
$\mathbf{F}_n$	All-digital precoder at node n	$N_{\mathsf{TX}} \times N_{\mathsf{s}}$
$\mathbf{W}_n^{\mathsf{RF}}$	Analog combiner at node n	$N_{\mathsf{RX}} \times N_{\mathsf{RF}}^{\mathsf{RX}}$
$\mathbf{F}_n^{\mathsf{RF}}$	Analog precoder at node n	$N_{\mathsf{TX}} \times N_{\mathsf{RF}}^{\mathsf{TX}}$
$\mathbf{W}_n^{\mathsf{BB}}$	Baseband combiner at node n	$N_{\mathsf{RF}}^{\mathsf{RX}} \times N_{\mathsf{s}}$
$\mathbf{F}_n^{\mathsf{BB}}$	Baseband precoder at node n	$N_{\mathsf{RF}}^{\mathsf{TX}} \times N_{\mathsf{s}}$

avoid ADC saturation. The general optimization problem can be formulated as

$$\begin{aligned} \mathscr{P}_0 : & \max_{\mathbf{W}_n^{\mathsf{BB}},\mathbf{W}_n^{\mathsf{RF}},\mathbf{W}_m^{\mathsf{BB}},\mathbf{W}_m^{\mathsf{RF}},\mathbf{F}_n^{\mathsf{BB}},\mathbf{F}_n^{\mathsf{RF}},\mathbf{F}_m^{\mathsf{BB}},\mathbf{F}_m^{\mathsf{RF}}} \mathcal{I}_{mn} + \mathcal{I}_{nm} \\ & \mathsf{s.t.}\ \|\mathbf{F}_m^{\mathsf{RF}}\mathbf{F}_m^{\mathsf{BB}}\|_F^2 = \|\mathbf{F}_n^{\mathsf{RF}}\mathbf{F}_n^{\mathsf{BB}}\|_F^2 = N_{\mathsf{s}} \\ & \mathbf{F}_n^{\mathsf{RF}}, \mathbf{F}_m^{\mathsf{RF}} \in \mathcal{F}_{\mathsf{RF}},\ \mathbf{W}_n^{\mathsf{RF}}, \mathbf{W}_m^{\mathsf{RF}} \in \mathcal{W}_{\mathsf{RF}} \end{aligned} \tag{2.2}$$

where $\mathcal{F}_{\mathsf{RF}}$ and $\mathcal{W}_{\mathsf{RF}}$ are the sets of the feasible (unit modulus) analog precoders and combiners, respectively, and $\mathcal{I}_{nm}$ is the spectral efficiency from node m to node n given by

$$\mathcal{I}_{nm} = \log\det\left(\mathbf{I} + \mathsf{snr}_{nm}\mathbf{H}_{nm}^{\mathsf{eff}}\mathbf{Q}_n^{-1}\mathbf{H}_{nm}^{\mathsf{eff}*}\right) \tag{2.3}$$

where $\mathbf{H}_{nm}^{\mathsf{eff}} = \mathbf{W}_n^{\mathsf{BB}*}\mathbf{W}_n^{\mathsf{RF}*}\mathbf{H}_{nm}\mathbf{F}_m^{\mathsf{RF}}\mathbf{F}_m^{\mathsf{BB}}$, and $\mathbf{Q}_n$ is given by

$$\mathbf{Q}_n = \mathsf{inr}_n\mathbf{H}_{nn}^{\mathsf{eff}}\mathbf{H}_{nn}^{\mathsf{eff}*} + \mathbf{I} \tag{2.4}$$

where snr_{nm} is the signal-to-noise ratio (SNR) of the link ($m->n$) and inr_n is the interference-to-noise ratio (INR) at the node n.

2.3.1 Hybrid Analog/Digital Beamforming

We perform the design of the hybrid A/D beamformers in two stages (analog and digital).

2.3.1.1 Analog Beamforming

We optimize the analog beamformers to jointly minimize the interference and preserve the signal space dimension, i.e., preserve the rank of the effective channel ($\text{rank}\left(\mathbf{W}_n^{\mathsf{RF}*}\mathbf{H}_{nm}\mathbf{F}_m^{\mathsf{RF}}\right) = N_{\mathsf{RF}}$). We refer to the *alternating minimization method*; i.e., we fix the precoder and solve for the combiner and vice versa. We perform this process of optimization in an iterative routine so the effective SI is minimized. Accordingly, the first subproblem is expressed by

$$\begin{aligned} \mathscr{P}_1 : &\min_{\mathbf{W}_n^{\mathsf{RF}}} \text{Tr}\left(\mathbf{W}_n^{\mathsf{RF}*}\mathbf{R}_n\mathbf{W}_n^{\mathsf{RF}}\right) \\ &\text{s.t. } \mathbf{W}_n^{\mathsf{RF}*}\mathbf{H}_{nm}\mathbf{F}_m^{\mathsf{RF}} = \alpha\mathbf{I}_{N_{\mathsf{RF}}} \\ &\quad \mathbf{W}_n^{\mathsf{RF}} \in \mathcal{W}_{\mathsf{RF}} \end{aligned} \tag{2.5}$$

where $\mathbf{R}_n$[3], a positive definite matrix, is the covariance of the precoded SI and noise, which is given by

$$\mathbf{R}_n = \mathsf{inr}_n\mathbf{H}_{nn}\mathbf{F}_n^{\mathsf{RF}}\mathbf{F}_n^{\mathsf{RF}*}\mathbf{H}_{nn}^* + \mathbf{I} \tag{2.6}$$

Now, we fix the analog combiner $\mathbf{W}_n^{\mathsf{RF}}$, as the solution of (2.5), and we solve for the analog precoder $\mathbf{F}_n^{\mathsf{RF}}$. Accordingly, we define the second subproblem as

$$\begin{aligned} \mathscr{P}_2 : &\min_{\mathbf{F}_n^{\mathsf{RF}}} \text{Tr}\left(\mathbf{F}_n^{\mathsf{RF}*}\mathbf{S}_n\mathbf{F}_n^{\mathsf{RF}}\right) \\ &\text{s.t. } \mathbf{W}_m^{\mathsf{RF}*}\mathbf{H}_{mn}\mathbf{F}_n^{\mathsf{RF}} = \beta\mathbf{I}_{N_{\mathsf{RF}}} \\ &\quad \mathbf{F}_n^{\mathsf{RF}} \in \mathcal{F}_{\mathsf{RF}} \end{aligned} \tag{2.7}$$

where $\mathbf{S}_n$, a positive definite matrix, is the covariance of the combined SI and noise which is given by

$$\mathbf{S}_n = \mathsf{inr}_n\mathbf{H}_{nn}^*\mathbf{W}_n^{\mathsf{RF}}\mathbf{W}_n^{\mathsf{RF}*}\mathbf{H}_{nn} + \mathbf{I} \tag{2.8}$$

Note that the problems (2.5) and (2.7) are not convex since they contain the unit modulus constraints $\left(\mathbf{W}_n^{\mathsf{RF}} \in \mathcal{W}_{\mathsf{RF}}, \mathbf{F}_n^{\mathsf{RF}} \in \mathcal{F}_{\mathsf{RF}}\right)$. Therefore, we consider a two-stage analog beamforming design:

[3]The term related to the Identity matrix $\mathbf{I}$ is added to (2.6) to ensure that the matrix $\mathbf{R}_n$ is invertible. However, it has no influence on the design regardless of the snr and/or inr. It can be removed if $\mathbf{R}_n$ is invertible in practice. The same reasoning applies to the matrix $\mathbf{S}_n$.

1. Relax the unit modulus constraint to preserve the convexity of the problems (2.5), (2.7) and solve for the unconstrained analog beamformers $\tilde{\mathbf{W}}_n^{\mathsf{RF}}$ and $\tilde{\mathbf{F}}_n^{\mathsf{RF}}$.

2. Once convergence is obtained, we project the unconstrained analog solution into the unit modulus space.

Theorem 1. The unconstrained analog beamformers, solutions of (2.5) and (2.7), are expressed by

$$\tilde{\mathbf{W}}_n^{\mathsf{RF}} = \alpha \mathbf{R}_n^{-1} \mathbf{H}_{nm} \tilde{\mathbf{F}}_m^{\mathsf{RF}} \left(\mathbf{H}_{nm} \tilde{\mathbf{F}}_m^{\mathsf{RF}*} \mathbf{R}_n^{-1} \mathbf{H}_{nm} \tilde{\mathbf{F}}_m^{\mathsf{RF}} \right)^{-1} \tag{2.9}$$

$$\tilde{\mathbf{F}}_n^{\mathsf{RF}} = \beta \mathbf{S}_n^{-1} \mathbf{H}_{mn}^{*} \tilde{\mathbf{W}}_m^{\mathsf{RF}} \left(\tilde{\mathbf{W}}_m^{\mathsf{RF}*} \mathbf{H}_{mn} \mathbf{S}_n^{-1} \mathbf{H}_{mn}^{*} \tilde{\mathbf{W}}_m^{\mathsf{RF}} \right)^{-1} \tag{2.10}$$

where $\alpha = 1/\sqrt{\mathrm{Tr}\left(\tilde{\mathbf{W}}_n^{\mathsf{RF}*} \tilde{\mathbf{W}}_n^{\mathsf{RF}} \right)}$ and $\beta = 1/\sqrt{\mathrm{Tr}\left(\tilde{\mathbf{F}}_n^{\mathsf{RF}*} \tilde{\mathbf{F}}_n^{\mathsf{RF}} \right)}$ are the normalization power coefficients, respectively.

Proof. The proof of Theorem (1) is given by Appendix A.1. □

Remark 1. The beamforming solutions entailed by Theorem 1 are coupled. Hence, an iterative routine is carried out until convergence.

Remark 2. For the analog beamformer solution $\mathbf{X} \in \mathbb{C}^{M \times N}$, M and N are the numbers of antennas and RF chains, respectively. M should be large enough to achieve a good multiplexing gain (sustaining N_{s} spatial streams wherein $N_{\mathsf{s}} \leq N$) and the remaining $P = M - N_{\mathsf{s}}$ DoF should be dedicated to suppress the interference.

Once the unconstrained analog beamformers $\left(\tilde{\mathbf{W}}_n^{\mathsf{RF}}, \tilde{\mathbf{F}}_n^{\mathsf{RF}} \right)$ are obtained, we then introduce the unit modulus constraint to obtain $\left(\mathbf{W}_n^{\mathsf{RF}}, \mathbf{F}_n^{\mathsf{RF}} \right)$.

2.3.1.2 Digital Beamforming

Once the analog beamformers are obtained to suppress SI in the analog domain to avoid ADC saturation and preserve the signal dimension, we design the digital beamformers to maximize spectral efficiency.

Theorem 2. The optimal digital beamformer $\mathbf{X}_n^{\mathsf{BB}}$ can be derived from the analog beamformer solution $\mathbf{X}_n^{\mathsf{RF}}$ as follows. We apply the singular value decomposition (SVD) $\mathbf{X}_n^{\mathsf{RF}} = \mathbf{U}_n^{\mathsf{RF}}\mathbf{S}_n^{\mathsf{RF}}\mathbf{V}_n^{\mathsf{RF}*}$ and then we express $\mathbf{X}_n^{\mathsf{BB}} = \mathbf{V}_n^{\mathsf{RF}}\left(\mathbf{S}_n^{\mathsf{RF}}\right)^{-1}\mathbf{Q}_\star$, where the columns of $\mathbf{Q}_\star \in \mathbb{C}^{M\times N}$ comprise the N dominant left singular vectors of $\mathbf{U}_n^{\mathsf{RF}*}\mathbf{A}_n$. Note that $\mathbf{X}_n^{\mathsf{RF}} \in \mathbb{C}^{M\times L}, \mathbf{X}_n^{\mathsf{BB}} \in \mathbb{C}^{L\times N}$ and $\mathbf{A}_n \in \mathbb{C}^{M\times N}$.

Proof. The proof of Theorem 2 is detailed in Appendix A.2. □

Algorithm 1 Hybrid Beamforming Design

function DIGITAL($\mathbf{X}_n^{\mathsf{RF}}, \mathbf{A}_n, N$)
Compute SVD $\mathbf{X}_n^{\mathsf{RF}} = \mathbf{U}_n^{\mathsf{RF}}\mathbf{S}_n^{\mathsf{RF}}\mathbf{V}_n^{\mathsf{RF}*}$
$\mathbf{Q} \leftarrow N$ Dominant left singular vectors of $\mathbf{U}_n^{\mathsf{RF}*}\mathbf{A}$
$\mathbf{X}_n^{\mathsf{BB}} \leftarrow \mathbf{V}_n^{\mathsf{RF}}(\mathbf{S}_n^{\mathsf{RF}})^{-1}\mathbf{Q}$
return $\mathbf{X}_n^{\mathsf{BB}}$
end function

Construct $\mathbf{F}_m^{\mathsf{RF}(0)}$, $\mathbf{F}_m^{\mathsf{BB}(0)}$, $\mathbf{W}_m^{\mathsf{RF}(0)}$ and $\mathbf{W}_m^{\mathsf{BB}(0)}$ with random phases for $(m \neq n)$ and set $\ell = 0$
repeat
  Compute $\mathbf{R}_n^{(\ell)}, n = 1, 2$ from (2.6)
  Obtain the unconstrained solution $\tilde{\mathbf{W}}_n^{\mathsf{RF}(\ell)}$ from (2.9)
  Project $\tilde{\mathbf{W}}_n^{\mathsf{RF}(\ell)}$ into the unit modulus space
  $\mathbf{W}_n^{\mathsf{BB}(\ell)} \leftarrow \text{Digital}\left(\mathbf{W}_n^{\mathsf{RF}(\ell)}, \mathbf{H}_{nm}\mathbf{F}_m^{\mathsf{RF}(\ell)}\mathbf{F}_m^{\mathsf{BB}(\ell)}, N_{\mathsf{s}}\right)$
  Compute $\mathbf{S}_n^{(\ell)}, n = 1, 2$ from (2.8)
  Obtain the unconstrained solution $\tilde{\mathbf{F}}_n^{\mathsf{RF}(\ell)}$ from (2.10)
  Project $\tilde{\mathbf{F}}_n^{\mathsf{RF}(\ell)}$ into the unit modulus space
  $\mathbf{F}_n^{\mathsf{BB}(\ell)} \leftarrow \text{Digital}\left(\mathbf{F}_n^{\mathsf{RF}(\ell)}, \mathbf{H}_{mn}^{*}\mathbf{W}_m^{\mathsf{RF}(\ell)}\mathbf{W}_m^{\mathsf{BB}(\ell)}, N_{\mathsf{s}}\right)$
  Normalize $\mathbf{F}_n^{\mathsf{BB}(\ell)} \leftarrow \frac{\sqrt{N_{\mathsf{s}}}}{\|\mathbf{F}_n^{\mathsf{RF}(\ell)}\mathbf{F}_n^{\mathsf{BB}(\ell)}\|_F}\mathbf{F}_n^{\mathsf{BB}(\ell)}$
  $\ell \leftarrow \ell + 1$
until Convergence
return $\mathbf{W}_n^{\mathsf{RF}}, \mathbf{W}_n^{\mathsf{BB}}, \mathbf{F}_n^{\mathsf{RF}}, \mathbf{F}_n^{\mathsf{BB}}, n = 1, 2$

2.3.2 All-Digital Beamforming

The all-digital beamforming will be designed in a similar way as the analog beamformers. Accordingly, the corresponding subproblems are given by

$$\begin{aligned} \mathscr{P}_3 : &\min_{\mathbf{W}_n} \operatorname{Tr}\left(\mathbf{W}_n^* \mathbf{G}_n \mathbf{W}_n\right) \\ &\mathsf{s.t.}\ \mathbf{W}_n^* \mathbf{H}_{nm} \mathbf{F}_m = \gamma \mathbf{I}_{N_\mathsf{s}} \end{aligned} \tag{2.11}$$

$$\begin{aligned} \mathscr{P}_4 : &\min_{\mathbf{F}_n} \operatorname{Tr}\left(\mathbf{F}_n^* \mathbf{D}_n \mathbf{F}_n\right) \\ &\mathsf{s.t.}\ \mathbf{W}_m^* \mathbf{H}_{mn} \mathbf{F}_n = \zeta \mathbf{I}_{N_\mathsf{s}} \end{aligned} \tag{2.12}$$

where γ and ζ are the power normalization coefficients defined as α and β while $\mathbf{G}_n$ and $\mathbf{D}_n$ are respectively expressed by

$$\mathbf{G}_n = \mathsf{inr}_n \mathbf{H}_{nn} \mathbf{F}_n \mathbf{F}_n^* \mathbf{H}_{nn}^* + \mathbf{I} \tag{2.13}$$

$$\mathbf{D}_n = \mathsf{inr}_n \mathbf{H}_{nn}^* \mathbf{W}_n \mathbf{W}_n^* \mathbf{H}_{nn} + \mathbf{I} \tag{2.14}$$

As we notice that the two subproblems (2.13) and (2.14) are convex since the all-digital combiners are not constrained by the unit modulus constraint. In a similar way, the optimal all-digital solutions are given by (similar to the unconstrained analog beamformers)

$$\mathbf{W}_n^{\mathsf{opt}} = \gamma \mathbf{G}_n^{-1} \mathbf{H}_{nm} \mathbf{F}_m \left(\mathbf{H}_{nm} \mathbf{F}_m \mathbf{G}_n^{-1} \mathbf{H}_{nm} \mathbf{F}_m\right)^{-1} \tag{2.15}$$

$$\mathbf{F}_n^{\mathsf{opt}} = \zeta \mathbf{D}_n^{-1} \mathbf{H}_{mn}^* \mathbf{W}_m \left(\mathbf{W}_m^* \mathbf{H}_{mn} \mathbf{D}_n^{-1} \mathbf{H}_{mn}^* \mathbf{W}_m\right)^{-1} \tag{2.16}$$

We observe the all-digital beamformer design at nodes m and n are coupled; therefore, an iterative routine is required to obtain convergence.

2.3.3 Convergence

The designs for all-digital and analog beamforming are identical. Consequently, analyzing the convergence of one inherently validates the convergence of the other. For the sake of clarity and without loss of generality, we focus on the convergence of the all-digital beamforming design. We thereby introduce the effective

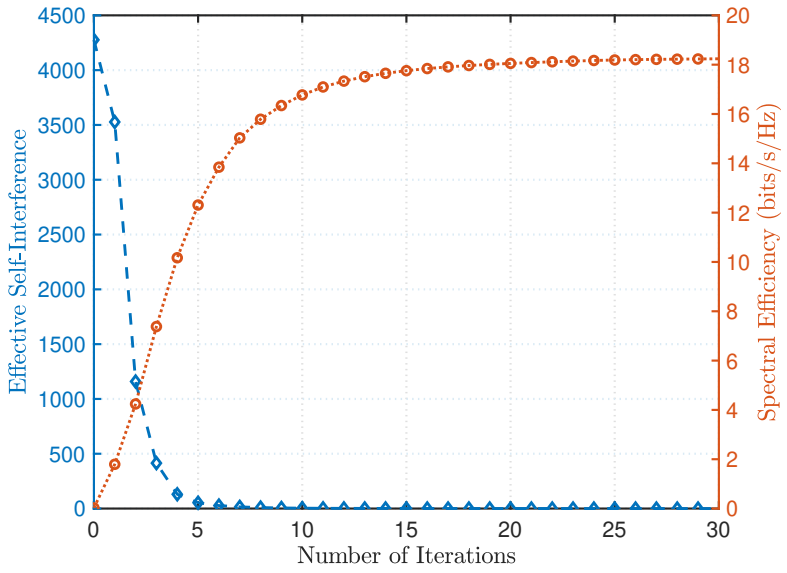

Figure 2.3: Results for all-digital beamforming: Effective SI (in linear scale) and spectral efficiency vs. number of iterations. The plot is produced with $\mathsf{snr} = 0$ dB, $\mathsf{inr} = 30$ dB, $N_{\mathsf{TX}} = N_{\mathsf{RX}} = 64$. The all-digital design uses prohibitively large amount of power and serves as a benchmark in this work.

SI cost function (2.17). At each iteration, we monitor the progress in the reducing the effective SI and increasing the spectral efficiency until convergence is attained.

$$\mathsf{esi}_n = \mathsf{inr}_n \mathrm{Tr}\left(\mathbf{W}_n^* \mathbf{H}_{nn} \mathbf{F}_n \mathbf{F}_n^* \mathbf{H}_{nn}^* \mathbf{W}_n\right) \tag{2.17}$$

Furthermore, Theorem 1 provides the local optimal solutions for the objective functions defined in subproblems (2.5), (2.7), (2.11) and (2.12). Convergence to this local optimum is assured by Algorithm 1 of the proposed design. It is noteworthy that the value of the effective SI diminishes with each iteration and is bounded below by zero, whereas the spectral efficiency increases at each iteration and is upper bounded by a ceiling.

Fig. 2.3 illustrates the convergence of the effective SI (2.17) as well as the spectral efficiency defined in the all-digital domain, for the recommended design approach. The graph indicates that the effective SI and the spectral efficiency rapidly

converge to a local optimum within merely 5-10 iterations. It is noteworthy that the effective SI becomes practically negligible after 5 iterations while the spectral efficiency converges to a ceiling after roughly 10 iterations.

2.3.4 Complexity Analysis

To evaluate the computational complexity of the proposed beamforming design, we need to compute the FLOPS for the following matrix operations. Multiplying matrices $\mathbf{A} \in \mathbb{C}^{m\times n}$ and $\mathbf{B} \in \mathbb{C}^{n\times p}$ requires nmp FLOPS. An inverse of an $n \times n$ matrix using Cholesky decomposition requires $\frac{n^3}{3}$ FLOPS whereas multiplication of a matrix $\mathbf{A} \in \mathbb{C}^{m\times n}$ and its Hermitian ($\mathbf{AA}^*$) requires $\frac{nm^2}{2}$ FLOPS. The computation of the pseudo-inverse $\mathbf{A}^\dagger$ of the matrix $\mathbf{A}$ requires $\frac{mn^2}{2} + \frac{n^3}{3} + n^2m$ if $n \leq m$, otherwise, it requires $\frac{nm^2}{2} + \frac{m^3}{3} + m^2n$.

Table 2.2: Computational complexity of the hybrid A/D algorithm 1. Results are produced with $N_{\mathsf{RX}} = N_{\mathsf{TX}} = 64$, $N_{\mathsf{RF}}^{\mathsf{RX}} = N_{\mathsf{RF}}^{\mathsf{TX}} = 2$ and $N_{\mathsf{s}} = 2$.

Operation	Complex Multiplications for Highest-Order Terms	FLOPS	Dominant Term Contribution (Total)
$\mathbf{W}_n^{\mathsf{RF}}$	$\frac{3}{2}N_{\mathsf{RX}}^2 N_{\mathsf{RF}}^{\mathsf{RX}} + 2(N_{\mathsf{RF}}^{\mathsf{TX}})^2 N_{\mathsf{RX}} + N_{\mathsf{RX}}^2 N_{\mathsf{RF}}^{\mathsf{TX}} + N_{\mathsf{TX}} N_{\mathsf{RX}} N_{\mathsf{RF}}^{\mathsf{TX}} + \frac{1}{3}N_{\mathsf{RX}}^3 + \frac{1}{3}(N_{\mathsf{RF}}^{\mathsf{TX}})^3$	1.4679e+05	$\frac{1}{3}N_{\mathsf{RX}}^3$ 59.53% (25.01%)
$\mathbf{F}_n^{\mathsf{RF}}$	$\frac{3}{2}N_{\mathsf{TX}}^2 N_{\mathsf{RF}}^{\mathsf{TX}} + 2(N_{\mathsf{RF}}^{\mathsf{RX}})^2 N_{\mathsf{TX}} + N_{\mathsf{TX}}^2 N_{\mathsf{RF}}^{\mathsf{RX}} + N_{\mathsf{RX}} N_{\mathsf{TX}} N_{\mathsf{RF}}^{\mathsf{RX}} + \frac{1}{3}N_{\mathsf{TX}}^3 + \frac{1}{3}(N_{\mathsf{RF}}^{\mathsf{RX}})^3$	1.4679e+05	$\frac{1}{3}N_{\mathsf{TX}}^3$ 59.53% (25.01%)
$\mathbf{W}_n^{\mathsf{BB}}$	$9N_{\mathsf{RX}}\left(N_{\mathsf{RF}}^{\mathsf{RX}}\right)^2 + 9N_{\mathsf{RX}}N_{\mathsf{s}}^2 + N_{\mathsf{RF}}^{\mathsf{RX}}N_{\mathsf{RX}}^2 + N_{\mathsf{s}}^3$	27912	$N_{\mathsf{RF}}^{\mathsf{RX}}N_{\mathsf{RX}}^2$ 58.70% (4.69%)
$\mathbf{F}_n^{\mathsf{BB}}$	$9N_{\mathsf{TX}}\left(N_{\mathsf{RF}}^{\mathsf{TX}}\right)^2 + 9N_{\mathsf{TX}}N_{\mathsf{s}}^2 + N_{\mathsf{RF}}^{\mathsf{TX}}N_{\mathsf{TX}}^2 + N_{\mathsf{s}}^3$	27912	$N_{\mathsf{RF}}^{\mathsf{TX}}N_{\mathsf{TX}}^2$ 58.70% (4.69%)

2.4 Target Metrics Analysis

Throughout this paper, we have emphasized that the primary goal of devising hybrid beamformers is to minimize interference in the analog domain, maintain the signal dimension, and subsequently enhance spectral efficiency. However, investigating additional metrics, such as the SINR and energy efficiency , can provide deeper engineering insights into the proposed algorithm. Moreover, both the upper bound and the all-digital beamforming design, despite its impracticability due to excessive power requirements, can function as benchmarks to assess the limitations of the technique we propose.

2.4.1 Signal-to-Interference-plus-Noise Ratio

We define the SINR at the ℓ-th RX RF chain of node n as

$$\mathsf{sinr}_{n,\ell} = \frac{\mathsf{snr}_{nm}\mathbf{w}_{n,\ell}^{\mathsf{RF}*}\mathbf{H}_{nm}\mathbf{F}_{m}^{\mathsf{RF}}\mathbf{F}_{m}^{\mathsf{BB}}\mathbf{F}_{m}^{\mathsf{BB}*}\mathbf{F}_{m}^{\mathsf{RF}*}\mathbf{H}_{nm}^{*}\mathbf{w}_{n,\ell}^{\mathsf{RF}}}{\mathsf{inr}_{n}\mathbf{w}_{n,\ell}^{\mathsf{RF}*}\mathbf{H}_{nn}\mathbf{F}_{n}^{\mathsf{RF}}\mathbf{F}_{n}^{\mathsf{BB}}\mathbf{F}_{n}^{\mathsf{BB}*}\mathbf{F}_{n}^{\mathsf{RF}*}\mathbf{H}_{nn}^{*}\mathbf{w}_{n,\ell}^{\mathsf{RF}} + 1} \tag{2.18}$$

2.4.2 Effective Self-Interference

We define the analog effective SI level at node n and at a given state (ℓ-th iteration) in Algorithm 1 as

$$\delta_{\ell} = \mathsf{inr}_{n} \times \mathrm{Tr}\left(\mathbf{W}_{n}^{\mathsf{RF}(\ell)*}\mathbf{H}_{nn}\mathbf{F}_{n}^{\mathsf{RF}(\ell)}\mathbf{F}_{n}^{\mathsf{BB}(\ell)}\mathbf{F}_{n}^{\mathsf{BB}(\ell)*}\mathbf{F}_{n}^{\mathsf{RF}(\ell)*}\mathbf{H}_{nn}^{*}\mathbf{W}_{n}^{\mathsf{RF}(\ell)}\right) \tag{2.19}$$

We further define the amount of analog effective SI suppressed at node n between two states in Algorithm 1, say iterations ℓ and t ($\ell > t$) is given by

$$\Delta_{t}^{\ell} = \frac{\delta_{t}}{\delta_{\ell}} \tag{2.20}$$

2.4.3 Energy Efficiency

The energy efficiency , expressed in bits/s/Watt or bits/Joule, is defined as the ratio between the spectral efficiency $\mathcal{I}(\mathsf{sinr})$ and the total power consumption ρ_{Total}. It is given by

$$\mathcal{J}(\mathsf{sinr}) = \frac{\mathcal{I}(\mathsf{sinr})}{\rho_{\mathsf{Total}}} \tag{2.21}$$

For hybrid A/D architecture as illustrated by Fig. 2.4, the total power consumption by the mmWave hybrid receiver is expressed by

$$\rho_{\mathsf{Total}}^{\mathsf{HC}} = N_{\mathsf{RX}}\left(\rho_{\mathsf{LNA}} + \rho_{\mathsf{SP}} + N_{\mathsf{RF}}^{\mathsf{RX}}\rho_{\mathsf{PS}}\right) + N_{\mathsf{RF}}^{\mathsf{RX}}\left(\rho_{\mathsf{RF}} + \rho_{\mathsf{C}} + 2\rho_{\mathsf{ADC}}\right) \tag{2.22}$$

where N_{RX} is the number of receive antennas and ρ_{RF} is the power consumption per RF chain which is defined by

$$\rho_{\mathsf{RF}} = \rho_{\mathsf{Mixer}} + \rho_{\mathsf{LO}} + \rho_{\mathsf{LPF}} + \rho_{\mathsf{BB}_{\mathsf{amp}}} \tag{2.23}$$

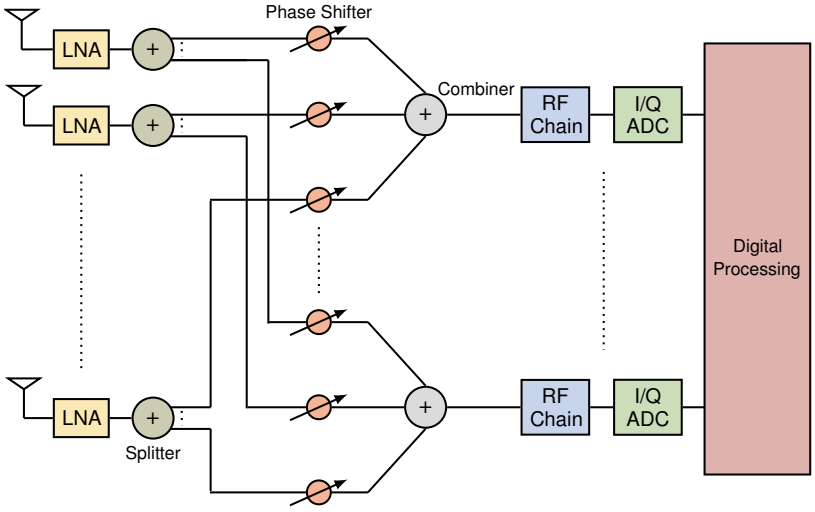

Figure 2.4: Illustration of a hybrid A/D combiner at the FD node. The combiner consists of multiple components such as low noise amplifiers (LNAs), phase shifters, RF chains, mixers, splitters, oscillators, filters and ADCs, etc. The power consumption of each component is shown in Table 2.3.

In Table 2.3, we provide exemplary data on the power consumption of each device. For all components, with the exception of the ADC, the power consumption remains independent of the bandwidth B and the number of bits b. However, the power consumption for ρ_{ADC} increases exponentially in relation to b and shows a linear correlation with B. This is in line with Walden's figure of merit for ADCs, denoted as c, which represents the energy consumed per conversion step for each Hz. Reference values for c can be found in Table 2.4.

2.4.4 Upper Bound on Spectral Efficiency

An ideal performance upper bound, although typically unattainable but valuable for comparative analysis, can be derived by presuming the absence of SI ($\mathsf{inr} = 0$) and relaxing hardware limitations. Under such conditions, the beamformers $\mathbf{W}_n$, $\mathbf{F}_m (m \neq n)$ need only to adhere to semi-unitary constraints. Consequently, the optimal precoders and combiners are determined by the dominant right and left singular vectors

Table 2.3: Power Consumption of Each Device [3].

Device	Notation	Value
Low Noise Amplifier	ρ_{LNA}	39 mW
Splitter	ρ_{SP}	19.5 mW
Combiner	ρ_{C}	19.5 mW
Phase Shifter	ρ_{PS}	2 mW
Mixer	ρ_{Mixer}	16.8 mW
Local Oscillator	ρ_{LO}	5 mW
Low Pass Filter	ρ_{LPF}	14 mW
Baseband Amplifier	$\rho_{\mathsf{BB_{amp}}}$	5 mW
ADC	ρ_{ADC}	$cB2^b$

Table 2.4: ADC Power Consumption Per Sample Per Level, c [3].

Scenario	Value	Generation
LPADC	5 fJ/step/Hz	Low Power (ideal future value)
IPADC	65 fJ/step/Hz	Intermediate Power
HPADC	494 fJ/step/Hz	High Power (state of the art)

of the inter-node channel matrix $\mathbf{H}_{nm}$, resulting in $\mathcal{I}_{nm} \leq \mathcal{I}_{\mathsf{Bound}}$ where

$$\mathcal{I}_{\mathsf{Bound}} = \sum_{\ell=0}^{N_{\mathsf{s}}-1} \log\left(1 + \sigma_\ell\left(\mathbf{H}\right)^2 \mathsf{snr}\right) \tag{2.24}$$

2.5 Numerical Results

We consider a two-node FD system operating at a carrier frequency of 28 GHz and a bandwidth $B = 1$ GHz. Parameters related to the inter-node channel are given by $C = 6$ clusters, $R_c = 8$ rays per cluster, and the angular spread of AoD/AoD is 20°. Parameters related to the SI channel are Rician factor $\kappa = 5$ dB, transceiver incline $\omega = \pi/6$ and transceiver gap $d = 2\lambda$, where λ is the wavelength of the carrier.

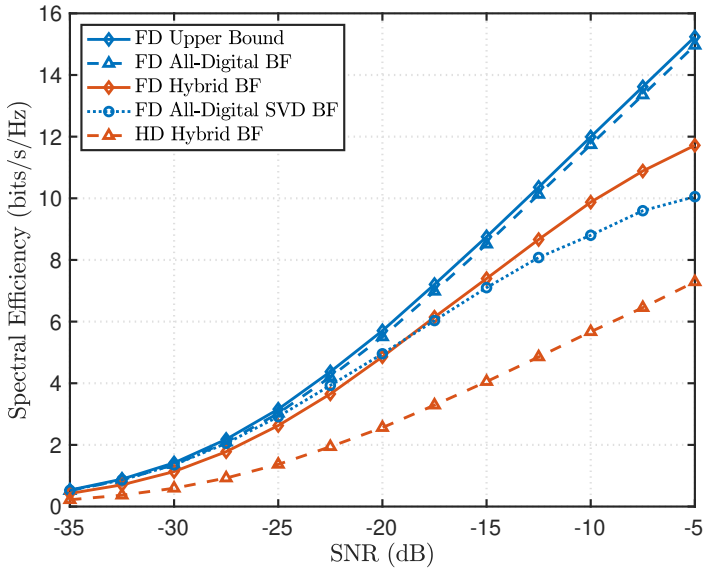

Figure 2.5: Spectral efficiency vs. SNR for different beamforming (BF) schemes. The plot is produced with $\mathsf{inr} = 15$ dB, $N_{\mathsf{TX}} = N_{\mathsf{RX}} = 64, N_{\mathsf{RF}}^{\mathsf{TX}} = N_{\mathsf{RF}}^{\mathsf{RX}} = 2$ and $N_{\mathsf{s}} = 2$. The all-digital design uses one RF chain per antenna element, which will use a prohibitively large amount of power, and is included here as a benchmark.

2.5.1 Comparison of Beamforming Schemes

Fig. 2.5 illustrates the spectral efficiency in relation to the average SNR for various beamforming methods. It is evident that the introduced FD Hybrid BF surpasses the HD mode, showcasing a significant rate gain that continues to increase with average SNR. This finding suggests the potential viability of the proposed FD design in cellular network settings, esp. considering that current BSs predominantly operate in HD mode. Additionally, our FD Hybrid BF design yields much better outcomes compared to the SVD method, even when the latter is executed in an all-digital framework. Specifically, as the average SNR escalates, the difference steadily widens, with the SVD method plateauing due to its inability to mitigate interference, and consequently overwhelming the ADCs. However, our FD Hybrid BF design incurs some rate losses when compared to the all-digital model and theoretical upper bound. Such losses can be attributed to the constraints on unit modulus and the diminished

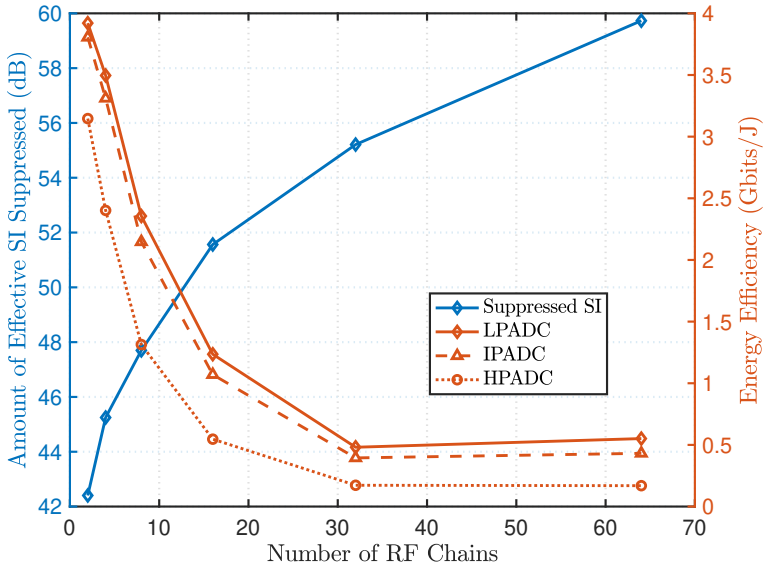

Figure 2.6: Results for hybrid beamforming: Amount of analog effective SI suppressed and energy efficiency for different number of RF chains. The energy efficiency is considered for the three ADC power modes. The plot is produced with $\mathsf{snr} = -5$ dB, $\mathsf{inr} = 15$ dB, $N_{\mathsf{TX}} = N_{\mathsf{RX}} = 128$, $N_{\mathsf{s}} = 2$ and 10 bits of ADC resolution.

DoF associated with RF chains in the hybrid setup, in contrast to the all-digital configuration.

2.5.2 Effect of the number of RF chains

The amount of effective SI suppressed, plotted in Fig. 2.6 is defined as

$$\Delta_0^\infty = \frac{\delta_0}{\delta_\infty} \tag{2.25}$$

where δ_0 and δ_∞ denote the effective SI level before running Algorithm 1 and after convergence. In other words, Δ_0^∞ measures the amount of effective SI rejected through beamforming in the analog domain.

Fig. 2.6 depicts the amount of effective SI suppressed and energy efficiency in relation to the number of RF chains across varying power modes. Notably, in settings with a large number of RF chains, the low power LPADC demonstrates superior

energy efficiency when contrasted with both intermediate IPADC and high power HPADC. This performance by LPADC can be anticipated, given its most favorable Walden figure of merit vs. IPADC and HPADC.

As the number of phase shifters directly correlates with the quantity of RF chains and antennas, there is a marked escalation in power consumption with an increase in the number of RF chains. Despite the enhancement in spectral efficiency as RF chains increase, power consumption rises at a pace that outstrips this, leading to a pronounced drop in energy efficiency. Conversely, with a minimal number of RF chains, the system attains optimal energy efficiency. This can be attributed to our adoption of a fully-connected array structure, wherein each RF chain connects to all antenna phase shifters.

In referencing the literature [161], a partially-connected array structure—where each RF chain links to a sub-array of antennas—demonstrates a distinct energy efficiency pattern compared to its fully-connected counterpart. The partially-connected structure tends to be more power-efficient when a sizable quantity of RF chains is integrated into the hardware. But, its reduced DoF translates into a dip in spectral efficiency. Yet, from an industrial perspective, prioritizing a limited number of RF chains becomes crucial to curtail power usage in hardware operating in the mmWave bands.

There's a certain latitude in sacrificing a bit of spectral efficiency. As we look to 5G advancements or even 6G, it becomes imperative to strike a balance between attaining peak spectral efficiency and curbing power consumption. Such a challenge often necessitates intricate optimization processes, compelling a shift in focus towards maximizing energy efficiency instead of solely emphasizing spectral efficiency.

In addition, we observe that by increasing the number of RF chains, the amount of effective SI suppressed, as shown by the difference before and after running Algorithm 1, is very large and reaches around 60 dB for 64 RF chains. Yet 32 and 16 RF chains can achieve reasonable amount of SI reduction, roughly 55.8 dB and 51.7

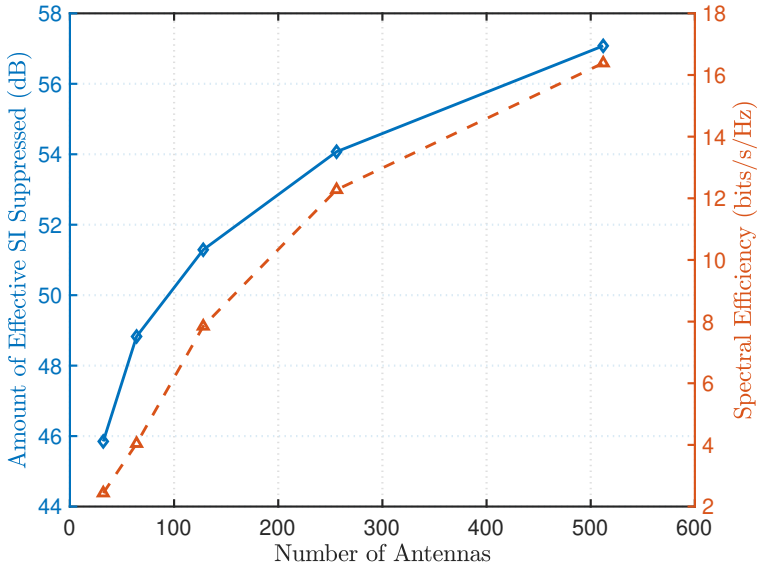

Figure 2.7: Results for hybrid beamforming: Amount of analog effective SI suppressed and spectral efficiency for different number of antennas. The plot is produced with $\mathsf{snr} = -5$ dB, $\mathsf{inr} = 15$ dB, $N_{\mathsf{RF}}^{\mathsf{TX}} = N_{\mathsf{RF}}^{\mathsf{RX}} = 16$ and $N_{\mathsf{s}} = 2$.

dB, respectively. Fig. 2.2 indicates that for a system to facilitate FD operation, a minimum of 50 dB of SI must be rejected. For a system outfitted with 128 antennas, a minimum of 16 RF chains is essential to prevent ADC saturation and make FD systems operational.

2.5.3 Effect of the number of antennas

Fig. 2.7 illustrates the amount of effective SI suppressed and the spectral efficiency with respect to the number of antennas. As the number of antennas increases, we achieve a more effective SI reduction of up to 63 dB with 512 antennas. With 16 RF chains, 32 and 64 antennas can bring the effective SI power, respectively, to 46 and 49 dB, respectively, which is not sufficient to avoid ADC saturation as illustrated by Fig. 2.2. Furthermore, 128 antennas can further reduce about 51.8 dB while 256 antennas can boost the SI reduction to around 57 dB. In addition, increasing DoF not only achieves large effective SI reduction but also increases the spectral efficiency

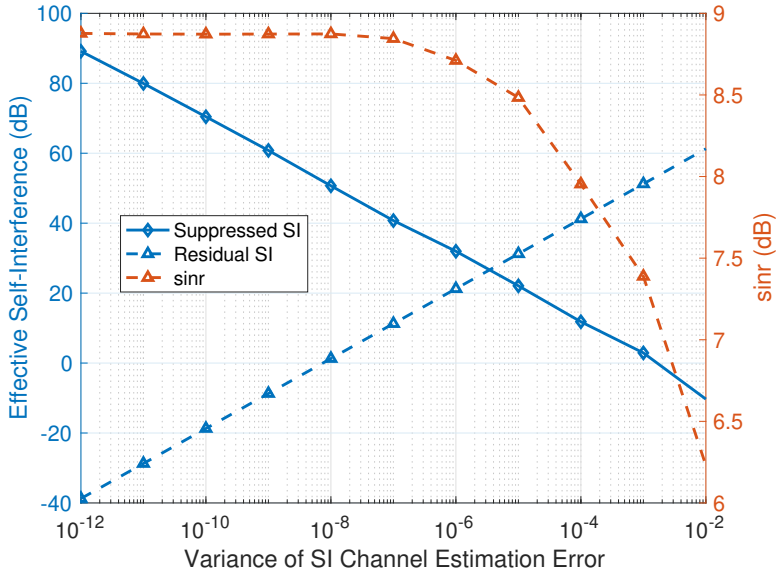

Figure 2.8: Results for analog-only architecture (single stream and single RF chain): sinr, residual and suppressed interference with respect to the variance of the SI channel estimation error. Results are produced with $\mathsf{snr} = 0$ dB, $\mathsf{inr} = 30$ dB and $N_{\mathsf{RX}} = N_{\mathsf{TX}} = 32$.

to around 16.5 bits/s/Hz for 512 antennas. Our joint beamforming design efficiently balances the use of the DoF between suppressing interference and increasing SE.

2.5.4 Channel estimation error

We address the influence of channel estimation error on the efficacy of our proposed models. Given the heightened sensitivity to SI levels, SI channel is anticipated to exert a more profound impact compared to inter-node channels. Based on that, we assume the inter-node channels $\mathbf{H}_{nm}, n \neq m$ are known whereas $\hat{\mathbf{H}}_{nn} = \mathbf{H}_{nn} + \tilde{\mathbf{H}}_{nn}$, where $\hat{\mathbf{H}}_{nn}$ is the SI channel estimate and $\tilde{\mathbf{H}}_{nn}$ is the estimation error, distributed as independent and identically (iid) zero-mean Gaussian with variance ϵ_n^2. Since $\tilde{\mathbf{H}}_{nn}$ is normalized to $\|\tilde{\mathbf{H}}_{nn}\|_F^2 = N_{\mathsf{RX}}^{(n)} N_{\mathsf{TX}}^{(n)}$, one has

$$\frac{\mathbb{E}\left[\|\tilde{\mathbf{H}}_{nn}\|_F^2\right]}{\mathbb{E}\left[\|\mathbf{H}_{nn}\|_F^2\right]} = \epsilon_n^2. \tag{2.26}$$

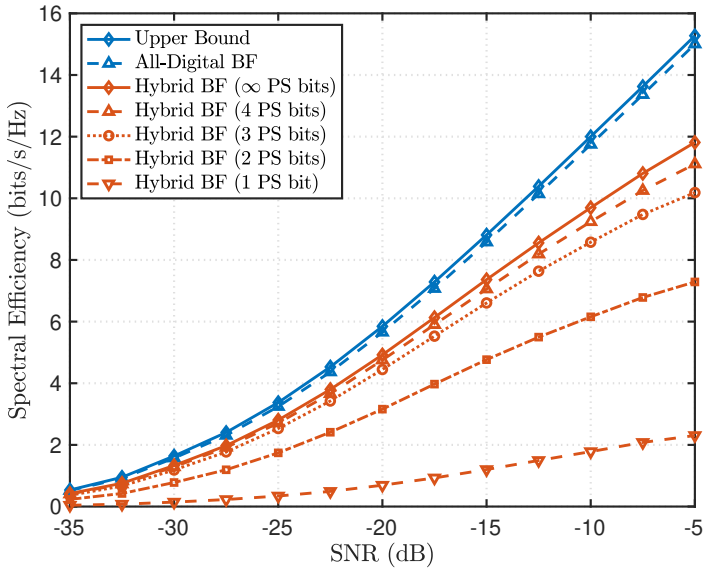

Figure 2.9: Spectral efficiency vs. SNR for different beamforming (BF) schemes. The hybrid BF is considered for different PS quantization bits. The results are obtained with $\mathsf{inr} = 15$ dB, $N_{\mathsf{TX}} = N_{\mathsf{RX}} = 64, N_{\mathsf{RF}}^{\mathsf{TX}} = N_{\mathsf{RF}}^{\mathsf{RX}} = 2, N_{\mathsf{s}} = 2$. The all-digital design uses one RF chain per antenna element, which will use prohibitively large amounts of power, and is included here as a benchmark.

The outcomes of this are depicted in Fig. 2.8 for an analog-only architecture comprising 32 antennas, single RF chain and single spatial stream in both directions, with $\mathsf{snr} = 0$ dB, $\mathsf{inr} = 30$ dB and channel estimation error power $\epsilon_n^2 = \epsilon_m^2$ across both nodes. Elevated channel estimation error power incurs more degradation into the system performance since the minimization of the SI power is not guaranteed with imperfect CSI. This leads to amplifying the residual SI power and reducing the amount of effective SI suppressed. Furthermore, since the channel estimation error is treated as additional source of interference, when the variance of the error increases, the resulting effective SI is also growing and therefore the sinr is affected. For example, the sinr is quite stable for $\epsilon^2 \leq 10^{-7}$, however, it decreases as ϵ^2 becomes higher than 10^{-6}.

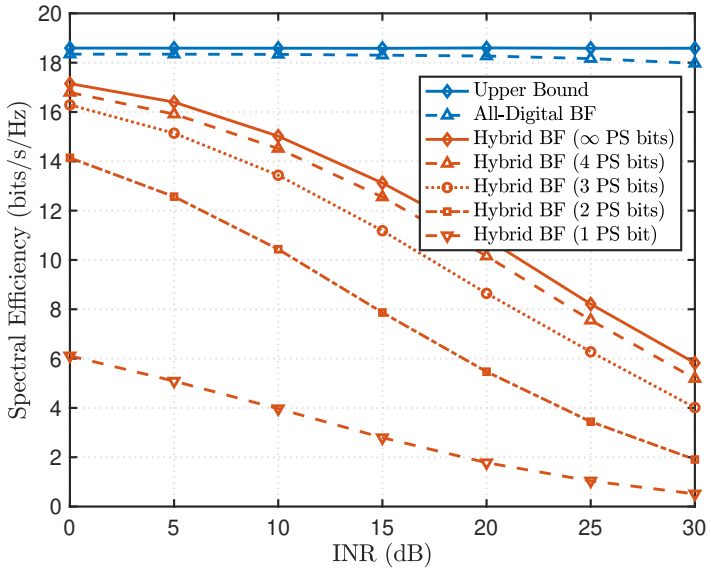

Figure 2.10: Spectral efficiency vs. INR for different beamforming (BF) schemes. The hybrid BF is considered for different PS quantization bits. The results are obtained with $\mathsf{snr} = 0$ dB, $N_{\mathsf{TX}} = N_{\mathsf{RX}} = 64, N_{\mathsf{RF}}^{\mathsf{TX}} = N_{\mathsf{RF}}^{\mathsf{RX}} = 2, N_{\mathsf{s}} = 2$. The all-digital design uses one RF chain per antenna element, which will use prohibitively large amounts of power, and is included here as a benchmark.

2.5.5 Phase shifter resolution

Fig. 2.9 illustrates the spectral efficiency vs. the average SNR for different BF schemes as well as the effect of different PS quantization bits. We observe that by decreasing the number PS bits, the performance gets worse; e.g., 4 PS bits incur an SNR degradation of -2.5 dB with respect to the infinite PS resolution. Further decreasing the number of PS bits introduces more SNR losses about -5 dB, -13 dB and -22.5 dB for 3, 2 and 1 bit, respectively. These observations are further confirmed by Fig. 2.10 wherein we illustrate the spectral efficiency vs. the average INR for different BF schemes as well as the effect of the PS resolution. With quantized PSs, the SI suppression becomes inaccurate; i.e., the interference is re-introduced into the system resulting into a poor spectral efficiency. By decreasing the PS resolution bits, the SI suppression accuracy also decreases; i.e., severe interference is re-injected into the

system and hence the spectral efficiency is subject to more degradation.

2.5.6 Practical Design and Tradeoffs

The objective of our proposed hybrid beamforming design is leveraging the available DoF in terms of antennas and RF chains to improve the spectral efficiency and reduce the SI power.

Starting with the worst case scenario $(N_{\mathsf{RX}}, N_{\mathsf{RF}}) = (1, 1)$, although lower complexity and power consumption are required, the spectral efficiency as well as the amount of SI suppression are very poor. This result is explained by the fact that the available DoF are not sufficient to suppress the SI and enhance the spectral efficiency, given that our design relies on a massive number of DoF.

For a fixed number of RF chains, e.g., $N_{\mathsf{RF}} = 16$, increasing the number of antennas (from 16 to 512) improves the spectral efficiency from 4.6713 to 28.7508 bits/s/Hz (around 83.75% improvement). This increase in number of antennas also achieves about 59.1286 dB and 72.2514 dB reduction in effective SI, respectively. In addition, for $N_{\mathsf{RF}} \in 32, 64, 128$, respectively, increasing the number of antennas achieves about 69.82%, 58.14% and 18.60% of spectral efficiency enhancement. In addition, the number of antennas increases the efficiency in suppressing the analog SI. For example, for a fixed number of RF chains such as $N_{\mathsf{RF}} = 4$, by increasing the number of antennas from 16 to 512, the amount of SI suppressed increases from 51.1346 dB to 66.8737 dB (around 15.7391 dB increase in SI suppression). For $N_{\mathsf{RF}} \in \{16, 32, 64, 128\}$, respectively, increasing the number of antennas also further enhances the efficiency in analog SI suppression about 13.1228 dB, 10.2706 dB, 9.5092 dB and 5.0863 dB, respectively. On the other hand, increasing the number of antennas substantially increases the computational complexity since it is dominated by $\frac{1}{3}N_{\mathsf{RX}}^3$ as detailed by the computational complexity analysis in Table 2.2. In addition, the hardware requires hefty power consumption for a massive number of antennas, e.g., with $N_{\mathsf{RF}} = 1$, increasing the number of antennas from 1 to 512 also increases

Table 2.5: Target metric results for different numbers of antennas (N_{RX}) and RF chains (N_{RF}). We consider the amount of effective SI suppressed in the analog domain Δ_0^∞ as defined by (2.20). The computational complexity is evaluated as the number of floating-point operations required to configure the analog combiner $\mathbf{W}_n^{\mathsf{RF}}$. Results are simulated with $\mathsf{snr} = 5$ dB, $\mathsf{inr} = 30$ dB, HPADC mode and 10 bits of ADC resolution. The total power consumption in dBm is evaluated at the receiver (2.22). Settings that enable FD operation ($\Delta_0^\infty \geq 50$ dB) are highlighted in bold font.

$(N_{\mathsf{RX}}, N_{\mathsf{RF}})$	**SE (bits/s/Hz)**	Δ_0^∞ **(dB)**	**Complexity (MFLOPS)**	**Power (dBm)**
(1,1)	0.0014	-122.7386	6.1667e-06	30.5404
(16,1)	1.1556	42.6378	0.0023	33.0963
(32,1)	2.1647	45.7153	0.0146	34.7828
(64,1)	4.0781	49.1768	0.1018	36.9408
(128,1)	6.8318	**52.0405**	0.7567	39.4527
(256,1)	9.4134	**55.7835**	5.8223	42.1906
(512,1)	12.0488	**58.2820**	45.6578	45.0580
(16,2)	1.3673	47.5886	0.0033	34.9749
(32,2)	2.8530	**50.9809**	0.0183	36.1742
(64,2)	5.9009	**54.2940**	0.1166	37.8845
(128,2)	10.7337	**57.4724**	0.8148	40.0621
(256,2)	16.3465	**60.6778**	6.0532	42.5873
(512,2)	21.5733	**63.5513**	46.5783	45.3331
(16,4)	1.4560	**51.1346**	0.0055	37.2852
(32,4)	3.7698	**53.7236**	0.0263	38.0727
(64,4)	6.5487	**57.0377**	0.1468	39.3166
(128,4)	12.2912	**60.2226**	0.9325	41.0721
(256,4)	18.7435	**63.4234**	6.5181	43.2863
(512,4)	23.4077	**66.8737**	48.4257	45.8361
(16,16)	4.6713	**59.1286**	0.0253	42.6952
(32,16)	6.4003	**61.0395**	0.0860	43.0208
(64,16)	9.7695	**63.8643**	0.3509	43.6067
(128,16)	17.0681	**66.3901**	1.6835	44.5843
(256,16)	23.4479	**69.1546**	9.3949	46.0552
(512,16)	28.7508	**72.2514**	59.6828	48.0269
(32,32)	9.6111	**66.3456**	0.2021	45.8234
(64,32)	12.8400	**66.6776**	0.6881	46.2474
(128,32)	20.8642	**70.3621**	2.8071	46.9883
(256,32)	26.4013	**73.5857**	13.4676	48.1733
(512,32)	31.8479	**76.6162**	75.1589	49.8688
(64,64)	15.0882	**71.2978**	1.6166	49.0604
(128,64)	25.1033	**74.5826**	0.5870	50.0469
(256,64)	32.6504	**77.4570**	22.4570	50.6578
(512,64)	36.0522	**80.8070**	107.7412	52.1510
(128,128)	32.0314	**76.9282**	12.9324	52.4913
(256,128)	36.0611	**79.0967**	44.0402	53.3792
(512,128)	39.3526	**82.0145**	179.6560	54.7457
(256,256)	43.1311	**81.6408**	103.4595	56.2375
(512,256)	52.8005	**83.4704**	352.32115	57.5322
(512,512)	60.6294	**86.0893**	827.6760	60.4262
Averaging Over Feasible Settings	**20.4712**	**66.9799**	**56.5116**	**46.1551**

Table 2.6: Increase in target metric for a fixed number of RF chains (N_{RF}) while varying the number of antennas (N_{RX}) from N_{RF} to 512. Extracted from Table 2.5.

N_{RF}	**SE (bits/s/Hz)**	Δ_0^∞ **(dB)**	**Complexity (MFLOPS)**	**Power (dB)**
1	10.89 (90.40%)	15.64	45.6555	11.9617
2	20.20 (93.66%)	15.96	46.5750	10.3582
4	21.95 (93.77%)	15.73	48.4202	8.5509
16	24.07 (83.75%)	13.12	59.6575	5.3317
32	22.23 (69.82%)	10.27	74.9568	4.0454
64	20.96 (58.14%)	9.50	106.1246	3.0906
128	7.32 (18.60%)	5.08	166.7236	2.2544
256	9.66 (18.31%)	1.82	248.8616	1.2947

Table 2.7: Increase in target metric for a fixed number of antennas (N_{RX}) while varying the number of RF chains (N_{RF}) from 1 to N_{RX}. Extracted from Table 2.5.

N_{RX}	**SE (bits/s/Hz)**	Δ_0^∞ **(dB)**	**Complexity (MFLOPS)**	**Power (dB)**
16	3.51 (75.26%)	16.49	0.0230	9.5989
32	7.44 (77.47%)	20.63	0.1875	11.0406
64	11.01 (72.97%)	22.12	1.5148	12.1196
128	25.19 (78.67%)	24.88	12.1757	13.0386
256	33.71 (78.17%)	25.85	97.6372	14.0469
512	48.58 (80.12%)	27.80	782.0182	15.3682

the power consumption by about 11.9617 dB. More information about the effect of increasing the number of antennas, with a fixed number of RF chains, are presented by Table 2.6.

For a fixed number of antennas, increasing the number of RF chains reduces the analog effective SI power. For $N_{\mathsf{RX}} = 64$, increasing the number of RF chains from 1 to 2 achieves about (49.1768 dB $<$ 50 dB, which is not a feasible setting) and 54.2940 dB; therefore, the new FD setting (with 2 RF chains) becomes feasible. Further increase in N_{RF} to 4, 16, 32 and 64 improves the amount of effective SI suppression to about 57.0377 dB, 63.8643 dB, 66.6776 dB and 71.2978 dB, respectively; i.e., switching N_{RF} from 1 to 64 further improves the total SI suppression for about 22.12

dB as shown by Table 2.7. With $N_{\mathsf{RX}} = 512$, increasing the RF chains from 1 to 512 achieves about 58.2820 dB and 86.0893 dB, respectively, which increases the SI suppression efficiency by about 27.80 dB. Moreover, similar to the effective SI reduction, increasing the number of RF chains also improves the SE; e.g., with fixed $N_{\mathsf{RX}} = 128$, increasing N_{RF} from 1 to 128 achieves about 6.8318 bits/s/Hz and 32.0314 bits/s/Hz which is 78.67% of spectral efficiency improvement. With $N_{\mathsf{RX}} = 256$, switching N_{RF} from 1 to 256 achieves about 9.4134 bits/s/Hz and 43.1311 bits/s/Hz, which is 78.17 % spectral efficiency enhancement. However, increasing the number of RF chains increases the computational complexity as well as the power consumption. For example, with $N_{\mathsf{RX}} = 32$ increasing N_{RF} from 1 to 32 requires about 0.0023 MFLOPS and 0.2021 MFLOPS, respectively, i.e., about 100 times increase in floating-point operations. This increase requires 34.7828 dBm and 45.8234 dBm, respectively, which is an 11.0406 dB increase in power consumption as illustrated by Table 2.7. More insights on the effect of the number of RF chains with fixed number of antennas can be found in Table 2.7.

For practical consideration, with 10 bits of ADC resolution, the maximum ADC dynamic range is around 60 dB. Given that we need to achieve a total of 120 dB SI isolation, according to Fig. 2.2, a minimum of 50 dB of SI has to be rejected by analog beamforming to enable FD operation. In Table 2.5, we highlight in bold the feasible FD system configurations ensuring at least 50 dB of analog SI suppression.

According to Table 2.5, systems settings achieving higher SI reduction and spectral efficiency, i.e. with large number of antennas and RF chains, also increases the complexity and power consumption and vice versa. Since the average is evaluated on the FD settings, i.e., a minimum of 50 dB of SI reduction is achieved, we therefore focus our discussion on the tradeoffs between the spectral efficiency vs. complexity and power consumption. If we allow a tolerance (lower bound on spectral efficiency) of $\overline{\mathsf{SE}} = 20.5 - 2 = 18.5$ bits/s/Hz based on the service provider or QoS requirements dictated by a given application/service to be supported in terms of spectral efficiency threshold, then we can pick the following settings $(N_{\mathsf{RX}}, N_{\mathsf{RF}}^{\mathsf{RX}}) = (512,2), (256,4),$

(512,4), (256,16), (512,16), (128,32), (256,32), (512,32), (128,64), (256,64), (512,64), (128,128), (256,128), (512,128), (256,256), (512,256), (512,512). The setting (512,512) achieves the best spectral efficiency (60.6294 bits/s/Hz) as well as the highest SI reduction; however, the computational complexity is huge (827.6760 MFLOPS) and hence the design is not suitable for practical consideration. The same observation can be made with respect to (512,256), (256,256), (512,128), (512,64) wherein the relative computational complexity, exceeding 100 MFLOPS, is far larger to those for other settings, and therefore they can be excluded from consideration. For example, (512,2) and (512,4) require high complexity of around 46.5 and 48.4 MFLOPS and yet the achievable spectral efficiency is around the average, so they can be discarded. As stated earlier, an acceptable spectral efficiency can be around the average and based on that, the other settings (512,16), (512,32), (256,32), (256,64), (128,128), (256,128) achieve better spectral efficiency and yet the complexity and power consumption are hefty. Now the designer is left with settings (256,4), (256,16), (128,32), and (128,64) which achieve good spectral efficiency around the average as well as satisfactory SI reduction but most importantly with reduced computational complexity ($\leq$ 10 MFLOPS) and power consumption compared to the other settings.

In terms of power consumption, the settings (128,32) and (256,16) achieve the closest values to the average power consumption. In terms of spectral efficiency, (256,16) achieves better spectral efficiency compared to (128,32) and yet the amount of SI reduction is quite similar (around 70 dB) while the setting (128,32) saves around 6.5878 MFLOPS. From an industrial point of view, the primary concern is the power consumption and computational complexity; hence, the setting (128,32) is the best candidate. The setting (256,4) requires the least power consumption (43.2863 dBm) among the four settings; however, in terms of computational complexity, SI reduction and spectral efficiency is worse when compared to (128,32). The setting (128,64) achieves the best spectral efficiency as well as the highest SI reduction, but the power consumption is about 5 dB more than that for (128,32). Consequently, the setting (128,32) achieves the best tradeoff among the considered target metrics to enable FD

system operation.

Furthermore, since 10-bit ADCs offer a maximum dynamic range of 60 dB and require at least 50 dB of SI reduction out of the 120 dB in Fig. 2.2, the setting $(N_{\mathsf{RX}}, N_{\mathsf{RF}}^{\mathsf{RX}}) = (128, 32)$ achieves about 70 dB of SI reduction. Thereby, the ADC may operate at lower dynamic range and hence fewer bits of resolution can be considered. Therefore, the proposed design may suggest ADC operating at low resolution and yet not saturated. This observation needs careful attention and considering low resolution ADC will be a future direction of this research.

2.6 Conclusion

Beamforming is a powerful tool for suppressing SI in mmWave FD systems. Using a hybrid A/D architecture to reduce the number of RF chains so as to reduce the power consumption imposes hardware constraints such the unit modulus constraint as well as quantized PSs. In this work, we propose a hybrid A/D beamforming design algorithm to achieve a large effective analog SI suppression to avoid the saturation of the analog front end and maximizing the sum spectral efficiency. More precisely, we introduced a constraint into the optimization problem to avoid assigning all the DoF for SI suppression. The constraint allocates a fraction of the DoF to ensure that the rank of effective channel is not experiencing deficiency in order to sustain a maximum number of admissible spatial streams and then guaranteeing a satisfactory multiplexing gain. We also investigate the effects of the number of PSs quantization bits, channel estimation error, number of RF chains, and number of antennas on spectral efficiency, energy efficiency, SINR per RF chain, and analog effective SI (residual and suppressed). The results show that our design achieves not only large SI reduction in the analog domain (around 67 dB on average) but also enhances the SE. We further determined the optimal number of RF chains and number of antennas to derive the best tradeoff in terms of spectral efficiency, analog effective SI suppression, computation complexity, and total power consumption. From an

industrial viewpoint, a practical design can be implemented with 128 antennas and 32 RF chains offering a 20.8642 bits/s/Hz, a reduced complexity of about 2.8071 MFLOPS, and significant SI suppression of about 70.3621 dB. This large amount of SI suppression may allow the ADC to reduce its dynamic range, i.e., operate using low bit resolution ADCs and therefore reducing the power consumption in the ADCs. Finally, the actual design/architecture can be extended to support partially-connected PSs structures and low resolution data converters as well as multiuser MIMO and wideband configurations.

Chapter 3: Single-Cell Single User MIMO

FD operation at the BS enables simultaneous transmission and reception of signals and promises considerable increases in spectral efficiency. FD operation however results in a new source of interference SI causing ADC saturation and a subsequent reduction in spectral efficiency gains. In this chapter[1], I present a novel design of precoders and combiners for mmWave BSs that leverages a hybrid A/D beamforming architecture. The proposed design balances SI reduction in the analog domain to avoid ADC saturation and in the digital domain to enable increased spectral efficiency. Our hybrid beamforming design requires a few iterations to converge and provides reasonable performance, significantly improving upon related work in the literature. For example, our hybrid FD design achieves spectral efficiency gains of 1.05x to 3.09x vs. several leading hybrid FD designs; an spectral efficiency gain of 1.91x vs. HD; and an spectral efficiency loss of 1.10x vs. an all-digital FD beamformer. The all-digital FD beamformer assumes there is no ADC saturation and uses one RF chain per antenna (which has prohibitive power consumption for a large number of antennas).

3.1 Introduction

MmWave bands are an integral part of 5G, and will continue to play a crucial role in enabling high data rates in next generation networks [153, 125, 123]. The increased transmission bandwidths come at a price of higher propagation losses which can be counteracted by the use of large antenna arrays at the BSs [55, 71].

[1]This chapter is based on the work published in the following journal paper: E. Balti, S. Akoum, I. Alfalujah and B. L. Evans, "Hybrid Beamforming Design For Full-Duplex Millimeter Wave Massive MIMO Systems," in *IEEE Transactions on Vehicular Technology.* This work was supported by AT&T labs, NVIDIA and Tektronix through their industrial affiliation with the 6G@UT research center at UT Austin.

The advent of FD communication technologies heralds a transformative era in the landscape of 5G and nascent 6G networks, introducing the capability for simultaneous bidirectional data transmission and reception within the same resource block (time/frequency). This groundbreaking advancement promises to revolutionize wireless communication by potentially doubling spectral efficiency and markedly reducing latency, thereby addressing the escalating demands for higher data throughput and more efficient spectrum utilization in an increasingly connected world [104]. The integration of FD communication, particularly through the deployment of mmWave-based FD for IAB, exemplifies the industry's commitment to harnessing this technology for enhancing network capabilities and fostering new communication paradigms [22]. The allure of FD technology extends beyond its promise of spectral efficiency enhancement; it can also lead to novel network architectures, more resilient communication links, and new real-time applications because of the reduced latency.

The realization of FD's full potential is intricately tied to overcoming significant technical challenges, chief among them being the mitigation of loopback SI [100]. SI in FD systems presents a formidable obstacle, as the power of the loopback interference signal can vastly exceed that of the incoming desired signal, leading to potential analog-to-digital (ADC) saturation. This not only compromises the spectral efficiency gains afforded by FD communication but also threatens the operational integrity of the system, rendering it incapable of achieving the anticipated performance enhancements. Addressing SI effectively requires a multifaceted approach, encompassing both analog and digital domain interference suppression techniques. The analog domain is particularly critical, as suppression at this stage is essential for preventing ADC saturation and ensuring that subsequent digital domain processing can refine the signal quality to achieve a noise floor that is conducive to high-quality communication [142].

In response to these challenges, our research focuses on the development and optimization of robust hybrid beamforming techniques specifically designed to address the unique demands of FD communication systems. By prioritizing interference

suppression in the analog domain, our work aims to lay the groundwork for FD systems to achieve their full potential, unlocking new dimensions of spectral and energy efficiency that can significantly contribute to the performance and sustainability of future wireless networks. Through comprehensive analysis and innovative design, we strive to mitigate the inherent limitations posed by SI, paving the way for FD technologies to become a cornerstone of advanced wireless communication strategies in the era of 5G and beyond.

3.1.1 Related Work

In FD transceivers, SI power suppression is typically achieved through a synergistic application of both active and passive techniques. Passive cancellation leverages the enhancement of path loss for the loopback SI signal, utilizing strategies such as array directivity, physical separation of antennas (antenna isolation), polarization, and the incorporation of radio-frequency (RF) absorbing materials. For instance, improvements in array directivity and strategic antenna placement have been shown to attenuate SI power by 30 dB and 47 dB, respectively, while cross-polarization techniques can facilitate up to 50 dB of SI reduction [81].

Conversely, active cancellation techniques are predicated on the precise knowledge of the transmitted signal and are typically executed in three distinct stages: RF suppression, antenna suppression, and digital suppression. RF suppression uses the known transmitted signal as a reference within the RF chain to reconstruct and subsequently subtract the SI. Antenna cancellation is achieved by generating two antiphase replicas of the transmitted signal through multiple TX and RX antennas, thereby nullifying the SI through the superposition of these antiphase replicas. Digital cancellation complements RF or antenna suppression methods by further attenuating the SI in the baseband, which, when combined with either RF or antenna suppression techniques, can result in approximately 60 dB of SI reduction, as both SI and noise are concurrently mitigated [81]. However, these techniques may encounter performance degradation due to nonlinearities introduced by data converters, power

amplifiers, in-phase and quadrature (I/Q) imbalance, and phase noise, leading to significant residual SI [156]. This highlights the complex interplay between various suppression methods and the inherent challenges in achieving optimal SI mitigation in FD communication systems. Table 1.2 summarizes the amount of SI to be canceled to enable FD operation for various network generations.

Recently, BFC algorithms have been specifically designed to mitigate SI in FD systems [21, 98, 132, 165, 22, 137]. BFC was originally considered in [92] based on a zero-forcing (ZF) constraint on the SI. Although this approach shows a very small loss compared to an SI-free scenario, the design assumes a single data stream and is implemented using an all-digital architecture. The all-digital FD beamformer uses one RF chain per antenna which has prohibitive power consumption for a large number of antennas. This design is later extended to support multiple data streams with hybrid beamforming [21]. The work [137] uses hybrid factorization of all-digital beamformers which has two main issues: it suffers from high SI leakage due to approximation errors and mitigates SI at the baseband rather than in the analog domain which can lead to the ADC saturation. The design [165] developed BFC based on ZF constraint on the SI. However, when projecting the analog beamformers on the unit modulus space, the ZF constraint is violated and high SI is re-introduced into the system resulting in a very low spectral efficiency. Moreover, [132] developed a frequency-selective hybrid beamforming design to maximize spectral efficiency; however, the SI is suppressed in the baseband using a LMMSE precoder. Although the results show spectral efficiency enhancement, the dynamic range and saturation of the ADC are not addressed by this work.

In [19, 17, 20], the authors present a unified framework for FD massive MIMO communications in cellular networks with low resolution data converters for LTE and mmWave bands. Although these papers provide accurate modeling of network irregularities and impairments, the design does not attempt to suppress SI.

In this chapter, we design hybrid A/D beamformers aiming at maximizing

the spectral efficiency. The use of the DoF in terms of antennas are balanced between maximizing the beamformed power and ensuring that large SI is reduced in the analog domain to avoid ADC saturation, e.g, increasing the number of antennas at the BS from 4 to 128 can achieve about 130 dB reduction of SI. As the literature states, the unit modulus constraint imposed on analog beamformers may violate the interference suppression constraint. Our model solves this shortcoming by using the *Alternating Projection* method to minimize the losses incurred by these successive projections. For example, by considering both the unit modulus and interference suppression constraints, our design achieves a notable increase in SE, showing an enhancement of approximately 70% compared to approaches that manage these constraints separately. Furthermore, our design requires just a few iterations to converge; e.g., 15 iterations lead to 180 dB reduction in SI as well as 25 dB increase in the uplink SINR per RF chain. Furthermore, our design achieves considerable gains in term of spectral efficiency compared to related work. For example, our hybrid FD design achieves spectral efficiency gains of 1.05x to 3.09x vs. several leading hybrid FD designs; an spectral efficiency gain of 1.91x vs. HD; and an spectral efficiency loss of 1.10x vs. an all-digital FD beamformer. The all-digital FD beamformer assumes no ADC saturation, and uses one RF chain per antenna which has prohibitive power consumption for a large number of antennas.

3.1.2 Contributions

In this chapter, we explore a single-user (in uplink/downlink) MIMO framework, focusing on a FD BS facilitating concurrent uplink and downlink communications. Our primary objective is the mitigation of interference through the joint optimization of beamforming weights. Initially, we procure an all-digital beamforming solution, predicated on the iterative routine under the assumption of perfect CSI. Leveraging these all-digital solutions, we subsequently derive hybrid A/D beamforming. Our approach allocates DoF to both maintain the signal's dimensionality and effectively suppress interference. The contributions of this work are detailed below:

- I design the all-digital beamformers to serve as both a performance benchmark, given their higher power consumption, and to establish an upper bound for spectral efficiency (SE). Our results indicate that the proposed all-digital solution closely approaches this upper bound.

- I develop robust hybrid A/D beamforming techniques for both users and the base station (BS), with the objective of minimizing SI and IUI, while maintaining the rank of the effective channels in both uplink and downlink communications.

- In our hybrid A/D design, I strategically manage the unit modulus constraint alongside interference suppression in the analog domain. This approach ensures that the unit modulus constraint does not compromise interference suppression, which is crucial for mitigating risks of ADC saturation. Our results, as illustrated in Fig. 2.2, demonstrate the effectiveness of this approach, achieving over 50 dB of SI reduction in the analog domain, enabling FD operation.

- I compare and analyze our beamforming design in terms of both computational cost and performance, including spectral efficiency and SI reduction. Given that the hybrid A/D beamforming design problem is non-convex, we also investigate the stability and convergence rates under various scenarios.

- I conduct a comprehensive comparative analysis, benchmark our hybrid A/D beamforming design against previous methods. This evaluation highlights the enhanced robustness and superior performance of our approach, demonstrating significant improvements in spectral efficiency and interference suppression compared to related work.

3.1.3 Structure

The rest of the chapter is organized as follows: Section 3.2 discusses the system and channel models, while the beamforming design for all-digital and hybrid architec-

tures are detailed in Section 3.3. Target metrics are analyzed in Section 3.4, whereas numerical results and their discussions appear in Section 3.5. Section 3.6 concludes the chapter.

3.2 System Model

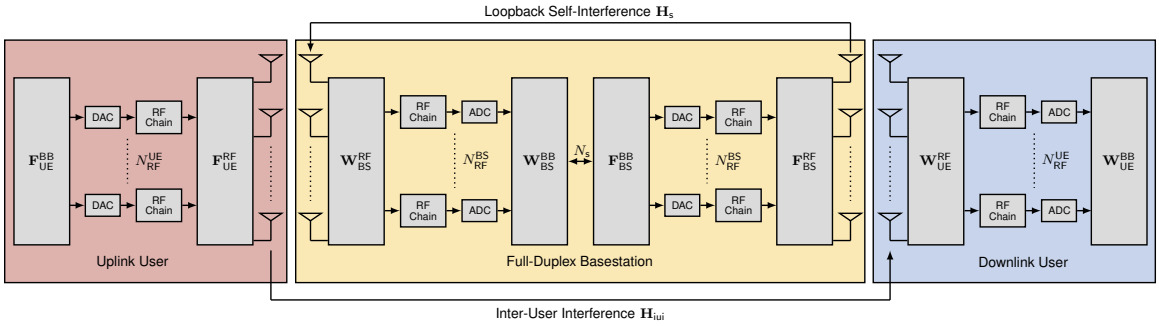

Figure 3.1: Basic abstraction of the hybrid A/D architecture of the FD BS and the uplink/downlink users. The number of streams that the BS can sustain is denoted by N_{s} while the number of RF chains at the BS and the users are denoted by $N_{\mathsf{RF}}^{\mathsf{BS}}$ and $N_{\mathsf{RF}}^{\mathsf{UE}}$, respectively. We further illustrate the loopback SI from the transmit to receive arrays of the BS and we denote it by $\mathbf{H}_{\mathsf{s}}$ the aggregate SI channel. Besides, the IUI channel from the uplink to the downlink user is denoted by $\mathbf{H}_{\mathsf{iui}}$.

I consider a single-user mmWave FD system wherein the uplink user sends N_{s} data streams to the FD BS while the latter sends N_{s} independent data streams (independent with respect to uplink streams) to the downlink user. The FD BS and the users are equipped with N_{BS} and N_{UE} antennas, respectively. In addition, the FD BS and the users have $N_{\mathsf{RF}}^{\mathsf{BS}}$ and $N_{\mathsf{RF}}^{\mathsf{UE}}$ RF chains, respectively. Note that the RF chains are subject to these constraints $N_{\mathsf{s}} \leq N_{\mathsf{RF}}^{\mathsf{BS}} \leq N_{\mathsf{BS}}$ and $N_{\mathsf{s}} \leq N_{\mathsf{RF}}^{\mathsf{UE}} \leq N_{\mathsf{UE}}$.

Assumption 1. We assume that the FD BS has separate arrays wherein one of them is dedicated for transmitting while the other is dedicated for receiving.

Assumption 2. We assume that the transmit and receive modules of the BS are equipped with the same number of antennas as well as the same number of RF chains and the same number of data streams (N_s). In addition, we presume that the uplink

and downlink users are equipped with the same number of antennas as well as the same number of RF chains and the same number of data streams.

Initially, the uplink user applies the digital precoder $\mathbf{F}_{\mathsf{UE}}^{\mathsf{BB}} \in \mathbb{C}^{N_{\mathsf{RF}}^{\mathsf{UE}} \times N_{\mathsf{s}}}$ to the N_{s} data streams followed by the analog precoder $\mathbf{F}_{\mathsf{UE}}^{\mathsf{RF}} \in \mathbb{C}^{N_{\mathsf{UE}} \times N_{\mathsf{RF}}^{\mathsf{UE}}}$. Note that the uplink precoded transmit signal can be written as $\mathbf{x}_{\mathsf{u}} = \mathbf{F}_{\mathsf{UE}}^{\mathsf{RF}} \mathbf{F}_{\mathsf{UE}}^{\mathsf{BB}} \mathbf{s}_{\mathsf{u}}$, where $\mathbf{s}_{\mathsf{u}}$ is the $N_{\mathsf{s}} \times 1$ uplink symbol vector with covariance matrix $\mathbb{E}\left[\mathbf{s}_{\mathsf{u}} \mathbf{s}_{\mathsf{u}}^{*}\right] = \frac{1}{N_{\mathsf{s}}} \mathbf{I}_{N_{\mathsf{s}}}$. To process the uplink received signal, the BS applies the analog combiner $\mathbf{W}_{\mathsf{BS}}^{\mathsf{RF}} \in \mathbb{C}^{N_{\mathsf{BS}} \times N_{\mathsf{RF}}^{\mathsf{BS}}}$ followed by the digital combiner $\mathbf{W}_{\mathsf{BS}}^{\mathsf{BB}} \in \mathbb{C}^{N_{\mathsf{RF}}^{\mathsf{BS}} \times N_{\mathsf{s}}}$ in order to extract the N_{s} data streams.

In the downlink scenario, the BS applies the digital precoder $\mathbf{F}_{\mathsf{BS}}^{\mathsf{BB}} \in \mathbb{C}^{N_{\mathsf{RF}}^{\mathsf{BS}} \times N_{\mathsf{s}}}$ to the N_{s} streams followed by the analog precoder $\mathbf{F}_{\mathsf{BS}}^{\mathsf{RF}} \in \mathbb{C}^{N_{\mathsf{BS}} \times N_{\mathsf{RF}}^{\mathsf{BS}}}$. Note that the downlink precoded transmit signal can be written as $\mathbf{x}_{\mathsf{d}} = \mathbf{F}_{\mathsf{BS}}^{\mathsf{RF}} \mathbf{F}_{\mathsf{BS}}^{\mathsf{BB}} \mathbf{s}_{\mathsf{d}}$, where $\mathbf{s}_{\mathsf{d}}$ is the $N_{\mathsf{s}} \times 1$ downlink symbol vector with covariance matrix $\mathbb{E}\left[\mathbf{s}_{\mathsf{d}} \mathbf{s}_{\mathsf{d}}^{*}\right] = \frac{1}{N_{\mathsf{s}}} \mathbf{I}_{N_{\mathsf{s}}}$. To process the downlink received signal, the user applies the analog combiner $\mathbf{W}_{\mathsf{UE}}^{\mathsf{RF}} \in \mathbb{C}^{N_{\mathsf{UE}} \times N_{\mathsf{RF}}^{\mathsf{UE}}}$ followed by the digital combiner $\mathbf{W}_{\mathsf{UE}}^{\mathsf{BB}} \in \mathbb{C}^{N_{\mathsf{RF}}^{\mathsf{UE}} \times N_{\mathsf{s}}}$ in order to extract the N_{s} data streams. Since the BS and the users are implemented using analog phase shifters, they are subject to the unit modulus constraint, i.e., each entry of the analog beamformer satisfies the following constraint

$$\begin{aligned} &\left|\left[\mathbf{F}_{\mathsf{BS}}^{\mathsf{RF}}\right]_{mn}\right|^2 = \left|\left[\mathbf{W}_{\mathsf{BS}}^{\mathsf{RF}}\right]_{mn}\right|^2 = \frac{1}{N_{\mathsf{BS}}} \\ &\forall\ 1 \leq m \leq N_{\mathsf{BS}},\ \forall\ 1 \leq n \leq N_{\mathsf{RF}}^{\mathsf{BS}} \end{aligned} \tag{3.1}$$

$$\begin{aligned} &\left|\left[\mathbf{F}_{\mathsf{UE}}^{\mathsf{RF}}\right]_{mn}\right|^2 = \left|\left[\mathbf{W}_{\mathsf{UE}}^{\mathsf{RF}}\right]_{mn}\right|^2 = \frac{1}{N_{\mathsf{UE}}} \\ &\forall\ 1 \leq m \leq N_{\mathsf{UE}},\ \forall\ 1 \leq n \leq N_{\mathsf{RF}}^{\mathsf{UE}} \end{aligned} \tag{3.2}$$

The normalized transmit power constraint in uplink and downlink are given by $\|\mathbf{F}_{\mathsf{UE}}^{\mathsf{RF}} \mathbf{F}_{\mathsf{UE}}^{\mathsf{BB}}\|_F^2 = N_{\mathsf{s}}$ and $\|\mathbf{F}_{\mathsf{BS}}^{\mathsf{RF}} \mathbf{F}_{\mathsf{BS}}^{\mathsf{BB}}\|_F^2 = N_{\mathsf{s}}$, respectively.

Since the BS transmits and receives simultaneously at the same resource block (time/frequency), a loopback SI signal gets leaked from the transmit to the receive arrays of the BS, leading to corrupt the uplink received signal at the BS. Equivalently,

the received uplink signal model $\left(\mathbf{y}_{\mathsf{u}} \in \mathbb{C}^{N_{\mathsf{s}} \times 1}\right)$ at the BS can be written as

$$\mathbf{y}_{\mathsf{u}} = \underbrace{\sqrt{\rho_{\mathsf{u}}}\mathbf{W}_{\mathsf{BS}}^{\mathsf{BB}*}\mathbf{W}_{\mathsf{BS}}^{\mathsf{RF}*}\mathbf{H}_{\mathsf{u}}\mathbf{F}_{\mathsf{UE}}^{\mathsf{RF}}\mathbf{F}_{\mathsf{UE}}^{\mathsf{BB}}\mathbf{s}_{\mathsf{u}}}_{\text{Desired Signal}} + \underbrace{\sqrt{\rho_{\mathsf{s}}}\mathbf{W}_{\mathsf{BS}}^{\mathsf{BB}*}\mathbf{W}_{\mathsf{BS}}^{\mathsf{RF}*}\mathbf{H}_{\mathsf{s}}\mathbf{F}_{\mathsf{BS}}^{\mathsf{RF}}\mathbf{F}_{\mathsf{BS}}^{\mathsf{BB}}\mathbf{s}_{\mathsf{d}}}_{\text{Self-Interference Signal}} + \underbrace{\mathbf{W}_{\mathsf{BS}}^{\mathsf{BB}*}\mathbf{W}_{\mathsf{BS}}^{\mathsf{RF}*}\mathbf{n}_{\mathsf{BS}}}_{\text{Filtered Noise}} \tag{3.3}$$

where ρ_{u} and ρ_{s} are the average receive uplink and SI powers, respectively. In addition, $\mathbf{H}_{\mathsf{u}}$ and $\mathbf{H}_{\mathsf{s}}$ are the narrowband uplink and SI channels, respectively, while $\mathbf{n}_{\mathsf{BS}}$ is the AWGN at the BS which is distributed as $\mathcal{CN}(\mathbf{0}, \sigma_{\mathsf{BS}}^2\mathbf{I}_{N_{\mathsf{BS}}})$, with σ_{BS}^2 being the noise variance at the BS.

Given that the BS operates in FD mode, the uplink and downlink users are transmitting and receiving, respectively, at the same. Consequently, the downlink user is vulnerable to the IUI incurred by the uplink user. Equivalently, the downlink received signal $\left(\mathbf{y}_{\mathsf{d}} \in \mathbb{C}^{N_{\mathsf{s}} \times 1}\right)$ at the UE is expressed by

$$\mathbf{y}_{\mathsf{d}} = \underbrace{\sqrt{\rho_{\mathsf{d}}}\mathbf{W}_{\mathsf{UE}}^{\mathsf{BB}*}\mathbf{W}_{\mathsf{UE}}^{\mathsf{RF}*}\mathbf{H}_{\mathsf{d}}\mathbf{F}_{\mathsf{BS}}^{\mathsf{RF}}\mathbf{F}_{\mathsf{BS}}^{\mathsf{BB}}\mathbf{s}_{\mathsf{d}}}_{\text{Desired Signal}} + \underbrace{\sqrt{\rho_{\mathsf{iui}}}\mathbf{W}_{\mathsf{UE}}^{\mathsf{BB}*}\mathbf{W}_{\mathsf{UE}}^{\mathsf{RF}*}\mathbf{H}_{\mathsf{iui}}\mathbf{F}_{\mathsf{UE}}^{\mathsf{RF}}\mathbf{F}_{\mathsf{UE}}^{\mathsf{BB}}\mathbf{s}_{\mathsf{u}}}_{\text{Inter-User Interference Signal}} + \underbrace{\mathbf{W}_{\mathsf{UE}}^{\mathsf{BB}*}\mathbf{W}_{\mathsf{UE}}^{\mathsf{RF}*}\mathbf{n}_{\mathsf{UE}}}_{\text{Filtered Noise}} \tag{3.4}$$

where ρ_{d} and ρ_{iui} are the average receive downlink and IUI powers, respectively. In addition, $\mathbf{H}_{\mathsf{d}}$ and $\mathbf{H}_{\mathsf{iui}}$ are the narrowband downlink and IUI channels, respectively, while $\mathbf{n}_{\mathsf{UE}}$ is the AWGN at the UE which is distributed as $\mathcal{CN}(\mathbf{0}, \sigma_{\mathsf{UE}}^2\mathbf{I}_{N_{\mathsf{UE}}})$, with σ_{UE}^2 being the noise variance at the UE.

The detailed architecture description of the proposed system is illustrated by Fig. 3.1.

3.2.1 Channel Model

In this work, we use the geometric channel model given by [22]

$$\mathbf{H} = \sqrt{\frac{N_{\mathsf{RX}}N_{\mathsf{TX}}}{CR_c}} \sum_{c=0}^{C-1} \sum_{r_c=0}^{R_c-1} \alpha_{r_c}\mathbf{a}_{\mathsf{RX}}(\theta_{r_c})\mathbf{a}_{\mathsf{TX}}^*(\phi_{r_c}) \tag{3.5}$$

where C is number of clusters, R_c is number of rays per cluster, and θ_{r_c} and ϕ_{r_c} are the AoA and AoD of the r_c-th ray, respectively. Each ray has a complex path gain

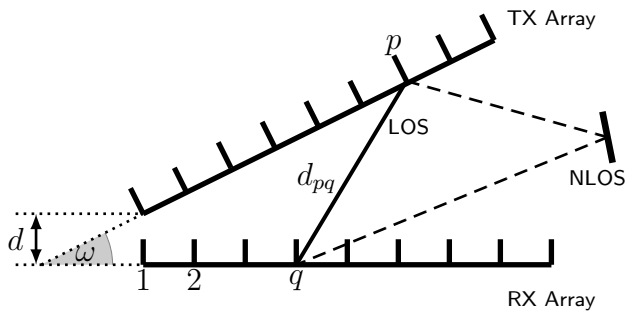

Figure 3.2: Relative position of TX and RX arrays at the FD BS. The BS consists of a two dedicated arrays for transmission and reception, respectively.

α_{r_c}. Also, $\mathbf{a}_{\mathsf{RX}}(\theta)$ and $\mathbf{a}_{\mathsf{TX}}(\phi)$ are the RX and TX antenna array response vectors, respectively. We adopt a uniform linear array wherein the generic expression of the array response vector (for TX or RX) is given by [22]

$$\mathbf{a}(\theta) = \frac{1}{\sqrt{N}}\left[1, \mathsf{e}^{i\frac{2\pi r}{\lambda}\sin(\theta)}, \ldots, \mathsf{e}^{i\frac{2\pi r}{\lambda}(N-1)\sin(\theta)}\right]^T. \tag{3.6}$$

where r and λ are the antenna spacing and the signal wavelength, respectively, while N is the number of antennas at TX or RX.

3.2.2 Self-Interference Channel Model

Per Fig. 3.2, the SI leakage at the BS is modeled by the channel matrix $\mathbf{H}_{\mathsf{s}}$. The separation, or transceiver gap, between TX and RX arrays is defined by distance d while the transceiver incline is determined by ω. The SI channel is decomposed into a deterministic LOS channel modeled by $\mathbf{H}_{\mathsf{LOS}}$, which is derived from the geometry of the transceiver, and a NLOS channel described by $\mathbf{H}_{\mathsf{NLOS}}$ which follows the geometric channel model defined by (3.5) [22]. The (q,p)-th entry of the LOS SI leakage is expressed by [22]

$$[\mathbf{H}_{\mathsf{LOS}}]_{qp} = \frac{1}{d_{pq}}\mathsf{e}^{-i2\pi\frac{d_{pq}}{\lambda}} \tag{3.7}$$

where d_{pq} is the distance between the p-th antenna in the TX array and q-th antenna in the RX array at BS given by (1.6). The aggregate SI channel matrix is given by

[22]

$$\mathbf{H}_{\mathsf{s}} = \sqrt{\frac{\kappa}{\kappa+1}}\mathbf{H}_{\mathsf{LOS}} + \sqrt{\frac{1}{\kappa+1}}\mathbf{H}_{\mathsf{NLOS}} \tag{3.8}$$

where κ is the Rician factor.

$$d_{pq} = \sqrt{\left(\frac{d}{\tan(\omega)} + (q-1)\frac{\lambda}{2}\right)^2 + \left(\frac{d}{\sin(\omega)} + (p-1)\frac{\lambda}{2}\right)^2 - 2\left(\frac{d}{\tan(\omega)} + (q-1)\frac{\lambda}{2}\right)\left(\frac{d}{\sin(\omega)} + (p-1)\frac{\lambda}{2}\right)\cos(\omega)} \tag{3.9}$$

Assumption 3. Note that the uplink, downlink and IUI channels follow the geometric channel model given by (3.5) while the SI channel is modeled by (3.8).

Assumption 4. In this work, we assume perfect CSI known at both the transmitter and receiver while designing the beamformers. In practice, the CSI can be accurately and efficiently obtained by channel estimation [7] at the receiver and further shared with the transmitter with feedback techniques [14, 94]. Nevertheless, we introduce the imperfect CSI after once the beamformers are designed, i.e., once the convergence is attained, in the simulation of Fig. 3.11.

3.3 Problem Formulation and Beamforming Design

3.3.1 Problem Formulation

The main objective of this work is to design the optimal beamformers in order to substantially reduce the interference and maximize the sum spectral efficiency of uplink and downlink UEs. The optimization problem can be expressed as

$$\begin{aligned}
\mathscr{P}: & \max_{\mathbf{W}_{\mathsf{BS}},\mathbf{W}_{\mathsf{UE}},\mathbf{F}_{\mathsf{BS}},\mathbf{F}_{\mathsf{UE}}} \mathcal{I}_{\mathsf{u}} + \mathcal{I}_{\mathsf{d}} \\
\text{s.t. } & \mathbf{W}_{\mathsf{BS}}^{*}\mathbf{W}_{\mathsf{BS}} = \mathbf{I}_{N_{\mathsf{s}}}, \\
& \mathbf{F}_{\mathsf{BS}}^{*}\mathbf{F}_{\mathsf{BS}} = \mathbf{I}_{N_{\mathsf{s}}}, \\
& \mathbf{W}_{\mathsf{UE}}^{*}\mathbf{W}_{\mathsf{UE}} = \mathbf{I}_{N_{\mathsf{s}}}, \\
& \mathbf{F}_{\mathsf{UE}}^{*}\mathbf{F}_{\mathsf{UE}} = \mathbf{I}_{N_{\mathsf{s}}}, \\
& \mathbf{W}_{\mathsf{BS}}^{*}\mathbf{H}_{\mathsf{s}}\mathbf{F}_{\mathsf{BS}} = \mathbf{0}, \\
& \mathbf{W}_{\mathsf{UE}}^{*}\mathbf{H}_{\mathsf{iui}}\mathbf{F}_{\mathsf{UE}} = \mathbf{0}.
\end{aligned} \tag{3.10}$$

where $\mathcal{I}_{\mathsf{u}}$ and $\mathcal{I}_{\mathsf{d}}$ are the uplink and downlink spectral efficiency, respectively, given by

$$\mathcal{I}_{\mathsf{u}} = \log\det\left(\mathbf{I}_{N_{\mathsf{s}}} + \rho_{\mathsf{u}}\mathbf{W}_{\mathsf{BS}}^{*}\mathbf{H}_{\mathsf{u}}\mathbf{F}_{\mathsf{UE}}\mathbf{Q}_{\mathsf{u}}^{-1}\mathbf{F}_{\mathsf{UE}}^{*}\mathbf{H}_{\mathsf{u}}^{*}\mathbf{W}_{\mathsf{BS}}\right) \tag{3.11}$$

$$\mathcal{I}_{\mathsf{d}} = \log\det\left(\mathbf{I}_{N_{\mathsf{s}}} + \rho_{\mathsf{d}}\mathbf{W}_{\mathsf{UE}}^{*}\mathbf{H}_{\mathsf{d}}\mathbf{F}_{\mathsf{BS}}\mathbf{Q}_{\mathsf{d}}^{-1}\mathbf{F}_{\mathsf{BS}}^{*}\mathbf{H}_{\mathsf{d}}^{*}\mathbf{W}_{\mathsf{UE}}\right) \tag{3.12}$$

where $\mathbf{Q}_{\mathsf{u}}$ and $\mathbf{Q}_{\mathsf{d}}$ are the covariance matrices of the interference-plus-noise power in uplink and downlink, respectively, given by

$$\mathbf{Q}_{\mathsf{u}} = \rho_{\mathsf{s}}\mathbf{W}_{\mathsf{BS}}^{*}\mathbf{H}_{\mathsf{s}}\mathbf{F}_{\mathsf{BS}}\mathbf{F}_{\mathsf{BS}}^{*}\mathbf{H}_{\mathsf{s}}^{*}\mathbf{W}_{\mathsf{BS}} + \sigma^{2}\mathbf{W}_{\mathsf{BS}}^{*}\mathbf{W}_{\mathsf{BS}} \tag{3.13}$$

$$\mathbf{Q}_{\mathsf{d}} = \rho_{\mathsf{iui}}\mathbf{W}_{\mathsf{UE}}^{*}\mathbf{H}_{\mathsf{iui}}\mathbf{F}_{\mathsf{UE}}\mathbf{F}_{\mathsf{UE}}^{*}\mathbf{H}_{\mathsf{iui}}^{*}\mathbf{W}_{\mathsf{UE}} + \sigma^{2}\mathbf{W}_{\mathsf{UE}}^{*}\mathbf{W}_{\mathsf{UE}} \tag{3.14}$$

Note that (3.10) maximizing the sum spectral efficiency ($\mathcal{I}_{\mathsf{u}} + \mathcal{I}_{\mathsf{d}}$) is a non-convex problem with unknown closed-form solution. Following similar approach as [137], we transform the problem (3.10, from maximizing the sum spectral efficiency) into convex sub-problems (minimizing the effective interference and preserving the signal dimension) yielding closed-form solutions of the beamformers.

While maximizing spectral efficiency involves many factors such as efficient use of bandwidth, optimizing power allocation, improving coding and modulation schemes, and strategically managing the resources in a network environment, other crucial factors include suppressing interference and preserving the signal dimension (the focus of our work). It is noteworthy that preserving the signal dimension is equivalent to preserving the rank of the effective channel [137], which is the beamformed channel given by ($\mathbf{H}_{\mathsf{effective}} = \mathbf{W}^{*}\mathbf{H}\mathbf{F}$). The logical progression from (3.10) to the convex sub-problems is justified as

- **From spectral efficiency/SINR Maximization to Interference Minimization**: Directly maximizing the spectral efficiency or its SINR approximation involves addressing both the signal power and interference components of the SINR equation. In FD systems, SI at the BS is a major deterrent to achieving high SINR for uplink/downlink transmissions. Therefore, we pivot

our strategy towards minimizing the SI/IUI as a critical step in enhancing sum uplink/downlink spectral efficiency.

- **Formulation of Subproblem**: specifically targets the minimization of SI/IUI power subject to beamforming constraints at the BS and UEs. This focused approach indirectly serves the goal of maximizing the sum spectral efficiency by improving the SINR condition. The constraints within subproblems, as will be defined later in subsection 3.3.2, ensure the preservation of signal dimensionality, which is crucial for maintaining the integrity of transmitted signals and the overall capacity of the system.

- **Motivation for Decomposition**: The decomposition into subproblem emerges logically from the necessity to manage the inherent challenges of FD communications, where simultaneous transmission and reception at the BS incurs SI. By addressing this interference through a dedicated subproblem, we lay a foundational groundwork for achieving our broader spectral efficiency maximization goal.

The optimization problem will be solved in the following steps:

1. Decompose the problem (3.10) into four subproblems to solve for each all-digital beamformer.

2. Once the all-digital beamformers are obtained, we decompose them into the equivalent analog and digital solutions.

3.3.2 All-Digital Beamforming

In this stage, we proceed to design the all-digital combiner $\mathbf{W}_{\mathsf{BS}} \in \mathbb{C}^{N_{\mathsf{BS}} \times N_{\mathsf{s}}}$ and precoder $\mathbf{F}_{\mathsf{BS}} \in \mathbb{C}^{N_{\mathsf{BS}} \times N_{\mathsf{s}}}$ at the BS node as well as the all-digital combiner $\mathbf{W}_{\mathsf{UE}} \in \mathbb{C}^{N_{\mathsf{UE}} \times N_{\mathsf{s}}}$ and precoder at the UE $\mathbf{F}_{\mathsf{UE}} \in \mathbb{C}^{N_{\mathsf{UE}} \times N_{\mathsf{s}}}$.

- **Optimization of BS Combiner:** We start by defining the first subproblem by defining the covariance matrix of the precoded SI and noise at the BS as

$$\mathbf{R}_1 = \rho_{\mathsf{s}} \mathbf{H}_{\mathsf{s}} \mathbf{F}_{\mathsf{BS}} \mathbf{F}_{\mathsf{BS}}^{*} \mathbf{H}_{\mathsf{s}}^{*} + \sigma_{\mathsf{BS}}^{2} \mathbf{I}_{N_{\mathsf{BS}}} \tag{3.15}$$

The first subproblem intends to design the all-digital combiner at the BS in such a way to minimize the SI power and preserve the rank of the effective channel as $\mathsf{rank}\left(\mathbf{W}_{\mathsf{BS}}^{*} \mathbf{H}_{\mathsf{u}} \mathbf{F}_{\mathsf{UE}}\right) = N_{\mathsf{s}}$. Thereby, the first subproblem can be expressed

$$\begin{aligned} \mathscr{P}_1 : & \min_{\mathbf{W}_{\mathsf{BS}}} \mathrm{Tr}\left(\mathbf{W}_{\mathsf{BS}}^{*} \mathbf{R}_1 \mathbf{W}_{\mathsf{BS}}\right) \\ & \mathsf{s.t.}\ \mathbf{W}_{\mathsf{BS}}^{*} \mathbf{H}_{\mathsf{u}} \mathbf{F}_{\mathsf{UE}} = \alpha \mathbf{I}_{N_{\mathsf{s}}} \end{aligned} \tag{3.16}$$

Note that $\mathbf{R}_1$ is a positive definite matrix ($\mathbf{R}_1 > 0$) and $\alpha = 1/\sqrt{\mathrm{Tr}\left(\mathbf{W}_{\mathsf{BS}}^{*} \mathbf{W}_{\mathsf{BS}}\right)}$ is a power normalization coefficient.

- **Optimization of BS Precoder:** Similarly, we define the second subproblem as to design the all-digital precoder at the BS in order to minimize the SI power and preserve the rank of the effective channel ($\mathsf{rank}\left(\mathbf{W}_{\mathsf{UE}}^{*} \mathbf{H}_{\mathsf{d}} \mathbf{F}_{\mathsf{BS}}\right) = N_{\mathsf{s}}$). We introduce the covariance matrix of the combined SI and noise as [2]

$$\mathbf{R}_2 = \rho_{\mathsf{s}} \mathbf{H}_{\mathsf{s}}^{*} \mathbf{W}_{\mathsf{BS}} \mathbf{W}_{\mathsf{BS}}^{*} \mathbf{H}_{\mathsf{s}} + \sigma_{\mathsf{BS}}^{2} \mathbf{I}_{N_{\mathsf{BS}}} \tag{3.17}$$

where ($\mathbf{R}_2 > 0$) is a positive definite matrix. Equivalently, the second subproblem exhibits the following generic form as

$$\begin{aligned} \mathscr{P}_2 : & \min_{\mathbf{F}_{\mathsf{BS}}} \mathrm{Tr}\left(\mathbf{F}_{\mathsf{BS}}^{*} \mathbf{R}_2 \mathbf{F}_{\mathsf{BS}}\right) \\ & \mathsf{s.t.}\ \mathbf{W}_{\mathsf{UE}}^{*} \mathbf{H}_{\mathsf{d}} \mathbf{F}_{\mathsf{BS}} = \beta \mathbf{I}_{N_{\mathsf{s}}} \end{aligned} \tag{3.18}$$

where $\beta = 1/\sqrt{\mathrm{Tr}\left(\mathbf{F}_{\mathsf{BS}}^{*} \mathbf{F}_{\mathsf{BS}}\right)}$ is a power normalization coefficient.

[2] The term related to the Identity matrix ($\sigma_{\mathsf{BS}}^{2} \mathbf{I}_{N_{\mathsf{BS}}}$) is added to (3.17) to ensure that the matrix $\mathbf{R}_2$ is invertible. The physical meaning of this is that it minimizes the norm of the precoder matrix. However, its effect is counteracted by β, which ensures that the transmit power is constant, i.e., $\|\mathbf{F}_{\mathsf{BS}} \mathbf{s}\|_F^2 = N_{\mathsf{s}}$. Therefore, the identity matrix role in (3.17) is to ensure that $\mathbf{R}_2$ is invertible, but it has no influence on the design regardless of the SNR/INR. It can be removed if $\mathbf{R}_2$ is invertible in practice. The same reasoning applies on the matrix $\mathbf{R}_4$.

- **Optimization of UE Combiner:** Regarding the third subproblem, we defined the covariance matrix of the precoded IUI and noise as

$$\mathbf{R}_3 = \rho_{\mathsf{iui}}\mathbf{H}_{\mathsf{iui}}\mathbf{F}_{\mathsf{UE}}\mathbf{F}_{\mathsf{UE}}^{*}\mathbf{H}_{\mathsf{iui}}^{*} + \sigma_{\mathsf{UE}}^{2}\mathbf{I}_{N_{\mathsf{UE}}} \tag{3.19}$$

where ($\mathbf{R}_3 > 0$) is a positive definite matrix. Similar to the previous subproblems, this subproblem aims to design the all-digital combiner at the UE in order to minimize the IUI and preserve the rank of the effective channel ($\mathsf{rank}\left(\mathbf{W}_{\mathsf{UE}}^{*}\mathbf{H}_{\mathsf{d}}\mathbf{F}_{\mathsf{BS}}\right) = N_{\mathsf{s}}$). The relative generic form is given by

$$\begin{aligned} \mathscr{P}_3 : & \min_{\mathbf{W}_{\mathsf{UE}}} \mathrm{Tr}\left(\mathbf{W}_{\mathsf{UE}}^{*}\mathbf{R}_3\mathbf{W}_{\mathsf{UE}}\right) \\ & \mathsf{s.t.}\ \mathbf{W}_{\mathsf{UE}}^{*}\mathbf{H}_{\mathsf{d}}\mathbf{F}_{\mathsf{BS}} = \gamma\mathbf{I}_{N_{\mathsf{s}}} \end{aligned} \tag{3.20}$$

where $\gamma = 1/\sqrt{\mathrm{Tr}\left(\mathbf{W}_{\mathsf{UE}}^{*}\mathbf{W}_{\mathsf{UE}}\right)}$ is a power normalization coefficient.

- **Optimization of UE Precoder:** The fourth problem aims to design the all-digital precoder at the UE in order to minimize the IUI while preserving the rank of effective uplink channel ($\mathsf{rank}\left(\mathbf{W}_{\mathsf{BS}}^{*}\mathbf{H}_{\mathsf{u}}\mathbf{F}_{\mathsf{UE}}\right) = N_{\mathsf{s}}$). We define the covariance matrix of the combined IUI and power as

$$\mathbf{R}_4 = \rho_{\mathsf{iui}}\mathbf{H}_{\mathsf{iui}}^{*}\mathbf{W}_{\mathsf{UE}}\mathbf{W}_{\mathsf{UE}}^{*}\mathbf{H}_{\mathsf{iui}} + \sigma_{\mathsf{UE}}^{2}\mathbf{I}_{N_{\mathsf{UE}}} \tag{3.21}$$

where ($\mathbf{R}_4 > 0$) is a positive definite matrix. The generic form the fourth subproblem is given by

$$\begin{aligned} \mathscr{P}_4 : & \min_{\mathbf{F}_{\mathsf{UE}}} \mathrm{Tr}\left(\mathbf{F}_{\mathsf{UE}}^{*}\mathbf{R}_4\mathbf{F}_{\mathsf{UE}}\right) \\ & \mathsf{s.t.}\ \mathbf{W}_{\mathsf{BS}}^{*}\mathbf{H}_{\mathsf{u}}\mathbf{F}_{\mathsf{UE}} = \zeta\mathbf{I}_{N_{\mathsf{s}}} \end{aligned} \tag{3.22}$$

where $\zeta = 1/\sqrt{\mathrm{Tr}\left(\mathbf{F}_{\mathsf{UE}}^{*}\mathbf{F}_{\mathsf{UE}}\right)}$ is a power normalization coefficient.

Remark 3. It is worth noticing from the subproblems (3.16), (3.18), (3.20) and (3.22) that the objective functions not only eliminate the interference (SI and IUI) but also preserve the DoF for the desired signals, which is formulated in the constraints. The engineering insight of the objective functions is to guarantee that the signal

Algorithm 2 All-Digital Beamforming Design

Input $\mathbf{H}_{\mathsf{u}}, \mathbf{H}_{\mathsf{d}}, \mathbf{H}_{\mathsf{s}}, \mathbf{H}_{\mathsf{iui}}$
Initialize $\mathbf{F}_{\mathsf{UE}}$, $\mathbf{F}_{\mathsf{BS}}$, $\mathbf{W}_{\mathsf{UE}}$
repeat
  Compute $\mathbf{R}_1$ (3.15)
  Obtain $\mathbf{W}_{\mathsf{BS}}$ (3.23) and normalize by α
  Compute $\mathbf{R}_2$ using updated $\mathbf{W}_{\mathsf{BS}}$ from step 5
  Obtain $\mathbf{F}_{\mathsf{BS}}$ (3.24) and normalize by β
  Compute $\mathbf{R}_3$ (3.19)
  Obtain $\mathbf{W}_{\mathsf{UE}}$ (3.25) using updated $\mathbf{F}_{\mathsf{BS}}$ from step 7 and normalize by γ
  Compute $\mathbf{R}_4$ (3.21) using updated $\mathbf{W}_{\mathsf{UE}}$ from step 9
  Obtain $\mathbf{F}_{\mathsf{UE}}$ (3.26) using updated $\mathbf{W}_{\mathsf{BS}}$ from step 5 and normalize by ζ
until Convergence

return $\mathbf{W}_{\mathsf{BS}}$, $\mathbf{W}_{\mathsf{UE}}$, $\mathbf{F}_{\mathsf{BS}}$ and $\mathbf{F}_{\mathsf{UE}}$

cannot suffer from distortions. The proposed objective functions can be interpreted as maximizing the SINR, where the numerator (signal space dimension) is kept unaltered while decreasing the denominator (interference). We also relaxed the semi-unitary constraints in (3.10) while solving (3.16), (3.18), (3.20) and (3.22), in order to preserve the convexity of these subproblems.

Theorem 3. The optimal all-digital combiners and precoders at the BS and UEs, solutions to the problems (3.16,3.18,3.20 and 3.22) are expressed by

$$\mathbf{W}_{\mathsf{BS}} = \mathbf{R}_1^{-1}\mathbf{H}_{\mathsf{u}}\mathbf{F}_{\mathsf{UE}}\left(\mathbf{F}_{\mathsf{UE}}^{*}\mathbf{H}_{\mathsf{u}}^{*}\mathbf{R}_1^{-1}\mathbf{H}_{\mathsf{u}}\mathbf{F}_{\mathsf{UE}}\right)^{-1} \tag{3.23}$$

$$\mathbf{F}_{\mathsf{BS}} = \mathbf{R}_2^{-1}\mathbf{H}_{\mathsf{d}}^{*}\mathbf{W}_{\mathsf{UE}}\left(\mathbf{W}_{\mathsf{UE}}^{*}\mathbf{H}_{\mathsf{d}}\mathbf{R}_2^{-1}\mathbf{H}_{\mathsf{d}}^{*}\mathbf{W}_{\mathsf{UE}}\right)^{-1} \tag{3.24}$$

$$\mathbf{W}_{\mathsf{UE}} = \mathbf{R}_3^{-1}\mathbf{H}_{\mathsf{d}}\mathbf{F}_{\mathsf{BS}}\left(\mathbf{F}_{\mathsf{BS}}^{*}\mathbf{H}_{\mathsf{d}}^{*}\mathbf{R}_3^{-1}\mathbf{H}_{\mathsf{d}}\mathbf{F}_{\mathsf{BS}}\right)^{-1} \tag{3.25}$$

$$\mathbf{F}_{\mathsf{UE}} = \mathbf{R}_4^{-1}\mathbf{H}_{\mathsf{u}}^{*}\mathbf{W}_{\mathsf{BS}}\left(\mathbf{W}_{\mathsf{BS}}^{*}\mathbf{H}_{\mathsf{u}}\mathbf{R}_4^{-1}\mathbf{H}_{\mathsf{u}}^{*}\mathbf{W}_{\mathsf{BS}}\right)^{-1} \tag{3.26}$$

Proof. The proof of Theorem 3 is provided in Appendix B.1. □

The proposed all-digital beamforming is summarized in Algorithm 2.

Remark 4. The beamforming solutions entailed by Theorem 3 are coupled. Hence, an iterative routine is carried out until the convergence. Note that the closed form-expressions in **Theorem** 3 will be normalized at every iteration in the routine, as detailed by Algorithm 2.

Remark 5. Given the all-digital beamformer solution $\mathbf{X} \in \mathbb{C}^{M \times N}$, M and N are the number of antennas and spatial streams, respectively. M should be large enough to sustain N spatial streams and the remaining $P = M - N$ DoF should be dedicated to suppress the interference.

3.3.3 Convergence

In this subsection, we prove the convergence of the all-digital beamforming algorithm 2. We show that the objective functions (3.16), (3.18), (3.20), (3.22) decrease in each iteration and converge to the local optimum in a few iterations, which makes it computationally efficient. The SI plus noise power at the BS, i.e., the objective function of (3.16) is given by

$$\begin{aligned}\mathbf{T}_1 =& \mathrm{Tr}\left(\mathbf{W}_{\mathsf{BS}}^{*}\mathbf{R}_1\mathbf{W}_{\mathsf{BS}}\right)\\ =& \mathrm{Tr}\left(\mathbf{W}_{\mathsf{BS}}^{*}\left(\rho_{\mathsf{s}}\mathbf{H}_{\mathsf{s}}\mathbf{F}_{\mathsf{BS}}\mathbf{F}_{\mathsf{BS}}^{*}\mathbf{H}_{\mathsf{s}}^{*}+\sigma_{\mathsf{BS}}^{2}\mathbf{I}_{N_{\mathsf{BS}}}\right)\mathbf{W}_{\mathsf{BS}}\right)\\ =& \underbrace{\mathrm{Tr}\left(\rho_{\mathsf{s}}\mathbf{W}_{\mathsf{BS}}^{*}\mathbf{H}_{\mathsf{s}}\mathbf{F}_{\mathsf{BS}}\mathbf{F}_{\mathsf{BS}}^{*}\mathbf{H}_{\mathsf{s}}^{*}\mathbf{W}_{\mathsf{BS}}\right)}_{\text{Effective SI Power }(\mathcal{J}_1)}+\sigma_{\mathsf{BS}}^{2}N_{\mathsf{s}}.\end{aligned} \tag{3.27}$$

Similarly, the SI plus noise power defined in (3.18) is given by

$$\begin{aligned}\mathbf{T}_2 =& \mathrm{Tr}\left(\mathbf{F}_{\mathsf{BS}}^{*}\mathbf{R}_2\mathbf{F}_{\mathsf{BS}}\right)\\ =& \mathrm{Tr}\left(\mathbf{F}_{\mathsf{BS}}^{*}\left(\rho_{\mathsf{s}}\mathbf{H}_{\mathsf{s}}^{*}\mathbf{W}_{\mathsf{BS}}\mathbf{W}_{\mathsf{BS}}^{*}\mathbf{H}_{\mathsf{s}}+\sigma_{\mathsf{BS}}^{2}\mathbf{I}_{N_{\mathsf{BS}}}\right)\mathbf{F}_{\mathsf{BS}}\right)\\ =& \underbrace{\mathrm{Tr}\left(\rho_{\mathsf{s}}\mathbf{F}_{\mathsf{BS}}^{*}\mathbf{H}_{\mathsf{s}}^{*}\mathbf{W}_{\mathsf{BS}}\mathbf{W}_{\mathsf{BS}}^{*}\mathbf{H}_{\mathsf{s}}\mathbf{F}_{\mathsf{BS}}\right)}_{\text{Effective SI Power }(\mathcal{J}_2)}+\sigma_{\mathsf{BS}}^{2}N_{\mathsf{s}}.\end{aligned} \tag{3.28}$$

In a similar fashion, the IUI and noise power defined in (3.20) is given by

$$\begin{aligned}\mathbf{T}_3 =& \mathrm{Tr}\left(\mathbf{W}_{\mathsf{UE}}^{*}\mathbf{R}_3\mathbf{W}_{\mathsf{UE}}\right)\\ =& \mathrm{Tr}\left(\mathbf{W}_{\mathsf{UE}}^{*}\left(\rho_{\mathsf{iui}}\mathbf{H}_{\mathsf{iui}}\mathbf{F}_{\mathsf{UE}}\mathbf{F}_{\mathsf{UE}}^{*}\mathbf{H}_{\mathsf{iui}}^{*}+\sigma_{\mathsf{UE}}^{2}\mathbf{I}_{N_{\mathsf{UE}}}\right)\mathbf{W}_{\mathsf{UE}}\right)\\ =& \underbrace{\mathrm{Tr}\left(\rho_{\mathsf{iui}}\mathbf{W}_{\mathsf{UE}}^{*}\mathbf{H}_{\mathsf{iui}}\mathbf{F}_{\mathsf{UE}}\mathbf{F}_{\mathsf{UE}}^{*}\mathbf{H}_{\mathsf{iui}}^{*}\mathbf{W}_{\mathsf{UE}}\right)}_{\text{Effective IUI Power }(\mathcal{J}_3)}+\sigma_{\mathsf{UE}}^{2}N_{\mathsf{s}}.\end{aligned} \tag{3.29}$$

The IUI and noise power are defined in (3.22) is given by

$$\begin{aligned}\mathbf{T}_4 =& \mathrm{Tr}\left(\mathbf{F}_{\mathsf{UE}}^{*}\mathbf{R}_4\mathbf{F}_{\mathsf{UE}}\right)\\ =& \mathrm{Tr}\left(\mathbf{F}_{\mathsf{UE}}^{*}\left(\rho_{\mathsf{iui}}\mathbf{H}_{\mathsf{iui}}^{*}\mathbf{W}_{\mathsf{UE}}\mathbf{W}_{\mathsf{UE}}^{*}\mathbf{H}_{\mathsf{iui}}+\sigma_{\mathsf{UE}}^{2}\mathbf{I}_{N_{\mathsf{UE}}}\right)\mathbf{F}_{\mathsf{UE}}\right)\\ =& \underbrace{\mathrm{Tr}\left(\rho_{\mathsf{iui}}\mathbf{F}_{\mathsf{UE}}^{*}\mathbf{H}_{\mathsf{iui}}^{*}\mathbf{W}_{\mathsf{UE}}\mathbf{W}_{\mathsf{UE}}^{*}\mathbf{H}_{\mathsf{iui}}\mathbf{F}_{\mathsf{UE}}\right)}_{\text{Effective IUI Power }(\mathcal{J}_4)}+\sigma_{\mathsf{UE}}^{2}N_{\mathsf{s}}.\end{aligned} \tag{3.30}$$

The local optimal solutions of the objective functions (3.27), (3.28), (3.29) and (3.30) are given by Theorem 3 and they are sure to converge to the locally optimal solution as it is guaranteed by Algorithm 2.

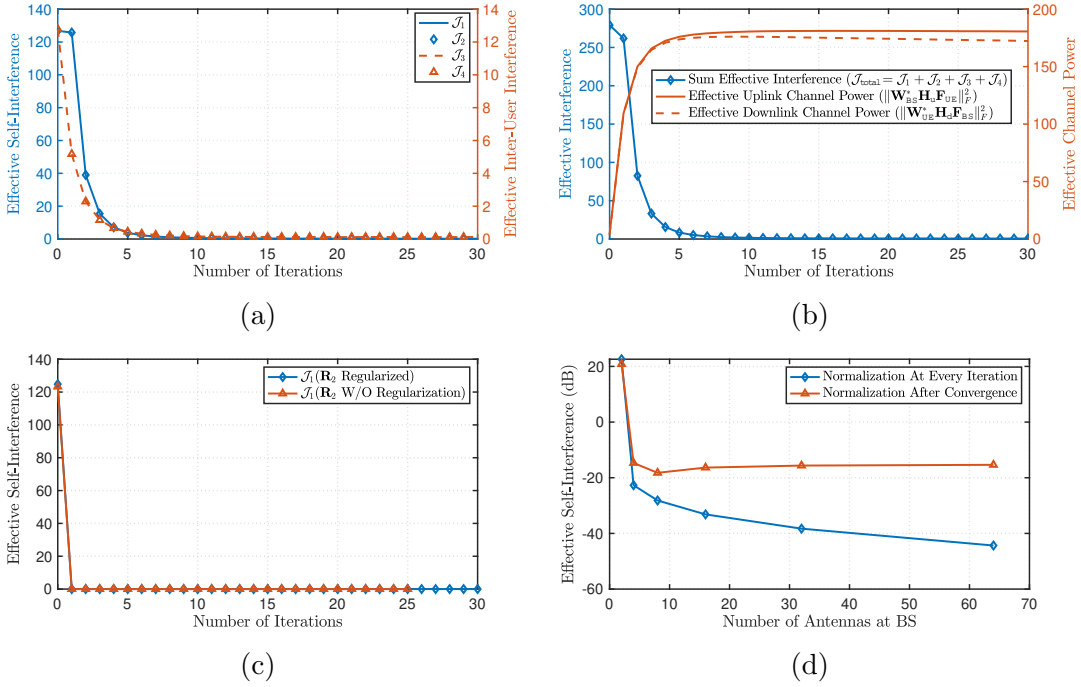

Figure 3.3: (a) Convergence of the objective functions (3.27), (3.28), (3.29) and (3.30) defining the effective interference in linear scale with respect to the number of iterations in Algorithm 2. (b) Illustration of the convergence of the sum objective function $\mathcal{J}_{\mathsf{total}} = \mathcal{J}_1 + \mathcal{J}_2 + \mathcal{J}_3 + \mathcal{J}_4$, as well as, the uplink/downlink beamformed/effective channel power. (c) Illustration of the monotonic decreasing of the SI power for $\mathbf{R}_2$ being with/without regularization. (d) Illustration of the effect of beamforming normalization; at every iteration and after the convergence. The plot is produced with $N_{\mathsf{BS}} = 64$, $N_{\mathsf{UE}} = 8$, $\mathsf{SNR} = 0$ dB, SI power $\rho_{\mathsf{s}} = 15$ dB and IUI power $\rho_{\mathsf{iui}} = 5$ dB.

Fig. 3.3a presents a compelling visualization of the monotonic decrease in individual costs over the course of 5-6 iterations, indicative of the algorithm's efficiency and targeted approach towards minimizing interference. Each subproblem, by design, aims to reduce interference while preserving the rank of the effective channel, a critical factor for maintaining or enhancing the system's capacity. The methodical decrease in these sub-objectives underscores the algorithm's capability to iteratively refine each aspect of the system's performance through precise adjustments. This disciplined optimization of individual costs not only contributes to the reduction of total interference but also aligns with the overarching goal of spectral efficiency en-

hancement.

Fig. 3.3b, the analysis reveals a simultaneous decrease in the total cost of interference ($\mathcal{J}_{\mathsf{total}} = \mathcal{J}_1 + \mathcal{J}_2 + \mathcal{J}_3 + \mathcal{J}_4$) alongside an increase in the effective channel power for both uplink and downlink communications. This phenomenon is emblematic of the algorithm's holistic impact, where the cumulative effect of minimizing individual interference translates into a substantial reduction in total system interference. The concurrent augmentation of effective channel power is a direct consequence of the algorithm's dual focus on interference mitigation and channel rank preservation. By ensuring that each iteration moves towards reducing $\mathcal{J}_1, \mathcal{J}_2, \mathcal{J}_3$, and $\mathcal{J}_4$, the algorithm inherently boosts the signal's strength relative to noise and interference, thereby maximizing spectral efficiency. Note that the rapid convergence of the algorithm, typically within 5-6 iterations as observed, signifies not only its computational efficiency but also its practical applicability in dynamic communication environments.

Fig. 3.3c investigates the effect of regularization of $\mathbf{R}_2$ on the effective SI. This regularization affects the design of the BS precoder at (3.24) which in turn affects the SI minimization in (3.23). The regularization term is introduced, as explained in footnote 2, to ensure that $\mathbf{R}_2$ is invertible in case it is singular. In Fig. 3.3c, we observe that the effect of the regularization term is negligible, since the power normalization coefficient β will compensate this effect and ensures that the transmit power ($\|\mathbf{F}_{\mathsf{BS}}\mathbf{s}\|_F^2 = N_{\mathsf{s}}$) constraint is maintained.

Fig. 3.3d evaluates the two beamforming optimization strategies—normalizing at every iteration versus normalizing after convergence—our empirical findings advocate for the former approach due to its pronounced benefits in achieving effective SI reduction and ensuring convergence stability. Although this method incurs a slower convergence rate and higher computational overhead $\mathcal{O}(KN_{\mathsf{BS}}N_{\mathsf{s}}^2)$ for normalizing $\mathbf{W}_{\mathsf{BS}}$, K is the number of iterations required for convergence and $\mathcal{O}(N_{\mathsf{BS}}N_{\mathsf{s}}^2)$ cost for the second approach, the consistent improvement in performance and the reliability of the optimization process across various scenarios firmly justify its adoption. The

Table 3.1: Comparative Analysis of Beamforming Normalization Techniques.

Metrics	Every Iteration	After Convergence
Performance (Effective SI)	✓	✗
Computational Cost	✗	✓
Rate of Convergence	✗	✓
Convergence Stability	✓	✗

strategy of normalizing at every iteration meticulously maintains the alignment with the optimization's constraints and goals, thereby facilitating a more controlled and predictable optimization trajectory. This is particularly vital in complex beamforming environments where the precision and dependability of the solution critically impact system performance. The choice to prioritize these aspects underscores our commitment to delivering robust and high-quality beamforming solutions, acknowledging that the increased computational cost is a worthwhile investment for the enhanced performance and stability it brings to the optimization process. Table 3.1 offers a comparative overview of the two beamforming normalization strategies.

3.3.4 Hybrid Analog/Baseband Beamforming

In mmWave communications, employing an all-digital beamforming approach that utilizes one RF chain per antenna alongside full precision data converters has prohibitively high power consumption for a large number of antennas. Despite its capability to achieve high SE, this method falls short in terms of energy efficiency. Nonetheless, this all-digital beamforming configuration can be utilized as a benchmark to evaluate the effectiveness of the proposed hybrid beamforming design, implemented with reduced number of RF chains, which is characterized by its lower power consumption.

In this work, we decompose the precoding and combining matrices into analog and baseband components, with the analog components being subject to constant amplitude constraints (unit modulus). Moreover, to prevent ADC saturation at the

receiver side, it's essential that interference—including SI and IUI is effectively mitigated at the analog combiners outputs. Following this, our methodology involves designing the precoders and combiners based on specific criteria. Initially, the analog precoders and combiners are designed to concurrently minimize interference in the analog domain and optimize the power of the beamformed signal. Subsequently, with the all-digital and analog beamformers established, the baseband precoders and combiners are derived using the LS method. This leads to the formulation of the optimization problem that guides our design process.

$$
\begin{aligned}
\mathscr{P}_5 : \max_{\substack{\mathbf{W}_{\mathsf{BS}}^{\mathsf{RF}}, \mathbf{F}_{\mathsf{BS}}^{\mathsf{RF}}, \mathbf{W}_{\mathsf{UE}}^{\mathsf{RF}}, \mathbf{F}_{\mathsf{UE}}^{\mathsf{RF}} \\ \mathbf{W}_{\mathsf{BS}}^{\mathsf{BB}}, \mathbf{F}_{\mathsf{BS}}^{\mathsf{BB}}, \mathbf{W}_{\mathsf{UE}}^{\mathsf{BB}}, \mathbf{F}_{\mathsf{UE}}^{\mathsf{BB}}}} & \mathcal{I}_{\mathsf{u}} + \mathcal{I}_{\mathsf{d}} \\
\text{s.t. } & \|\mathbf{F}_{\mathsf{BS}}^{\mathsf{RF}} \mathbf{F}_{\mathsf{BS}}^{\mathsf{BB}}\|_F^2 = N_{\mathsf{s}} \\
& \|\mathbf{F}_{\mathsf{UE}}^{\mathsf{RF}} \mathbf{F}_{\mathsf{UE}}^{\mathsf{BB}}\|_F^2 = N_{\mathsf{s}} \\
& \mathbf{F}_{\mathsf{BS}}^{\mathsf{RF}}, \mathbf{F}_{\mathsf{UE}}^{\mathsf{RF}} \in \mathcal{F}_{\mathsf{RF}} \\
& \mathbf{W}_{\mathsf{BS}}^{\mathsf{RF}}, \mathbf{W}_{\mathsf{UE}}^{\mathsf{RF}} \in \mathcal{W}_{\mathsf{RF}} \\
& \mathbf{W}_{\mathsf{BS}}^{\mathsf{RF}*} \mathbf{H}_{\mathsf{s}} \mathbf{F}_{\mathsf{BS}}^{\mathsf{RF}} = \mathbf{0} \\
& \mathbf{W}_{\mathsf{UE}}^{\mathsf{RF}*} \mathbf{H}_{\mathsf{iui}} \mathbf{F}_{\mathsf{UE}}^{\mathsf{RF}} = \mathbf{0}
\end{aligned}
\tag{3.31}
$$

where $\mathcal{F}_{\mathsf{RF}}$ and $\mathcal{W}_{\mathsf{RF}}$ are the sets of feasible analog precoders and combiners, respectively, wherein the beamformers are implemented using phased array with unit modulus entries.

3.3.4.1 Analog Beamforming

We adopt an approach in which maximizing the beamformed power and minimizing the interference constitutes the analog beamformers' main roles, as it is important to mitigate the interference power before the ADC stages to avoid dynamic range issues. With a fixed baseband beamformers ($\mathbf{W}_{\mathsf{BS}}^{\mathsf{BB}}, \mathbf{F}_{\mathsf{BS}}^{\mathsf{BB}}, \mathbf{W}_{\mathsf{UE}}^{\mathsf{BB}}, \mathbf{F}_{\mathsf{UE}}^{\mathsf{BB}}$), Problem

(3.31) becomes

$$\begin{aligned}
\mathscr{P}_6 : & \max_{\mathbf{W}_{\mathsf{BS}}^{\mathsf{RF}}, \mathbf{F}_{\mathsf{BS}}^{\mathsf{RF}}, \mathbf{W}_{\mathsf{UE}}^{\mathsf{RF}}, \mathbf{F}_{\mathsf{UE}}^{\mathsf{RF}}} \mathcal{I}_{\mathsf{u}} + \mathcal{I}_{\mathsf{d}} \\
\text{s.t. } & \mathbf{F}_{\mathsf{BS}}^{\mathsf{RF}}, \mathbf{F}_{\mathsf{UE}}^{\mathsf{RF}} \in \mathcal{F}_{\mathsf{RF}} \\
& \mathbf{W}_{\mathsf{BS}}^{\mathsf{RF}}, \mathbf{W}_{\mathsf{UE}}^{\mathsf{RF}} \in \mathcal{W}_{\mathsf{RF}} \\
& \mathbf{W}_{\mathsf{BS}}^{\mathsf{RF}*} \underbrace{\mathbf{H}_{\mathsf{s}} \mathbf{F}_{\mathsf{BS}}^{\mathsf{RF}}}_{=\mathbf{C}} = \mathbf{0} \\
& \mathbf{W}_{\mathsf{UE}}^{\mathsf{RF}*} \underbrace{\mathbf{H}_{\mathsf{iui}} \mathbf{F}_{\mathsf{UE}}^{\mathsf{RF}}}_{=\mathbf{C}} = \mathbf{0}
\end{aligned} \tag{3.32}$$

To minimize the interference (last two constraints in (3.32)), we adopt the the Moore-Penrose pseudoinverse approach ($\mathbf{C}\mathbf{C}^{\dagger}\mathbf{C}$) to construct the interference null space projection matrix as

$$\mathbf{P}_{\perp} = \mathbf{I} - \mathbf{C}\mathbf{C}^{\dagger} \tag{3.33}$$

$\mathbf{C}$ is defined in 3.31 as the beamformed interference channel.

Without loss of generality, we proceed the analysis to solve for the analog beamformers at the BS and in a similar way, we derive the analog beamformers at the users.

For a fixed $\mathbf{F}_{\mathsf{BS}}^{\mathsf{RF}}, \mathbf{F}_{\mathsf{UE}}^{\mathsf{RF}}$ and $\mathbf{F}_{\mathsf{UE}}^{\mathsf{BB}}$, in a trivial sense, the design of the analog combiner at the BS should follow these steps

1. Maximize the received power by taking the $N_{\mathsf{RF}}^{\mathsf{BS}}$ dominant left singular vectors of the uplink beamformed channel $\mathbf{H}_{\mathsf{u}} \mathbf{F}_{\mathsf{UE}}^{\mathsf{RF}} \mathbf{F}_{\mathsf{UE}}^{\mathsf{BB}}$.

2. Suppress the effective SI by projecting the BS analog combiner on the SI null-space ($\mathbf{P}_{\perp}$).

3. Project the BS analog combiner onto the unit modulus space ($\mathcal{W}_{\mathsf{RF}}$).

Unfortunately, the unit modulus constraint not only removes the convexity of the problem (3.32) but also violates the interference suppression constraint. As argued

in [156], if the unit modulus constraint is handled separately from the interference suppression constraint, large losses are incurred into the system performance. To solve this shortcoming, we refer to the *"Alternating Projection Method"* to properly handle the two constraints. To seek for the optimal space wherein the best analog combiner lies, we introduce an iterative routine to alternate the projections between the unit modulus space and the interference null space.

Now, we fix $\mathbf{W}_{\mathsf{BS}}^{\mathsf{RF}}$ (solved from the previous routine) as well as $\mathbf{W}_{\mathsf{UE}}^{\mathsf{RF}}$ and $\mathbf{W}_{\mathsf{UE}}^{\mathsf{BB}}$, and we proceed to solve for the analog precoder $\mathbf{F}_{\mathsf{BS}}^{\mathsf{RF}}$ as detailed in the following steps as

1. Maximize the received power by taking the $N_{\mathsf{RF}}^{\mathsf{BS}}$ dominant left singular vectors of the uplink beamformed channel $\mathbf{H}_{\mathsf{u}}^{*}\mathbf{W}_{\mathsf{UE}}^{\mathsf{RF}}\mathbf{W}_{\mathsf{UE}}^{\mathsf{BB}}$.
2. Given we re-write the interference suppression constraint to be $\mathbf{F}_{\mathsf{BS}}^{\mathsf{RF}*}\mathbf{H}_{\mathsf{s}}^{*}\mathbf{W}_{\mathsf{BS}}^{\mathsf{RF}} = \mathbf{0}$, mitigate the effective SI by projecting the BS analog precoder on the SI null-space ($\mathbf{P}_{\perp}$), with $\mathbf{C} = \mathbf{H}_{\mathsf{s}}^{*}\mathbf{W}_{\mathsf{RF}}$.
3. Project the BS analog precoder on the unit modulus space ($\mathcal{F}_{\mathsf{RF}}$).
4. Apply the alternating projection method to seek for the optimal subspace of the BS analog precoder.

In a similar reasoning, as detailed for the derivation of the analog beamformers at the BS, we design the analog beamformers at the users. Detailed derivation is illustrated in Algorithm 3.

3.3.4.2 Baseband Beamforming

Now we derive the baseband beamformers using the LS method. Given that the analog as well as the all-digital beamformers are obtained, the baseband beamformers at the BS and users are, respectively, given by

$$\mathbf{W}_{\mathsf{BS}}^{\mathsf{BB}} = \mathbf{W}_{\mathsf{BS}}^{\mathsf{RF}\dagger}\mathbf{W}_{\mathsf{BS}} \tag{3.34}$$

$$\mathbf{F}_{\mathsf{BS}}^{\mathsf{BB}} = \mathbf{F}_{\mathsf{BS}}^{\mathsf{RF}\dagger}\mathbf{F}_{\mathsf{BS}} \tag{3.35}$$

$$\mathbf{W}_{\mathsf{UE}}^{\mathsf{BB}} = \mathbf{W}_{\mathsf{UE}}^{\mathsf{RF}\dagger}\mathbf{W}_{\mathsf{UE}} \tag{3.36}$$

$$\mathbf{F}_{\mathsf{UE}}^{\mathsf{BB}} = \mathbf{F}_{\mathsf{UE}}^{\mathsf{RF}\dagger}\mathbf{F}_{\mathsf{UE}} \tag{3.37}$$

To satisfy the transmit power constraint in (3.31), we normalize the digital precoders at BS and uplink UE, respectively, by a factor of $\frac{\sqrt{N_s}}{\|\mathbf{F}_{\mathsf{BS}}^{\mathsf{RF}}\mathbf{F}_{\mathsf{BS}}^{\mathsf{BB}}\|_F}$ and $\frac{\sqrt{N_s}}{\|\mathbf{F}_{\mathsf{UE}}^{\mathsf{RF}}\mathbf{F}_{\mathsf{UE}}^{\mathsf{BB}}\|_F}$.

Remark 6. Since the hybrid analog/baseband beamformers at the BS and the users are coupled, we proceed with an iterative routine up until the convergence. Detailed steps of the hybrid design are summarized in Algorithm 3.

Algorithm 3 Hybrid Beamforming Design

function ANALOG($\mathbf{A}, \mathbf{C}, L$)
$\mathbf{X}_{\mathsf{RF}} \leftarrow L$ Dominant left singular vectors of $\mathbf{A}$
$\mathbf{P}_{\perp} \leftarrow \mathbf{I} - \mathbf{C}\mathbf{C}^{*}$ (Interference null-space matrix)
Set $n = 0$
repeat
  $\mathbf{X}_{\mathsf{RF}}^{(n+1)} \leftarrow \mathbf{P}_{\perp}\mathbf{X}_{\mathsf{RF}}^{(n)}$
  for $i \leftarrow 1 : M$ and $j \leftarrow 1 : L$ **do**
    $\left(\mathbf{X}_{\mathsf{RF}}^{(n)}\right)_{ij} \leftarrow \left(\mathbf{X}_{\mathsf{RF}}^{(n+1)}\right)_{ij} / |\left(\mathbf{X}_{\mathsf{RF}}^{(n+1)}\right)_{ij}|$
  end for
  $n \leftarrow n + 1$
until Convergence
return $\mathbf{X}_{\mathsf{RF}} \in \mathbb{C}^{M \times L}$
end function

Input $\mathbf{H}_{\mathsf{u}}$, $\mathbf{H}_{\mathsf{d}}$, $\mathbf{H}_{\mathsf{s}}$ and $\mathbf{H}_{\mathsf{iui}}$
Initialize $\mathbf{F}_{\mathsf{UE}}^{\mathsf{RF}}$, $\mathbf{F}_{\mathsf{UE}}^{\mathsf{BB}}$, $\mathbf{W}_{\mathsf{UE}}^{\mathsf{RF}}$, $\mathbf{W}_{\mathsf{UE}}^{\mathsf{BB}}$ and $\mathbf{F}_{\mathsf{BS}}^{\mathsf{RF}}$
Obtain $\mathbf{W}_{\mathsf{BS}}, \mathbf{F}_{\mathsf{BS}}, \mathbf{W}_{\mathsf{UE}}$ and $\mathbf{F}_{\mathsf{UE}}$ from Algorithm 2
Set $k = 0$
repeat
  $\mathbf{W}_{\mathsf{BS}}^{\mathsf{RF}(k+1)} \leftarrow \text{ANALOG}(\mathbf{H}_{\mathsf{u}}\mathbf{F}_{\mathsf{UE}}^{\mathsf{RF}(k)}\mathbf{F}_{\mathsf{UE}}^{\mathsf{BB}(k)}, \mathbf{H}_{\mathsf{s}}\mathbf{F}_{\mathsf{BS}}^{\mathsf{RF}(k)}, N_{\mathsf{RF}}^{\mathsf{BS}})$
  $\mathbf{W}_{\mathsf{BS}}^{\mathsf{BB}(k+1)} \leftarrow \mathbf{W}_{\mathsf{BS}}^{\mathsf{RF}(k+1)\dagger}\mathbf{W}_{\mathsf{BS}}$ (LS Solution)
  $\mathbf{F}_{\mathsf{BS}}^{\mathsf{RF}(k+1)} \leftarrow \text{ANALOG}(\mathbf{H}_{\mathsf{d}}^{*}\mathbf{W}_{\mathsf{UE}}^{\mathsf{RF}(k)}\mathbf{W}_{\mathsf{UE}}^{\mathsf{BB}(k)}, \mathbf{H}_{\mathsf{s}}^{*}\mathbf{W}_{\mathsf{BS}}^{\mathsf{RF}(k+1)}, N_{\mathsf{RF}}^{\mathsf{BS}})$
  $\mathbf{F}_{\mathsf{BS}}^{\mathsf{BB}(k+1)} \leftarrow \mathbf{F}_{\mathsf{BS}}^{\mathsf{RF}(k+1)\dagger}\mathbf{F}_{\mathsf{BS}}$
  $\mathbf{W}_{\mathsf{UE}}^{\mathsf{RF}(k+1)} \leftarrow \text{ANALOG}(\mathbf{H}_{\mathsf{d}}\mathbf{F}_{\mathsf{BS}}^{\mathsf{RF}(k+1)}\mathbf{F}_{\mathsf{BS}}^{\mathsf{BB}(k+1)}, \mathbf{H}_{\mathsf{iui}}\mathbf{F}_{\mathsf{UE}}^{\mathsf{RF}(k)}, N_{\mathsf{RF}}^{\mathsf{UE}})$
  $\mathbf{W}_{\mathsf{UE}}^{\mathsf{BB}(k+1)} \leftarrow \mathbf{W}_{\mathsf{UE}}^{\mathsf{RF}(k+1)\dagger}\mathbf{W}_{\mathsf{UE}}$
  $\mathbf{F}_{\mathsf{UE}}^{\mathsf{RF}(k+1)} \leftarrow \text{ANALOG}(\mathbf{H}_{\mathsf{u}}^{*}\mathbf{W}_{\mathsf{BS}}^{\mathsf{RF}(k+1)}\mathbf{W}_{\mathsf{BS}}^{\mathsf{BB}(k+1)}, \mathbf{H}_{\mathsf{iui}}^{*}\mathbf{W}_{\mathsf{UE}}^{\mathsf{RF}(k+1)}, N_{\mathsf{RF}}^{\mathsf{UE}})$
  $\mathbf{F}_{\mathsf{UE}}^{\mathsf{BB}(k+1)} \leftarrow \mathbf{F}_{\mathsf{UE}}^{\mathsf{RF}(k+1)\dagger}\mathbf{F}_{\mathsf{UE}}$
  $k \leftarrow k + 1$
until Convergence
Normalize the digital precoders at BS and UE as $\mathbf{F}_{\mathsf{BS}}^{\mathsf{BB}} \leftarrow \frac{\sqrt{N_{\mathsf{s}}}}{\|\mathbf{F}_{\mathsf{BS}}^{\mathsf{RF}}\mathbf{F}_{\mathsf{BS}}^{\mathsf{BB}}\|_F}\mathbf{F}_{\mathsf{BS}}^{\mathsf{BB}}$, $\mathbf{F}_{\mathsf{UE}}^{\mathsf{BB}} \leftarrow \frac{\sqrt{N_{\mathsf{s}}}}{\|\mathbf{F}_{\mathsf{UE}}^{\mathsf{RF}}\mathbf{F}_{\mathsf{UE}}^{\mathsf{BB}}\|_F}\mathbf{F}_{\mathsf{UE}}^{\mathsf{BB}}$

return $\mathbf{W}_{\mathsf{BS}}^{\mathsf{RF}}, \mathbf{W}_{\mathsf{BS}}^{\mathsf{BB}}, \mathbf{F}_{\mathsf{BS}}^{\mathsf{RF}}, \mathbf{F}_{\mathsf{BS}}^{\mathsf{BB}}, \mathbf{W}_{\mathsf{UE}}^{\mathsf{RF}}, \mathbf{W}_{\mathsf{UE}}^{\mathsf{BB}}, \mathbf{F}_{\mathsf{UE}}^{\mathsf{RF}}, \mathbf{F}_{\mathsf{UE}}^{\mathsf{BB}}$

Table 3.2: Complexity Analysis

Beamformer	**Cost**
$\mathbf{W}_{\mathsf{BS}}, \mathbf{F}_{\mathsf{BS}}$	$\mathcal{O}(N_{\mathsf{BS}}^3)$
$\mathbf{W}_{\mathsf{UE}}, \mathbf{F}_{\mathsf{UE}}$	$\mathcal{O}(N_{\mathsf{UE}}^3)$
$\mathbf{W}_{\mathsf{BS}}^{\mathsf{RF}}, \mathbf{F}_{\mathsf{BS}}^{\mathsf{RF}}$	$\mathcal{O}\left(N_{\mathsf{inner}}(N_{\mathsf{UE}}N_{\mathsf{s}}^2 + 2N_{\mathsf{BS}}^2 N_{\mathsf{RF}}^{\mathsf{BS}})\right)$
$\mathbf{W}_{\mathsf{UE}}^{\mathsf{RF}}, \mathbf{F}_{\mathsf{UE}}^{\mathsf{RF}}$	$\mathcal{O}\left(N_{\mathsf{inner}}(N_{\mathsf{BS}}N_{\mathsf{s}}^2 + 2N_{\mathsf{UE}}^2 N_{\mathsf{RF}}^{\mathsf{UE}})\right)$
$\mathbf{W}_{\mathsf{BS}}^{\mathsf{BB}}, \mathbf{F}_{\mathsf{BS}}^{\mathsf{BB}}$	$\mathcal{O}(N_{\mathsf{BS}}(N_{\mathsf{BS}}^{\mathsf{RF}})^2 + N_{\mathsf{BS}}^{\mathsf{RF}} N_{\mathsf{BS}} N_{\mathsf{s}})$
$\mathbf{W}_{\mathsf{UE}}^{\mathsf{BB}}, \mathbf{F}_{\mathsf{UE}}^{\mathsf{BB}}$	$\mathcal{O}(N_{\mathsf{UE}}(N_{\mathsf{UE}}^{\mathsf{RF}})^2 + N_{\mathsf{UE}}^{\mathsf{RF}} N_{\mathsf{UE}} N_{\mathsf{s}})$

3.3.5 Complexity Analysis

The overall computational complexity of evaluating $\mathbf{W}_{\mathsf{BS}}$ is dominated by the matrix inversion and multiplication steps involving $N_{\mathsf{BS}} \times N_{\mathsf{BS}}$ matrices, leading to a complexity of $\mathcal{O}(N_{\mathsf{BS}}^3)$ due to the inverse $\mathbf{R}_1$ and $\mathbf{H}_{\mathsf{u}}^* \mathbf{R}_1^{-1} \mathbf{H}_{\mathsf{u}}$ operations. The computational cost of designing the analog beamformer $\mathbf{W}_{\mathsf{BS}}^{\mathsf{RF}}$ is primarily driven by the SVD of $(\mathbf{H}_{\mathsf{u}} \mathbf{F}_{\mathsf{UE}}^{\mathsf{RF}} \mathbf{F}_{\mathsf{UE}}^{\mathsf{BB}})$ and the construction of the SI null-space, with complexities of $\mathcal{O}(N_{\mathsf{UE}} N_{\mathsf{s}})$ and $\mathcal{O}(N_{\mathsf{BS}}^2 N_{\mathsf{RF}}^{\mathsf{BS}})$, respectively. Iterating these operations N_{inner} times results in an overall complexity of $\mathcal{O}\left(N_{\mathsf{inner}}(N_{\mathsf{UE}}N_{\mathsf{s}}^2 + 2N_{\mathsf{BS}}^2 N_{\mathsf{RF}}^{\mathsf{BS}})\right)$, underscoring the significant computational effort required. The complexity of designing $\mathbf{W}_{\mathsf{BS}}^{\mathsf{BB}}$ requires the computation of the pseudo-inverse $\mathcal{O}(N_{\mathsf{BS}}(N_{\mathsf{BS}}^{\mathsf{RF}})^2)$ and matrix multiplication $\mathcal{O}(N_{\mathsf{BS}}^{\mathsf{RF}} N_{\mathsf{BS}} N_{\mathsf{s}})$ resulting in a total computational cost $\mathcal{O}(N_{\mathsf{BS}}(N_{\mathsf{BS}}^{\mathsf{RF}})^2 + N_{\mathsf{BS}}^{\mathsf{RF}} N_{\mathsf{BS}} N_{\mathsf{s}})$. Table 3.2 provides a summary of the computational complexity involved in the design of all beamformers.

3.4 Target Metrics Analysis

As we mention throughout the chapter, the main objective of designing the hybrid beamformers is to maximize the sum spectral efficiency. Nevertheless, exploring other target metrics such as outage probability, SINR and energy efficiency is beneficial to obtain more engineering insights into the proposed algorithm. In addition, the

upper bound as well as the all-digital beamforming design, which is impractical as it would consume a prohibitively large amount of power, may serve as benchmarking tools for the proposed technique.

3.4.1 Outage Probability

Given a transmission strategy, the CDF or in other terms the outage probability for rate R (bits/s/Hz) is defined by [95]

$$P_{\mathsf{out}}(\mathsf{snr}, R) = \mathbb{P}[\mathcal{I}(\mathsf{snr}) < R]. \tag{3.38}$$

In the presence of robust channel codes and under the condition of no outage, the probability of error is minimal; thus, the probability of outage offers an effective approximation of the actual block error probability. Contemporary radio systems, including the UMTS and LTE, operate based on a designated target error probability. The foremost performance metric is the maximum data rate[3] corresponding to each snr, such that the outage probability remains below ϵ [95]

$$R_{\epsilon}(\mathsf{snr}) = \max_{\zeta} \{\zeta : P_{\mathsf{out}}(\mathsf{snr}, \zeta) \leq \epsilon\} \tag{3.39}$$

3.4.2 Signal-to-Interference-plus-Noise Ratio

We define uplink SINR at the ℓ-th RF chain at the BS as

$$\begin{aligned} \mathsf{sinr}_{\ell} =& \frac{\rho_{\mathsf{u}} \mathbf{w}_{\mathsf{BS},\ell}^{\mathsf{RF}*} \mathbf{H}_{\mathsf{u}} \mathbf{F}_{\mathsf{UE}}^{\mathsf{RF}} \mathbf{F}_{\mathsf{UE}}^{\mathsf{BB}} \mathbf{F}_{\mathsf{UE}}^{\mathsf{BB}*} \mathbf{F}_{\mathsf{UE}}^{\mathsf{RF}*} \mathbf{H}_{\mathsf{u}}^{*} \mathbf{w}_{\mathsf{BS},\ell}^{\mathsf{RF}}}{\rho_{\mathsf{s}} \mathbf{w}_{\mathsf{BS},\ell}^{\mathsf{RF}*} \mathbf{H}_{\mathsf{s}} \mathbf{F}_{\mathsf{BS}}^{\mathsf{RF}} \mathbf{F}_{\mathsf{BS}}^{\mathsf{BB}} \mathbf{F}_{\mathsf{BS}}^{\mathsf{BB}*} \mathbf{F}_{\mathsf{BS}}^{\mathsf{RF}*} \mathbf{H}_{\mathsf{s}}^{*} \mathbf{w}_{\mathsf{BS},\ell}^{\mathsf{RF}} + \sigma_{\mathsf{BS}}^2} \\ =& \frac{\mathsf{snr}_{\mathsf{u}} \mathbf{w}_{\mathsf{BS},\ell}^{\mathsf{RF}*} \mathbf{H}_{\mathsf{u}} \mathbf{F}_{\mathsf{UE}}^{\mathsf{RF}} \mathbf{F}_{\mathsf{UE}}^{\mathsf{BB}} \mathbf{F}_{\mathsf{UE}}^{\mathsf{BB}*} \mathbf{F}_{\mathsf{UE}}^{\mathsf{RF}*} \mathbf{H}_{\mathsf{u}}^{*} \mathbf{w}_{\mathsf{BS},\ell}^{\mathsf{RF}}}{\rho_{\mathsf{s}}/\sigma_{\mathsf{BS}}^2 \mathbf{w}_{\mathsf{BS},\ell}^{\mathsf{RF}*} \mathbf{H}_{\mathsf{s}} \mathbf{F}_{\mathsf{BS}}^{\mathsf{RF}} \mathbf{F}_{\mathsf{BS}}^{\mathsf{BB}} \mathbf{F}_{\mathsf{BS}}^{\mathsf{BB}*} \mathbf{F}_{\mathsf{BS}}^{\mathsf{RF}*} \mathbf{H}_{\mathsf{s}}^{*} \mathbf{w}_{\mathsf{BS},\ell}^{\mathsf{RF}} + 1} \end{aligned} \tag{3.40}$$

[3]In this study, we conceptualize 'rate with outage' as the average data rate accurately decoded at the receiver end, which aligns with the definition of throughput. In alternate methodologies, the 'rate with outage' is integrated into the transmit data rate. For the purpose of our method, we consider the probability of burst occurrences (outage) and multiply by $(1 - \epsilon)$; in the case of the transmit data rate methodology, the term $(1 - \epsilon)$ is excluded.

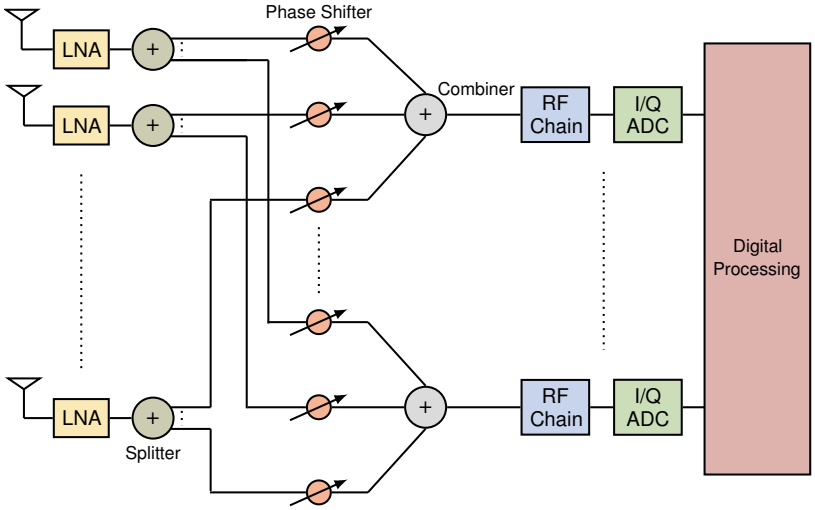

Figure 3.4: Illustration of a hybrid A/D combiner at the BS. The combiner consists of multiple components such as LNAs, phase shifters, RF chains, mixers, splitters, oscillators, filters and ADCs, etc. The power consumption of each component is shown in Table 3.3.

while the downlink SINR at the u-th RF chain at the user is expressed by

$$\begin{aligned}\mathsf{sinr}_u =& \frac{\rho_{\mathsf{d}}\mathbf{w}_{\mathsf{UE},u}^{\mathsf{RF}*}\mathbf{H}_{\mathsf{d}}\mathbf{F}_{\mathsf{BS}}^{\mathsf{RF}}\mathbf{F}_{\mathsf{BS}}^{\mathsf{BB}}\mathbf{F}_{\mathsf{BS}}^{\mathsf{BB}*}\mathbf{F}_{\mathsf{BS}}^{\mathsf{RF}*}\mathbf{H}_{\mathsf{d}}^{*}\mathbf{w}_{\mathsf{BS},u}^{\mathsf{RF}}}{\rho_{\mathsf{iui}}\mathbf{w}_{\mathsf{UE},u}^{\mathsf{RF}*}\mathbf{H}_{\mathsf{iui}}\mathbf{F}_{\mathsf{UE}}^{\mathsf{RF}}\mathbf{F}_{\mathsf{UE}}^{\mathsf{BB}}\mathbf{F}_{\mathsf{UE}}^{\mathsf{BB}*}\mathbf{F}_{\mathsf{UE}}^{\mathsf{RF}*}\mathbf{H}_{\mathsf{iui}}^{*}\mathbf{w}_{\mathsf{UE},u}^{\mathsf{RF}}+\sigma_{\mathsf{UE}}^{2}} \\ =& \frac{\mathsf{snr}_{\mathsf{d}}\mathbf{w}_{\mathsf{UE},u}^{\mathsf{RF}*}\mathbf{H}_{\mathsf{d}}\mathbf{F}_{\mathsf{BS}}^{\mathsf{RF}}\mathbf{F}_{\mathsf{BS}}^{\mathsf{BB}}\mathbf{F}_{\mathsf{BS}}^{\mathsf{BB}*}\mathbf{F}_{\mathsf{BS}}^{\mathsf{RF}*}\mathbf{H}_{\mathsf{d}}^{*}\mathbf{w}_{\mathsf{BS},u}^{\mathsf{RF}}}{\rho_{\mathsf{iui}}/\sigma_{\mathsf{UE}}^{2}\mathbf{w}_{\mathsf{UE},u}^{\mathsf{RF}*}\mathbf{H}_{\mathsf{iui}}\mathbf{F}_{\mathsf{UE}}^{\mathsf{RF}}\mathbf{F}_{\mathsf{UE}}^{\mathsf{BB}}\mathbf{F}_{\mathsf{UE}}^{\mathsf{BB}*}\mathbf{F}_{\mathsf{UE}}^{\mathsf{RF}*}\mathbf{H}_{\mathsf{iui}}^{*}\mathbf{w}_{\mathsf{UE},u}^{\mathsf{RF}}+1}\end{aligned} \tag{3.41}$$

where $\rho_{\mathsf{s}}/\sigma_{\mathsf{BS}}^2$ is the SI-to-noise ratio while $\rho_{\mathsf{iui}}/\sigma_{\mathsf{BS}}^2$ is the IUI-to-noise ratio.

3.4.3 Energy Efficiency

The energy efficiency, expressed in bits/s/Watt or bits/Joule, is defined as the ratio between the spectral efficiency $\mathcal{I}(\mathsf{sinr})$ and the total power consumption ρ_{Total}. It is given by

$$\mathcal{E}(\mathsf{snr}) = \frac{\mathcal{I}(\mathsf{snr})}{\rho_{\mathsf{Total}}} \tag{3.42}$$

For hybrid A/D architecture as illustrated by Fig. 3.1, the total power consumption by the mmWave hybrid receiver is expressed by

$$\rho_{\mathsf{Total}}^{\mathsf{HC}} = N_{\mathsf{RX}} \left(\rho_{\mathsf{LNA}} + \rho_{\mathsf{SP}} + N_{\mathsf{RF}} \rho_{\mathsf{PS}} \right) + N_{\mathsf{RF}} \left(\rho_{\mathsf{RF}} + \rho_{\mathsf{C}} + 2\rho_{\mathsf{ADC}} \right) \tag{3.43}$$

where N_{RX} is the number of receive antennas and ρ_{RF} is the power consumption per RF chain which is defined by

$$\rho_{\mathsf{RF}} = \rho_{\mathsf{M}} + \rho_{\mathsf{LO}} + \rho_{\mathsf{LPF}} + \rho_{\mathsf{BB}_{\mathsf{amp}}} \tag{3.44}$$

Examples of the power consumption of each device is presented in Table 3.3. The power consumption of all components except the ADC is independent of the bandwidth B and number of bits b. For the ADC, ρ_{ADC} grows exponentially with b and linearly with B and with Walden's figure of merit for ADCs c, which is the energy consumption per conversion step per Hz. Common values of c are given in Table 3.4.

Table 3.3: Power Consumption of Each Device [3].

Device	**Notation**	**Value**
Low Noise Amplifier [162]	ρ_{LNA}	39 mW
Splitter	ρ_{SP}	19.5 mW
Combiner [162]	ρ_{C}	19.5 mW
Phase Shifter [77, 163]	ρ_{PS}	2 mW
Mixer [80]	ρ_{M}	16.8 mW
Local Oscillator [106]	ρ_{LO}	5 mW
Low Pass Filter [106]	ρ_{LPF}	14 mW
Baseband Amplifier [106]	$\rho_{\mathsf{BB}_{\mathsf{amp}}}$	5 mW
ADC	ρ_{ADC}	$cB2^b$

Table 3.4: ADC Power Consumption Per Sample Per Level, c [3].

Scenario	**Value**	**Generation**
LPADC	5 fJ/step/Hz	Low Power (ideal future value)
IPADC	65 fJ/step/Hz	Intermediate Power
HPADC	494 fJ/step/Hz	High Power (state of the art)

In this manuscript, we carefully chose three plausible models representing the power consumption of individual components, which are approximately identifiable with both present and prospective generations of technology. These ADCs possess specific figures of merit denoted as c, which are delineated in Table 3.4.

3.4.4 Upper Bound on Spectral Efficiency

A performance upper bound, not achievable in general but useful for benchmarking purposes, can be obtained by assuming no SI and IUI ($\rho_{\mathsf{s}} = \rho_{\mathsf{iui}} = 0$) and neglecting hardware constraints, so that $\mathbf{W}_{\mathsf{BS}},\ \mathbf{F}_{\mathsf{BS}},\ \mathbf{W}_{\mathsf{UE}},\ \mathbf{F}_{\mathsf{UE}}$ are only constrained to be semi-unitary matrices. Then the optimal combiners and precoders are respectively given by the dominant left and right singular vectors of the uplink/downlink channels matrices, yielding $\mathcal{I}_{\mathsf{u}} + \mathcal{I}_{\mathsf{d}} \leq \mathcal{I}_{\mathsf{Bound}}$ where

$$\mathcal{I}_{\mathsf{Bound}} = \sum_{\ell=0}^{N_{\mathsf{s}}-1} \log\left(1 + \sigma_\ell\left(\mathbf{H}_{\mathsf{u}}\right)^2 \mathsf{SNR}\right) + \sum_{\ell=0}^{N_{\mathsf{s}}-1} \log\left(1 + \sigma_\ell\left(\mathbf{H}_{\mathsf{d}}\right)^2 \mathsf{SNR}\right) \tag{3.45}$$

With the optimum beamformers diagonalizing the channel $\mathbf{H} \in \mathbb{C}^{N_{\mathsf{r}} \times N_{\mathsf{t}}}$ and allocating power via waterfilling, the capacity bound equals

$$\mathcal{I}_{\mathsf{WF}} = \sum_{\ell=0}^{N_{\mathsf{min}}-1} \left[\log\left(\frac{\mathsf{SNR}}{N_{\mathsf{t}}} \frac{\lambda_\ell\left(\mathbf{H}^*\mathbf{H}\right)}{\eta}\right)\right]^+ \tag{3.46}$$

where $N_{\mathsf{min}} = \min(N_{\mathsf{t}}, N_{\mathsf{r}}) \geq N_{\mathsf{s}}$, and the optimized power per ℓ-th stream is given by

$$P_\ell^\star = \left[\frac{1}{\eta} - \frac{N_{\mathsf{t}}}{\mathsf{SNR}\lambda_\ell\left(\mathbf{H}^*\mathbf{H}\right)}\right]^+, \quad \ell = 0, \ldots, N_{\mathsf{min}-1}, \tag{3.47}$$

where η must satisfy that $\sum_\ell P_\ell^\star = N_{\mathsf{t}}$. Note $\lambda_\ell(\mathbf{X})$ is the ℓ-th eigen value of $\mathbf{X}$ in descending order and $[x]^+ = \max(0, x)$.

3.5 Numerical Analysis

In this section, we provide numerical results of the system performance along with the discussion. Unless otherwise stated, Table 3.5 gives the parameter values used in the simulations. For each case, 1000 channels realizations were generated to perform the Monte Carlo simulation in MATLAB.

3.5.1 Beamforming Schemes: A Comparison

Fig. 3.5 depicts the sum spectral efficiency versus average SNR across different beamforming strategies, highlighting that the proposed FD hybrid BF distinctly

Table 3.5: System Parameters.

Parameter	**Value**
Carrier Frequency	28 GHz
Bandwidth (B)	1 GHz
Number of BS Antennas (N_{BS})	16, 32, 64, 128, 256, 512
Number of UE Antennas (N_{UE})	4, 8
Number of Spatial Streams (N_{s})	1, 2
Number of RF Chains at BS ($N_{\mathsf{RF}}^{\mathsf{BS}}$)	1, 2, 4, 8, 16, 32, 64, 128
Number of RF Chains at UE ($N_{\mathsf{RF}}^{\mathsf{UE}}$)	1, 2, 4
Number of Clusters (C)	6
Number of Rays per Cluster (R_c)	8
AoA/AoD Angular Spread	20°
Transceivers Gap (d)	2λ
Transceivers Incline (ω)	$\frac{\pi}{6}$
Rician Factor (κ)	5 dB
Average Receive SI Power (ρ_{s})	15, 30 dB
Average Receive IUI Power (ρ_{iui})	5 dB

outperforms both the all-digital BF and HD hybrid BF modes, with a rate gain that expands as the average SNR increases. This performance indicates the practical applicability of our FD approach in cellular networks, where BSs typically operate in HD mode. Furthermore, our FD hybrid BF design yields superior outcomes compared to the SVD method, even within an all-digital context. As average SNR rises, the advantage of our approach becomes more pronounced, with the SVD method reaching a saturation point due to its failure to suppress interference, thereby overloading the ADCs. Nonetheless, there are observed rate losses in our FD hybrid BF relative to all-digital designs and the theoretical upper bound, attributed to the unit modulus constraint and reduced DoF due to fewer RF chains in the hybrid setup compared to all-digital configurations.

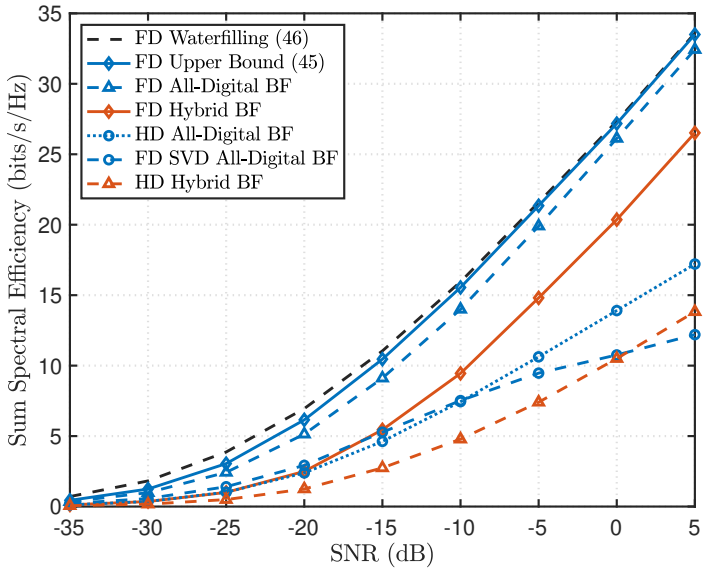

Figure 3.5: Sum spectral efficiency vs. SNR for different beamforming (BF) schemes. The plot is produced with average receive SI power $\rho_{\mathsf{s}} = 30$ dB, IUI power $\rho_{\mathsf{iui}} = 5$ dB, $N_{\mathsf{BS}} = 64, N_{\mathsf{RF}}^{\mathsf{BS}} = 4, N_{\mathsf{UE}} = 8, N_{\mathsf{RF}}^{\mathsf{UE}} = 4$. The all-digital design uses one RF chain per antenna element, which will use a prohibitively large amount of power, and is included here as a benchmark.

3.5.2 Effect of The Average Inter-User Interference

Fig. 3.6 displays the relationship between downlink spectral efficiency and average IUI power across various beamforming architectures. Notably, a reduction in IUI power correlates with an enhancement in downlink spectral efficiency for most schemes, with the exception of HD and theoretical upper bound scenarios, which are inherently immune to interference effects. In the realm of all-digital beamforming, performance is slightly influenced by IUI power, yet the associated rate losses remain minimal. Remarkably, our FD hybrid BF demonstrates resilience to escalating IUI power, significantly surpassing the performance of HD mode implemented in all-digital beamforming. A persistent performance discrepancy between our hybrid approach and all-digital BF can be attributed to the unit modulus constraint alongside a decrease in DoF due to a limited number of RF chains. Furthermore, our FD

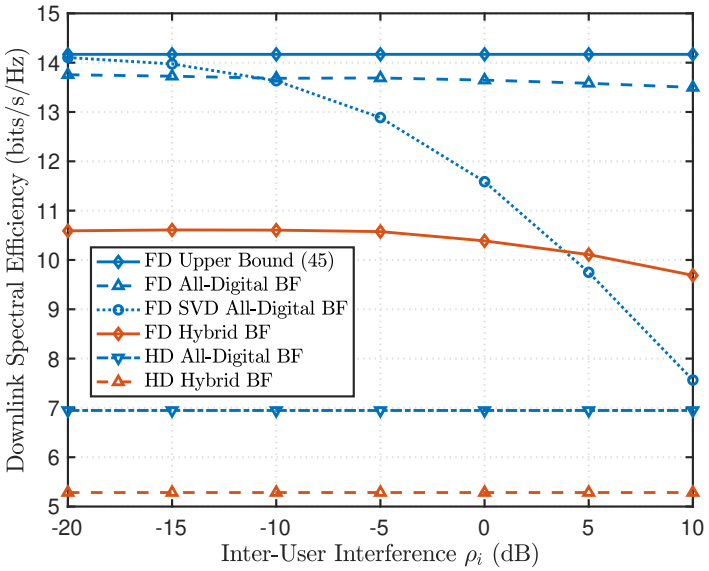

Figure 3.6: Downlink spectral efficiency vs. the average receive IUI power for different BF schemes. The plot is simulated with $\mathsf{SNR} = 0$ dB, $N_{\mathsf{BS}} = 64, N_{\mathsf{RF}}^{\mathsf{BS}} = 4, N_{\mathsf{UE}} = 8, N_{\mathsf{RF}}^{\mathsf{UE}} = 4$. The all-digital design uses one RF chain per antenna element, which will use a prohibitively large amount of power, and is included here as a benchmark.

design consistently exceeds the performance of the FD all-digital SVD method across the spectrum of IUI power levels, with a notable exception in the lower IUI power range (-20 to -10 dB), where the SVD method momentarily surpasses our proposed design. This exception occurs as IUI power diminishes to around -20 dB, at which point interference impact becomes minimal, allowing the SVD to align closely with the defined theoretical upper bound.

3.5.3 Effect of The Number of Antennas at The Base Station

Fig. 3.7 demonstrates the CDF of uplink spectral efficiency across varying N_{BS} at the BS. An increase in N_{BS} correspondingly enhances the CDF, while a reduction in antennas leads to a decrease. With a larger N_{BS}, the system gains ample DoF, which is crucial for balancing spatial multiplexing gains and interference suppression. However, when N_{BS} is limited, there's insufficient DoF to meet both objectives, ad-

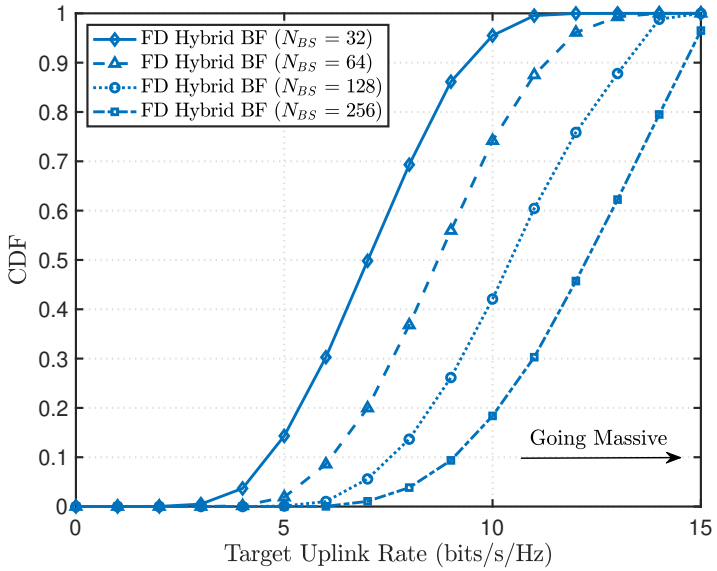

Figure 3.7: CDF of the uplink spectral efficiency for different number of BS antennas. The plot is produced with $N_{\mathsf{RF}}^{\mathsf{UE}} = 2, N_{\mathsf{RF}}^{\mathsf{BS}} = 4, N_{\mathsf{UE}} = 8$ while the average receive SI power is $\rho_{\mathsf{s}} = 30$ dB.

versely affecting performance. For instance, at $N_{\mathsf{BS}} = 32$, the system faces a 98.8% probability of outage when attempting to deliver a service at 10 bits/s/Hz. Conversely, increasing N_{BS} to 256 enhances DoF, significantly improves system coverage, and reduces outage probability to around 18%.

3.5.4 Uplink Spectral Efficiency vs. Effective Self-Interference

Fig. 3.8 illustrates the effective SI and uplink spectral efficiency with respect to the number of antennas at the BS. The effective analog SI, plotted in Fig. 3.8, is defined as

$$\delta_{\infty} = \rho_{\mathsf{s}} \mathrm{Tr}\left(\mathbf{W}_{\mathsf{BS}}^{\mathsf{RF}*}\mathbf{H}_{\mathsf{s}}\mathbf{F}_{\mathsf{BS}}^{\mathsf{RF}}\mathbf{F}_{\mathsf{BS}}^{\mathsf{BB}}\mathbf{F}_{\mathsf{BS}}^{\mathsf{BB}*}\mathbf{F}_{\mathsf{BS}}^{\mathsf{RF}*}\mathbf{H}_{\mathsf{s}}^{*}\mathbf{W}_{\mathsf{BS}}^{\mathsf{RF}}\right) \tag{3.48}$$

The subscript "∞" indicates that Algorithm 3 reached convergence and the effective analog SI δ_{∞} is evaluated for this state (convergence). As N_{BS} increases, effective SI reduction enhances significantly, reaching up to -138 dB with 128 antennas. With 2 RF chains at the BS, employing 32 antennas reduces the effective SI power to -60 dB,

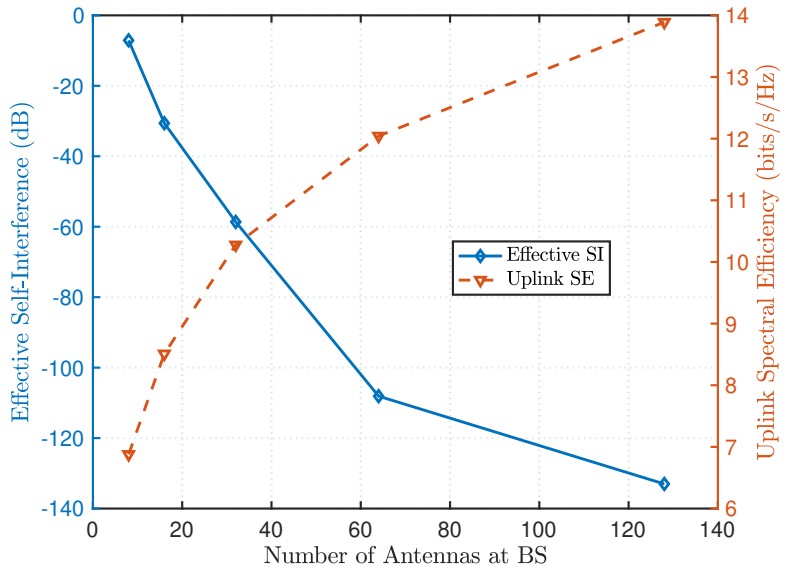

Figure 3.8: Effective SI and uplink spectral efficiency with respect to the number of antennas at BS. Results are simulated with $N_{\mathsf{RF}}^{\mathsf{BS}} = 2$, $N_{\mathsf{UE}} = 8$, $N_{\mathsf{RF}}^{\mathsf{UE}} = 2$, $\mathsf{SNR} = 0$ dB and average receive SI power $\rho_{\mathsf{s}} = 30$ dB. In our system model, the uplink spectral efficiency is not affected by inter-user interference.

a level adequate to prevent ADC saturation as shown in Fig. 2.2. Utilizing 64 antennas allows for further SI mitigation to about -110 dB; however, setups with 8 and 16 antennas achieve only -5 dB and -30 dB in effective SI reduction, respectively, which are insufficient for FD operations. The increase in DoF not only facilitates substantial SI reduction but also boosts the uplink spectral efficiency to 14 bits/s/Hz for configurations with 128 antennas. Thus, our joint beamforming design effectively harmonizes the allocation of DoF between enhancing uplink spectral efficiency and suppressing interference.

3.5.5 Uplink Energy Efficiency vs. Amount of Self-Interference Suppressed

Fig. 3.9 illustrates the amount of effective SI suppressed and uplink energy efficiency vs. number of BS antennas for different power modes. We define the

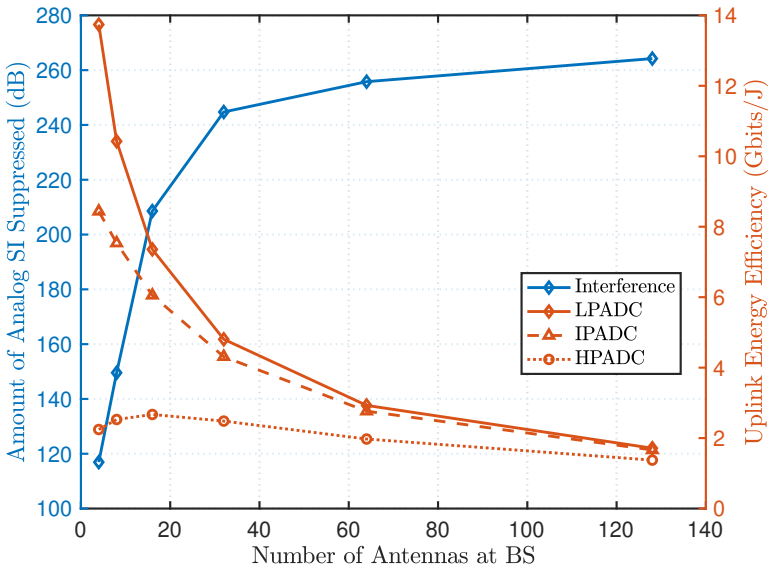

Figure 3.9: Amount of analog SI suppressed and uplink energy efficiency for the hybrid A/D beamformers, with respect to the number of RF chains at the BS. Results are simulated with $N_{\mathsf{BS}} = 512$, $N_{\mathsf{UE}} = 8$, $N_{\mathsf{RF}}^{\mathsf{UE}} = 2$, $\mathsf{SNR} = 0$ dB, average receive SI power $\rho_{\mathsf{s}} = 30$ dB and 10 bits of ADC resolution.

amount of analog SI suppressed Δ as

$$\Delta = \frac{\delta_0}{\delta_\infty} \tag{3.49}$$

where δ_0 denotes the effective SI before running Algorithm 3. Increasing N_{BS} significantly enhances the SI suppression capabilities post-application of Algorithm 3, with suppression levels exceeding 260 dB ($\times 10^{26}$) for configurations with 128 antennas. Configurations with 32 and 64 antennas also exhibit substantial SI suppression, achieving approximately 243 dB and 257 dB, respectively. Nonetheless, the magnitude of SI suppression alone does not elucidate the adequacy of residual effective SI levels for ADC tolerance. For instance, while 16 antennas at the BS can suppress SI by about 210 dB, the residual effective SI remains at -30 dB, falling short of the -50 dB threshold necessary to prevent ADC saturation and facilitate FD operations. Moreover, it is observed that the LPADC mode yields superior energy efficiency relative to both IPADC and HPADC modes, particularly in scenarios with an extensive antenna

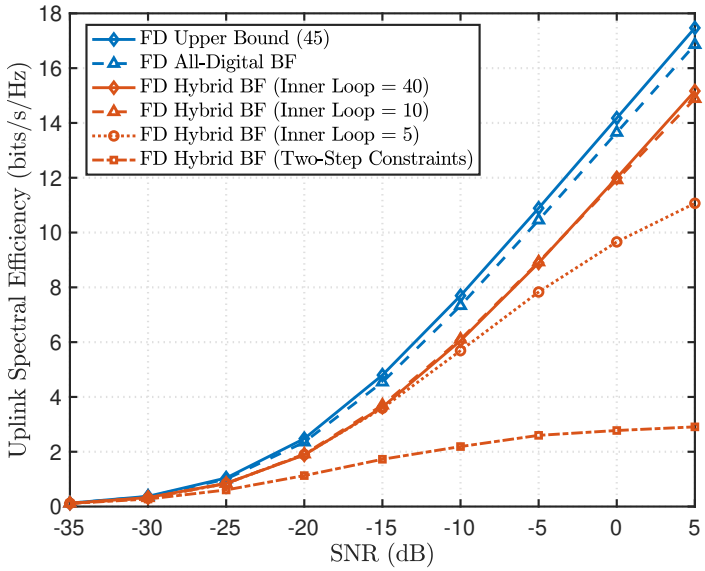

Figure 3.10: Uplink spectral efficiency vs. SNR for different beamforming (BF) schemes and for various iterations of the inner loop in Algorithm 3. Results are simulated with $N_{\mathsf{BS}} = 64$, $N_{\mathsf{RF}}^{\mathsf{BS}} = 2$, $N_{\mathsf{UE}} = 8$, $N_{\mathsf{RF}}^{\mathsf{UE}} = 2$ and $\rho_{\mathsf{s}} = 30$ dB.

array at the BS. This outcome aligns with expectations, considering LPADC's lower Walden figures of merit in comparison to those of IPADC and HPADC. Furthermore, as the number of phase shifters is directly proportional to both the count of RF chains and antennas, power consumption escalates significantly with an increase in N_{BS}. Despite the uplink spectral efficiency enhancement associated with a greater number of antennas, the rate of power consumption acceleration surpasses the spectral efficiency improvement, leading to a marked decline in energy efficiency.

3.5.6 Unit Modulus and Interference Suppression Constraints: Joint vs. Two-Step Designs

In Fig. 3.10, uplink spectral efficiency versus average SNR is compared across various beamforming configurations and the number of inner loop iterations. The plot shows that performance significantly deteriorates when the unit modulus and interference suppression constraints are handled separately, as seen in the "Two-Step

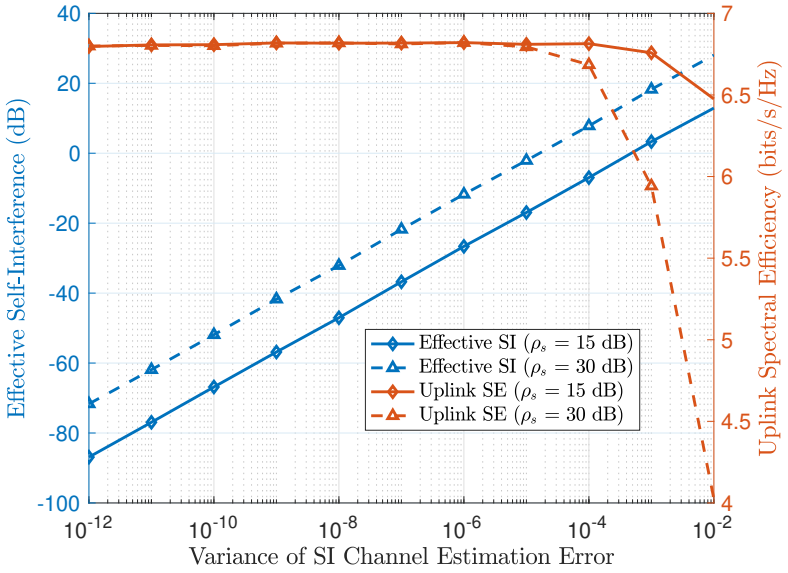

Figure 3.11: Effective SI and uplink spectral efficiency with respect to the variance of the SI channel estimation error for different average receive SI power ρ_{s}. Results are simulated for analog-only architecture (single stream and single RF chain) with $N_{\mathsf{BS}} = 64$, $N_{\mathsf{UE}} = 8$, and $\mathsf{SNR} = 0$ dB.

Constraints." This degradation primarily results from the unit modulus constraint compromising interference suppression, thus increasing interference and reducing uplink spectral efficiency. Conversely, as constraints are considered jointly, this performance gap narrows with more inner loop iterations. For example, at 5 dB SNR, the two-step design achieves about 3 bits/s/Hz, while the joint design reaches 15.5 bits/s/Hz, translating to a 70% improvement in spectral efficiency. Additionally, increasing inner loop iterations beyond 10 doesn't yield spectral efficiency improvements, indicating that convergence is reached, highlighting the effectiveness of our joint constraint management strategy.

3.5.7 Effects of The Average Self-Interference Power and Imperfect Channel State Information

Fig 3.11 demonstrates the impact of the variance of $\tilde{\mathbf{H}}\mathsf{s}$, representing SI channel estimation error, and varying levels of average receive SI power, ρ_{s}, on both effective SI level and uplink spectral efficiency. The beamforming approach relies on $\hat{\mathbf{H}}\mathsf{s}$ for SI channel estimates, treating $\tilde{\mathbf{H}}\mathsf{s}$ as an additional interference factor. Consequently, while beamformers are designed to suppress effective SI, they do not directly address interference caused by estimation errors. An increase in the error's variance amplifies its effect, leading to less effective SI suppression. This degradation becomes particularly pronounced as ρ_{s} increases, underscoring the challenge of managing SI in the presence of significant channel estimation inaccuracies. We can deduce this from (3.50), the effective SI incurred from the estimation error is measured as

$$\delta_{\mathsf{Error}} = \rho_{\mathsf{s}} \mathrm{Tr}\left(\mathbf{W}_{\mathsf{BS}}^{\mathsf{RF}*}\tilde{\mathbf{H}}_{\mathsf{s}}\mathbf{F}_{\mathsf{BS}}^{\mathsf{RF}}\mathbf{F}_{\mathsf{BS}}^{\mathsf{BB}}\mathbf{F}_{\mathsf{BS}}^{\mathsf{BB}*}\mathbf{F}_{\mathsf{BS}}^{\mathsf{RF}*}\tilde{\mathbf{H}}_{\mathsf{s}}^{*}\mathbf{W}_{\mathsf{BS}}^{\mathsf{RF}}\right) \tag{3.50}$$

The presence of estimation error as an ancillary source of SI implies that an increase in the error's variance directly escalates SI power, thereby adversely affecting spectral efficiency. Moreover, an augmented average SI power leads to notable degradation in system performance, notably lowering uplink spectral efficiency. This correlation, which aligns with expectations, is substantiated through the analysis conducted for Fig. 3.6, illustrating the critical influence of SI power levels and estimation error variance on system efficiency.

3.5.8 Effect of the Outer Loop Iterations: Uplink SINR vs. Effective Self-Interference

Fig. 3.12 presents the variation in effective SI and uplink SINR per RF chain across a spectrum of outer loop iterations. It is noted that effective SI begins to stabilize around -180 dB after a few iterations, exhibiting minimal fluctuation and achieving a near-constant level post-15 iterations. Conversely, the convergence trajectory of uplink SINR demonstrates enhanced steadiness with 25 dB increase, with no

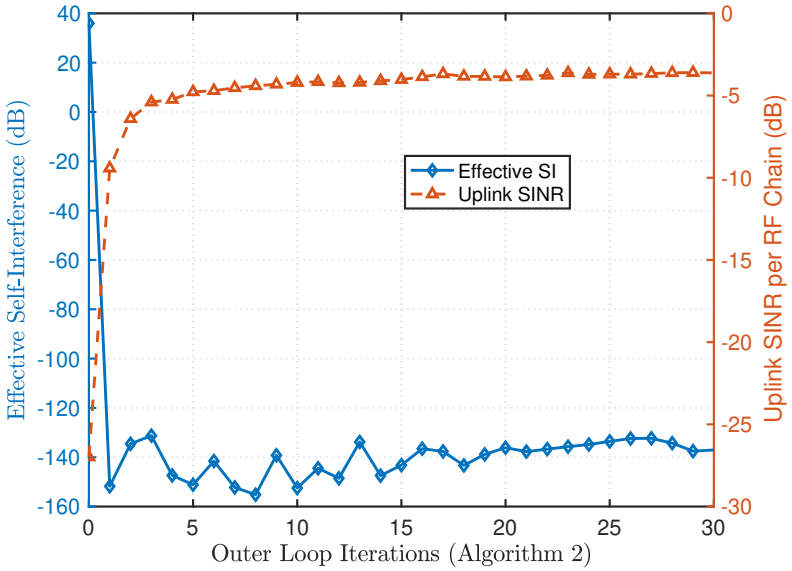

Figure 3.12: Effective SI and uplink SINR per RF chain with respect to the number of iterations of outer loop in Algorithm 3. Results are simulated with $N_{\mathsf{BS}} = 128$, $N_{\mathsf{RF}}^{\mathsf{BS}} = 2$, $N_{\mathsf{UE}} = 8$ and $N_{\mathsf{RF}}^{\mathsf{UE}} = 2$.

observable oscillations and a stabilization at -4 dB after merely 5 iterations. These findings indicate that global convergence, as regulated by the outer loop, is effectively realized within a limited number of iterations, highlighting the efficiency of the beamforming design in rapidly achieving optimal performance metrics.

3.5.9 Effect of the Inner Loop Iterations: Convergence of Alternating Projections Method

We note a consistent decrease in the cost functions, namely effective SI and IUI, as the alternating projections routine progresses through iterations. The convergence of the routine exhibits stability, typically requiring a modest number of iterations, averaging around 10. While providing a mathematical proof of convergence poses challenges due to the involvement of non-convex constraints, empirical results from simulations affirm the convergence of the alternating projections routine.

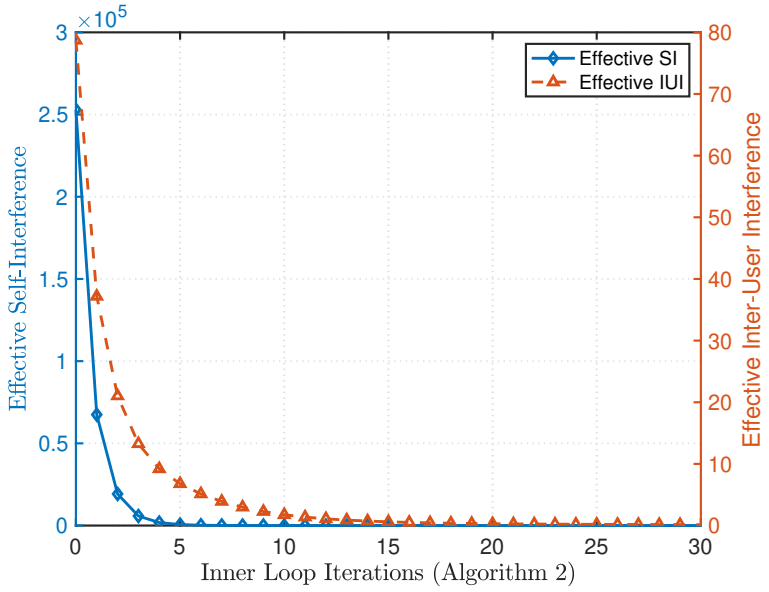

Figure 3.13: Effective SI and IUI with respect to the number of iterations of inner loop in Algorithm 3. Results are simulated with $N_{\mathsf{BS}} = 256$, $N_{\mathsf{RF}}^{\mathsf{BS}} = 2$, $N_{\mathsf{UE}} = 8$ and $N_{\mathsf{RF}}^{\mathsf{UE}} = 2$.

3.5.10 Comparison With Previous Beamforming Techniques

In our analysis, we benchmark our proposed FD hybrid A/D beamforming design against several prior methodologies to assess its performance. Notably, we compare it with the approach from Valcarce *et al.* [98] (denoted as "RM"), Xiao *et al.* [156] ("ZPX"), our earlier work [22] ("EBC"), the method from Satyanarayana *et al.* [137] ("KMPAL"), and Robert *et al.* [132] ("IHS"). In these referenced studies [156, 137, 22, 132], the designs exhibit significant sensitivity to the level of SI as performance notably declines (unless the SI level is minimal). This is primarily due to these designs not maintaining the unit modulus constraint in the hybrid A/D beamformers, thus violating interference suppression constraints and leading to performance degradation. Specifically, in [156], Xiao *et al.* adopt a zero-forcing-matched filter for beamforming design (referred to as method 2 in [156]), but the imposition of unit modulus constraints disrupts the zero-forcing condition for SI suppression, reintroducing SI into the system and significantly impacting spectral efficiency. In our

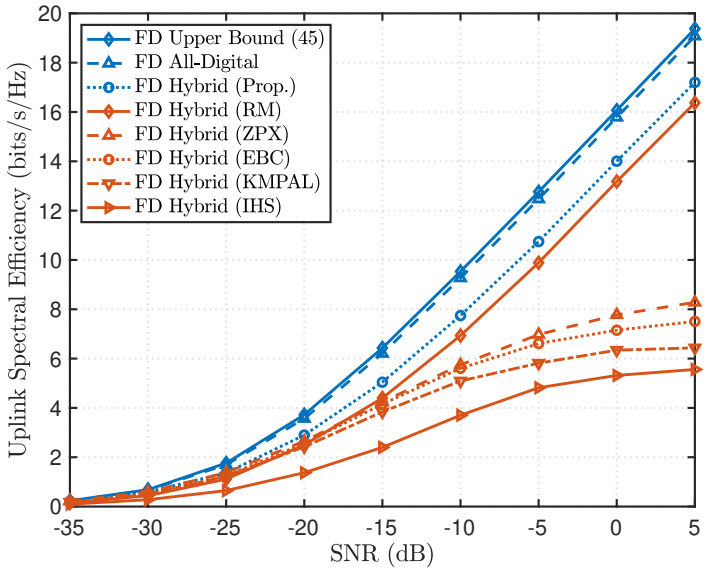

Figure 3.14: A comprehensive comparison with previous methods. Results are simulated with $N_{\mathsf{BS}} = 128$, $N_{\mathsf{RF}}^{\mathsf{BS}} = 2$, $N_{\mathsf{UE}} = 8, N_{\mathsf{RF}}^{\mathsf{UE}} = 2, \rho_{\mathsf{s}} = 20$ dB and $\rho_{\mathsf{iui}} = 5$ dB.

preceding work [22], we initially relaxed the unit modulus constraint during the hybrid A/D beamformer design phase, yet post-optimization imposition of this constraint contradicted the design prerequisites, thereby impairing system performance. Additionally, Satyanarayana *et al.* [137] commence with deriving all-digital beamformers, and apply a convex quadratically-constrained quadratic programming (QCQP) to obtain the digital and the unconstrained analog (without being constrained on unit modulus constraint) solutions. The subsequent introduction of this constraint leads to a compromise in interference suppression, adversely affecting spectral efficiency. Furthermore, Robert *et al.* [132] utilize SVD for all-digital beamforming and apply orthogonal matching pursuit (OMP) for equivalent hybrid analog and baseband solutions. Adjustments to suppress SI through baseband beamforming modifications make the design vulnerable to SI levels due to inadequate analog domain mitigation. Conversely, the "RM" design [98] proves more resilient against SI by approximating all-digital counterparts in Euclidean distance, while the analog RF combiner is optimized to minimize SI power before the ADC, appropriately addressing the unit

modulus constraint during beamformer design to mitigate interference effects. The baseband combiner is then tailored to eliminate residual SI, enhancing spectral efficiency. Our design exhibits a slight performance gap compared to "RM" [98], which can be attributed to our analog precoder being specifically designed to both maximize beamformed power and suppress SI, unlike in [98] where the analog precoder does not explicitly incorporate an interference suppression constraint, relying instead on the analog combiner for SI mitigation. This distinct approach enables our design to surpass the performance seen in [98].

3.6 Conclusion

In this chapter, I developed an iterative beamforming algorithm tailored for FD mmWave multiuser MIMO configurations. Our methodology optimizes hybrid A/D beamformers to mitigate SI and IUI. Leveraging the convex nature of the all-digital optimization problem, we derive closed-form solutions by employing the Lagrange multipliers. Further, our baseband design is informed by both all-digital and analog beamformers, utilizing the LS method for derivation. The analog beamforming component of our design meets critical objectives, including the amplification of received power, implementation of analog-domain interference suppression, and adherence to the unit modulus constraint. Through the application of the alternating projection method, we achieved a synergistic balance among these constraints.

The design yields a substantial enhancement in uplink spectral efficiency by 70%, concurrently achieving interference suppression below the -50 dB threshold necessary in the analog domain to prevent ADC saturation. Remarkably, an increase in BS antennas further diminishes effective SI to -130 dB and elevates uplink spectral efficiency to 14 bits/s/Hz. At its core, our approach deftly navigates the DoF, tackling both interference suppression and spectral efficiency optimization with finesse. A key hallmark of our algorithm is its rapid convergence, typically within $5-10$ iterations, which is critical for minimizing latency and reducing the overhead associated with

beamforming configurations. This efficiency in convergence underscores the significant time savings our method offers. Moreover, our strategy demonstrates superior performance over existing hybrid beamforming approaches and the HD methodology, underscoring the transformative potential of FD mmWave technology in cellular networks.

Chapter 4: Integrated Access and Backhaul

In this chapter[1], I consider an IAB node operating in FD mode. I analyze simultaneous transmission from the New Radio gNB to the IAB node on the backhaul uplink, IAB node to a UE on the access downlink, and IAB transmitter to the IAB receiver on the SI channel. Our contributions are as follows: (1) the development of a low-complexity algorithm for jointly designing hybrid analog/digital beamformers across all three nodes, aimed at maximizing the sum spectral efficiency of the access and backhaul links by mitigating SI and optimizing received power; (2) the derivation of an all-digital beamforming approach and spectral efficiency upper bound for benchmarking purposes; and (3) comprehensive simulations comparing FD and HD modes, hybrid and all-digital beamforming algorithms, and the proposed hybrid beamforming against conventional methods, including the spectral efficiency upper bound. The simulation results demonstrate a substantial reduction in SI power and a notable increase in sum spectral efficiency with the proposed algorithm.

4.1 Introduction

Future wireless networks are expected to have densely deployed BSs to support future applications, such as the Internet of Things, virtual/augmented reality, and vehicle-to-everything. However, traditional fiber backhauling is often unavailable or prohibitively expensive for carrier operators. IAB technology has emerged as a cost-effective alternative. In the case of IAB, only a few BSs are connected to the traditional wired infrastructures while the others relay the backhaul traffic wirelessly

[1]This chapter is based on the work published in the following conference paper: E. Balti, C. Dick and B. L. Evans, "Low Complexity Hybrid Beamforming for mmWave Full-Duplex Integrated Access and Backhaul," *GLOBECOM 2022 - 2022 IEEE Global Communications Conference*, Rio de Janeiro, Brazil, 2022, pp. 1606-1611. This work was supported by NVIDIA, an affiliate of the WNCG 6G@UT Research Center at UT Austin.

[38, 169]. In a typical IAB framework, the access and backhaul links share the same frequency spectrum, which results in resource collision; thus, resource management is required to resolve this issue. Owing to the simplicity of implementation, many previous studies have incorporated HD constraints in their frameworks [122]. In the HD IAB approach, the access and backhaul links must use the given radio resources orthogonally, be it in time or frequency. While this helps prevent collisions in the two links, it fails to exploit the full potential of the given radio resources.

4.1.1 Related Work

Although FD brings many advantages, it suffers from loopback SI, which is caused by the simultaneous transmission and reception over the same resource blocks. This loopback signal cannot be neglected as the SI power can be several orders of magnitude stronger than the signal power received from the UE, which can render FD systems dysfunctional [21]. To address this limitation, related work proposed robust beamforming design to suppress the SI signal and achieve acceptable spectral efficiency [132, 75, 160, 32]. Authors in [134] proposed a hybrid A/D beamforming for FD systems with limited dynamic range. In addition, authors in [59] proposed a low complexity frequency-domain successive SI cancellation for FD radios. Authors in [93, 30] proposed a robust beamforming design for an intelligent reflecting surfaces assisted FD multiuser systems to wipe out SI and improve sum spectral efficiency.

4.1.2 Contributions

In this chapter, I consider an FD IAB system wherein the gNB communicates with the IAB node through the backhaul link, while the user is receiving from the IAB node through the access channel. The main contributions can be summarized as

- To address SI, I propose a low complexity hybrid analog/digital beamforming to cancel SI, avoid ADC saturation and maximize sum spectral efficiency of the access and backhaul links.

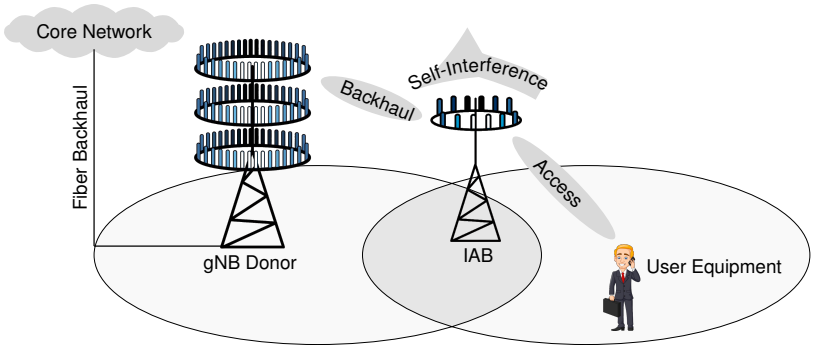

Figure 4.1: Full-duplex integrated access and backhaul for a single-user case. The gNB donor, linked to the core network by fiber backhaul, communicates with the IAB node through wireless backhaul. The user equipment is served by the IAB node through the wireless access link. Simultaneous transmission and reception of the IAB node over the same time/frequency resources blocks incurs loopback self-interference.

- I derive an all-digital solution and upper bound, and compare full vs. half duplex, hybrid vs. all-digital beamforming, conventional SI cancellation, and upper bound.

4.1.3 Structure

The rest of this chapter is organized as follows: Section 4.2 describes the system model. Section 4.3 presents the optimization problem and beamforming design. Section 4.4 gives numerical results. Section 4.5 concludes the chapter.

4.2 System Model

Per Fig. 4.1, the system transmits from gNB to IAB nodes on backhaul uplink, IAB node to user equipment on access downlink, and IAB transmitter to receiver on SI channel.

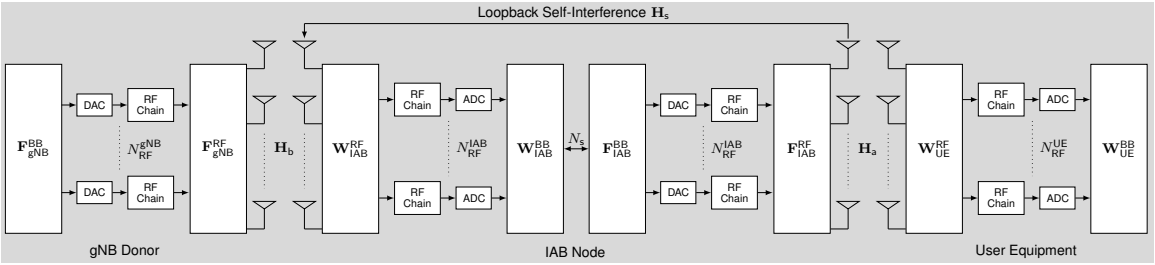

Figure 4.2: Basic abstraction of the hybrid analog/digital architecture of the full-duplex integrated access and backhaul system. The backhaul channel is between the gNB donor and IAB node, and the access channel is between the IAB node and the user equipment.

4.2.1 Access and Backhaul Channels Model

Per Fig. 4.2, the backhaul uplink channel, $\mathbf{H_b}$, and the downlink access channel, $\mathbf{H_a}$, each have the form

$$\mathbf{H} = \sqrt{\frac{N_{\mathsf{RX}} N_{\mathsf{TX}}}{C R_c}} \sum_{c=0}^{C-1} \sum_{r_c=0}^{R_c-1} \alpha_{r_c} \mathbf{a}_{\mathsf{RX}}(\theta_{r_c}) \mathbf{a}^*_{\mathsf{TX}}(\phi_{r_c}) \tag{4.1}$$

where C is number of clusters, R_c is number of rays per cluster, and θ_{r_c} and ϕ_{r_c} are the AoA and AoD of the r_c-th ray, respectively. Each ray has a relative time delay τ_{r_c} and complex path gain α_{r_c}. Also, $\mathbf{a}_{\mathsf{RX}}(\theta)$ and $\mathbf{a}_{\mathsf{TX}}(\phi)$ are the RX and TX antenna array response vectors, respectively. The array response vector is given by

$$\mathbf{a}_{\mathsf{X}}(\theta) = \frac{1}{\sqrt{N_{\mathsf{X}}}} \left[1, \mathrm{e}^{j\frac{2\pi d}{\lambda}\sin(\theta)}, \ldots, \mathrm{e}^{j\frac{2\pi d}{\lambda}(N_{\mathsf{X}}-1)\sin(\theta)}\right]^T. \tag{4.2}$$

where X is the TX or RX and N_{X} is the number antennas.

4.2.2 Self-Interference Channel Model

Per Fig. 4.3, the SI leakage at the BS is modeled by the channel matrix $\mathbf{H_s}$. The separation, or transceiver gap, between TX and RX arrays is defined by distance d while the transceiver incline is determined by ω. The SI channel is decomposed into a static LOS channel modeled by $\mathbf{H}_{\mathsf{LOS}}$, which is derived from the geometry of the transceiver, and a NLOS channel described by $\mathbf{H}_{\mathsf{NLOS}}$ which follows the geometric

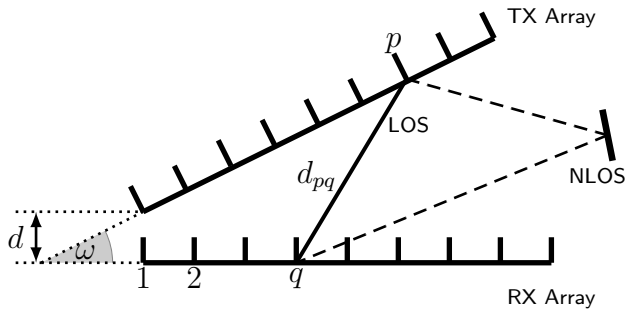

Figure 4.3: Relative position of TX and RX arrays at BS. Given that the TX and RX arrays are collocated, the far-field assumption that the signal impinges on the antenna array as a planar wave does not hold. Instead, for FD transceivers, it is more suitable to assume that the signal impinges on the array as a spherical wave for the near-field LOS channel.

channel model defined by (3.5). The (q, p)-th entry of the LOS SI leakage matrix can be written as

$$[\mathbf{H}_{\mathsf{LOS}}]_{qp} = \frac{1}{d_{pq}} \mathsf{e}^{-j2\pi \frac{d_{pq}}{\lambda}} \tag{4.3}$$

where d_{pq} is the distance between the p-th antenna in the TX array and q-th antenna in the RX array at BS given by (1.6). The aggregate SI channel matrix can be obtained by

$$\mathbf{H}_{\mathsf{s}} = \underbrace{\sqrt{\frac{\kappa}{\kappa+1}}\mathbf{H}_{\mathsf{LOS}}}_{\text{Near-Field}} + \underbrace{\sqrt{\frac{1}{\kappa+1}}\mathbf{H}_{\mathsf{NLOS}}}_{\text{Far-Field}} \tag{4.4}$$

where κ is the Rician factor.

$$d_{pq} = \sqrt{\left(\frac{d}{\tan(\omega)} + (q-1)\frac{\lambda}{2}\right)^2 + \left(\frac{d}{\sin(\omega)} + (p-1)\frac{\lambda}{2}\right)^2 - 2\left(\frac{d}{\tan(\omega)} + (q-1)\frac{\lambda}{2}\right)\left(\frac{d}{\sin(\omega)} + (p-1)\frac{\lambda}{2}\right)\cos(\omega)} \tag{4.5}$$

4.2.3 Signal Model

Received signals at the IAB ($\mathbf{y}_{\mathsf{b}}$) and UE ($\mathbf{y}_{\mathsf{a}}$) are given by

$$\mathbf{y}_{\mathsf{b}} = \underbrace{\sqrt{\rho_{\mathsf{b}}}\mathbf{W}_{\mathsf{IAB}}^{*}\mathbf{H}_{\mathsf{b}}\mathbf{F}_{\mathsf{gNB}}\mathbf{s}_{\mathsf{b}}}_{\text{Desired Signal}} + \underbrace{\sqrt{\rho_{\mathsf{s}}}\mathbf{W}_{\mathsf{IAB}}^{*}\mathbf{H}_{\mathsf{s}}\mathbf{F}_{\mathsf{IAB}}\mathbf{s}_{\mathsf{a}}}_{\text{Self-Interference Signal}} + \underbrace{\mathbf{W}_{\mathsf{IAB}}^{*}\mathbf{n}_{\mathsf{IAB}}}_{\text{AWGN}} \tag{4.6}$$

$$\mathbf{y}_{\mathsf{a}} = \underbrace{\sqrt{\rho_{\mathsf{a}}}\mathbf{W}_{\mathsf{UE}}^{*}\mathbf{H}_{\mathsf{a}}\mathbf{F}_{\mathsf{IAB}}\mathbf{s}_{\mathsf{a}}}_{\text{Desired Signal}} + \underbrace{\mathbf{W}_{\mathsf{UE}}^{*}\mathbf{n}_{\mathsf{UE}}}_{\text{AWGN}} \tag{4.7}$$

where $\mathbf{W}_{\mathsf{IAB}} \in \mathbb{C}^{N_{\mathsf{IAB}} \times N_{\mathsf{s}}}$ and $\mathbf{F}_{\mathsf{IAB}} \in \mathbb{C}^{N_{\mathsf{IAB}} \times N_{\mathsf{s}}}$ are the all-digital combiner and precoder at the IAB node, respectively. $\mathbf{W}_{\mathsf{UE}} \in \mathbb{C}^{N_{\mathsf{UE}} \times N_{\mathsf{s}}}$ and $\mathbf{F}_{\mathsf{gNB}} \in \mathbb{C}^{N_{\mathsf{gNB}} \times N_{\mathsf{s}}}$ being the all-digital combiner and precoder at the UE and gNB, respectively. Also, N_{s} is the number of spatial streams and N_{X} is the number of antennas at node X.

4.3 Beamforming Design

The objective of designing of the beamformers is to maximize the received power for backhaul and access links and simultaneously reject the SI. In this work, we propose a hybrid analog/digital beamforming design wherein large amount of SI is suppressed in the analog domain to avoid the ADC saturation while residual SI is wiped out in the digital domain.

4.3.1 Hybrid Beamforming: Analog Stage

In this stage, we proceed to design the analog combiner $\mathbf{W}_{\mathsf{IAB}}^{\mathsf{RF}} \in \mathbb{C}^{N_{\mathsf{IAB}} \times N_{\mathsf{RF}}^{\mathsf{IAB}}}$ and precoder $\mathbf{F}_{\mathsf{IAB}}^{\mathsf{RF}} \in \mathbb{C}^{N_{\mathsf{IAB}} \times N_{\mathsf{RF}}^{\mathsf{IAB}}}$ at the IAB node as well as the analog combiner at UE $\mathbf{W}_{\mathsf{UE}}^{\mathsf{RF}} \in \mathbb{C}^{N_{\mathsf{UE}} \times N_{\mathsf{RF}}^{\mathsf{UE}}}$ and the analog precoder at the gNB $\mathbf{F}_{\mathsf{gNB}}^{\mathsf{RF}} \in \mathbb{C}^{N_{\mathsf{gNB}} \times N_{\mathsf{RF}}^{\mathsf{gNB}}}$, where $N_{\mathsf{RF}}^{\mathsf{X}}$ is the number of RF chains at node X. To avoid the ADC saturation, large amount of SI has to be rejected in the analog domain which consequently requires a robust design. The covariance matrix of the precoded SI and noise at the IAB node is expressed by

$$\mathbf{R}_{\mathsf{IAB}} = \rho_{\mathsf{s}}\mathbf{H}_{\mathsf{s}}\mathbf{F}_{\mathsf{IAB}}^{\mathsf{RF}}\mathbf{F}_{\mathsf{IAB}}^{\mathsf{RF}*}\mathbf{H}_{\mathsf{s}}^{*} + \sigma^2\mathbf{I}_{N_{\mathsf{IAB}}} \tag{4.8}$$

where σ^2 is the noise variance. Our objective is to jointly design the analog combiners $\mathbf{W}_{\mathsf{IAB}}^{\mathsf{RF}}$, $\mathbf{W}_{\mathsf{UE}}^{\mathsf{RF}}$ and precoders $\mathbf{F}_{\mathsf{gNB}}^{\mathsf{RF}}$, $\mathbf{F}_{\mathsf{IAB}}^{\mathsf{RF}}$ to minimize the SI power at the IAB node and preserve the dimension of the signal space, i.e., $\mathsf{rank}\left(\mathbf{W}_{\mathsf{IAB}}^{\mathsf{RF}*}\mathbf{H}_{\mathsf{b}}\mathbf{F}_{\mathsf{gNB}}^{\mathsf{RF}}\right) = \min\left(N_{\mathsf{RF}}^{\mathsf{IAB}}, N_{\mathsf{RF}}^{\mathsf{gNB}}\right)$ and $\mathsf{rank}\left(\mathbf{W}_{\mathsf{UE}}^{\mathsf{RF}*}\mathbf{H}_{\mathsf{a}}\mathbf{F}_{\mathsf{IAB}}^{\mathsf{RF}}\right) = \min\left(N_{\mathsf{RF}}^{\mathsf{UE}}, N_{\mathsf{RF}}^{\mathsf{IAB}}\right)$. We formulate the

optimization problem accordingly

$$\begin{aligned} \mathscr{P}_1 : &\min_{\mathbf{W}_{\mathsf{IAB}}^{\mathsf{RF}}} \mathrm{Tr}\left(\mathbf{W}_{\mathsf{IAB}}^{\mathsf{RF}*}\mathbf{R}_{\mathsf{IAB}}\mathbf{W}_{\mathsf{IAB}}^{\mathsf{RF}}\right) \\ &\mathsf{s.t.}\ \mathbf{W}_{\mathsf{IAB}}^{\mathsf{RF}*}\mathbf{H}_{\mathsf{b}}\mathbf{F}_{\mathsf{gNB}}^{\mathsf{RF}} = \alpha\mathbf{I}_{N_{\mathsf{RF}}^{\mathsf{IAB}}} \end{aligned} \tag{4.9}$$

where $\mathbf{R}_{\mathsf{IAB}}$ is a positive definite matrix ($\mathbf{R}_{\mathsf{IAB}} > 0$) and $\alpha = 1/\sqrt{\mathrm{Tr}\left(\mathbf{W}_{\mathsf{IAB}}^{\mathsf{RF}*}\mathbf{W}_{\mathsf{IAB}}^{\mathsf{RF}}\right)}$ is a power normalization coefficient.

To design the analog precoder at the IAB $\mathbf{F}_{\mathsf{IAB}}^{\mathsf{RF}}$, we proceed similarly as $\mathbf{W}_{\mathsf{IAB}}^{\mathsf{RF}}$. The covariance matrix of the combined SI and noise is expressed by

$$\mathbf{S}_{\mathsf{IAB}} = \rho_{\mathsf{s}}\mathbf{H}_{\mathsf{s}}^{*}\mathbf{W}_{\mathsf{IAB}}^{\mathsf{RF}}\mathbf{W}_{\mathsf{IAB}}^{\mathsf{RF}*}\mathbf{H}_{\mathsf{s}} + \sigma^2\mathbf{I}_{N_{\mathsf{IAB}}} \tag{4.10}$$

where ($\mathbf{S}_{\mathsf{IAB}} > 0$) is a positive definite matrix. Then, we formulate the problem accordingly

$$\begin{aligned} \mathscr{P}_2 : &\min_{\mathbf{F}_{\mathsf{IAB}}^{\mathsf{RF}}} \mathrm{Tr}\left(\mathbf{F}_{\mathsf{IAB}}^{\mathsf{RF}*}\mathbf{S}_{\mathsf{IAB}}\mathbf{F}_{\mathsf{IAB}}^{\mathsf{RF}}\right) \\ &\mathsf{s.t.}\ \mathbf{W}_{\mathsf{UE}}^{\mathsf{RF}*}\mathbf{H}_{\mathsf{a}}\mathbf{F}_{\mathsf{IAB}}^{\mathsf{RF}} = \beta\mathbf{I}_{N_{\mathsf{RF}}^{\mathsf{IAB}}} \end{aligned} \tag{4.11}$$

where $\beta = 1/\sqrt{\mathrm{Tr}\left(\mathbf{F}_{\mathsf{IAB}}^{\mathsf{RF}*}\mathbf{F}_{\mathsf{IAB}}^{\mathsf{RF}}\right)}$ is a power normalization coefficient.

Theorem 4. The optimal analog combiner and precoder at the IAB node, solutions to the problems (4.9) and (4.11) are expressed by

$$\mathbf{W}_{\mathsf{IAB}}^{\mathsf{RF}} = \alpha\mathbf{R}_{\mathsf{IAB}}^{-1}\mathbf{H}_{\mathsf{b}}\mathbf{F}_{\mathsf{gNB}}^{\mathsf{RF}}\left(\mathbf{F}_{\mathsf{gNB}}^{\mathsf{RF}*}\mathbf{H}_{\mathsf{b}}^{*}\mathbf{R}_{\mathsf{IAB}}^{-1}\mathbf{H}_{\mathsf{b}}\mathbf{F}_{\mathsf{gNB}}^{\mathsf{RF}}\right)^{-1} \tag{4.12}$$

$$\mathbf{F}_{\mathsf{IAB}}^{\mathsf{RF}} = \beta\mathbf{S}_{\mathsf{IAB}}^{-1}\mathbf{H}_{\mathsf{a}}^{*}\mathbf{W}_{\mathsf{UE}}^{\mathsf{RF}*}\left(\mathbf{W}_{\mathsf{UE}}^{\mathsf{RF}*}\mathbf{H}_{\mathsf{a}}\mathbf{S}_{\mathsf{IAB}}^{-1}\mathbf{H}_{\mathsf{a}}^{*}\mathbf{W}_{\mathsf{UE}}^{\mathsf{RF}}\right)^{-1} \tag{4.13}$$

Proof. The proof of Theorem 4 is provided in Appendix C.1. □

In this design, the analog precoder at gNB $\mathbf{F}_{\mathsf{gNB}}^{\mathsf{RF}}$ and combiner at UE $\mathbf{F}_{\mathsf{gNB}}^{\mathsf{RF}}$ can be selected regardless of Problems (4.9) and (4.11).

Proposition 1. The analog combiner at the UE that minimizes the SI and hence the MSE is the Wiener filter or LMMSE receiver $\mathbf{W}_{\mathsf{MMSE}}$. The filter design problem can be defined as

$$\mathscr{P}_3 : \mathbf{W}_{\mathsf{MMSE}} = \arg\min_{\mathbf{W}} \mathbb{E}\left[\|\mathbf{s} - \mathbf{y}\|_2^2\right] \tag{4.14}$$

For the analog precoder at the gNB, we adopt the Regularized Zero-Forcing filter $\mathbf{F}_{\mathsf{RegZF}}$. The expressions of the analog combiner and precoder at the UE and gNB, respectively, are given by

$$\mathbf{W}_{\mathsf{UE}}^{\mathsf{RF}} = \left(\mathbf{H}_{\mathsf{a}}\mathbf{F}_{\mathsf{IAB}}^{\mathsf{RF}}\mathbf{F}_{\mathsf{IAB}}^{\mathsf{RF}*}\mathbf{H}_{\mathsf{a}}^{*} + \frac{N_{\mathsf{UE}}}{\mathsf{SNR}_{\mathsf{a}}}\mathbf{I}_{N_{\mathsf{UE}}}\right)^{-1}\mathbf{H}_{\mathsf{a}}\mathbf{F}_{\mathsf{IAB}}^{\mathsf{RF}} \tag{4.15}$$

$$\mathbf{F}_{\mathsf{gNB}}^{\mathsf{RF}} = \left(\mathbf{H}_{\mathsf{b}}^{*}\mathbf{W}_{\mathsf{IAB}}^{\mathsf{RF}}\mathbf{W}_{\mathsf{IAB}}^{\mathsf{RF}*}\mathbf{H}_{\mathsf{b}} + \frac{N_{\mathsf{IAB}}}{\mathsf{SNR}_{\mathsf{b}}}\mathbf{I}_{N_{\mathsf{IAB}}}\right)^{-1}\mathbf{H}_{\mathsf{b}}^{*}\mathbf{W}_{\mathsf{IAB}}^{\mathsf{RF}} \tag{4.16}$$

where $\mathsf{SNR}_{\mathsf{x}} = \frac{\rho_{\mathsf{x}}}{\sigma^2}$, $\mathsf{x} \in \{a, b\}$.

The analog beamformers designed in Eqs. (4.12-4.16) are unconstrained solutions, i.e., they do not satisfy the constant amplitude (CA) constraint. To satisfy such constraint, they have to be projected onto the subspace of the CA constraint. Equivalently, the unconstrained solutions are updated as follows

$$\mathbf{X}_{\mathsf{RF}} \longleftarrow \frac{1}{\sqrt{N}}\exp\left(\mathsf{i}\angle\mathbf{X}_{\mathsf{RF}}\right) \tag{4.17}$$

where N and $\angle\mathbf{X}$ are the number of rows and angles of the complex matrix $\mathbf{X}$, respectively.

4.3.2 Hybrid Beamforming: Digital Stage

Once the analog beamformers are designed to reject large amount of SI to avoid the ADC saturation, the analog cancellation is not perfect, i.e., there are some residual SI left over after the analog stage. The digital beamformers which are interpreted as the last line of defense come to further remove this residual SI.

Theorem 5. The optimal digital beamformer $\mathbf{X}_{\mathsf{BB}}$ can be expressed in terms of the analog beamformer $\mathbf{X}_{\mathsf{RF}}$ as follows. We first apply the SVD $\mathbf{X}_{\mathsf{RF}} = \mathbf{U}_{\mathsf{RF}}\mathbf{S}_{\mathsf{RF}}\mathbf{V}_{\mathsf{RF}}^{*}$. Second we express $\mathbf{X}_{\mathsf{BB}} = \mathbf{V}_{\mathsf{RF}}\mathbf{S}_{\mathsf{RF}}^{-1}\mathbf{Q}_{\star}$, where the columns of $\mathbf{Q}_{\star} \in \mathbb{C}^{M\times N}$ comprise the N dominant left singular vectors of $\mathbf{U}_{\mathsf{RF}}^{*}\mathbf{A}$. Note that $\mathbf{X}_{\mathsf{RF}} \in \mathbb{C}^{M\times L}$, $\mathbf{X}_{\mathsf{BB}} \in \mathbb{C}^{L\times N}$ and $\mathbf{A} \in \mathbb{C}^{M\times N}$.

Proof. The proof of Theorem 5 is reported in Appendix C.2. □

4.3.3 All-Digital Beamforming

In mmWave communications, all-digital beamforming using one RF chain per antenna with full precision data converters is not a practical design. Although it achieves high spectral efficiency, it is not energy efficient. However, such a design may serve as a benchmarking tool to measure the efficacy of the proposed hybrid beamforming design. To this end, we design an all-digital beamformer to cancel SI and maximize the sum spectral efficiency by extending the routine we are using for analog beamforming design. The first extension is the all-digital beamformer $\mathbf{X} \in \mathbb{C}^{M \times N}$ would have different dimensions compared to the analog beamfomers, where M and N are the numbers of antennas and spatial streams, respectively. The second extension is that the all-digital beamformer design is unconstrained; i.e., the CA constraint does not exist for such a design.

Remark 7. Given the all-digital beamformer solution $\mathbf{X} \in \mathbb{C}^{M \times N}$, M and N are the number of antennas and spatial streams, respectively. M should be large enough to sustain N spatial streams and the remaining $P = M - N$ degrees of freedom should dedicated to suppress the SI.

We introduce the expressions of the spectral efficiency for the backhaul and access links, respectively, as follows

$$\mathcal{I}_{\mathsf{b}} = \log\det\left(\mathbf{I}_{N_{\mathsf{s}}} + \rho_{\mathsf{b}}\mathbf{W}_{\mathsf{IAB}}^{*}\mathbf{H}_{\mathsf{b}}\mathbf{F}_{\mathsf{gNB}}\mathbf{Q}_{\mathsf{b}}^{-1}\mathbf{F}_{\mathsf{gNB}}^{*}\mathbf{H}_{\mathsf{b}}^{*}\mathbf{W}_{\mathsf{IAB}}\right) \tag{4.18}$$

$$\mathcal{I}_{\mathsf{a}} = \log\det\left(\mathbf{I}_{N_{\mathsf{s}}} + \rho_{\mathsf{a}}\mathbf{W}_{\mathsf{UE}}^{*}\mathbf{H}_{\mathsf{a}}\mathbf{F}_{\mathsf{IAB}}\mathbf{Q}_{\mathsf{a}}^{-1}\mathbf{F}_{\mathsf{IAB}}^{*}\mathbf{H}_{\mathsf{a}}^{*}\mathbf{W}_{\mathsf{UE}}\right) \tag{4.19}$$

where $\mathbf{Q}_{\mathsf{b}}$ is the covariance matrix of the SI and noise power for the backhaul link and $\mathbf{Q}_{\mathsf{a}}$ is the covariance matrix of the noise power for the access link, respectively given by

$$\mathbf{Q}_{\mathsf{b}} = \rho_{\mathsf{s}}\mathbf{W}_{\mathsf{IAB}}^{*}\mathbf{H}_{\mathsf{s}}\mathbf{F}_{\mathsf{IAB}}\mathbf{F}_{\mathsf{IAB}}^{*}\mathbf{H}_{\mathsf{s}}^{*}\mathbf{W}_{\mathsf{IAB}} + \sigma^{2}\mathbf{W}_{\mathsf{IAB}}^{*}\mathbf{W}_{\mathsf{IAB}} \tag{4.20}$$

$$\mathbf{Q}_{\mathsf{a}} = \sigma^{2}\mathbf{W}_{\mathsf{IAB}}^{*}\mathbf{W}_{\mathsf{IAB}} \tag{4.21}$$

Lemma 1. For the interference-free case, the optimal beamformers diagonalize the channel. By applying the SVD on the channel, we retrieve the singular values and extract the first N_{s} modes associated with the spatial streams. The upper bound for backhaul or access link is given by

$$\mathcal{I}_{\mathsf{Bound}} = \sum_{\ell=0}^{N_{\mathsf{s}}-1} \log\left(1 + \sigma_{\ell}\left(\mathbf{H}\right)^{2} \mathsf{SNR}\right) \tag{4.22}$$

Algorithm 4 Hybrid Beamforming Design

function DIGITAL($\mathbf{X}_{\mathsf{RF}}, \mathbf{A}, N$)
Compute SVD $\mathbf{X}_{\mathsf{RF}} = \mathbf{U}_{\mathsf{RF}}\mathbf{S}_{\mathsf{RF}}\mathbf{V}^{*}_{\mathsf{RF}}$
$\mathbf{Q} \leftarrow N$ Dominant left singular vectors of $\mathbf{U}^{*}_{\mathsf{RF}}\mathbf{A}$
$\mathbf{X}_{\mathsf{BB}} \leftarrow \mathbf{V}_{\mathsf{RF}}\mathbf{S}^{-1}_{\mathsf{RF}}\mathbf{Q}$
return $\mathbf{X}_{\mathsf{BB}}$
end function

Input $\mathbf{H}_{\mathsf{s}}, \mathbf{H}_{\mathsf{a}}, \mathbf{H}_{\mathsf{b}}$
Initialize $\mathbf{F}^{\mathsf{RF}}_{\mathsf{gNB}}$, $\mathbf{F}^{\mathsf{RF}}_{\mathsf{IAB}}$, $\mathbf{W}^{\mathsf{RF}}_{\mathsf{IAB}}$, $\mathbf{W}^{\mathsf{RF}}_{\mathsf{UE}}$, $\mathbf{F}^{\mathsf{BB}}_{\mathsf{gNB}}$, $\mathbf{F}^{\mathsf{BB}}_{\mathsf{IAB}}$, $\mathbf{W}^{\mathsf{BB}}_{\mathsf{IAB}}$, $\mathbf{W}^{\mathsf{BB}}_{\mathsf{UE}}$
Set $\mathbf{W}_{\mathsf{IAB}} \leftarrow \mathbf{W}^{\mathsf{RF}}_{\mathsf{IAB}}\mathbf{W}^{\mathsf{BB}}_{\mathsf{IAB}}$, $\mathbf{F}_{\mathsf{IAB}} \leftarrow \mathbf{F}^{\mathsf{RF}}_{\mathsf{IAB}}\mathbf{F}^{\mathsf{BB}}_{\mathsf{IAB}}$, $\mathbf{W}_{\mathsf{IAB}} \leftarrow \mathbf{W}^{\mathsf{RF}}_{\mathsf{UE}}\mathbf{W}^{\mathsf{BB}}_{\mathsf{UE}}$ and $\mathbf{F}_{\mathsf{gNB}} \leftarrow \mathbf{F}^{\mathsf{RF}}_{\mathsf{gNB}}\mathbf{F}^{\mathsf{BB}}_{\mathsf{gNB}}$
Compute $\mathbf{R}_{\mathsf{IAB}}$ and $\mathbf{S}_{\mathsf{IAB}}$ from (4.8) and (4.10)
Obtain $\mathbf{W}^{\mathsf{RF}}_{\mathsf{IAB}}$ and $\mathbf{F}^{\mathsf{RF}}_{\mathsf{IAB}}$ from (4.12) and (4.13)
Obtain $\mathbf{W}^{\mathsf{RF}}_{\mathsf{UE}}$ and $\mathbf{F}^{\mathsf{RF}}_{\mathsf{gNB}}$ from (4.15) and (4.16)
Project the analog beamformers on the CA subspace (4.17)
$\mathbf{W}^{\mathsf{BB}}_{\mathsf{IAB}} \leftarrow \text{DIGITAL}\left(\mathbf{W}^{\mathsf{RF}}_{\mathsf{IAB}}, \mathbf{H}_{\mathsf{b}}\mathbf{F}_{\mathsf{gNB}}, N_{\mathsf{s}}\right)$
$\mathbf{F}^{\mathsf{BB}}_{\mathsf{IAB}} \leftarrow \text{DIGITAL}\left(\mathbf{F}^{\mathsf{RF}}_{\mathsf{IAB}}, \mathbf{H}^{*}_{\mathsf{a}}\mathbf{W}_{\mathsf{UE}}, N_{\mathsf{s}}\right)$
$\mathbf{W}^{\mathsf{BB}}_{\mathsf{UE}} \leftarrow \text{DIGITAL}\left(\mathbf{W}^{\mathsf{RF}}_{\mathsf{UE}}, \mathbf{H}_{\mathsf{a}}\mathbf{F}_{\mathsf{IAB}}, N_{\mathsf{s}}\right)$
$\mathbf{F}^{\mathsf{BB}}_{\mathsf{gNB}} \leftarrow \text{DIGITAL}\left(\mathbf{F}^{\mathsf{RF}}_{\mathsf{gNB}}, \mathbf{H}^{*}_{\mathsf{b}}\mathbf{W}_{\mathsf{IAB}}, N_{\mathsf{s}}\right)$
Set $\mathbf{W}_{\mathsf{IAB}} \leftarrow \mathbf{W}^{\mathsf{RF}}_{\mathsf{IAB}}\mathbf{W}^{\mathsf{BB}}_{\mathsf{IAB}}$, $\mathbf{F}_{\mathsf{IAB}} \leftarrow \mathbf{F}^{\mathsf{RF}}_{\mathsf{IAB}}\mathbf{F}^{\mathsf{BB}}_{\mathsf{IAB}}$, $\mathbf{W}_{\mathsf{IAB}} \leftarrow \mathbf{W}^{\mathsf{RF}}_{\mathsf{UE}}\mathbf{W}^{\mathsf{BB}}_{\mathsf{UE}}$ and $\mathbf{F}_{\mathsf{gNB}} \leftarrow \mathbf{F}^{\mathsf{RF}}_{\mathsf{gNB}}\mathbf{F}^{\mathsf{BB}}_{\mathsf{gNB}}$
Repeat Steps (11-19) until the convergence of (4.9) and (4.11)
return $\mathbf{F}^{\mathsf{RF}}_{\mathsf{gNB}}$, $\mathbf{F}^{\mathsf{RF}}_{\mathsf{IAB}}$, $\mathbf{W}^{\mathsf{RF}}_{\mathsf{IAB}}$, $\mathbf{W}^{\mathsf{RF}}_{\mathsf{UE}}$, $\mathbf{F}^{\mathsf{BB}}_{\mathsf{gNB}}$, $\mathbf{F}^{\mathsf{BB}}_{\mathsf{IAB}}$, $\mathbf{W}^{\mathsf{BB}}_{\mathsf{IAB}}$, $\mathbf{W}^{\mathsf{BB}}_{\mathsf{UE}}$

4.3.4 Convergence

In this subsection, we prove the convergence of the proposed algorithm 4. Since the digital beamforming solutions are derived in terms of the analog beamformers,

the convergence of the hybrid analog/digital beamforming algorithm depends on the convergence of the analog solutions themselves. In other terms, it is sufficient to prove the convergence of the objective functions in (4.9) and (4.11). We show that the objective function decreases in each iteration and converges to the local optimum in a few iterations, which makes it computationally efficient. The total SI plus noise power at the IAB node, i.e., the objective function of (4.9) is given by

$$\begin{aligned}\mathbf{R} =& \mathrm{Tr}\left(\mathbf{W}_{\mathsf{IAB}}^{\mathsf{RF}*}\mathbf{R}_{\mathsf{IAB}}\mathbf{W}_{\mathsf{IAB}}^{\mathsf{RF}}\right)\\ =& \mathrm{Tr}\left(\mathbf{W}_{\mathsf{IAB}}^{\mathsf{RF}*}\left(\rho_{\mathsf{s}}\mathbf{H}_{\mathsf{s}}\mathbf{F}_{\mathsf{IAB}}^{\mathsf{RF}}\mathbf{F}_{\mathsf{IAB}}^{\mathsf{RF}*}\mathbf{H}_{\mathsf{s}}^{*}+\sigma^2\mathbf{I}_{N_{\mathsf{IAB}}}\right)\mathbf{W}_{\mathsf{IAB}}^{\mathsf{RF}}\right)\\ =& \underbrace{\mathrm{Tr}\left(\rho_{\mathsf{s}}\mathbf{W}_{\mathsf{IAB}}^{\mathsf{RF}*}\mathbf{H}_{\mathsf{s}}\mathbf{F}_{\mathsf{IAB}}^{\mathsf{RF}}\mathbf{F}_{\mathsf{IAB}}^{\mathsf{RF}*}\mathbf{H}_{\mathsf{s}}^{*}\mathbf{W}_{\mathsf{IAB}}^{\mathsf{RF}}\right)}_{\text{Effective SI Power }(\mathcal{J})}+\sigma^2 N_{\mathsf{RF}}.\end{aligned} \tag{4.23}$$

Similarly, the SI plus noise power defined in (4.11) is given by

$$\begin{aligned}\mathbf{S} =& \mathrm{Tr}\left(\mathbf{F}_{\mathsf{IAB}}^{\mathsf{RF}*}\mathbf{S}_{\mathsf{IAB}}\mathbf{F}_{\mathsf{IAB}}^{\mathsf{RF}}\right)\\ =& \mathrm{Tr}\left(\mathbf{F}_{\mathsf{IAB}}^{\mathsf{RF}*}\left(\rho_{\mathsf{s}}\mathbf{H}_{\mathsf{s}}^{*}\mathbf{W}_{\mathsf{IAB}}^{\mathsf{RF}}\mathbf{W}_{\mathsf{IAB}}^{\mathsf{RF}*}\mathbf{H}_{\mathsf{s}}+\sigma^2\mathbf{I}_{N_{\mathsf{IAB}}}\right)\mathbf{F}_{\mathsf{IAB}}^{\mathsf{RF}}\right)\\ =& \mathrm{Tr}\left(\rho_{\mathsf{s}}\mathbf{F}_{\mathsf{IAB}}^{\mathsf{RF}*}\mathbf{H}_{\mathsf{s}}^{*}\mathbf{W}_{\mathsf{IAB}}^{\mathsf{RF}}\mathbf{W}_{\mathsf{IAB}}^{\mathsf{RF}*}\mathbf{H}_{\mathsf{s}}\mathbf{F}_{\mathsf{IAB}}^{\mathsf{RF}}\right)+\sigma^2 N_{\mathsf{RF}}.\end{aligned} \tag{4.24}$$

It is noteworthy to state that the objective functions in (4.23) and (4.24) have the same generic form and so the solutions as well. The local optimal solutions of the objective functions (4.9) and (4.11) are given by Theorem 4 and they are sure to converge to the locally optimal solution as it is guaranteed by Algorithm 4. The effective SI power decreases in each iteration and it is lower bounded by zero.

Fig. 4.4 illustrates the progress of the effective SI power with respect to the number of iterations. We notice that the algorithm converges in just 10 iterations requiring 0.7 Mflops in total. In addition, we observe that the analog beamforming drops the SI power from 128 to 16 to prevent the ADC saturation (8x) while the digital beamforming drops the SI power from 16 to 10.06 (1.5x). Since the objective function (4.11) has the same generic form as (4.9), the results in Fig. 4.4 also hold for the problem (4.11).

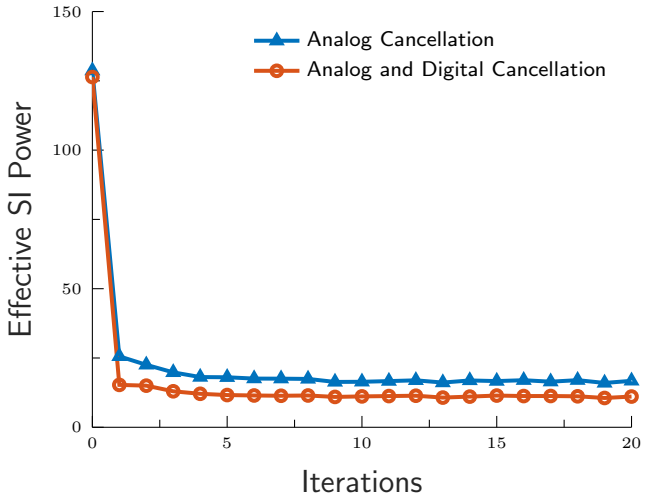

Figure 4.4: Convergence of the effective SI power function implemented in analog ($\mathcal{J}$) defined in the objective function (4.23) and hybrid analog/digital for the proposed hybrid beamforming algorithm 4. The plot is produced with $\mathsf{SNR} = 0$ dB and SI power $\rho_{\mathsf{s}} = 15$ dB.

4.3.5 Complexity Analysis

Table 4.1 analyzes the computational complexity of the proposed hybrid beamforming algorithm. Multiplying matrices $\mathbf{A} \in \mathbb{C}^{m\times n}$ and $\mathbf{B} \in \mathbb{C}^{n\times p}$ requires nmp flops. An inverse of an $n \times n$ matrix using Cholesky decomposition requires $\frac{n^3}{3}$ flops whereas multiplication of a matrix $\mathbf{A} \in \mathbb{C}^{m\times n}$ and its Hermitian ($\mathbf{A}\mathbf{A}^*$) requires $\frac{nm^2}{2}$ flops.

Table 4.1: Computational complexity of the hybrid beamforming algorithm. Parameters values are selected from Table 4.2.

Operation	Complex Multiplications for Highest-Order Terms	Flops	Dominant Term	Contribution (Total)
$\mathbf{W}_{\mathsf{IAB}}^{\mathsf{RF}}$	$\frac{3}{2}N_{\mathsf{IAB}}^2 N_{\mathsf{RF}}^{\mathsf{IAB}} + \frac{1}{3}N_{\mathsf{IAB}}^3 + N_{\mathsf{gNB}}N_{\mathsf{IAB}}N_{\mathsf{RF}}^{\mathsf{gNB}} + \frac{1}{3}\left(N_{\mathsf{RF}}^{\mathsf{gNB}}\right)^3 + N_{\mathsf{IAB}}^2 N_{\mathsf{RF}}^{\mathsf{gNB}}$	21165	$\frac{1}{3}N_{\mathsf{IAB}}^3$	51.61% (16.06%)
$\mathbf{F}_{\mathsf{IAB}}^{\mathsf{RF}}$	$\frac{3}{2}N_{\mathsf{IAB}}^2 N_{\mathsf{RF}}^{\mathsf{IAB}} + \frac{1}{3}N_{\mathsf{IAB}}^3 + N_{\mathsf{UE}}N_{\mathsf{IAB}}N_{\mathsf{RF}}^{\mathsf{UE}} + \frac{1}{3}\left(N_{\mathsf{RF}}^{\mathsf{UE}}\right)^3 + N_{\mathsf{IAB}}^2 N_{\mathsf{RF}}^{\mathsf{UE}}$	19373	$\frac{1}{3}N_{\mathsf{IAB}}^3$	56.38% (16.06%)
$\mathbf{F}_{\mathsf{gNB}}^{\mathsf{RF}}$	$\frac{3}{2}N_{\mathsf{gNB}}^2 N_{\mathsf{RF}}^{\mathsf{gNB}} + \frac{1}{3}N_{\mathsf{gNB}}^3$	13995	$\frac{1}{3}N_{\mathsf{gNB}}^3$	78.05% (16.06%)
$\mathbf{W}_{\mathsf{IAB}}^{\mathsf{BB}}$	$9\left(N_{\mathsf{RF}}^{\mathsf{IAB}}\right)^2 N_{\mathsf{IAB}} + 9N_{\mathsf{s}}^2 N_{\mathsf{IAB}} + N_{\mathsf{IAB}}^2 N_{\mathsf{s}} + N_{\mathsf{s}}^3$	4360	$N_{\mathsf{IAB}}^2 N_{\mathsf{s}}$	46.97% (3.03%)
$\mathbf{F}_{\mathsf{IAB}}^{\mathsf{BB}}$	$9\left(N_{\mathsf{RF}}^{\mathsf{IAB}}\right)^2 N_{\mathsf{IAB}} + 9N_{\mathsf{s}}^2 N_{\mathsf{IAB}} + N_{\mathsf{IAB}}^2 N_{\mathsf{s}} + N_{\mathsf{s}}^3$	4360	$N_{\mathsf{IAB}}^2 N_{\mathsf{s}}$	46.97% (3.01%)
$\mathbf{F}_{\mathsf{gNB}}^{\mathsf{BB}}$	$9\left(N_{\mathsf{RF}}^{\mathsf{gNB}}\right)^2 N_{\mathsf{gNB}} + 9N_{\mathsf{s}}^2 N_{\mathsf{gNB}} + N_{\mathsf{gNB}}^2 N_{\mathsf{s}} + N_{\mathsf{s}}^3$	4360	$N_{\mathsf{gNB}}^2 N_{\mathsf{s}}$	46.97% (3.01%)
$\mathbf{W}_{\mathsf{UE}}^{\mathsf{BB}}$	$9\left(N_{\mathsf{RF}}^{\mathsf{UE}}\right)^2 N_{\mathsf{UE}} + 9N_{\mathsf{s}}^2 N_{\mathsf{UE}} + N_{\mathsf{UE}}^2 N_{\mathsf{s}} + N_{\mathsf{s}}^3$	328	$9\left(N_{\mathsf{RF}}^{\mathsf{UE}}\right)^2 N_{\mathsf{UE}}$	43.90% (0.21%)
$\mathbf{W}_{\mathsf{UE}}^{\mathsf{RF}}$	$\frac{3}{2}N_{\mathsf{UE}}^2 N_{\mathsf{RF}}^{\mathsf{UE}} + \frac{1}{3}N_{\mathsf{UE}}^3$	70	$\frac{3}{2}N_{\mathsf{UE}}^2 N_{\mathsf{RF}}^{\mathsf{UE}}$	69.23% (0.07%)

Table 4.2: System parameters.

Parameter	**Value**
Carrier frequency	28 GHz
Bandwidth	850 MHz
Number of gNB/IAB Antennas ($N_{\mathsf{gNB}}/N_{\mathsf{IAB}}$)	32
Number of UE Antennas (N_{UE})	4
Number of Clusters (C)	6
Number of Rays per Cluster (R_c)	8
AoA/AoD Angular Spread	20°
Transceivers Gap (d)	2λ
Transceivers Incline (ω)	$\frac{\pi}{6}$
Rician Factor (κ)	5 dB
SI Power (ρ_{s})	15 dB
Number of Spatial Streams (N_{s})	2
Number of RF Chains (N_{RF})	2

4.4 Numerical Analysis

Table 4.2 gives the parameter values used in the simulations. For each case, 1000 channels realizations were generated to perform the Monte Carlo simulation in MATLAB.

Among the three FD hybrid beamforming solutions in Fig. 4.5, SVD and [132] are very sensitive to SI because the relative analog beamformers ignore SI cancellation, which leads to ADC saturation and hence more performance loss. Our approach, however, introduces analog beamformer design to reduce a large amount of SI power as shown in Fig. 4.4. The performance of the proposed system is improved by the optimal digital beamforming solution which further suppresses residual SI. At $\mathsf{SNR} = 5$ dB, we notice the proposed FD system achieves a gain of around 4.71, and 6.2 bits/s/Hz with respect to SVD, work [132], respectively. In addition, our proposed FD beamforming algorithm outperforms the HD mode, which is a goal of this work, and achieves a gain of 8.62 bits/s/Hz at $\mathsf{SNR} = 5$ dB.

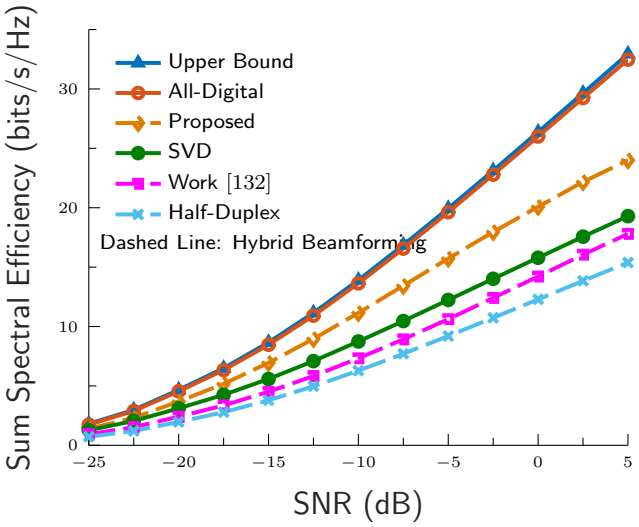

Figure 4.5: Sum spectral efficiency results: Performance comparison between the proposed algorithm with the related works as well as the benchmarking tools.

4.5 Conclusion

In this chapter, I proposed a low complexity hybrid A/D beamforming design for a FD IAB system. The proposed algorithm designs the hybrid precoders for the gNB Donor and IAB node, and the hybrid combiners for the IAB node and user equipment. In simulation, the algorithm converges in five iterations while reducing a large amount of SI in the analog domain to avoid ADC saturation. In addition, the hybrid beamforming results are further improved by the implementation of the optimal digital beamformers which wipe out the residual SI. Simulations show that the proposed FD beamforming design outperforms the related works in terms of spectral efficiency as well as it beats the HD mode which demonstrates the feasibility of the proposed design for practical consideration.

Chapter 5: Single-Cell Multiuser MIMO

The implementation of FD communication, which allows simultaneous transmission and reception on the same frequency and time, necessitates significant suppression of SI. In this chapter[1], we focus on a wideband single-cell multiuser context where an FD BS engages concurrently with multiple users in both uplink and downlink directions at mmWave band. We explore the design of beamformers at both the users and BS, leveraging dense antenna arrays to facilitate SI and multiuser interference suppression via beamforming cancellation techniques. Typically, BS beamformers are executed using a hybrid analog/digital approach with a limited number of RF chains, presenting certain inherent limitations that must be addressed. Our study centers on a hybrid architecture that incorporates a partially-connected analog stage based on phase shifters with finite resolution. To prevent ADC saturation, our proposed design strategically suppresses SI in the analog domain using a combination of analog precoding and combining at BS. Subsequently, we develop baseband beamformers to further mitigate residual SI and multiuser interference while enhancing uplink/downlink beamformed powers. Through comprehensive numerical simulations, we demonstrate that our proposed beamforming techniques can significantly improve beam patterns, interference suppression, spectral and energy efficiency, showcasing considerable performance advantages.

[1]This chapter is based on the following journal paper: E. Balti, and B. L. Evans, "Millimeter Wave Full-Duplex Multiuser MIMO: Joint Beamforming Design and Optimization". This work was supported by AT&T labs and Tektronix through their industrial affiliation with the 6G@UT research center at UT Austin.

5.1 Introduction

Mobile networks are increasingly integrating mmWave bands within the range of 30-300 GHz[2]. Present 5G NR standards encompass mmWave FR2 bands up to a threshold of 52.6 GHz. Subsequent standards are projected to expand the FR2 bands beyond this threshold into the FR2 bands, venturing into sub-terahertz (sub-THz) bands slotted for 6G communications systems.

The availability of extensive bandwidths in mmWave frequencies presents a great opportunity for increased data transmission rates. However, designing communication systems that operate at mmWave frequencies poses significant challenges. To overcome path losses and ensure resilient link margins, mmWave communications relies on beamforming benefits derived from extensive antenna arrays. These arrays integrate numerous elements, ranging from dozens to hundreds in count, which results in complexity associated with MIMO system designs and user operations. These operations must ensure optimal performance while efficiently utilizing scarce bandwidth resources.

FD technology offers needed spectral efficiency and is gaining significant attention in the realm of physical layer communication. FD allows simultaneous TX and RX on the same carrier frequency, unlike traditional HD methods that partition time or bandwidth to achieve TX-RX separation [104, 146]. FD not only holds the promise of doubling spectral efficiency but also introduces flexibility to point-to-point communication and multiple access schemes. Additionally, it can reduce latency associated with HD operations [136]. However, the primary challenge hindering widespread FD adoption is SI, wherein a node's transmission leaks into its own receiver, potentially overpowering the desired signal from a remote node.

Extensive efforts have been made to address SI mitigation methods for FD. Results show promising outcomes have been reported for single-antenna FD nodes op-

[2]Technically, mmWave frequencies are categorized between 30 and 300 GHz, but the broader industry defines them within the range of 10 to 300 GHz.

erating in microwave frequencies [24, 63, 37], employing a combination of techniques [74]. These techniques span three domains: propagation domain methods that optimize antenna design and placement passively [49, 78]; analog-circuit domain methods that actively create an analog SI replica and subtract it from the received signal to prevent RX front-end saturation [70]; and digital domain methods that estimate and subtract residual SI at the baseband [78]. With respect to the digital domain, successful SI mitigation necessitates sufficiently low residual SI levels in order to fully leverage the dynamic range of ADCs.

In contrast, in microwave-band systems, BFC to mitigate SI leads to a spectral efficiency trade-offs as some spatial DoF are allocated to SI mitigation [41, 65, 48, 67]. However, in mmWave systems with large antenna arrays, the abundant DoF makes BFC-based SI mitigation highly appealing in maintaining spectral efficiency.

5.1.1 Related Works

Early FD mmWave research initially explored propagation domain methods for SI mitigation. One approach, as seen in [92], applied ZF constraints to SI with a single data stream in each direction. This approach, although primarily designed for all-digital beamforming, showed promise with a small performance loss in mmWave scenarios, indicating that ZF constraints had limited impact.

In analog beamforming, [156] demonstrated that direct projection of optimal all-digital beamforming weights onto the feasible set led to significant performance degradation, even with infinite-resolution phase shifters. The issue was addressed in [97], extending to multiple data streams with hybrid beamforming in [96]. Other FD designs for hybrid beamformers were explored in [137, 118, 6, 131, 73, 134].

Another method [137] adopted a hybrid factorization by LS approximation of all-digital beamformers. However, this approach suffered from high SI leakage due to LS approximation errors and suppressed SI at the baseband rather than in the analog domain. In contrast, [118], [73], and [134] aimed to suppress SI in the

analog domain. [118] leveraged a result from [145], factoring beamforming matrices into analog and digital stages without error when the number of RF chains exceeded twice the number of data streams. This condition did not always hold in practice. [73] designed the hybrid beamformers based on angular information about the far-field channel responses, assuming perfect suppression of the LoS near-field component of SI channels through antenna isolation techniques. [6] and [134] employed exhaustive search methods for RF stage design, solving convex optimization problems for each candidate. [6] proposed a joint design with active analog cancellation, while [134] assumed perfect knowledge of the remaining SI, canceled in the digital domain.

Among these works, [97, 96, 137, 118] assumed unquantized phase shifters, while [6, 131, 73, 134] used Discrete Fourier Transform (DFT) codebooks for the analog stages. The latter designs allowed for implementation with $\log_2 N$-bit phase shifters, where N represented the number of antenna elements. Consequently, as the array size increased, the required precision for these designs grew, exacerbated by the fact that the number of phase shifters was proportional to the array size N. This prompted the exploration of alternatives that permitted flexibility in phase-shifter resolution, enabling a trade-off between performance and cost.

5.1.2 Contributions

In this chapter, I delve into the design of BFC for FD mmWave multiuser multiple-input multiple-output (MU-MIMO) systems. These systems involve a FD BS serving multiple HD uplink and downlink users. Our focus is on overcoming challenges associated with achieving adequate SI suppression in the analog domain, preventing ADC saturation, and dealing with the constraints of the common hybrid A/D architecture found in mmWave transceivers. Specifically, we concentrate on partially-connected, known for their better energy efficiency compared to the fully-connected array, in the analog stage implementations that utilize phase shifters. These phase shifters have finite resolution, resulting in complex beamformer entries with the same magnitudes and discrete phases. Such constraints are particularly relevant

for the lower-resolution phase shifters commonly used in practice to manage power consumption and hardware costs [152, 83, 99]. To our knowledge, this is the first study addressing a MU-MIMO scenario using a practical, energy-efficient (partially-connected) BS architecture, while also considering arbitrary quantized PS resolutions within a multicarrier OFDM waveform context.

The main contributions of this work can be summarized as follows:

1. I propose a novel design for all-digital beamformers aimed at improving spectral efficiency. This design extends the current literature from narrowband single-user scenarios to a wideband multiuser framework, applicable to both uplink and downlink FD BS mmWave transceivers supporting multiple streams. The proposed all-digital framework demonstrates near-optimal performance and serves as a foundational reference and benchmark for future hybrid A/D designs.

2. I introduce a methodology for deriving hybrid precoders and combiners for the FD BS, based on a partially-connected phase shifter framework in the analog stage, while carefully accounting for the quantization effects of phase shifters. This design is also adaptable to fully-connected array configurations, providing flexibility for different system architectures.

3. In addressing the challenge of minimizing interference in the analog domain to prevent ADC saturation, I developed a method for designing analog beamformers that mitigates the losses associated with CAQP, which have been shown in the literature to conflict with effective interference suppression.

4. I propose a method for computing the baseband beamformers at the FD BS, balancing the trade-off between interference suppression and maximizing beamformed power for uplink and downlink transmissions.

5.1.3 Structure

The rest of this chapter is organized as follows: Section 5.2 presents the system model in terms of architectures, signals and beam-patterns formulation. Section 5.3 explains the proposed all-digital beamforming at FD BS and uplink/downlink users while Section 5.4 delves into the design of hybrid analog/digital beamforming at FD BS. Numerical results are described in Section 5.5 while conclusive summaries are reported in Section 5.6.

5.2 System Model

We consider a single-cell MU-MIMO systems wherein the BS is equipped with N_{BS} antennas and operates in FD mode. The BS independently serves U uplink and K downlink UEs wherein each user is equipped with N_{UE} antennas and operates in HD mode. Each uplink user sends a single spatial stream to the BS and to guarantee that the BS sustains serving multiple users, we assume that $N_{\mathsf{s}}^{\mathsf{RX}} = U$, where $N_{\mathsf{s}}^{\mathsf{RX}}$ is the number of layers (spatial streams) sustainable at the BS. Besides, we assume that the maximum number of served users satisfies $U \leq L_{\mathsf{RX}}$, where L_{RX} is the number of RX RF chains at the BS. This is motivated by the spatial multiplexing gain of the proposed MU-MIMO hybrid beamforming system, which is restricted by $\min(L_{\mathsf{RX}}, U)$ for $N_{\mathsf{BS}}^{\mathsf{RX}} > N_{\mathsf{UE}}$. Since the BS is operating in FD mode, a loopback SI is leaked from the transmit to the received arrays of the BS. Detailed description of the BS architecture is illustrated by Fig. 5.1. Similar to the uplink scenario, the BS is transmitting $N_{\mathsf{s}}^{\mathsf{TX}}$ layers/spatial streams to serve K downlink users. We further assume that $K = N_{\mathsf{s}}^{\mathsf{TX}}$ as well as the maximum number of served users satisfies $K \leq L_{\mathsf{TX}}$, where L_{TX} is the number of TX RF chains at the BS.

In alignment with numerous benchmark studies, we adopt OFDM as the foundational waveform. Subsequently, the index of the OFDM subcarrier is represented as $n = 0, \ldots, N_{\mathsf{sc}} - 1$, where N_{sc} denotes the number of active subcarriers. To streamline notation, the signal models have been articulated for a generic subcarrier with index

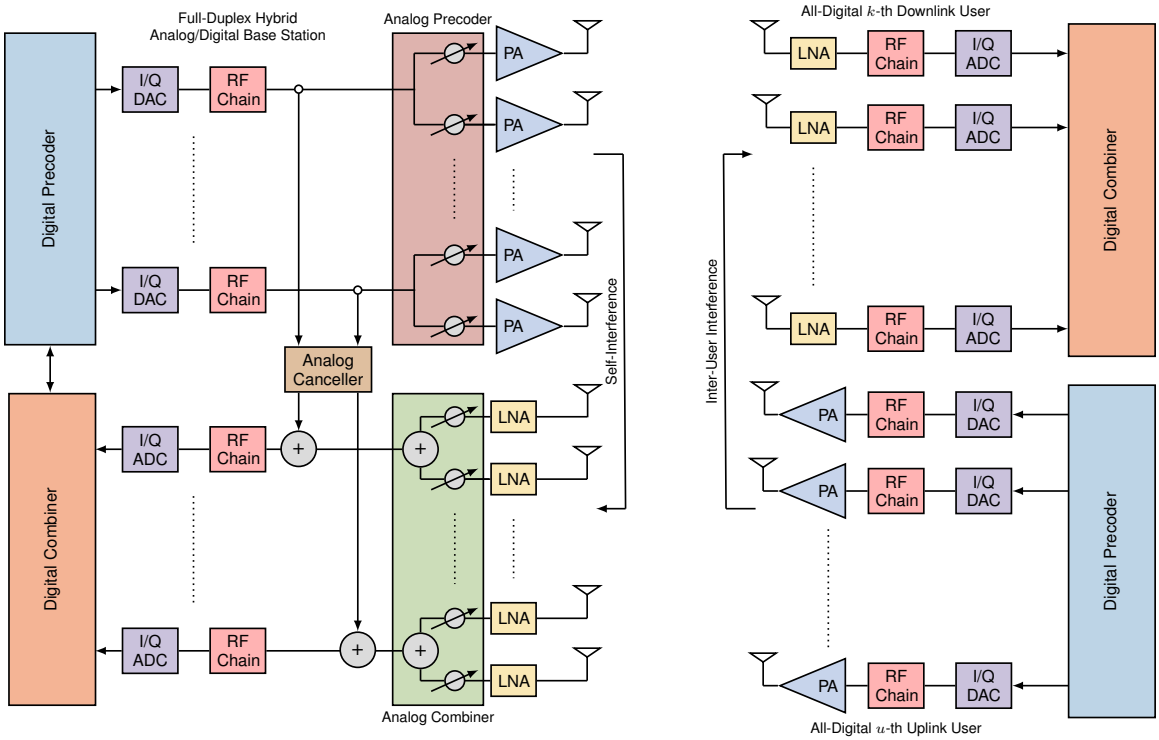

Figure 5.1: MU-MIMO scenario: Basic abstraction of the hybrid A/D partially-connected architecture of the FD BS (left hand side) as well as the all-digital architectures of the uplink/downlink users (right hand side), illustrating various modules of the system such as ADCs, DACs, RF chains, A/D precoders and combiners, phase shifters, Low noise amplifiers, power amplifiers, and the analog canceller. The uplink user is corrupted by the SI while the downlink user is subject to the IUI incurred by the uplink user. The analog canceller consists of an analog-circuit domain methods actively construct an analog replica of the SI and subtract it from the received signal in order to avoid the ADC saturation. Our contribution is to design to hybrid A/D beamformers to spatially suppress the SI as well as the IUI and multiuser interference (MUI) or multistream interference.

Table 5.1: System Model Notations and Variables.

Variable	**Definition**	**Size**
$N_{\mathsf{BS}}^{\mathsf{RX}}$	Number of RX antennas at BS	–
$N_{\mathsf{BS}}^{\mathsf{TX}}$	Number of TX antennas at BS	–
N_{UE}	Number of antennas at UE	–
L_{RX}	Number of RX RF chains at BS	–
L_{TX}	Number of TX RF chains at BS	–
U	Number of UL users	–
K	Number of DL users	–
N_{sc}	Number of active subcarriers	–
$\mathbf{W}_{\mathsf{BS},n}$	All-digital BS combiner at subcarrier n	$N_{\mathsf{BS}}^{\mathsf{RX}} \times U$
$\mathbf{F}_{\mathsf{BS},n}$	All-digital BS precoder at subcarrier n	$N_{\mathsf{BS}}^{\mathsf{TX}} \times K$
$\mathbf{W}_{\mathsf{BS}}^{\mathsf{RF}}$	Analog BS combiner	$N_{\mathsf{BS}}^{\mathsf{RX}} \times L_{\mathsf{RX}}$
$\mathbf{F}_{\mathsf{BS}}^{\mathsf{RF}}$	Analog BS precoder	$N_{\mathsf{BS}}^{\mathsf{TX}} \times L_{\mathsf{TX}}$
$\mathbf{W}_{\mathsf{BS},n}^{\mathsf{BB}}$	Baseband BS combiner at subcarrier n	$L_{\mathsf{RX}} \times U$
$\mathbf{F}_{\mathsf{BS},n}^{\mathsf{BB}}$	Baseband BS precoder at subcarrier n	$L_{\mathsf{TX}} \times K$
$\mathbf{w}_{k,n}$	All-digital k-th UE combiner at subcarrier n	$N_{\mathsf{UE}} \times 1$
$\mathbf{f}_{u,n}$	All-digital u-th UE precoder at subcarrier n	$N_{\mathsf{UE}} \times 1$

n.

Remark 8. In the subsequent system model, we operate under the assumption of a static channel for the sake of clarity. Nonetheless, the OFDM-based system model presented herein possesses the capability to be readily adapted to accommodate time-varying channels and the detection of mobile targets.

To process the uplink signal received from the users, the BS applies the analog combiner $\mathbf{W}_{\mathsf{BS}}^{\mathsf{RF}}$ followed by the digital combiner $\mathbf{W}_{\mathsf{BS},n}^{\mathsf{BB}}$. In the downlink scenario, the BS applies the digital precoder $\mathbf{F}_{\mathsf{BS},n}^{\mathsf{BB}}$ on the K streams followed by the analog precoder $\mathbf{F}_{\mathsf{BS}}^{\mathsf{RF}}$. Since the analog precoder and combiner at the BS are implemented using analog phase shifters, they are constrained by CAQP.

5.2.1 Downlink Signal Model

The beamformed spatial TX signal samples at the BS and at the n-th subcarrier within an OFDM symbol index is given by

$$\mathbf{x}_{\mathsf{BS},n} = \mathbf{F}_{\mathsf{BS}}^{\mathsf{RF}} \sum_{k=0}^{K-1} \mathbf{f}_{\mathsf{BS},k,n}^{\mathsf{BB}} x_{\mathsf{BS},k,n} \tag{5.1}$$

where $\mathbf{F}_{\mathsf{BS}}^{\mathsf{RF}}$ and $\mathbf{f}_{\mathsf{BS},k,n}$ are the analog precoder and the frequency-dependent digital precoders for the k-th stream, respectively, while $x_{\mathsf{BS},k,n}, k = 0, \ldots, K-1$, denote the spatially multiplexed data symbols. After combining, the received signal at the k-th downlink user and at the n-th subcarrier is given by

$$\begin{aligned} y_{k,n} = & \underbrace{\mathbf{w}_{k,n}^{*} \mathbf{H}_{k,n} \mathbf{F}_{\mathsf{BS}}^{\mathsf{RF}} \mathbf{f}_{\mathsf{BS},k,n}^{\mathsf{BB}} x_{\mathsf{BS},k,n}}_{\text{Desired Signal}} + \underbrace{\mathbf{w}_{k,n}^{*} \sum_{\mathsf{u}=0}^{U-1} \mathbf{H}_{k,\mathsf{u},n} \mathbf{f}_{\mathsf{u},n} x_{\mathsf{u},n}}_{\text{Inter-User Interference (IUI)}} \\ & + \underbrace{\mathbf{w}_{k,n}^{*} \sum_{\mathsf{k} \neq k}^{K-1} \mathbf{H}_{\mathsf{k},n} \mathbf{F}_{\mathsf{BS}}^{\mathsf{RF}} \mathbf{f}_{\mathsf{BS},\mathsf{k},n}^{\mathsf{BB}} x_{\mathsf{BS},\mathsf{k},n}}_{\text{Multiuser Interference (MUI)}} + \underbrace{\mathbf{w}_{k,n}^{*} \mathbf{n}_{\mathsf{UE},n}}_{\text{Filtered Noise}} \end{aligned} \tag{5.2}$$

where $\mathbf{n}_{\mathsf{UE},n} \in \mathbb{C}^{N_{\mathsf{UE}} \times 1}$ is the AWGN at the UE which is distributed as $\mathcal{CN}(\mathbf{0}, \mathbf{I}_{N_{\mathsf{UE}}})$, $\mathbf{f}_{\mathsf{BS},k,n}^{\mathsf{BB}}$, which is the k-th column of $\mathbf{F}_{\mathsf{BS},n}^{\mathsf{BB}}$, is the BS baseband precoder intended to the

k-th downlink user, $\mathbf{w}_k$ is the combiner of the k-th downlink user, $\mathbf{H}_{k,n} \in \mathbb{C}^{N_{\mathsf{UE}} \times N_{\mathsf{BS}}^{\mathsf{TX}}}$ is the downlink channel from the BS to the k-th downlink user. $\mathbf{H}_{k,\mathsf{u},n} \in \mathbb{C}^{N_{\mathsf{UE}} \times N_{\mathsf{UE}}}$ is the IUI channel between the u-th uplink and the k-th downlink users.

5.2.2 Uplink Signal Model

After combining, the received signal ($\mathbf{y}_n \in \mathbb{C}^{U \times 1}$) at the BS for subcarrier n is given by

$$\begin{aligned} \mathbf{y}_n =& \mathbf{W}_{\mathsf{BS},n}^{\mathsf{BB}*} \mathbf{W}_{\mathsf{BS}}^{\mathsf{RF}*} \sum_{\mathsf{u}=0}^{U-1} \mathbf{H}_{\mathsf{u},n} \mathbf{f}_{\mathsf{u},n} x_{\mathsf{u},n} + \mathbf{W}_{\mathsf{BS},n}^{\mathsf{BB}*} \mathbf{W}_{\mathsf{BS}}^{\mathsf{RF}*} \mathbf{n}_{\mathsf{BS},n} \\ &+ \mathbf{W}_{\mathsf{BS},n}^{\mathsf{BB}*} \mathbf{W}_{\mathsf{BS}}^{\mathsf{RF}*} \mathbf{H}_{\mathsf{SI},n} \mathbf{F}_{\mathsf{BS}}^{\mathsf{RF}} \mathbf{F}_{\mathsf{BS},n}^{\mathsf{BB}} \mathbf{x}_{\mathsf{BS},n} \end{aligned} \tag{5.3}$$

where $x_{\mathsf{u},n}$ is the complex symbol scalar sent by the u-th user at subcarrier n and $\mathbf{H}_{\mathsf{SI},n} \in \mathbb{C}^{N_{\mathsf{BS}}^{\mathsf{RX}} \times N_{\mathsf{BS}}^{\mathsf{TX}}}$ is the n-th SI subcarrier. Note that $\mathbf{H}_{\mathsf{u},n} \in \mathbb{C}^{N_{\mathsf{BS}}^{\mathsf{RX}} \times N_{\mathsf{UE}}}$ is the UL subcarrier n between the u-th user and the BS. We denote by $\mathbf{n}_{\mathsf{BS},n} \in \mathbb{C}^{N_{\mathsf{BS}}^{\mathsf{RX}} \times 1}$ the AWGN at the BS which is distributed as $\mathcal{CN}(\mathbf{0}, \mathbf{I}_{N_{\mathsf{BS}}^{\mathsf{RX}}})$. After decomposing the first term in (5.3), the uplink received signal at the BS for subcarrier n and transmitted from the u-th user is expressed by

$$\begin{aligned} y_{u,n} =& \underbrace{\mathbf{w}_{\mathsf{BS},u,n}^{\mathsf{BB}*} \mathbf{W}_{\mathsf{BS}}^{\mathsf{RF}*} \mathbf{H}_{u,n} \mathbf{f}_{u,n} x_{u,n}}_{\text{Desired Signal}} + \underbrace{\mathbf{w}_{\mathsf{BS},u,n}^{\mathsf{BB}*} \mathbf{W}_{\mathsf{BS}}^{\mathsf{RF}*} \mathbf{n}_{\mathsf{BS},n}}_{\text{Filtered Noise}} \\ &+ \underbrace{\mathbf{w}_{\mathsf{BS},u,n}^{\mathsf{BB}*} \mathbf{W}_{\mathsf{BS}}^{\mathsf{RF}*} \mathbf{H}_{\mathsf{SI},n} \mathbf{F}_{\mathsf{BS}}^{\mathsf{RF}} \mathbf{F}_{\mathsf{BS},n}^{\mathsf{BB}} \mathbf{x}_{\mathsf{BS},n}}_{\text{Self-Interference}} \\ &+ \underbrace{\mathbf{w}_{\mathsf{BS},u,n}^{\mathsf{BB}*} \mathbf{W}_{\mathsf{BS}}^{\mathsf{RF}*} \sum_{\mathsf{u} \neq u}^{U-1} \mathbf{H}_{\mathsf{u},n} \mathbf{f}_{\mathsf{u},n} x_{\mathsf{u},n}}_{\text{Multiuser Interference (MUI)}} \end{aligned} \tag{5.4}$$

where $\mathbf{w}_{\mathsf{BS},u}^{\mathsf{BB}} \in \mathbb{C}^{L_{\mathsf{RX}} \times 1}$, which is the u-th column vector of $\mathbf{W}_{\mathsf{BS}}^{\mathsf{BB}}$, is the baseband combiner applied at the BS to extract the u-th uplink stream.

5.2.3 Beam Patterns

The effective BS TX beam pattern for the k-th downlink user can be expressed as

$$\mathsf{G}^{\mathsf{TX}}_{\mathsf{BS},k,n}(\theta) = |\mathbf{a}_{\mathsf{TX},n}(\theta)^{*}\mathbf{F}^{\mathsf{RF}}_{\mathsf{BS},n}\mathbf{f}^{\mathsf{BB}}_{\mathsf{BS},k,n}|^2. \tag{5.5}$$

where $\mathbf{a}_{\mathsf{TX},n}(\theta)$ is the array response given by

$$\mathbf{a}_{\mathsf{TX},n}(\theta) = \left[1, \mathsf{e}^{i\Phi_n(\theta)}, \ldots, \mathsf{e}^{i(N_{\mathsf{TX}-1})\Phi_n(\theta)}\right]^T, \tag{5.6}$$

where N_{TX} is the number of antennas, $\Phi_n(\theta) = 2\pi\frac{d_{\mathsf{ant}}}{\lambda_n}\sin(\theta)$, d_{ant} is the antenna elements separation and λ_n is the wavelength of the subcarrier n.

Similarly, we express the BS RX beam pattern for the ℓ-th RX RF chain as

$$\mathsf{G}^{\mathsf{RX}}_{\mathsf{BS},\ell,n}(\theta) = |\mathbf{w}^{\mathsf{RF}*}_{\mathsf{BS},\ell}\mathbf{a}_{\mathsf{RX},\ell,n}(\theta)|^2, \tag{5.7}$$

where $\mathbf{w}^{\mathsf{RF}}_{\mathsf{BS},\ell} \in \mathbb{C}^{(N^{\mathsf{RX}}_{\mathsf{BS}}/L_{\mathsf{RX}})\times 1}$ and $\mathbf{a}_{\mathsf{RX},\ell,n}(\theta) \in \mathbb{C}^{(N^{\mathsf{RX}}_{\mathsf{BS}}/L_{\mathsf{RX}})\times 1}$ with $\ell = 1, \ldots, L_{\mathsf{RX}}$, respectively. According to the partially-connected structure of the BS in Fig. 5.1, wherein each RF chain is connected to a subarray of antennas, the analog beamformer (precoder/combiner) at the ℓ-th RF chain has the following structure

$$\mathbf{W}^{\mathsf{RF}} = \begin{bmatrix} \mathbf{w}^{\mathsf{RF}}_1 & \mathbf{0} & \ldots & \mathbf{0} \\ \mathbf{0} & \mathbf{w}^{\mathsf{RF}}_2 & \mathbf{0} & \vdots \\ \vdots & \mathbf{0} & \ddots & \mathbf{0} \\ \mathbf{0} & \ldots & \mathbf{0} & \mathbf{w}^{\mathsf{RF}}_L \end{bmatrix}, \tag{5.8}$$

where $\mathbf{0}$ is the zero vector and L is the number of RF chains.

5.3 All-Digital Beamforming

As a foundational basis for the hybrid A/D design, which will be elucidated in the next Section, and to serve as a performance benchmark, we introduce an all-digital beamforming design approach for both precoder and combiner ($\mathbf{F}_{\mathsf{BS},n}, \mathbf{W}_{\mathsf{BS},n}$) at the BS. This design assumes one RF chain as well as a data converter per antenna, in

order to transform all processing to purely baseband without any hardware-imposed limitations. Note that even in this case, i.e., without constraints on $(\mathbf{F}_{\mathsf{BS},n}, \mathbf{W}_{\mathsf{BS},n})$ beyond being semi-unitary, maximizing the sum spectral efficiency is a non-convex problem and hence no closed-form solution can be found. Equivalently, the beamformers have to be jointly deigned in order to maximize the received power and suppress the interference. Accordingly, the uplink (downlink) SINR for the u-th user (k-th user), respectively, for subcarrier n are expressed by (5.9) and (5.10), respectively.

$$\mathsf{sinr}_{u,n} = \frac{\mathsf{snr}_{u,n}|\mathbf{w}^{*}_{\mathsf{BS},u,n}\mathbf{H}_{u,n}\mathbf{f}_{u,n}|^2}{\sum\limits_{\mathsf{u}\neq u}^{U-1} \mathsf{snr}_{\mathsf{u},n}|\mathbf{w}^{*}_{\mathsf{BS},u,n}\mathbf{H}_{\mathsf{u},n}\mathbf{f}_{\mathsf{u},n}|^2 + \mathsf{inr}_n \mathbf{w}^{*}_{\mathsf{BS},u,n}\mathbf{H}_{\mathsf{SI},n}\mathbf{F}_{\mathsf{BS},n}\mathbf{F}^{*}_{\mathsf{BS},n}\mathbf{H}^{*}_{\mathsf{SI},n}\mathbf{w}_{\mathsf{BS},u,n} + 1} \tag{5.9}$$

$$\mathsf{sinr}_{k,n} = \frac{\mathsf{snr}_{k,n}|\mathbf{w}^{*}_{k,n}\mathbf{H}_{k,n}\mathbf{f}_{\mathsf{BS},k,n}|^2}{\sum\limits_{\mathsf{k}\neq k}^{K-1} \mathsf{snr}_{\mathsf{k},n}|\mathbf{w}^{*}_{k,n}\mathbf{H}_{\mathsf{k},n}\mathbf{f}_{\mathsf{BS},\mathsf{k},n}|^2 + \sum\limits_{\mathsf{u}=0}^{U-1} \mathsf{snr}_{\mathsf{u},n}|\mathbf{w}^{*}_{k,n}\mathbf{H}_{k,\mathsf{u},n}\mathbf{f}_{\mathsf{u},n}|^2 + 1} \tag{5.10}$$

Note that $\mathsf{snr}_{u,n}$ and inr_n are the SNR of the u-th user and the INR, respectively, across the subcarrier n. Equivalently, the sum uplink and downlink spectral efficiency at the subcarrier n for all the users is given by

$$\mathcal{I}_n^{\mathsf{sum}} = \sum_{u=0}^{U-1} \log\left(1 + \mathsf{sinr}_{u,n}\right) + \sum_{k=0}^{K-1} \log\left(1 + \mathsf{sinr}_{k,n}\right) \tag{5.11}$$

In other terms, maximizing the sum spectral efficiency is equivalent to simultaneously maximizing the received power and minimizing the interference, i.e., the designed beamformers have to sharply steer the power towards the desired receiver and assign nulls towards the interference directions. Accordingly, the optimization

problem can be formulated as

$$\begin{aligned}
\underset{\substack{\mathbf{W}_{\mathsf{BS},n},\mathbf{W}_n \\ \mathbf{F}_{\mathsf{BS},n},\mathbf{F}_n}}{\text{maximize}} \quad & \mathcal{J}_n^{\mathsf{sum}} && (5.12a)\\
\text{subject to} \quad & \mathbf{F}_{\mathsf{BS},n}^{*}\mathbf{F}_{\mathsf{BS},n} = \mathbf{I}_K && (5.12b)\\
& \mathbf{W}_{\mathsf{BS},n}^{*}\mathbf{W}_{\mathsf{BS},n} = \mathbf{I}_U && (5.12c)\\
& \|\mathbf{w}_{k,n}\|^2 = \|\mathbf{f}_{u,n}\|^2 = 1, \forall k, u && (5.12d)\\
& \mathbf{W}_{\mathsf{BS},n}^{*}\mathbf{H}_{\mathsf{SI},n}\mathbf{F}_{\mathsf{BS},n} = \mathbf{0} && (5.12e)\\
& \mathbf{w}_{\mathsf{BS},u,n}^{*}\mathbf{H}_{\mathsf{u},n}\mathbf{f}_{\mathsf{u},n} = 0, \forall u \neq \mathsf{u} && (5.12f)\\
& \mathbf{w}_{k,n}^{*}\mathbf{H}_{\mathsf{k},n}\mathbf{f}_{\mathsf{BS,k},n} = 0, \forall k \neq \mathsf{k} && (5.12g)\\
& \mathbf{w}_{k,n}^{*}\mathbf{H}_{k,\mathsf{u},n}\mathbf{f}_{\mathsf{u},n} = 0, \forall \mathsf{u}, k && (5.12h)
\end{aligned}$$

where $\mathbf{W}_{\mathsf{BS},n} = [\mathbf{w}_{\mathsf{BS},u,n}]_{u=0}^{U-1}$, $\mathbf{F}_{\mathsf{BS},n} = [\mathbf{f}_{\mathsf{BS},k,n}]_{k=0}^{K-1}$, $\mathbf{W}_n = [\mathbf{w}_{k,n}]_{k=0}^{K-1}$ and $\mathbf{F}_n = [\mathbf{f}_{u,n}]_{u=0}^{U-1}$. Note that problem (5.12a) is hard to solve since the variables are coupled in the constraints 5.12e, 5.12f, 5.12g and 5.12h. Note that if we fix the precoders $\mathbf{F}_{\mathsf{BS},n}$ and $\mathbf{F}_n$, we can maximize the sum spectral efficiency with respect to $\mathbf{W}_{\mathsf{BS},n}$ and $\mathbf{W}_n$. This leads to the maximization routine to solve problem 5.12a

- Given $\mathbf{F}_{\mathsf{BS},n}$ and $\mathbf{F}_n$ solve

$$\begin{aligned}
\underset{\mathbf{W}_{\mathsf{BS},n},\mathbf{W}_n}{\text{maximize}} \quad & \mathcal{J}_n^{\mathsf{sum}} && (5.13a)\\
\text{subject to} \quad & \mathbf{W}_{\mathsf{BS},n}^{*}\mathbf{W}_{\mathsf{BS},n} = \mathbf{I}_U && (5.13b)\\
& \|\mathbf{w}_{k,n}\|^2 = 1, \forall k && (5.13c)\\
& \mathbf{W}_{\mathsf{BS},n}^{*}\mathbf{H}_{\mathsf{SI},n}\mathbf{F}_{\mathsf{BS},n} = \mathbf{0} && (5.13d)\\
& \mathbf{w}_{\mathsf{BS},u,n}^{*}\mathbf{H}_{\mathsf{u},n}\mathbf{f}_{\mathsf{u},n} = 0, \forall u \neq \mathsf{u} && (5.13e)\\
& \mathbf{w}_{k,n}^{*}\mathbf{H}_{\mathsf{k},n}\mathbf{f}_{\mathsf{BS,k},n} = 0, \forall k \neq \mathsf{k} && (5.13f)\\
& \mathbf{w}_{k,n}^{*}\mathbf{H}_{k,\mathsf{u},n}\mathbf{f}_{\mathsf{u},n} = 0, \forall \mathsf{u}, k && (5.13g)
\end{aligned}$$

- Given $\mathbf{W}_{\mathsf{BS},n}$ and $\mathbf{W}_n$ solve

$$\begin{aligned}
\underset{\mathbf{F}_{\mathsf{BS},n},\mathbf{F}_n}{\text{maximize}} \quad & \mathcal{J}_n^{\mathsf{sum}} && \text{(5.14a)}\\
\text{subject to} \quad & \mathbf{F}_{\mathsf{BS},n}^{*}\mathbf{F}_{\mathsf{BS},n} = \mathbf{I}_K && \text{(5.14b)}\\
& \|\mathbf{f}_{u,n}\|^2 = 1, \forall u && \text{(5.14c)}\\
& \mathbf{F}_{\mathsf{BS},n}^{*}\mathbf{H}_{\mathsf{SI},n}^{*}\mathbf{W}_{\mathsf{BS},n} = \mathbf{0} && \text{(5.14d)}\\
& \mathbf{f}_{\mathsf{BS},k,n}^{*}\mathbf{H}_{\mathsf{k},n}^{*}\mathbf{w}_{\mathsf{k},n} = 0, \forall \mathsf{k} \neq k && \text{(5.14e)}\\
& \mathbf{f}_{u,n}^{*}\mathbf{H}_{k,u,n}^{*}\mathbf{w}_{k,n} = 0, \forall u, k && \text{(5.14f)}
\end{aligned}$$

These stages are iterated until obtaining the convergence. Note that the subproblems 5.13a and 5.14a exhibit the same generic structure

$$\begin{aligned}
\underset{\mathbf{X}_n}{\text{maximize}} \quad & \log\det\left(\mathbf{I}_N + \rho_n \mathbf{X}_n^{*}\mathbf{A}_n\mathbf{A}_n^{*}\mathbf{X}_n\right) && \text{(5.15a)}\\
\text{subject to} \quad & \mathbf{X}_n^{*}\mathbf{X}_n = \mathbf{I}_N && \text{(5.15b)}\\
& \mathbf{X}_n^{*}\mathbf{C}_n = \mathbf{0} && \text{(5.15c)}
\end{aligned}$$

where ρ_n is the SNR, ζ_n is the INR, $\mathbf{X}_n \in \mathbb{C}^{M\times N}$ is the variable to be solved, $\mathbf{A}_n \in \mathbb{C}^{M\times N}$ is the beamformed uplink/downlink channel and $\mathbf{C}_n \in \mathbb{C}^{M\times P}$ is the beamformed interference channel. Note that M is the number of antennas, N is the signal of interest dimension and P is the interfering signal dimension. To solve the generic problem 5.15a, There are some DoF M, N and P that have to be satisfied. Accordingly, if $M \geq N + P$, i.e., the number of antennas is large enough to support N spatial streams after dedicating P DoF to satisfy the interference suppression constraint (5.15c). However, if $M < N + P$, the problem is not feasible.

Note that in this generic problem, the variable M and N are (in subproblem 5.13a, $M = N_{\mathsf{BS}}^{\mathsf{RX}}, N = U$ when solving $\mathbf{W}_{\mathsf{BS},n}$, $M = N_{\mathsf{UE}}, N = 1$ when solving $\mathbf{W}_n$) and (in subproblem 5.14a, $M = N_{\mathsf{BS}}^{\mathsf{TX}}, N = K$ when solving $\mathbf{F}_{\mathsf{BS},n}$, $M = N_{\mathsf{UE}}, N = 1$ when solving $\mathbf{F}_n$).

Table 5.2: Required Degree of Freedom for the BS and the users.

Degree of Freedom	**Data Streams**	**Interference**		
		SI	**UL Streams**	**DL Streams**
$N_{\mathsf{BS}}^{\mathsf{TX}}$	K	U	–	$K-1$
$N_{\mathsf{BS}}^{\mathsf{RX}}$	U	K	$U-1$	–
N_{UE} (DL)	1	–	U	$K-1$
N_{UE} (UL)	1	–	–	K

At the TX side of the BS, the precoder $\mathbf{F}_{\mathsf{BS},n}$ has to transmit K streams and suppress the SI incurred by the U streams (from the BS RX antennas) as well as the interference between the K-streams intended to downlink users (requiring at least $K-1$ DoF to suppress the interference between the K streams, as each stream can interfere with $K-1$ other streams), i.e., the number of BS TX antennas has to satisfy $N_{\mathsf{BS}}^{\mathsf{TX}} \geq 2K+U-1$. At the RX side of the BS, the combiner $\mathbf{W}_{\mathsf{BS},n}$ needs to sustain U uplink streams and suppress the SI incurred by the K downlink streams as well as the uplink multi-stream interference $U-1$. Therefore, the number of BS RX antennas has to satisfy $N_{\mathsf{BS}}^{\mathsf{RX}} \geq 2U+K-1$. At the downlink user, the combiner $\mathbf{w}_{k,n}$ needs to sustain one layer/stream and suppress the interference incurred by $K-1$ downlink streams as well as the U uplink streams, i.e., $N_{\mathsf{UE}} \geq U+K$. At the uplink user, the precoder transmits one stream, and has to null the interference intended to the K downlink users, i.e., $N_{\mathsf{UE}} \geq 1+K$. In practical circumstances, these conditions are generally satisfied when using massive number of antennas at mmWave bands. Details are summarized in Table 5.2.

Remark 9. In the generic problem 5.15a, the cost function (spectral efficiency) is expressed for a system supporting multiple streams N, with a variable $\mathbf{X}_n \in \mathbb{C}^{M\times N}$ and a beamformed channel $\mathbf{A}_n \in \mathbb{C}^{M\times N}$. In our problem, each user supports only a single stream, i.e., $N=1$. Therefore, the variable and the beamformed channel are reduced to vectors $\mathbf{x}_n \in \mathbb{C}^{M\times 1}$ and $\mathbf{a}_n \in \mathbb{C}^{M\times 1}$, respectively, when formulating the solution in the sequel.

Let $\mathbf{N}_{\mathsf{NSP}} \in \mathbb{C}^{M \times M}$ be the null-space projection (NSP) matrix for suppressing the interference and constructing solvable optimization problems in order to maximize the beamformed power according to the constraints. The NSP matrix $\mathbf{N}_{\mathsf{NSP}} = \mathbf{I} - \mathbf{C}_n \mathbf{C}_n^{\dagger}$ spans the null-space of the interference, i.e., any given beamformer projected by this matrix will definitely reject the interference.

For the u-th BS combiner $\mathbf{w}_{\mathsf{BS},u,n}$, the beamformed SI channel is given by

$$\mathbf{C}_{\mathsf{BS},u,n}^{\mathsf{RX}} = \left[\underbrace{\mathbf{H}_{\mathsf{SI},n}\mathbf{F}_{\mathsf{BS},n}}_{K \text{ SI Nulls}}, \underbrace{[\mathbf{H}_{\mathsf{u},n}\mathbf{f}_{\mathsf{u},n}]_{\substack{\mathsf{u}=0 \\ \mathsf{u}\neq u}}^{U-1}}_{U-1 \text{ MUI Nulls}} \right] \tag{5.16}$$

The NSP matrix $\mathbf{N}_{\mathsf{NSP}}$ is given by $\mathbf{I} - \mathbf{C}_{\mathsf{BS},u,n}^{\mathsf{RX}} \mathbf{C}_{\mathsf{BS},u,n}^{\mathsf{RX}\dagger}$. To maximize the beamformed power, the u-th BS combiner $\mathbf{w}_{\mathsf{BS},u,n}$ has to be aligned (matched filter) with the uplink beamformed channel ($\mathbf{a}_{u,n} = \mathbf{H}_{u,n}\mathbf{f}_{u,n}$). Therefore, the u-th BS combiner $\mathbf{w}_{\mathsf{BS},u,n}$ is given by

$$\mathbf{w}_{\mathsf{BS},u,n} = \frac{\mathbf{N}_{\mathsf{NSP}}\mathbf{a}_{u,n}}{\|\mathbf{N}_{\mathsf{NSP}}\mathbf{a}_{u,n}\|} \tag{5.17}$$

In a similar way, the beamformed interference channels for the u-th BS precoder $\mathbf{f}_{\mathsf{BS},k,n}$, the k-th downlink user and the u-th uplink user are, respectively, given by

$$\mathbf{C}_{\mathsf{BS},k,n}^{\mathsf{TX}} = \left[\underbrace{\mathbf{H}_{\mathsf{SI},n}^{*}\mathbf{W}_{\mathsf{BS},n}}_{U \text{ SI Nulls}}, \underbrace{\left[\mathbf{H}_{\mathsf{k},n}^{*}\mathbf{w}_{\mathsf{k},n}\right]_{\substack{\mathsf{k}=0 \\ \mathsf{k}\neq k}}^{K-1}}_{K-1 \text{ MUI Nulls}} \right] \tag{5.18}$$

$$\mathbf{C}_{\mathsf{UE},k,n}^{\mathsf{RX}} = \left[\underbrace{[\mathbf{H}_{k,\mathsf{u},n}\mathbf{f}_{\mathsf{u},n}]_{\mathsf{u}=0}^{U-1}}_{U \text{ IUI Nulls}}, \underbrace{[\mathbf{H}_{\mathsf{k},n}\mathbf{f}_{\mathsf{BS},\mathsf{k},n}]_{\substack{\mathsf{k}=0 \\ \mathsf{k}\neq k}}^{K-1}}_{K-1 \text{ MUI Nulls}} \right] \tag{5.19}$$

$$\mathbf{C}_{\mathsf{UE},u,n}^{\mathsf{TX}} = \underbrace{\left[\left[\mathbf{H}_{\mathsf{k},u,n}^{*}\mathbf{w}_{\mathsf{k},n}\right]_{\mathsf{k}=0}^{K-1}\right]}_{K \text{ IUI Nulls}} \tag{5.20}$$

Details on designing the all-digital beamformers are given by Algorithm 5.

Algorithm 5 All-Digital Beamforming Design

Function AllDigital($\mathbf{C}_n, \mathbf{a}_n$)
Construct the NSP matrix $\mathbf{N}_{\mathsf{NSP}} \leftarrow \mathbf{I} - \mathbf{C}_n\mathbf{C}_n^{\dagger}$
$\mathbf{X}_n \leftarrow \mathbf{N}_{\mathsf{NSP}}\mathbf{a}_n$
Normalize $\mathbf{X}_n \leftarrow \frac{\mathbf{X}_n}{\|\mathbf{X}_n\|}$
return $\mathbf{X}_n$
End Function

Initialize $\mathbf{F}_{\mathsf{BS},n} = [\mathbf{f}_{\mathsf{BS},k,n}]_{k=0}^{K-1}$ and $\mathbf{F}_n = [\mathbf{f}_{u,n}]_{u=0}^{U-1}$
repeat
  $\mathbf{w}_{\mathsf{BS},u,n} \leftarrow$ AllDigital$(\mathbf{C}^{\mathsf{RX}}_{\mathsf{BS},u,n}, \mathbf{H}_{u,n}\mathbf{f}_{u,n})$ $\forall u$
  $\mathbf{w}_{k,n} \leftarrow$ AllDigital$(\mathbf{C}^{\mathsf{RX}}_{\mathsf{UE},k,n}, \mathbf{H}_{k,n}\mathbf{f}_{\mathsf{BS},k,n})$ $\forall k$
  $\mathbf{f}_{\mathsf{BS},k,n} \leftarrow$ AllDigital$(\mathbf{C}^{\mathsf{TX}}_{\mathsf{BS},k,n}, \mathbf{H}^{*}_{k,n}\mathbf{w}_{k,n})$ $\forall k$
  $\mathbf{f}_{u,n} \leftarrow$ AllDigital$(\mathbf{C}^{\mathsf{TX}}_{\mathsf{UE},u,n}, \mathbf{H}^{*}_{u,n}\mathbf{w}_{\mathsf{BS},u,n})$ $\forall u$
until Convergence
return $\mathbf{W}_{\mathsf{BS},n}, \mathbf{F}_{\mathsf{BS},n}, \mathbf{W}_n, \mathbf{F}_n$

Now we proceed with the complexity analysis; with $K, U << N_{\mathsf{UE}}, N^{\mathsf{RX}}_{\mathsf{BS}}, N^{\mathsf{RX}}_{\mathsf{BS}}$, the cost of $\mathbf{w}_{\mathsf{BS},u,n}$ is dominated by the computation of $\mathbf{C}^{\mathsf{RX}}_{\mathsf{BS},u,n}$ and the NSP matrices. Therefore, the overall complexity to compute $\mathbf{w}_{\mathsf{BS},u,n}$ is $\mathcal{O}\left((K+U-1)\left(N^{\mathsf{RX}}_{\mathsf{BS}}\right)^2 + \left(N^{\mathsf{RX}}_{\mathsf{BS}}\right)^2\right)$. Since K, U are much smaller than $N^{\mathsf{RX}}_{\mathsf{BS}}$, the dominant term becomes $\mathcal{O}\left(\left(N^{\mathsf{RX}}_{\mathsf{BS}}\right)^2\right)$. In a similar case, the complexity of $\mathbf{f}_{\mathsf{BS},k,n}$ is dominated by $\mathcal{O}\left(\left(N^{\mathsf{TX}}_{\mathsf{BS}}\right)^2\right)$ while the cost of $\mathbf{w}_{k,n}$ and $\mathbf{f}_{u,n}$ is $\mathcal{O}\left(\left(N_{\mathsf{UE}}\right)^2\right)$.

5.4 MU-MIMO Hybrid Analog/Digital Beamforming at the Base Station

Throughout this work, we assumed that the users are implemented in all-digital architecture, while in this Section, we adopt the hybrid A/D architecture at the BS. In the sequel, we tackle the problem of designing and optimizing the hybrid A/D beamformers at the BS in order to maximize the beamformed power and suppress the interference to avoid the ADC saturation. Unlike the all-digital case, the analog beamformers are implemented using finite-resolution phased array, i.e., their entries

are conditioned upon having CAQP constraint is considered in the design. Given that the SI is the most detrimental signal compared to the IUI, we leverage the NSP method to design the analog beamformers so that to achieve a large SI reduction at the output of the RF combiner at the BS. While the baseband beamformers at the BS are designed to suppress the IUI as well as maximizing the beamformed power. Note that the digital beamformers are designed for each subcarrier, however, the analog beamformers are common for all the subcarriers.

5.4.1 Hybrid Combiner Design

5.4.1.1 Analog Combiner

The analog BS combiner is designed to suppress the SI power at its output. According to the system model 5.4), the effective interference channel between the TX streams and the RX RF chains can be given by

$$\mathbf{C}_{\mathsf{SI},n} = \mathbf{W}_{\mathsf{BS}}^{\mathsf{RF}*}\mathbf{H}_{\mathsf{SI},n}\mathbf{F}_{\mathsf{BS}}^{\mathsf{RF}}\mathbf{F}_{\mathsf{BS},n}^{\mathsf{BB}}, \tag{5.21}$$

with $\mathbf{C}_{\mathsf{SI},n} \in \mathbb{C}^{L_{\mathsf{RX}}\times K}$. In particular, the matrix elements $c_{\mathsf{SI},\ell,k,n} = [\mathbf{C}_{\mathsf{SI},n}]_{\ell,k}$ with $\ell = 1,\ldots,L_{\mathsf{RX}}$ and $k = 0,\ldots,K-1$, represents the effective SI channel between the k-th downlink user and the ℓ-th RX RF chain at subcarrier n. To reject the SI in the ℓ-th RX RF chain, the analog combiner $\mathbf{w}_{\mathsf{BS},\ell}^{\mathsf{RF}}$ should satisfy the following condition

$$\mathbf{c}_{\mathsf{SI},\ell,n} = \mathbf{w}_{\mathsf{BS},\ell}^{\mathsf{RF}*}\mathbf{H}_{\mathsf{SI},n}^{(\ell,:)}\mathbf{F}_{\mathsf{BS}}^{\mathsf{RF}}\mathbf{F}_{\mathsf{BS},n}^{\mathsf{BB}} = \mathbf{0}^T, \tag{5.22}$$

where $\mathbf{H}_{\mathsf{SI},n}^{(\ell,:)} \in \mathbb{C}^{\left(N_{\mathsf{BS}}^{\mathsf{RX}}/L_{\mathsf{RX}}\right)\times N_{\mathsf{BS}}^{\mathsf{TX}}}$, $\mathbf{w}_{\mathsf{BS},\ell}^{\mathsf{RF}}$ is the ℓ-th column of $\mathbf{W}_{\mathsf{BS}}^{\mathsf{RF}}$, and $\mathbf{c}_{\mathsf{SI},\ell,n} \in \mathbb{C}^{1\times K}$ is the ℓ-th row of the matrix (5.21). While the condition 5.22 is expressed for a given subcarrier n, we can extend this condition to support $\mathcal{N}_{\mathsf{freq}}$ subcarriers across the whole transmission bandwidth to suppress the wideband SI signal. It can be expressed as

$$\begin{aligned}\mathbf{w}_{\mathsf{BS},\ell}^{\mathsf{RF}*}&\underbrace{\left[\mathbf{H}_{\mathsf{SI},n_1}^{(\ell,:)}\mathbf{F}_{\mathsf{BS}}^{\mathsf{RF}}\mathbf{F}_{\mathsf{BS},n_1}^{\mathsf{BB}},\ldots,\mathbf{H}_{\mathsf{SI},n_{\mathcal{N}_{\mathsf{freq}}}}^{(\ell,:)}\mathbf{F}_{\mathsf{BS}}^{\mathsf{RF}}\mathbf{F}_{\mathsf{BS},n_{\mathcal{N}_{\mathsf{freq}}}}^{\mathsf{BB}}\right]}_{\mathbf{B}_\ell}\\ &= \mathbf{w}_{\mathsf{BS},\ell}^{\mathsf{RF}*}\mathbf{B}_\ell = \mathbf{0}^T,\end{aligned} \tag{5.23}$$

where $n_1, \ldots, n_{\mathcal{N}_{\mathsf{freq}}}$ are the indices of the subcarriers for which the NSP method is applied.

The goal of designing the ℓ-th RF combiner $\mathbf{w}_{\mathsf{BS},\ell}^{\mathsf{RF}}$ is to minimize the gain of the SI channel at the ℓ-th RX RF chain. Accordingly, the optimization problem can be stated as

$$\underset{\mathbf{w}_{\mathsf{BS},\ell}^{\mathsf{RF}}}{\text{minimize}} \quad \|\mathbf{w}_{\mathsf{BS},\ell}^{\mathsf{RF}*}\mathbf{B}_\ell\|_F^2 \tag{5.24a}$$

$$\text{subject to} \quad \mathbf{w}_{\mathsf{BS},\ell}^{\mathsf{RF}} \in \mathbb{V}_{b_r}^{\left(N_{\mathsf{BS}}^{\mathsf{RX}}/L_{\mathsf{RX}}\right)\times 1}, \ \ell = 1, \ldots, L_{\mathsf{RX}} \tag{5.24b}$$

Note that due to the unit modulus constraint, the problem (5.24a) is not convex and therefore no closed-form solution can be derived. Instead, we will refer to an iterative method to solve (5.24a). Similar to the all-digital design, the NSP matrix can be derived from (5.23) based on the Moore-Penrose pseudoinverse method ($\mathbf{B}_\ell \mathbf{B}_\ell^\dagger \mathbf{B}_\ell = \mathbf{B}_\ell$) as

$$\mathbf{N}_{\mathsf{SI},\ell}^{\mathsf{RX}} = \mathbf{I} - \mathbf{B}_\ell \mathbf{B}_\ell^\dagger. \tag{5.25}$$

To minimize the cost function (5.24a), the RF combiner has to be projected on the SI null-space using the NSP matrix $\mathbf{N}_{\mathsf{SI},\ell}$. However, the CAQP constraint (5.24b) violates the NSP concept, thus, the SI is re-introduced resulting in a severe degradation of the system performance. To circumvent this shortcoming, we refer to the *alternating projections* method to handle the CAQP constraint without violating the SI minimization cycle. To seek for the optimal space wherein the best RF combiner lies, we propose an iterative routine to alternate the projections between the CAQP space and the SI null-space. The convergence is obtained when the losses incurred by the CAQP are minimized and the RF combiner entries are unchanged. Finally, we define the average SI suppressed, between the DL k-th stream and ℓ-th RX RF chain, among the overall transmission bandwidth with a total of N_{sc} subcarriers as

$$\overline{c}_{\mathsf{SI},\ell,k} = \frac{1}{N_{\mathsf{sc}}} \sum_{n=0}^{N_{\mathsf{sc}}-1} |c_{\mathsf{SI},\ell,k,n}|^2, \tag{5.26}$$

We further define the per-user effective spectral efficiency, i.e., averaged over the total transmission bandwidth as well as for U users with $\mathsf{sinr}_{0,n}, \ldots, \mathsf{sinr}_{U-1,n}$ at subcarrier n, as

$$\overline{\mathcal{I}} = \frac{1}{N_{\mathsf{sc}} U} \sum_{n=0}^{N_{\mathsf{sc}}-1} \sum_{u=0}^{U-1} \log\left(1 + \mathsf{sinr}_{u,n}\right) \tag{5.27}$$

5.4.1.2 Baseband Combiner

The baseband combiner is designed so that it simultaneously maximizes the receive beamforming gain and suppresses the residual SI and IUI. Similar to the all-digital design, we leverage the NSP method to construct the baseband combiner. Accordingly, the NSP condition for the uplink user u at subcarrier n can be written as

$$\begin{aligned} \mathbf{w}_{\mathsf{BS},u,n}^{\mathsf{BB}*} \underbrace{\left[\underbrace{\mathbf{W}_{\mathsf{BS}}^{\mathsf{RF}*} \mathbf{H}_{\mathsf{SI},n} \mathbf{F}_{\mathsf{BS}}^{\mathsf{RF}} \mathbf{F}_{\mathsf{BS},n}^{\mathsf{BB}}}_{K \text{ Residual SI Nulls}}, \underbrace{\left[\mathbf{W}_{\mathsf{BS}}^{\mathsf{RF}*} \mathbf{H}_{\mathsf{u},n} \mathbf{f}_{\mathsf{u},n}\right]_{\substack{\mathsf{u}=0 \\ \mathsf{u}\neq u}}^{U-1}}_{U-1 \text{ MUI Nulls}} \right]}_{\mathbf{D}_{u,n}} \\ = \mathbf{w}_{\mathsf{BS},u,n}^{\mathsf{BB}*} \mathbf{D}_{u,n} = \mathbf{0}^T, \end{aligned} \tag{5.28}$$

Subsequently, the optimization problem of the baseband combiner can be stated as

$$\underset{\mathbf{w}_{\mathsf{BS},u,n}^{\mathsf{BB}}}{\text{maximize}} \quad |\mathbf{w}_{\mathsf{BS},u,n}^{\mathsf{BB}*} \mathbf{W}_{\mathsf{BS}}^{\mathsf{RF}*} \mathbf{H}_{u,n} \mathbf{f}_{u,n}|^2 \tag{5.29a}$$

$$\text{subject to} \quad \|\mathbf{W}_{\mathsf{BS}}^{\mathsf{RF}} \mathbf{w}_{\mathsf{BS},u,n}^{\mathsf{BB}}\| = 1, \forall u, \tag{5.29b}$$

$$\mathbf{w}_{\mathsf{BS},u,n}^{\mathsf{BB}*} \mathbf{D}_{u,n} = \mathbf{0}^T, \ \forall u. \tag{5.29c}$$

To maximize the cost function (5.29a), a matched-filter solution can be adopted as

$$\tilde{\mathbf{w}}_{\mathsf{BS},u,n}^{\mathsf{BB}} = \mathbf{W}_{\mathsf{BS}}^{\mathsf{RF}*} \mathbf{H}_{u,n} \mathbf{f}_{u,n}, \forall u \tag{5.30}$$

Then, the corresponding NSP matrix for the UL user u and subcarrier n can be derived by

$$\mathbf{N}_{\mathsf{BB},u,n}^{\mathsf{RX}} = \mathbf{I} - \mathbf{D}_{u,n}\mathbf{D}_{u,n}^{\dagger}. \tag{5.31}$$

Therefore, the baseband combiner solution is expressed by

$$\mathbf{w}_{\mathsf{BS},u,n}^{\mathsf{BB}} = \mathbf{N}_{\mathsf{BB},u,n}^{\mathsf{RX}}\tilde{\mathbf{w}}_{\mathsf{BS},u,n}^{\mathsf{BB}}. \tag{5.32}$$

Note that the baseband combiner $\mathbf{w}_{\mathsf{BS},u,n}^{\mathsf{BB}}$ (5.32) needs to be normalized so that the constraint (5.29b) is satisfied.

5.4.2 Hybrid Precoder Design

Building on the signal model (5.4), the effective SI channel at subcarrier n between the TX and RX streams at the FD BS can be first expressed as

$$\mathbf{S}_{\mathsf{SI},n} = \mathbf{W}_{\mathsf{BS},n}^{\mathsf{BB}*}\mathbf{W}_{\mathsf{BS}}^{\mathsf{RF}*}\mathbf{H}_{\mathsf{SI},n}\mathbf{F}_{\mathsf{BS}}^{\mathsf{RF}}\mathbf{F}_{\mathsf{BS},n}^{\mathsf{BB}}, \tag{5.33}$$

The main purpose to design the analog precoder $\mathbf{F}_{\mathsf{BS}}^{\mathsf{RF}}$ is to minimize the SI power at the RF combiner, before the ADC, while the baseband precoder $\mathbf{F}_{\mathsf{BS},n}^{\mathsf{BB}}$ is designed to suppress the residual SI and IUI, and maximize the TX beamforming gain.

5.4.2.1 Analog Precoder

Based on the signal model (5.4), the effective SI channel between the TX RF chains to the RX RF chains is expressed by

$$\mathbf{P}_{\mathsf{SI},n} = \mathbf{F}_{\mathsf{BS}}^{\mathsf{RF}*}\mathbf{H}_{\mathsf{SI},n}^{*}\mathbf{W}_{\mathsf{BS}}^{\mathsf{RF}}\mathbf{W}_{\mathsf{BS},n}^{\mathsf{BB}}, \tag{5.34}$$

where $\mathbf{P}_{\mathsf{SI},n} \in \mathbb{C}^{L_{\mathsf{TX}} \times U}$. Specifically, the elements $[\mathbf{C}_{\mathsf{SI},n}]_{u,\ell}$ with $u = 0, \ldots, U-1$ and $\ell = 1, \ldots, L_{\mathsf{TX}}$ represents the effective SI channel between the ℓ-th TX RF chain and u-th UL stream. To suppress the SI between the ℓ-th TX RF chain and the UL streams, the analog precoder should satisfy the following condition

$$\mathbf{p}_{\mathsf{SI},\ell,n} = \mathbf{f}_{\mathsf{BS},\ell}^{\mathsf{RF}*}\mathbf{H}_{\mathsf{SI},n}^{(:,\ell)*}\mathbf{W}_{\mathsf{BS}}^{\mathsf{RF}}\mathbf{W}_{\mathsf{BS},n}^{\mathsf{BB}} = \mathbf{0}^{T}, \tag{5.35}$$

where $\mathbf{H}_{\mathsf{SI},n}^{(:,\ell)} \in \mathbb{C}^{N_{\mathsf{BS}}^{\mathsf{RX}} \times \left(N_{\mathsf{BS}}^{\mathsf{TX}}/L_{\mathsf{TX}}\right)}$, $\mathbf{f}_{\mathsf{BS},\ell}^{\mathsf{RF}}$ is the ℓ-th column of $\mathbf{F}_{\mathsf{BS}}^{\mathsf{RF}}$, and $\mathbf{p}_{\mathsf{SI},\ell,n} \in \mathbb{C}^{1\times U}$ is the ℓ-th row of the matrix (5.34). While the condition (5.35) is expressed for a given subcarrier n, we can extend this condition to support $\mathcal{N}_{\mathsf{freq}}$ subcarriers across the whole transmission bandwidth to suppress the wideband SI signal. It can be expressed as

$$\begin{aligned}\mathbf{f}_{\mathsf{BS},\ell}^{\mathsf{RF}*} \underbrace{\left[\mathbf{H}_{\mathsf{SI},n_1}^{(:,\ell)*}\mathbf{W}_{\mathsf{BS}}^{\mathsf{RF}}\mathbf{W}_{\mathsf{BS},n_1}^{\mathsf{BB}}, \ldots, \mathbf{H}_{\mathsf{SI},n_{\mathcal{N}_{\mathsf{freq}}}}^{(:,\ell)*}\mathbf{W}_{\mathsf{BS}}^{\mathsf{RF}}\mathbf{W}_{\mathsf{BS},n_{\mathcal{N}_{\mathsf{freq}}}}^{\mathsf{BB}}\right]}_{\mathbf{A}_\ell} \\ = \mathbf{f}_{\mathsf{BS},\ell}^{\mathsf{RF}*}\mathbf{A}_\ell = \mathbf{0}^T,\end{aligned} \tag{5.36}$$

The goal of designing the ℓ-th RF precoder $\mathbf{f}_{\mathsf{BS},\ell}^{\mathsf{RF}}$ is to minimize the gain of the SI channel. Accordingly, the optimization problem can be stated as

$$\underset{\mathbf{f}_{\mathsf{BS},\ell}^{\mathsf{RF}}}{\text{minimize}} \quad \|\mathbf{f}_{\mathsf{BS},\ell}^{\mathsf{RF}*}\mathbf{A}_\ell\|_F^2 \tag{5.37a}$$

$$\text{subject to} \quad \mathbf{f}_{\mathsf{BS},\ell}^{\mathsf{RF}} \in \mathbb{V}_{b_t}^{\left(N_{\mathsf{BS}}^{\mathsf{TX}}/L_{\mathsf{TX}}\right)\times 1},\ \ell = 1, \ldots, L_{\mathsf{TX}} \tag{5.37b}$$

This problem is also not convex due to the CAQP constraint (5.37b), and therefore the closed-form solution is not available. Similar to the analog combiner, the NSP matrix can be derived from (5.36) and it is given by

$$\mathbf{N}_{\mathsf{SI},\ell}^{\mathsf{TX}} = \mathbf{I} - \mathbf{A}_\ell\mathbf{A}_\ell^\dagger. \tag{5.38}$$

To minimize the gain of the effective SI channel, the analog precoder $\mathbf{f}_{\mathsf{BS},\ell}^{\mathsf{RF}}$ needs to be projected on the NSP matrix $\mathbf{N}_{\mathsf{SI},\ell}^{\mathsf{TX}}$. As arguing for the analog combiner, the CAQP constraint violates the NSP concept and hence the interference is re-injected which limits the system performance. In order to minimize the losses incurred by the CAQP constraint, we proceed with alternating projections. Details will be given by Algorithm 6.

Remark 10. Note that the analog precoder and combiner at the BS are coupled. Therefore, we will proceed with an *alternating optimization* approach. In other terms, we can fix the analog precoder and solve for the analog combiner and vice versa. Consequently, an iterative routine is required to obtain the convergence.

5.4.2.2 Baseband Precoder

The main objective to design the baseband precoder is to maximize the transmit beamforming gain and suppress the residual SI as well as the MUI between the DL users, i.e., the effective TX response at the other users' directions $\mathsf{G}^{\mathsf{TX}}_{\mathsf{BS},k,n}(\theta_{\mathsf{k}}) \approx 0$ with $\mathsf{k} \neq k$. Accordingly, the NSP condition for the downlink user k at subcarrier n can be written as

$$\begin{aligned}\mathbf{f}^{*}_{\mathsf{BS},k,n} \underbrace{\left[\underbrace{\mathbf{F}^{\mathsf{RF}*}_{\mathsf{BS}}\mathbf{H}^{*}_{\mathsf{SI},n}\mathbf{W}^{\mathsf{RF}}_{\mathsf{BS}}\mathbf{W}^{\mathsf{BB}}_{\mathsf{BS},n}}_{K \text{ Residual SI Nulls}}, \underbrace{\left[\mathbf{F}^{\mathsf{RF}*}_{\mathsf{BS}}\mathbf{H}^{*}_{\mathsf{k},n}\mathbf{w}_{\mathsf{k},n}\right]^{K-1}_{\substack{\mathsf{k}=0\\ \mathsf{k}\neq k}}}_{K-1 \text{ MUI Nulls}}\right]}_{\mathbf{E}_{k,n}} \\ = \mathbf{f}^{*}_{\mathsf{BS},k,n}\mathbf{E}_{k,n} = \mathbf{0}^{T},\end{aligned} \tag{5.39}$$

Maximizing the TX beamforming gain (5.40a) and suppressing the interference (5.40c) can be reformulated as in the following optimization problem

$$\underset{\mathbf{f}^{\mathsf{BB}}_{\mathsf{BS},k,n}}{\text{maximize}} \quad |\mathbf{f}^{\mathsf{BB}*}_{\mathsf{BS},k,n}\mathbf{F}^{\mathsf{RF}*}_{\mathsf{BS}}\mathbf{H}^{*}_{k,n}\mathbf{w}_{k,n}|^{2} \tag{5.40a}$$

$$\text{subject to} \quad \|\mathbf{F}^{\mathsf{RF}}_{\mathsf{BS}}\mathbf{f}^{\mathsf{BB}}_{\mathsf{BS},k,n}\| = 1, \forall k, \tag{5.40b}$$

$$\mathbf{f}^{\mathsf{BB}*}_{\mathsf{BS},k,n}\mathbf{E}_{k,n} = \mathbf{0}^{T}, \ \forall k. \tag{5.40c}$$

The cost function (5.40a) can be maximized using a matched-filter option as

$$\tilde{\mathbf{f}}^{\mathsf{BB}}_{\mathsf{BS},k,n} = \mathbf{F}^{\mathsf{RF}*}_{\mathsf{BS}}\mathbf{H}^{*}_{k,n}\mathbf{w}_{k,n} \tag{5.41}$$

While the NSP matrix can be derived as

$$\mathbf{N}^{\mathsf{RX}}_{\mathsf{BB},k,n} = \mathbf{I} - \mathbf{E}_{k,n}\mathbf{E}^{\dagger}_{k,n} \tag{5.42}$$

Therefore, the baseband precoder solution is given by

$$\mathbf{f}^{\mathsf{BB}}_{\mathsf{BS},k,n} = \mathbf{N}^{\mathsf{RX}}_{\mathsf{BB},k,n}\tilde{\mathbf{f}}^{\mathsf{BB}}_{\mathsf{BS},k,n} \tag{5.43}$$

Then, the baseband precoder (5.43) needs to be normalized to satisfy the constraint (5.40b).

The hybrid precoding and combining design is summarized in Algorithm 6.

Algorithm 6 Hybrid Beamforming Design

Initialize $\mathbf{W}_{\mathsf{BS}}^{\mathsf{RF}}$, $\mathbf{W}_{\mathsf{BS},n}^{\mathsf{BB}}$, $\mathbf{F}_{\mathsf{BS}}^{\mathsf{RF}}$, and $\mathbf{F}_{\mathsf{BS},n}^{\mathsf{BB}}$
{ *Alternating optimization cycle, i.e., fix the precoders and solve for the combiners and vice versa* (**Remark 10**)}
repeat
  Construct the NSP matrix $\mathbf{N}_{\mathsf{SI},\ell}^{\mathsf{RX}}, \forall \ell$ (5.25)
  Set $p = 0$
  { *Alternating projections between NSP and CAQP*}
  repeat
    $\mathbf{w}_{\mathsf{BS},\ell}^{\mathsf{RF}(p+1)} \leftarrow \mathbf{N}_{\mathsf{SI},\ell}^{\mathsf{RX}} \mathbf{w}_{\mathsf{BS},\ell}^{\mathsf{RF}(p)}, \forall \ell$
    $\mathbf{w}_{\mathsf{BS},\ell}^{\mathsf{RF}(p)} \leftarrow \mathsf{e}^{i\mathcal{Q}\left\{\angle \mathbf{w}_{\mathsf{BS},\ell}^{\mathsf{RF}(p+1)}; b_r\right\}}, \forall \ell$
    $p \leftarrow p + 1$
  until *local convergence*
  Construct the NSP matrix $\mathbf{N}_{\mathsf{BB},u,n}^{\mathsf{RX}}, \forall u$ (5.31) from the optimized $\mathbf{W}_{\mathsf{BS}}^{\mathsf{RF}}$
  $\mathbf{w}_{\mathsf{BS},u,n}^{\mathsf{BB}} \leftarrow \mathbf{N}_{\mathsf{BB},u,n}^{\mathsf{RX}} \tilde{\mathbf{w}}_{\mathsf{BS},u,n}^{\mathsf{BB}}, \forall u$
  Construct the NSP matrix $\mathbf{N}_{\mathsf{SI},\ell}^{\mathsf{TX}}, \forall \ell$ (5.38) from the optimized $\mathbf{W}_{\mathsf{BS}}^{\mathsf{RF}}$ and $\mathbf{W}_{\mathsf{BS},n}^{\mathsf{BB}}$
  Set $q = 0$
  { *Alternating projections between NSP and CAQP*}
  repeat
    $\mathbf{f}_{\mathsf{BS},\ell}^{\mathsf{RF}(q+1)} \leftarrow \mathbf{N}_{\mathsf{SI},\ell}^{\mathsf{TX}} \mathbf{f}_{\mathsf{BS},\ell}^{\mathsf{RF}(q)}, \forall \ell$
    $\mathbf{f}_{\mathsf{BS},\ell}^{\mathsf{RF}(q)} \leftarrow \mathsf{e}^{i\mathcal{Q}\left\{\angle \mathbf{f}_{\mathsf{BS},\ell}^{\mathsf{RF}(q+1)}; b_t\right\}}, \forall \ell$
    $q \leftarrow q + 1$
  until *local convergence*
  Construct the NSP matrix $\mathbf{N}_{\mathsf{BB},k,n}^{\mathsf{TX}}, \forall k$ (5.42) from the optimized $\mathbf{F}_{\mathsf{BS}}^{\mathsf{RF}}$, $\mathbf{W}_{\mathsf{BS}}^{\mathsf{RF}}$, and $\mathbf{W}_{\mathsf{BS},n}^{\mathsf{BB}}$
  $\mathbf{f}_{\mathsf{BS},k,n}^{\mathsf{BB}} \leftarrow \mathbf{N}_{\mathsf{BB},k,n}^{\mathsf{TX}} \tilde{\mathbf{f}}_{\mathsf{BS},k,n}^{\mathsf{BB}}, \forall k$
  $\mathbf{F}_{\mathsf{BS},n}^{\mathsf{BB}} \leftarrow \frac{\sqrt{K}}{\|\mathbf{F}_{\mathsf{BS}}^{\mathsf{RF}} \mathbf{F}_{\mathsf{BS},n}^{\mathsf{BB}}\|_F} \mathbf{F}_{\mathsf{BS},n}^{\mathsf{BB}}$
until *global convergence*
return $\mathbf{W}_{\mathsf{BS}}^{\mathsf{RF}}$, $\mathbf{W}_{\mathsf{BS},n}^{\mathsf{BB}}$, $\mathbf{F}_{\mathsf{BS}}^{\mathsf{RF}}$, and $\mathbf{F}_{\mathsf{BS},n}^{\mathsf{BB}}$

With $K, U < L_{\mathsf{RX}}, L_{\mathsf{TX}} << N_{\mathsf{BS}}^{\mathsf{RX}}, N_{\mathsf{BS}}^{\mathsf{TX}}$, the total computational complexity of $\mathbf{w}_{\mathsf{BS},\ell}^{\mathsf{RF}}$ and $\mathbf{f}_{\mathsf{BS},\ell}^{\mathsf{RF}}$ is dominated by $\mathcal{O}\left(N_{\mathsf{inner}}\left(N_{\mathsf{BS}}^{\mathsf{RX}}/L_{\mathsf{RX}}\right)^2\right)$ and $\mathcal{O}\left(N_{\mathsf{inner}}\left(N_{\mathsf{BS}}^{\mathsf{TX}}/L_{\mathsf{TX}}\right)^2\right)$, respectively. While the total cost of $\mathbf{w}_{\mathsf{BS},u,n}^{\mathsf{BB}}$ and $\mathbf{f}_{\mathsf{BS},k,n}^{\mathsf{BB}}$ is dominated by $\mathcal{O}\left(N_{\mathsf{outer}} K^2 \mathcal{N}_{\mathsf{freq}}^3 \left(N_{\mathsf{BS}}^{\mathsf{RX}}/L_{\mathsf{RX}}\right)\right)$

and $\mathcal{O}\left(N_{\mathsf{outer}}U^2\mathcal{N}_{\mathsf{freq}}^3\left(N_{\mathsf{BS}}^{\mathsf{TX}}/L_{\mathsf{TX}}\right)\right)$, respectively.

5.5 Numerical Results

In this section, we evaluate the proposed beamforming techniques for all-digital as well as the hybrid MU-MIMO architectures. We consider linear arrays at BS and users wherein equipped with 64 and 8 antennas, respectively. For the hybrid MU-MIMO partially-connected architecture, the BS is equipped with 2 TX/RX RF chains, i.e., each RF chain is connected to a sub-array of 32 antennas. The system operating frequency is 28 GHz with a bandwidth of 500 MHz. For the uplink, downlink and IUI channels, we use the geometric channel model based on clusters and rays as it precisely captures the mmWave characteristics, while the SI channel follows the Rician model as described in [22]. Furthermore, a performance upper bound, not achievable in general but useful for benchmarking goals, can be derived by assuming interference-free and neglecting hardware constraints, so that $\mathbf{W}_{\mathsf{BS},n}, \mathbf{W}_n, \mathbf{F}_{\mathsf{BS},n}, \mathbf{F}_n$ are only constrained to be semi-unitary matrices. Then the optimal beamformers are given by the dominant left and right singular vectors of the uplink/downlink channels matrices, yielding $\bar{\mathcal{I}}_{\mathsf{uplink}} + \bar{\mathcal{I}}_{\mathsf{downlink}} \leq \bar{\mathcal{I}}_{\mathsf{bound}}$

$$\bar{\mathcal{I}}_{\mathsf{bound}} = \frac{1}{N_{\mathsf{sc}}U}\sum_{n=0}^{N_{\mathsf{sc}}-1}\sum_{u=0}^{U-1}\log\left(1+\mathsf{snr}_{u,n}\sigma_{u,n}^2(\mathbf{H}_{u,n})\right) + \frac{1}{N_{\mathsf{sc}}K}\sum_{n=0}^{N_{\mathsf{sc}}-1}\sum_{k=0}^{K-1}\log\left(1+\mathsf{snr}_{k,n}\sigma_{k,n}^2(\mathbf{H}_{k,n})\right) \tag{5.44}$$

5.5.1 Beam Patterns Analysis

Figure 5.2 provides a visualization of the optimized beam patterns for both the downlink users and the BS. In Figure 5.2a, the effective RX patterns for the two downlink users are presented. Notably, these patterns demonstrate a minimization of IUI achieved by introducing nulls in the directions of the uplink users. Additionally, the mitigation of MUI is evident as nulls are allocated to the other downlink users. For instance, consider the first downlink user (indicated by the blue-colored beam)

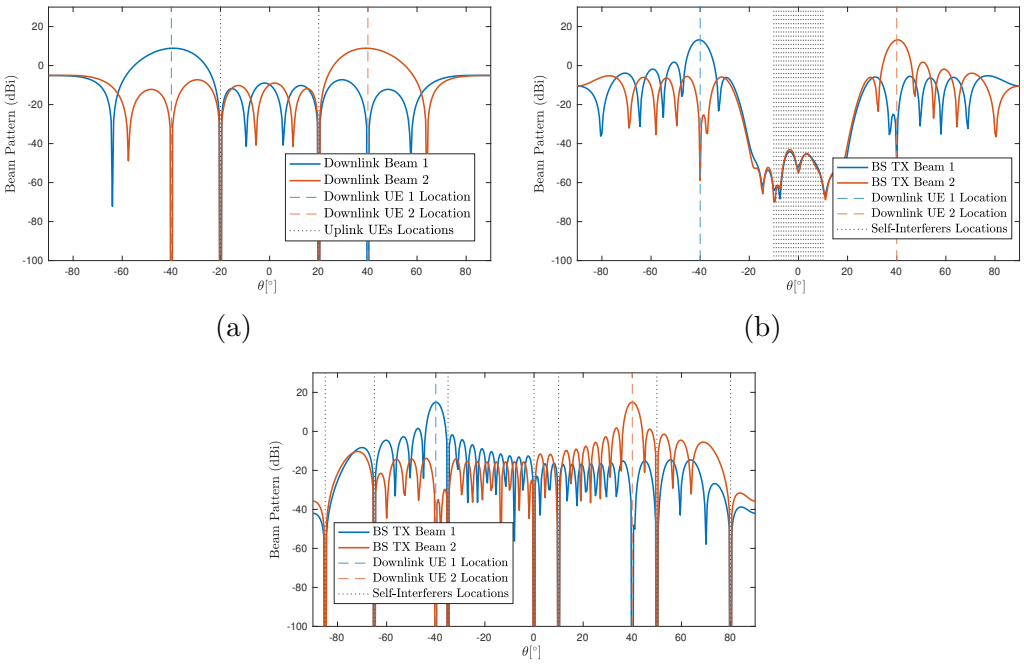

Figure 5.2: Illustration of the beam-patterns for the hybrid MU-MIMO architecture at the BS. (a). Effective RX beam patterns at the downlink users wherein located at $-40°$ and $40°$, while the uplink users are located at $-20°$ and $20°$. (b). Effective TX beam-pattern of the BS transmitting two streams, wherein the self-interferers are leaking within the floor bounded by $-10°$ and $10°$, which can be interpreted as a line-of-sight SI. (c). Effective TX beam-pattern of the BS transmitting to the downlink users at $-40°$ and $40°$, wherein the self-interferers are leaking from different directions, which can be viewed as an external random non line-of-sight SI. Note that the BS is equipped with 4 TX/RX RF chains and each sub-array is equipped with 32 antennas, while each user is equipped with 8 antennas.

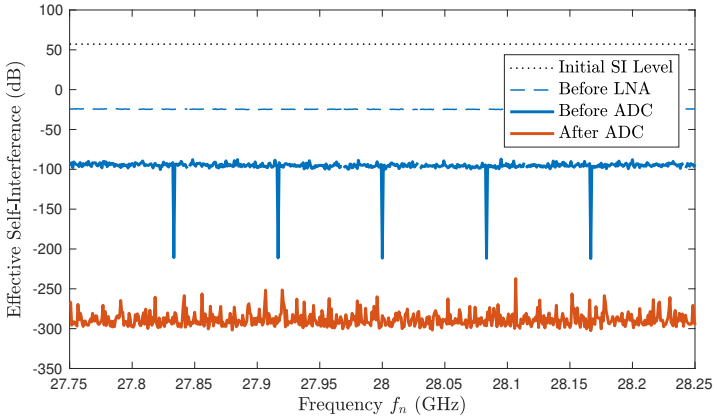

Figure 5.3: Illustration of SI suppression at different stages in MU-MUMO hybrid architecture and across the whole transmission bandwidth. The system parameters are: $\mathcal{N}_{\mathsf{freq}} = 5$, $K = U = 2$, 2 TX/RX RF chains at the BS and each sub-array is equipped with 32 antennas, while each user is equipped with 8 antennas.

positioned at $-40°$, which effectively suppresses IUI from the uplink users located at $-20°$ and $20°$, as well as the multistream interference originating from the second downlink user (represented by the red-colored beam) situated at $40°$.

Figures 5.2b and 5.2c further illustrate the effective TX beam pattern of the BS, where two beams are generated for the two downlink users. These patterns reflect a deliberate nulling of interference emanating from the other user's direction while concurrently achieving substantial SI suppression.

5.5.2 Self-Interference Suppression Analysis

Fig. 5.3 provides an illustrative depiction of the effective SI suppression at various stages encompassing the entire bandwidth within the context of the hybrid A/D partially-connected structure. Initially, the SI level undergoes a reduction to approximately 52 dB following physical TX/RX isolation measures. Subsequently, through the implementation of hybrid A/D precoding, denoted as $\mathbf{F}_{\mathsf{BS},n}^{\mathsf{BB}}$ and $\mathbf{F}_{\mathsf{BS}}^{\mathsf{RF}}$, an additional SI reduction of about 77 dB is achieved. This results in a lower effective SI level (prior to LNA) maintained at approximately -25 dB. Further SI reduction

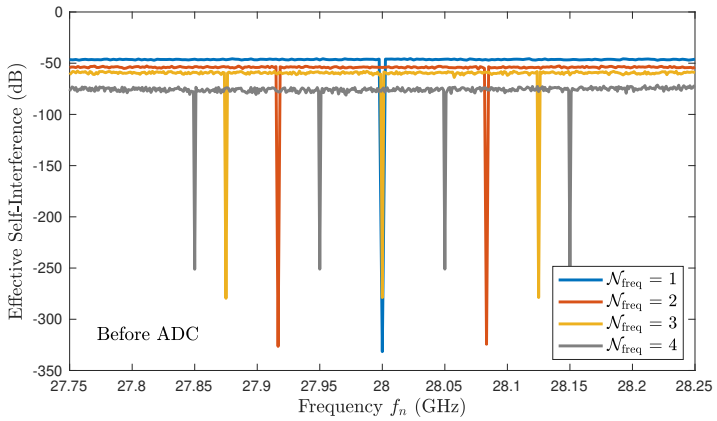

Figure 5.4: Illustration of the SI suppression in MU-MIMO hybrid architecture, showing the effective SI level right before the ADC across the whole transmission bandwidth and for different subcarriers $\mathcal{N}_{\mathsf{freq}}$. The considered system parameters are: $K = U = 2$, 2 TX/RX RF chains at the BS and each sub-array is equipped with 32 antennas, while each user is equipped with 8 antennas.

is accomplished by applying RF combining techniques at the Base BS, denoted as $\mathbf{W}_{\mathsf{BS}}^{\mathsf{RF}}$, which achieves roughly 73 dB of SI suppression. The average effective SI level is consequently sustained at approximately -98 dB (before ADC), a level sufficient to prevent ADC saturation. Notably, for frequencies designated as null frequencies ($\mathcal{N}_{\mathsf{freq}} = 5$), the effective SI level experiences a substantial reduction to approximately -200 dB. Moreover, the integration of a digital combiner at the BS, represented by ($\mathbf{W}_{\mathsf{BS},n}^{\mathsf{BB}}$), contributes to substantial SI suppression on each subcarrier. The average SI level is consistently maintained at approximately -300 dB.

Fig. 5.4 illustrates the characteristics of the frequency-domain beamformed SI channel, prior to ADC. This analysis pertains to the hybrid A/D partially-connected structure at the BS and focuses on evaluating the impact of the number of frequency nulls, denoted as $\mathcal{N}_{\mathsf{freq}}$, on the effectiveness of SI suppression. The chosen frequency nulls are distributed uniformly across the entire bandwidth, following the formula $f_{n'} = 27.75 + 0.5\frac{n'}{\mathcal{N}_{\mathsf{freq}}+1}$ GHz, where $n' = 1, 2, \ldots, \mathcal{N}_{\mathsf{freq}}$ [23]. The results reveal a clear trend: increasing the number of frequency nulls significantly enhances the effectiveness of SI suppression. For instance, when $\mathcal{N}_{\mathsf{freq}} = 1$, the average effective SI suppression

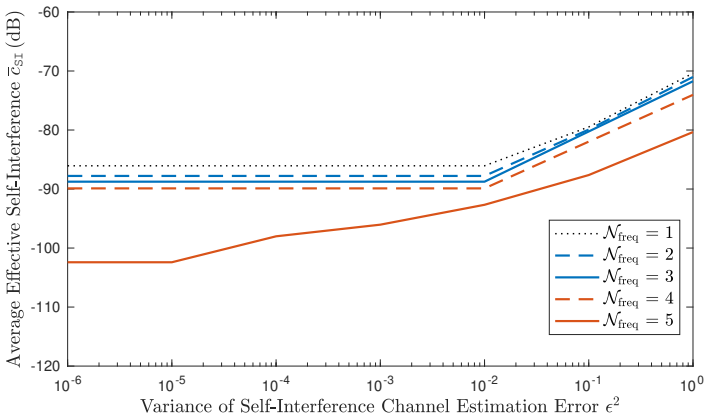

Figure 5.5: Illustration of the effective SI suppression performance, averaged over the total number of subcarriers, with respect to the relative SI channel estimation error ϵ^2. The considered system parameters are: $K = U = 2$, 2 TX/RX RF chains at the BS and each sub-array is equipped with 32 antennas, while each user is equipped with 8 antennas.

within the analyzed frequency channel is approximately -48 dB. However, by increasing the number of nulls to $\mathcal{N}_{\mathsf{freq}} = 4$, an impressive effective SI suppression level of approximately -75 dB is attainable. This observation underscores the substantial impact of the number of frequency nulls on SI mitigation.

In Fig. 5.5, we model the estimation process through additive SI channel estimation error $\tilde{\mathbf{H}}_{\mathsf{SI},n} \in \mathbb{C}^{N_{\mathsf{BS}}^{\mathsf{RX}} \times N_{\mathsf{BS}}^{\mathsf{TX}}}$, with entries distributed as independent Complex Gaussian, given by

$$\hat{\mathbf{H}}_{\mathsf{SI},n} = \mathbf{H}_{\mathsf{SI},n} + \tilde{\mathbf{H}}_{\mathsf{SI},n} \tag{5.45}$$

while the variance of the SI channel estimation error is expressed by

$$\epsilon_n^2 = \frac{\mathbb{E}\left[\|\tilde{\mathbf{H}}_{\mathsf{SI},n}\|_F^2\right]}{\mathbb{E}\left[\|\mathbf{H}_{\mathsf{SI},n}\|_F^2\right]} \tag{5.46}$$

We proceed to evaluate the impact of imperfect SI channel estimates on the achievable SI suppression performance within the framework of the presented beamforming scheme of the partially-connected structure. In this assessment, we examine how the level of SI channel estimation error, characterized by the parameter ϵ in

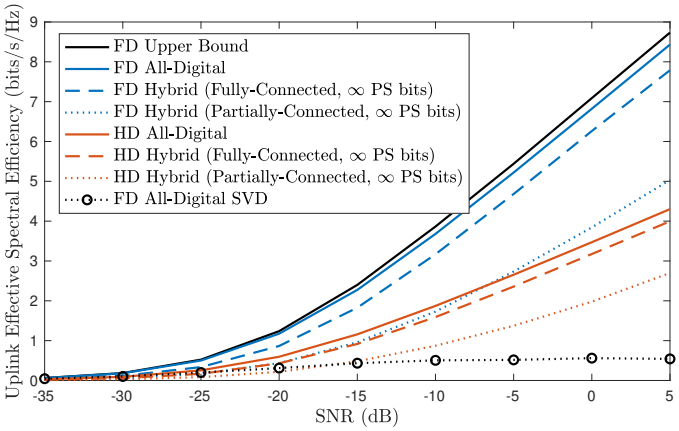

Figure 5.6: Per-user uplink effective spectral efficiency simulated with $U = 2$ uplink users and an average $\mathsf{inr} = 30$ dB. Note that the BS is equipped with 2 TX/RX RF chains and each sub-array (for partially-connected structure) is equipped with 32 antennas, while each user is equipped with 8 antennas. Scenario is simulated with ∞ resolution of PS.

(5.46), influences system performance. As depicted in Fig. 5.5, it becomes evident that the degree of SI suppression achievable is quite sensitive to the accuracy of estimation. As originally designed, the considered configurations exhibit varying levels of SI suppression, contingent on the number of nulls, when accurate SI channel estimates are available. Conversely, as anticipated, a reduction in SI channel estimation accuracy leads to a scenario where SI suppression essentially converges to the case of $\mathcal{N}_{\mathsf{freq}} = 0$. In this scenario, the efficacy of beamforming SI suppression becomes negligible, and SI suppression is primarily reliant on physical isolation measures.

5.5.3 Spectral Efficiency Analysis

Fig. 5.6 provides a comprehensive representation of per-user effective uplink spectral efficiency across a range of average SNR for various beamforming schemes. In this analysis, we utilize both the upper bound and the all-digital performance, which, it's important to note, demands a significantly high power consumption and serves as a benchmark for evaluation. Notably, the fully-connected structure consistently demonstrates near-optimal performance throughout the considered SNR range.

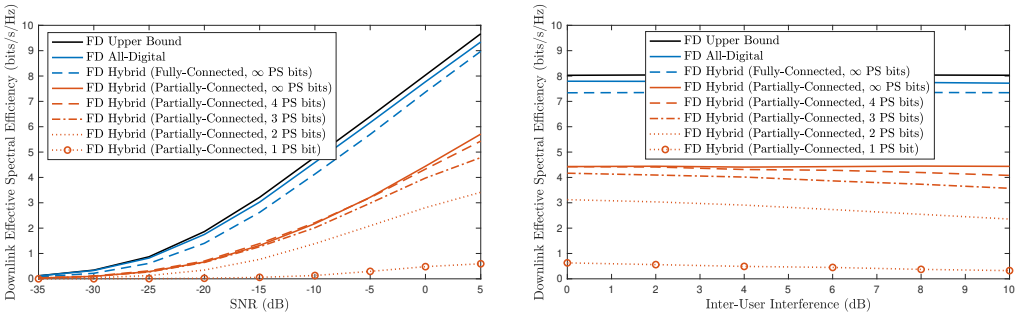

(a) (b)

Figure 5.7: Illustration of the per-user downlink effective spectral efficiency for different phases shifters resolution at the BS and users. (a). Results are obtained with $U = K = 2$ users and an average IUI of 5 dB while varying the average SNR. (b). Results are achieved with $U = K = 2$ users and an average SNR of 0 dB while varying the average IUI. Note that the BS is equipped with 2 TX/RX RF chains and each sub-array (for partially-connected structure) is equipped with 64 antennas, while each user is equipped with 8 antennas. Note that the IUI is incurred by the uplink users to corrupt the downlink users since the communications (uplink/downlink) occur at the same frequency band.

This indicates that the proposed algorithm can effectively approximate the performance of an all-digital beamforming scheme, even when employing a limited number of RF chains. In contrast, the partially-connected structure exhibits lower spectral efficiency compared to the fully-connected architecture. This discrepancy arises from the reduced number of connections between the RF chains and the antenna phase shifters, resulting in a loss of degrees of freedom and consequently lower SE. However, it is crucial to highlight that the partially-connected structure, particularly in the FD scenario, offers substantial performance gains over HD beamforming schemes, which include the all-digital, fully-connected, and partially-connected configurations. Notably, the FD all-digital SVD scheme, when interference is absent, converges precisely to the upper bound. In Fig. 5.6, the partially-connected structure consistently outperforms the FD all-digital SVD across the entire SNR range, primarily due to the relatively high average SI-to-noise ratio (inr = 30 dB), which results in the early saturation of the FD all-digital SVD at approximately 0.7 bits/s/Hz.

Fig. 5.7a provides a comprehensive analysis of per-user downlink effective spectral efficiency concerning the average SNR for different beamforming schemes, along with an evaluation of the impact of varying phase shifter quantization levels. Notably, when employing 4 bits of resolution or more, the performance closely approaches the ideal case of infinite resolution. However, a reduction in resolution leads to a degradation in performance. For instance, a quantization level of 3 bits results in an SNR loss of 5 dB compared to the infinite resolution case, while achieving an SE of 4.8 bits/s/Hz. Further reduction in resolution exacerbates the SNR loss, highlighting the trade-off between quantization precision and performance.

These findings are further corroborated by Fig. 5.7b, which illustrates spectral efficiency in relation to the average IUI for different beamforming schemes and various phase shifter resolution levels. It is evident that the introduction of quantized phase shifters leads to a departure from accurate SI suppression, resulting in the reintroduction of interference into the system and subsequently, a decline in spectral efficiency. Decreasing the phases shifters resolution bits amplifies this accuracy reduction, leading to more pronounced interference and, consequently, severe spectral efficiency degradation.

5.5.4 Energy Efficiency Analysis

We define the energy efficiency, expressed in bits/s/Watt or bits/Joule, as the ratio between the spectral efficiency and the total power consumption [161]

$$\mathcal{J} = \frac{\mathcal{I}}{\rho_{\mathsf{common}} + L_{\mathsf{TX}}\rho_{\mathsf{RF}} + N_{\mathsf{TX}}\rho_{\mathsf{PA}} + N_{\mathsf{PS}}\rho_{\mathsf{PS}}}, \tag{5.47}$$

where ρ_{common} is the common power at the TX. ρ_{RF}, ρ_{PA}, and ρ_{PS} are the power each RF chain, power amplifier, and phase shifter, respectively. The number of phase shifters N_{PS} is expressed by

$$N_{\mathsf{PS}} = \begin{cases} N_{\mathsf{BS}}^{\mathsf{TX}} L_{\mathsf{TX}} & \text{Fully-Connected} \\ N_{\mathsf{BS}}^{\mathsf{TX}} & \text{Partially-Connected} \end{cases}. \tag{5.48}$$

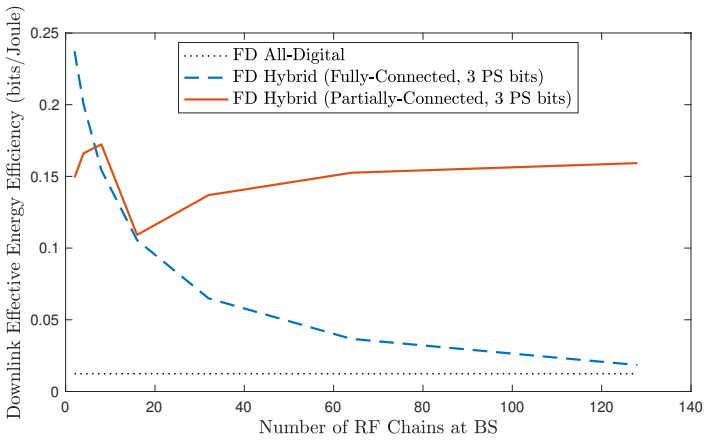

Figure 5.8: Illustration of the per-user downlink effective energy efficiency for different BS architectures. Results are obtained with $U = K = 2$ users, average $\mathsf{inr} = 30$ dB, average IUI of 5 dB, 3 bits of phase shifters resolution, while varying the number of RF chains at the BS. Note that the BS is equipped with 256 antennas, while each user is equipped with 8 antennas.

In this subsection, we conduct a performance comparison between two hybrid A/D architectures at the BS with a focus on energy efficiency, defined as (5.47). Our simulations employ the following parameters: $\rho_{\mathsf{common}} = 10$ W, $\rho_{\mathsf{RF}} = 100$ mW, $\rho_{\mathsf{PS}} = 10$ mW, and $\rho_{\mathsf{PA}} = 100$ mW, as detailed in [126].

The simulation results, presented in Fig. 5.8, reveal distinct behaviors between the three architectural structures. For all-digital architecture though achieves the best spectral efficiency, it consumes prohibitively large amount of power resulting in a poor energy efficiency. In the case of the fully-connected structure, the number of phase shifters N_{PS} scales linearly with L_{TX} and $N_{\mathsf{BS}}^{\mathsf{TX}}$. Consequently, increasing L_{TX} leads to a substantial rise in power consumption. However, the Spectral Efficiency achieved by the fully-connected structure closely approaches that of the all-digital architecture when L_{TX} closely matches the number of antennas $N_{\mathsf{BS}}^{\mathsf{TX}}$. Beyond this point, increasing L_{TX} yields minimal gains in spectral efficiency. This discrepancy between power consumption and SE results in a significant reduction in energy efficiency, approaching the lower limit established by the all-digital architecture.

Conversely, in the partially-connected structure, the number of phase shifters N_{PS} remains independent of L_{TX}. Consequently, the dominant component of total power consumption remains relatively stable across varying RF chain numbers. Simultaneously, spectral efficiency gradually approaches that of the all-digital structure with increasing L_{TX}. The combined improvement in spectral efficiency and the relatively unchanged power consumption contribute to an overall increase in energy efficiency as L_{TX} increases in the partially-connected structure.

Notably, Fig. 5.8 highlights an intersection point at $L_{\mathsf{TX}} = 6, 16$ where the energy efficiency for both hybrid A/D structures converges. Specifically, the fully-connected structure exhibits higher energy efficiency with a smaller number of RF chains, while the partially-connected structure proves more energy-efficient with a relatively larger number of RF chains. This observation carries valuable insights for RF chain implementation in hybrid architectures. The spectral efficiency of the fully-connected structure can approach the performance of the all-digital architecture when the number of RF chains is slightly larger than that of the number of users (data streams). Therefore, there is no need to implement more RF chains considering the energy efficiency. In contrast, the partially-connected structure benefits from leveraging a larger RF chain count, achievable with low-complexity hardware, to enhance both spectral and energy efficiency.

5.5.5 Comparative Study

In our analysis, we benchmark our proposed FD hybrid A/D beamforming design against several prior methodologies to assess its performance. Notably, we compare it with the approach from Valcarce *et al.* [98] (denoted as "RM"), Xiao *et al.* [156] ("ZPX"), our earlier work [22] ("EBC"), the method from Satyanarayana *et al.* [137] ("KMPAL"), and Robert *et al.* [132] ("IHS"). In these referenced studies [156, 137, 22, 132], the designs exhibit significant sensitivity to the level of SI as performance notably declines (unless the SI level is minimal). This is primarily due to these designs not maintaining the unit modulus constraint in the hybrid A/D

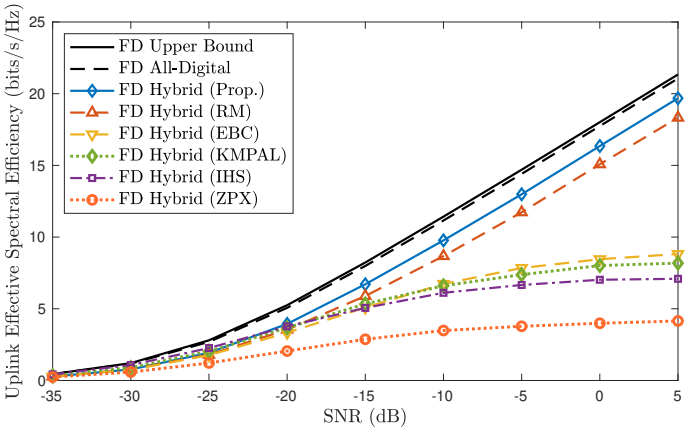

Figure 5.9: A comprehensive comparison with previous methods in terms of the per-user uplink effective spectral efficiency. Results are obtained with $U = K = 2$ users, average $\mathsf{inr} = 30$ dB, average IUI of 5 dB, ∞-bits of phase shifters resolution and $L_{\mathsf{RX}} = L_{\mathsf{TX}} = 4$. Note that the BS is equipped with 256 antennas, while each user is equipped with 8 antennas.

beamformers, thus violating interference suppression constraints and leading to performance degradation. Specifically, in [156], Xiao *et al.* adopt a zero-forcing-matched filter for beamforming design (referred to as method 2 in [156]), but the imposition of unit modulus constraints disrupts the zero-forcing condition for SI suppression, reintroducing SI into the system and significantly impacting spectral efficiency. In our preceding work [22], we initially relaxed the unit modulus constraint during the hybrid A/D beamformer design phase, yet post-optimization imposition of this constraint contradicted the design prerequisites, thereby impairing system performance. Additionally, Satyanarayana *et al.* [137] commence with deriving all-digital beamformers, and apply a convex QCQP to obtain the digital and the unconstrained analog (without being constrained on unit modulus constraint) solutions. The subsequent introduction of this constraint leads to a compromise in interference suppression, adversely affecting spectral efficiency. Furthermore, Robert *et al.* [132] utilize SVD for all-digital beamforming and apply orthogonal matching pursuit (OMP) for equivalent hybrid analog and baseband solutions. Adjustments to suppress SI through baseband beamforming modifications make the design vulnerable to SI levels due to

inadequate analog domain mitigation. Conversely, the "RM" design [98] proves more resilient against SI by approximating all-digital counterparts in Euclidean distance, while the analog RF combiner is optimized to minimize SI power before the ADC, appropriately addressing the unit modulus constraint during beamformer design to mitigate interference effects. The baseband combiner is then tailored to eliminate residual SI, enhancing spectral efficiency. Our design exhibits a slight performance gap compared to "RM" [98], which can be attributed to our analog precoder being specifically designed to both maximize beamformed power and suppress SI, unlike in [98] where the analog precoder does not explicitly incorporate an interference suppression constraint, relying instead on the analog combiner for SI mitigation. This distinct approach enables our design to surpass the performance seen in [98].

5.6 Conclusion

In this chapter, we examined a wideband single-cell multiuser framework where a FD base BS engages in simultaneous communication with multiple uplink and downlink users. We explored both all-digital and hybrid A/D beamforming, introducing several innovative beamformer designs and optimization strategies to tackle the issues of SI and multiuser interference. Given the rigorous limitations of the hybrid architecture, such as the absence of amplitude control in phase shifters and the challenge of finite-resolution phase shifters, we demonstrated the feasibility of integrating these constraints into our design, achieving significant interference reduction in the analog domain to prevent ADCs saturation. Specifically, our analog beamformers effectively suppress wideband SI through the implementation of multiple frequency nulls. Concurrently, the baseband beamformers are meticulously designed to enhance beamformed powers and minimize residual SI and multiuser interference, as evidenced by the effective beam patterns. We adopted a partially-connected array approach for the hybrid architecture to boost energy efficiency. Our method outperforms existing hybrid beamforming techniques and the HD approach, highlighting the transforma-

tive potential of FD millimeter-wave technology in cellular networks and integrated sensing and communications.

Chapter 6: Massive MIMO Cellular Networks

In this chapter[1], I provide a unified framework for FD massive MIMO cellular networks with low-resolution ADCs and DACs. An objective of this work is to derive an accurate model to account for a wide variety of network irregularities and imperfections, including loopback SI that arises in FD systems and quantization error from low-resolution data converters. Our contributions for forward and reverse links include (1) deriving SQINR under pilot contamination, LMMSE channel estimation and channel hardening; (2) deriving closed-form and approximate analytical expressions of spectral efficiency; (3) deriving asymptotic results and power scaling laws with respect to the number of quantization bits, base station antennas, and users, as well as base station and user equipment power budgets; and (4) analyzing outage probability and spectral efficiency vs. cell shape, shadowing, noise, cellular interference, pilot contamination, pilot overhead, and frequency reuse. Cell shapes include hexagonal, square, and PPP tessellations. In simulation, we quantify spectral and energy efficiency as well as the impact of SI power, inter-user interference, and cell shape on outage probability. We carry out the analysis for sub-7 GHz LTE bands

[1]This chapter is based on the work published in the following journal paper: E. Balti and B. L. Evans, "A Unified Framework for Full-Duplex Massive MIMO Cellular Networks With Low Resolution Data Converters," in *IEEE Open Journal of the Communications Society*, vol. 4, pp. 1-28, 2023. In addition, this work is an extension of the following conference papers:

- E. Balti and B. L. Evans, "Full-Duplex Massive MIMO Cellular Networks with Low Resolution ADC/DAC," *GLOBECOM 2022 - 2022 IEEE Global Communications Conference*, Rio de Janeiro, Brazil, 2022, pp. 1649-1654
- E. Balti and B. L. Evans, "Reverse Link Analysis for Full-Duplex Cellular Networks with Low Resolution ADC/DAC," *2022 IEEE 23rd International Workshop on Signal Processing Advances in Wireless Communication (SPAWC)*, Oulu, Finland, 2022, pp. 1-5
- E. Balti and B. L. Evans, "Forward Link Analysis for Full-Duplex Cellular Networks with Low Resolution ADC/DAC," *2022 IEEE 23rd International Workshop on Signal Processing Advances in Wireless Communication (SPAWC)*, Oulu, Finland, 2022, pp. 1-5

These works were supported by NVIDIA and AT&T Labs through their industrial affiliation with the 6G@UT research center at UT Austin.

and then extend the framework to support mmWave bands.

6.1 Introduction

With increasing demand for higher data rate, lower latency, and higher reliability from a growing number of wireless users and services, RF technologies seek to use the limited available spectrum more effectively. Beyond the connections from base stations to mobile and fixed wireless subscribers, cellular systems also provide backhaul from BSs to the Internet and other networks. Installing optical fiber or other cabling for backhaul can be prohibitively expensive and in some cases not allowed by law.

As far back as 2011, microwave and satellite RF bands had become commonly used to support backhaul [148]. Currently, mmWave technology, which refers to the spectrum in the 10-300 GHz range[1], has emerged as a promising solution for providing large bandwidths. In particular, mmWave is an attractive band for integrated access and backhaul [107, 52, 79].

One proposed solution to address the scarcity of spectrum is to employ FD transceivers [134]. FD systems have emerged as a viable solution to enable the efficient use of spectrum by allowing transmission and reception using the same resource blocks [133]. A direct consequence is the potential to reduce latency and overhead as well as double the spectral efficiency vs. HD systems [10]. Moreover, FD transceivers are cost efficient since the transmit and receive arrays can be placed into a single dedicated array for shared transmission and reception [15, 21, 16]. These benefits call for the integration of FD into practical consideration, e.g., machine-to-machine communications as well as integrated access and backhaul which have been recently adopted in 3GPP Release 17 [1].

[1]Although a rigorous definition of mmWave frequencies would place them between 30 and 300 GHz, industry has loosely defined them to include the spectrum from 10 to 300 GHz.

Due to the dramatic differences in received power from near and far transmitters, FD systems are constrained by loopback self-interference (SI) that leaks from the transmit array to the colocated receive array and that can be up to 100 dB stronger than the desired received signal [73, 169]. Without proper SI cancellation, the ADCs can be swamped by SI, thereby resulting in very poor communication performance.

6.1.1 Prior Works

Recent publications have proposed robust beamforming design to suppress SI and enable FD operation [75, 32, 139]. Authors [28, 130, 129] have proposed beamforming techniques such as ZF, MMSE, and NSP to suppress SI. In massive MIMO systems in particular, BSs employ many more antennas than those available on UE. Having a massive number of antennas enables not only enough spatial multiplexing gain but also sufficient DoF to reduce SI and improve spectral efficiency significantly. In addition, authors in [12] investigated FD massive MIMO relaying with low resolution ADC in terms of spectral and energy efficiency. They derived the ZF as well as closed-form expressions for spectral efficiency and the tradeoff between energy and spectral efficiency for various system configurations. Moreover, work [158] proposed a beam-domain approach using hybrid time-switching and power splitting for FD massive MIMO systems to improve spectral efficiency. Furthermore, authors in [173] proposed an antenna selection scheme to cancel the loopback SI and used a genetic algorithm to solve the non-convex optimization problem.

Several authors have harnessed the advantages of both FD and massive MIMO [110, 151, 140]. In fact, the authors in [110] and [151] investigated a multipair decode-and-forward relay employing FD massive MIMO and proved that as the number of antennas goes to infinity, SI is asymptotically suppressed. In [140], an SI-aware receive filter for the uplink (reverse link) and precoder for the downlink (forward link) are designed.

Although employing a massive number of antennas has many benefits, it comes

with a tradeoff of hefty power consumption. In fact, having a large number of antennas leads to pronounced growth in the power consumption and hardware cost as each RF processing chain requires a pair of high-resolution ADCs (e.g. 10-12 bits each for commercial applications) [167, 11]. A b-bit ADC with a sampling frequency f_s requires $2^b \cdot f_s$ computations per second. Consequently, the power consumption grows exponentially with the resolution and linearly with the sampling frequency [105]. To circumvent this, low-resolution ADCs (1-3 bits) have been suggested for massive MIMO to reduce power consumption at the expense of spectral efficiency [40, 45, 168, 90, 102, 91].

Related works have proposed power-efficient system designs based on low-resolution ADCs and DACs. In [76], the authors investigated a FD massive MIMO amplify-and-forward relay with low-resolution ADCs while the authors in [86] studied a massive MIMO mixed-ADC system, wherein a few of the high-resolution ADCs are allocated for channel estimation with 1-bit ADCs used for payload reception. In addition, the authors in [168] considered a mixed DAC/ADC multipair amplify-and-forward massive MIMO relay, analyzed sum spectral efficiency, and proposed a power allocation scheme with the aim of maximizing the sum spectral efficiency. An uplink spectral efficiency of a HD massive MIMO with low-resolution ADCs and a spectral/energy efficiency trade-off analysis in mixed ADC scenarios have been investigated over Rician channels in [167, 166], respectively.

6.1.2 Contributions

In this chapter, we propose a unified framework for analysis of FD massive MIMO cellular networks with low-resolution ADCs/DACs for different network topologies such as hexagonal lattice, square grid, and PPP tessellation. The BSs operate in FD mode under low-resolution ADCs/DACs and are each equipped with a massive number of antennas, while the UEs operate with a single antenna in HD mode under infinite ADC/DAC resolution. More importantly, we propose separate analysis frameworks for reverse and forward links under pilot contamination, and use

matched filters in the receiver and for the precoder at the FD BSs. Since the BSs operate in FD, loopback SI is created at the BS transceiver wherein the precoded signal transmitted by the BS leaks to the BS combiner and consequently corrupts the uplink signals received from the users. In addition, downlink users are vulnerable to the IUI incurred by the uplink UEs since the BSs operate in FD mode.

To characterize the reverse and forward link performance measures, we evaluate the average signal-to-quantization-plus-interference-plus-noise ratio (SQINR[2]) among the users (either on the reverse or forward link). The channels are estimated in the reverse link phase wherein the UEs send the pilots to the BSs which estimate the channels and compute the precoders and combiners. We propose the forward link CSI acquisition based on the channel reciprocity property of TDD systems. As long as the forward and reverse transmissions occur within the channel coherence time, the physical channel is reciprocal. This property is exploited for Massive MIMO [101] to avoid the large channel feedback to the BS in the reverse link phase. The only issue is that the receive and transmit RF chains in the transceivers (i.e. the hardware from the antenna to the ADC in the receive path and from the DAC to the antenna in the transmit path) are not reciprocal, thereby calibration is required to compensate hardware asymmetry. To facilitate the analysis, we assume TDD channel reciprocity with perfect calibration.

For channel modeling, we consider channel hardening; for channel estimation, we consider the LMMSE approach. Capitalizing on both, we evaluate the CDF, spectral efficiency, and energy efficiency vs. the average SQINR for reverse and forward links under several scenarios. To the best of our knowledge, this is the first work proposing a unified framework for FD massive MIMO in multiuser and multicell cases

[2]The word "quantization" introduced in the term SQINR is derived from the application of low-resolution ADCs/DACs as the received signal becomes quantized rather than continuous in amplitude. Although the application of low-resolution ADCs/DACs reduces the power consumption, it incurs nonlinear distortion. One approach models the nonlinear distortion as additive noise. Other approach uses Bussgang Theory to linearize this distortion for the sake of simplicity and tractability and approximate the nonlinearity as a gain plus additive noise.

with low-resolution ADCs/DACs.

The main contributions of this chapter are summarized as follows:

- I derive expressions for the received signals and the corresponding SQINR for both the reverse and forward links, considering factors such as channel hardening, LMMSE channel estimation, low-resolution ADCs/DACs, and pilot contamination.

- I derive both closed-form and approximate analytical expressions for the spectral efficiency of the reverse and forward links. The additive quantization noise model (AQNM[3]) is used to model the quantization errors in ADCs and DACs. Our findings indicate that spectral efficiency is significantly impacted by the use of low-resolution ADCs/DACs, and this degradation cannot be fully offset by simply increasing the number of BS antennas. Therefore, each UE must adopt high-resolution ADCs/DACs to ensure optimal performance. Since each UE only requires two ADCs for IQ sampling in the reverse link, and two DACs for IQ sampling in the forward link, high-resolution data converters at the UEs are a feasible solution.

- I analyze the effects of network imperfections and irregularities, such as varying cell shapes, shadowing, noise, and cellular interference, on the reverse and forward links. Cellular interference includes pilot contamination, as well as inter-cell and intra-cell interference. Additionally, we examine the impact of pilot overhead, user density per cell, and frequency reuse factors on both the CDF and spectral efficiency.

- Evaluate the effects of FD operation, including SI channel power, SI signal power, and IUI, on users in both the reverse and forward links.

[3]To facilitate the analytical evaluation of systems with low-resolution ADCs/DACs, we adopt the widely recognized AQNM from the literature.

- Derive asymptotic results and power scaling laws for both reverse and forward links to provide engineering insights into the proposed system model.
- Demonstrate the generality of the proposed model by showing that the results align with existing literature for several special cases. Although some cases, such as single-user, single-cell, and high-resolution scenarios, are less common, analyzing these cases offers valuable insights.
- Evaluate the numerical results for the CDF, spectral efficiency, and energy efficiency using different tessellation structures, including hexagonal lattice, square grid, and PPP tessellation.

6.1.3 Structure

The chapter is organized as follows. The system model is introduced in Section 6.2. The reverse and forward links analysis are presented in Sections 6.3 and 6.4, respectively. Derivation of asymptotic results as well as power scaling laws are reported in Section 6.5. Section 6.6 extends the modeling of the reverse and forward links from sub-7 GHz LTE bands to 5G LTE millimeter wave bands. Section 6.7 defines performance measures of energy efficiency and outage probability. The numerical results and their discussion are presented in Section 6.8 while Section 6.9 concludes the chapter.

6.2 Network Model

We consider a macrocellular network where each BS operates in FD mode and is equipped with $N_{\mathsf{a}} \gg 1$ antennas. Each UE operates in HD mode and has a single antenna.

Table 6.1: Definition of symbols commonly used in this chapter in alphabetical order.

Variable	**Symbol**
Bandwidth	B
Number of ADC/DAC resolution bits	b
Fraction of pilot overhead	β
Set of cells reusing the same pilot dimensions	$\mathcal{C}$
Walden's figure of merit for ADCs and DACs	c
Shadowing (Variance)	$\chi(\sigma_{\mathsf{dB}})$
Copilot distance between the cell of interest and its first tier of copilot cells	D_{copilot}
Fractional frequency reuse factor	Δ
Pathloss exponent	η
Precoder applied from ℓ-th BS to k-th user in l-th cell	$\boldsymbol{f}_{\ell,(l,k)}$
Large scale fading between ℓ-th BS and the k-th user served by l-th BS	$G_{\ell,(k,l)}$
Small scale fading between the n-th user in ℓ-th cell and the k-th user in l-th cell	$\boldsymbol{g}_{(\ell,n),(l,k)}$
Self-interference channel	$\boldsymbol{H}_{\mathsf{SI}}$
Small scale fading between ℓ-th BS and the k-th user served by l-th BS	$\boldsymbol{h}_{\ell,(k,l)}$
LMMSE channel estimate	$\hat{\boldsymbol{h}}$
LMMSE channel estimation error	$\tilde{\boldsymbol{h}}$
Spectral efficiency of k-th user for matched filter	$\mathcal{I}_k^{\mathsf{MF}}$
Effective spectral efficiency	$\mathcal{I}^{\mathsf{eff}}$
Energy efficiency	$\mathcal{J}$
Number of users in ℓ-th cell	K_ℓ
BSs density	λ_{BS}
UEs density	λ_{UE}
Pathloss offset	L_{ref}
Self-interference channel power	μ_{SI}^2
Variance of LMMSE channel estimation error	MMSE
Number of antennas at BS	N_{a}
Number of coherence tiles	N_{c}
Number of pilots per cell	N_{p}
BSs location process	$\boldsymbol{\Phi}_{\mathsf{BS}}$
UEs location process	$\boldsymbol{\Phi}_{\mathsf{UE}}$
Power between ℓ-th BS and k-th user in l-th cell	$P_{\ell,(l,k)}$
Outage probability for a threshold ζ	$P_{\mathsf{out}}(\zeta)$
Self-interference power	P_{SI}
Maximum uplink (downlink) power	$P_u(P_d)$
Additive quantization noise	$\boldsymbol{q}$
Distance between ℓ-th BS and the k-th user served by l-th BS	$r_{\ell,(k,l)}$
Inverse of the signal-to-quantization-plus-noise ratio	ρ
Forward-to-reverse links SNR ratio	ϱ
Signal-to-interference-plus-noise ratio of k-th user	sinr_k
Signal-to-noise ratio from ℓ-th BS to k-th user in l-th cell	$\mathsf{SNR}_{\ell,(l,k)}$
Signal-to-quantization-plus-interference-plus-noise ratio of k-th user	sqinr_k
SQINR of k-th user based on LMMSE channel estimation	$\mathbb{E}[\mathsf{sqinr}_k]$
SQINR of k-th user based on channel hardening	$\overline{\mathsf{sqinr}}_k$
Large scale fading between n-th user in ℓ-th BS and the k-th user in l-th BS	$T_{(\ell,n),(l,k)}$
Noise (variance)	$\boldsymbol{v}(\sigma^2)$
Combiner at ℓ-th BS from the k-th user in l-th cell	$\boldsymbol{w}_{\ell,(l,k)}$
Precoded symbols vector transmitted by ℓ-th BS	$\boldsymbol{x}_\ell$
Power control (Reverse)/Power allocation (Forward)	ϑ

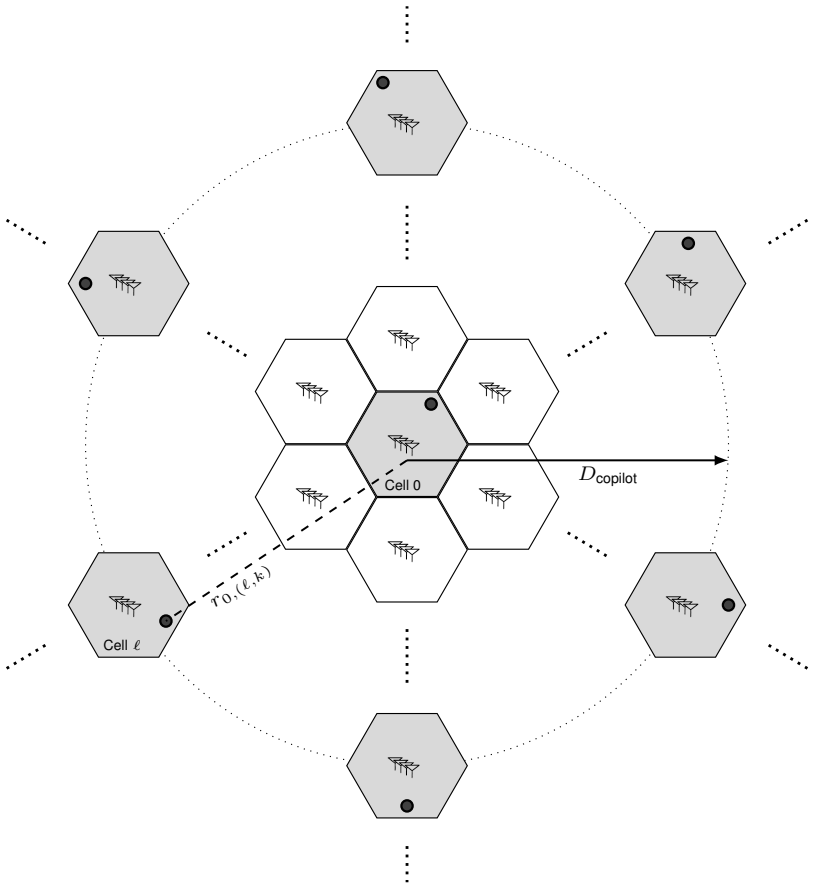

Figure 6.1: Hexagonal lattice network. The cell of interest and the cells belonging to subset $\mathcal{C}$, i.e., all the ones reusing the same pilot dimensions, are shaded and a copilot user equipment in each cell is indicated by a circle. Also indicated is the distance $r_{0,(\ell,k)}$ between the cell of interest cell 0 and the k-th user equipment served by the cell ℓ. In addition, indicated is the distance D_{copilot} between the cell of interest and its first tier of copilot cells.

6.2.1 Network Geometry

Recent research on modern cellular networks has proposed various approaches to address the modeling and performance analysis of reverse and forward links. The Wyner model [155] gained enormous attention for its simplicity as it considers inter-cell interference to be constant or a single random variable to account for fading. However, it has been shown in [157] that this model suffers from shortcomings in the cases where the inter-cell interference is spatially averaged, e.g., a CDMA network congested by a high load. In the same context, existing work suggests a network model consisting of regular and deterministic BS deployment, e.g., hexagonal or square grid-based model shown by Figs. 6.1 and 6.2a. Although this network model is regular, closed-form expressions for the communication performance are not tractable and instead the derivation is based on approximations and Monte Carlo simulation. It has been shown that the grid-based model is an upper bound to the actual performance retrieved from real data, e.g., the SINR coverage based upon a square grid is an upper bound to network measurements [9, 111].

Limitations of previous approaches led to the development of random spatial models for network modeling. This new perspective brought two important results. First, tractable derivations of communication performance such as rate and SINR expressions became possible. Second, random spatial models were at least as accurate as grid-based models and in many cases more accurate with respect to actual networks. For example, Fig. 6.2b is a PPP distribution of both BS deployment and UE locations, which provides accurate SINR statistics for real urban networks [147].

6.2.2 Large-Scale Fading

The locations of BSs form a stationary and ergodic point process $\mathbf{\Phi}_{\mathrm{BS}} \subset \mathbb{R}^2$ of density λ_{BS}, and the UE positions follow an independent point process $\mathbf{\Phi}_{\mathrm{UE}} \subset \mathbb{R}^2$ of density λ_{UE}, which is also stationary and ergodic. Together, they model a realistic macrocellular network scenario.

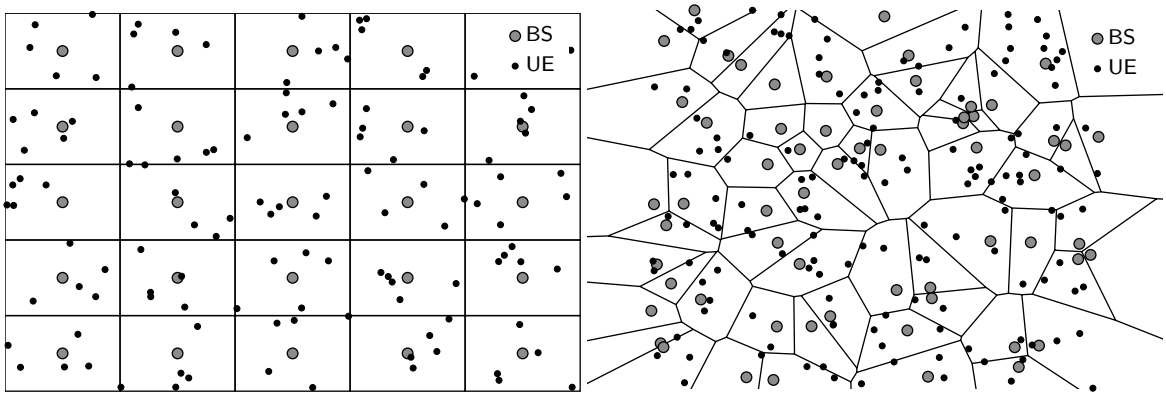

(a) Square Grid. (b) PPP Voronoi Tessellation.

Figure 6.2: Realization of homogeneous cellular networks. (a) Square grid consists of regular deployment of BSs while the UEs are uniformly distributed in the cells. (b) PPP network model wherein the deployment of BSs and UEs are distributed according to a PPP.

Each UE is associated with the BS from which it has the strongest large-scale channel gain and we denote by K_ℓ^u and K_ℓ^d the number of uplink and downlink UEs served by the ℓ-th BS. The large-scale gain comprises pathloss with exponent $\eta > 2$ and shadowing that is independently and identically distributed (IID) across the paths. In particular, the large-scale gain between the ℓ-th BS and the k-th user connected to the l-th BS is

$$G_{\ell,(l,k)} = \frac{L_{\text{ref}}}{r^{\eta}_{\ell,(l,k)}} \chi_{\ell,(l,k)}, \tag{6.1}$$

with L_{ref} as the pathloss intercept at a unit distance, $r_{\ell,(l,k)}$ the link distance, and $\chi_{\ell,(l,k)}$ as the shadowing coefficient satisfying $\mathbb{E}[\chi^{2/\eta}] < \infty$. Further, we introduce large-scale fading between the UEs to model the IUI. We denote $T_{(\ell,n),(l,k)}$ as the large-scale channel gain between the n-th user and the k-th user associated with the ℓ-th and l-th BSs, respectively.

Without loss of generality, we denote the 0-th BS as the focus of interest and drop its subscript for notational compactness. For large-scale gains,

- $G_{0,(l,k)} = G_{(l,k)}$ relates the BS of interest with the k-th UE associated with the

l-th BS.

- $G_{\ell,(0,k)} = G_{\ell,k}$ relates the ℓ-th BS with the k-th UE associated with the BS of interest.
- $G_{0,(0,k)} = G_k$ relates the BS of interest with its own k-th UE.
- $K_0 = K$ is the number of UEs served by the BS of interest.

The same scripting and compact notation are applied to other quantities.

6.2.3 Small-Scale Fading

We denote $\mathbf{h}_{\ell,(l,k)} \sim \mathcal{N}_{\mathbb{C}}(\mathbf{0}, \mathbf{I})$ as the normalized reverse link $N_{\mathsf{a}} \times 1$ small-scale fading between the k-th user located in cell l and the BS in cell ℓ and $\mathbf{h}^*_{\ell,(l,k)}$ as the forward link reciprocal, assuming TDD with perfect calibration [53]. In addition, we denote by $\mathbf{g}_{(\ell,n),(l,k)} \sim \mathcal{N}_{\mathbb{C}}(0, \sigma^2_{\text{iui}})$ the 1×1 small-scale fading between the n-th user in cell ℓ and the k-th user in cell l [40]. We further denote by $\mathbf{H}_{\mathsf{SI}} \sim \mathcal{N}_{\mathbb{C}}(\mathbf{0}, \mu^2_{\mathsf{SI}})$ the SI channel matrix ($N_{\mathsf{a}} \times N_{\mathsf{a}}$) [40].

Remark 11. In this work, we assume perfect knowledge of the SI channel. The estimation of the SI channel can be carried out with conventional methods such as LS or MMSE estimators. If the channel matrix is sparse, then a compressive sensing method will be the best candidate, in particular, for a channel matrix of large dimension. In addition, we consider an estimate of the SI channel ($\hat{\mathbf{H}}_{\mathsf{SI}}$) while the estimation error can be accounted as additional source of SI. Note that tackling the SI channel estimation problem is out of the scope of this work.

6.2.4 Number of Users per Cell

Regardless of the regularity of the network lattice, disparities may come to play across the BSs due to shadowing and randomness of user locations.

Without shadowing, any user is associated with the tagged BS in its Voronoi cell, and the number of users, conditioned on the cell area, is a random variable with mean λ_{UE} multiplied by the cell area $\mathcal{A}$. If $\mathbf{\Phi}_{\mathsf{UE}}$ is a PPP, then the number of users follows a Poisson distribution. Depending on how the cell area is distributed, the distribution of the number of users per cell can be evaluated. For example, if $\mathbf{\Phi}_{\mathsf{UE}}$ is a PPP, such number in a lattice network is Poisson distributed with average $\lambda_{\mathsf{UE}}/\lambda_{\mathsf{BS}}$ while, for an irregular network with PPP distributed BSs, the corresponding distribution is approximated in [46].

In the presence of shadowing, a user is not necessarily associated with the nearest BS. Although the shadowing per link is strong and independent, the number of users per BS still follows a Poisson distribution with mean $\lambda_{\mathsf{UE}}/\lambda_{\mathsf{BS}}$ regardless of the BS locations. In fact, when shadowing increases significantly, it dominates the pathloss and each BS becomes equally likely to be the one serving a particular user. For instance, let's consider a region with a finite area $\mathcal{A}$ consisting of $\mathcal{A}\lambda_{\mathsf{BS}}$ BSs and $\mathcal{A}\lambda_{\mathsf{UE}}$ UEs, all located randomly. When the shadowing strengthens, the number of users served by each BS follows a Binomial distribution $\mathcal{B}\left(\mathcal{A}\lambda_{\mathsf{UE}}, \frac{1}{\mathcal{A}\lambda_{\mathsf{BS}}}\right)$, since each UE has equal probability $\frac{1}{\mathcal{A}\lambda_{\mathsf{UE}}}$ of being associated with any of the $\mathcal{A}\lambda_{\mathsf{BS}}$ BSs. For a region with infinite area ($\mathcal{A} \longrightarrow \infty$) and with a constant mean $\lambda_{\mathsf{UE}}/\lambda_{\mathsf{BS}}$, the Binomial distribution converges to a Poisson distribution [29].

6.2.5 Full-Duplex and Low Resolution ADC/DAC

Fig. 6.3 illustrates a basic abstraction of a BS operating in FD mode. The uplink UEs send the data to the BS independently from the data intended for the downlink UE transmitted from the BS. Since the BS transmits and receives simultaneously using the same resource blocks, SI leakage is created as loopback from TX to RX arrays of the BS.

Without loss of generality, we illustrate the analysis of a FD system with low resolution ADCs/DACs for a single-cell scenario. Then we generalize the analysis to

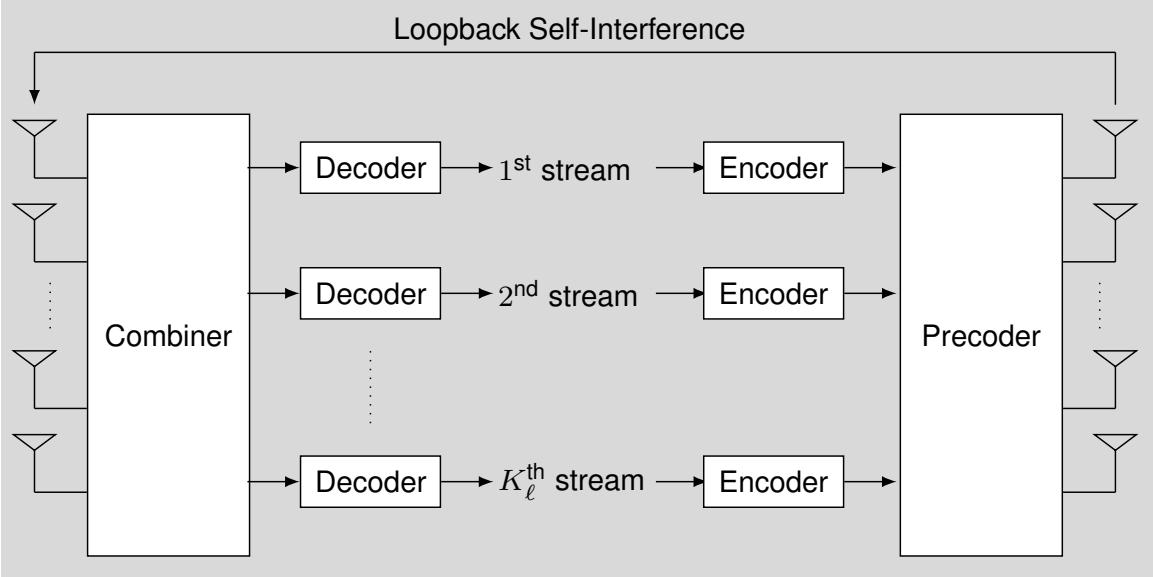

Figure 6.3: Basic abstraction of a full-duplex base station: The uplink UE sends the data to the BS independently from the data intended to the downlink UE sent from the BS. Since the BS transmits and receives simultaneously at the same resource blocks, SI leakage is created in the form of a loopback from TX to RX sides of the BS.

a multi-cell network for reverse and forward links.

The received uplink signal $\mathbf{y}^u$ at the BS prior to quantization is given by

$$\mathbf{y}^u = \sqrt{P_u}\mathbf{H}_u\mathbf{x}_u + \sqrt{P_d}\mathbf{H}_{\mathsf{SI}}\mathbf{y}_q^d + \mathbf{n}_u, \tag{6.2}$$

where the downlink unquantized precoded signal $\mathbf{y}^d$ is given by

$$\mathbf{y}^d = \mathbf{F}\mathbf{x}_d. \tag{6.3}$$

Here, $\mathbf{F}$ is the precoder. By approximating the quantization effects using the AQNM, the received signal $\mathbf{y}^u$ and transmitted signal $\mathbf{y}^d$ after quantization at the BS can be modeled as

$$\mathbf{y}_q^u = \alpha_u\mathbf{y}^u + \mathbf{q}_u \tag{6.4}$$

$$\mathbf{y}_q^d = \alpha_d\mathbf{y}^d + \mathbf{q}_d. \tag{6.5}$$

We define the covariance matrices for the AQNM [40] as

$$\mathbf{R}_{\mathbf{q}_u} = \mathbb{E}[\mathbf{q}_u \mathbf{q}_u^*] = \alpha_u(1-\alpha_u)\,\mathrm{diag}\left(P_u \mathbf{H}_u \mathbf{H}_u^* + \mathbf{Q} + \sigma^2 \mathbf{I}_{N_\mathsf{a}}\right) \tag{6.6}$$

$$\mathbf{R}_{\mathbf{q}_d} = \mathbb{E}[\mathbf{q}_d \mathbf{q}_d^*] = \alpha_d(1-\alpha_d)\,\mathrm{diag}\left(\mathbf{F}\mathbf{F}^*\right), \tag{6.7}$$

where $\mathbf{Q}$ is given by

$$\mathbf{Q} = P_u \mathbf{H}_{\mathsf{SI}} \left(\alpha_d^2 \mathbf{F}\mathbf{F}^* + \mathbf{R}_{\mathbf{q}_d}\right) \mathbf{H}_{\mathsf{SI}}^*. \tag{6.8}$$

6.3 Reverse Link Analysis

At the channel estimation stage, we assume the BS operates in HD mode with full-resolution ADCs and DACs [168]. In other words, in the absence of the SI and quantization error due to limited ADC/DAC resolution, the received signal (sent from the k-th uplink UE) at the BS of interest, assuming no pilot contamination and single-cell single-user case, is given by

$$\mathbf{y}_k^u = \sqrt{G_k P_k}\mathbf{h}_k + \mathbf{v}_k. \tag{6.9}$$

Upon data transmission from the users (in a multicell and multiuser scenario), the BS operates in full-duplex mode with low-resolution ADCs/DACs. Consequently, the BS of interest observes the following received signal vector

$$\begin{aligned} \mathbf{y}_q^u =& \alpha_u \sum_{\ell} \sum_{k=0}^{K_\ell - 1} \sqrt{G_{\ell,k} P_{\ell,k}} \mathbf{h}_{\ell,k} s_{\ell,k} + \alpha_u \sqrt{P_{\mathsf{SI}}} \mathbf{H}_{\mathsf{SI}} \mathbf{q}_d \\ &+ \alpha_u \alpha_d \sqrt{P_{\mathsf{SI}}} \sum_{k=0}^{K-1} \mathbf{H}_{\mathsf{SI}} \mathbf{f}_k s_k^d + \mathbf{q}_u + \alpha_u \mathbf{v}. \end{aligned} \tag{6.10}$$

Next, we will consider two channel estimation/acquisition approaches, LMMSE and channel hardening, wherein the pilot contamination will come to play.

Remark 12. As illustrated in Fig. 6.3, the BS consists of two antennas arrays dedicated for transmission and reception and hence the uplink and downlink channels estimation can be carried out separately.

6.3.1 LMMSE Channel Estimation

Decomposing the channel into an estimate and an error term entails a new formulation of the received signal vector

$$\begin{aligned}\mathbf{y}_q^u =&\alpha_u \sum_{\ell} \sum_{k=0}^{K_\ell - 1} \sqrt{G_{\ell,k} P_{\ell,k}} \left(\hat{\mathbf{h}}_{\ell,k} + \tilde{\mathbf{h}}_{\ell,k} \right) s_{\ell,k} + \alpha_u \mathbf{v} \\ &+ \alpha_u \alpha_d \sqrt{P_{\mathsf{SI}}} \sum_{k=0}^{K-1} \mathbf{H}_{\mathsf{SI}} \mathbf{f}_k s_k^d + \alpha_u \sqrt{P_{\mathsf{SI}}} \mathbf{H}_{\mathsf{SI}} \mathbf{q}_d + \mathbf{q}_u.\end{aligned} \tag{6.11}$$

Note that $\hat{\mathbf{h}}_{\ell,k}$ is the LMMSE channel estimate and $\tilde{\mathbf{h}}_{\ell,k}$ is the channel estimation error which is uncorrelated with the channel estimate and has variance given by

$$\mathsf{MMSE}_k = \frac{1}{1 + \frac{P_k}{P_u} \mathsf{SNR}_k^u}, \tag{6.12}$$

where P_d is the total power transmitted from the BS at the cell of interest and P_k is the power transmitted from the k-th user to the BS of interest.

Since the number of coherence tiles N_{c} is finite,[4] the number of orthogonal pilot dimensions $N_{\mathsf{p}} < N_{\mathsf{c}}$ is also finite. While it is possible to assign orthogonal pilots to K active users in certain cells, it is impossible to preserve pilot orthogonality over the entire network especially when having many cells. When the system runs out of orthogonal pilots, pilots have to be reused across network cells. Eventually, this reuse incurs interference or *pilot contamination* during the estimation stage. For each user, the BS of interest would like to estimate the quantity

$$\sqrt{\frac{P_k}{P_u} G_k} \mathbf{h}_k, \ k = 0, \ldots, K-1, \tag{6.13}$$

However, with pilot contamination, the BS ends up estimating

$$\sqrt{\frac{P_k}{P_u} G_k} \mathbf{h}_k + \sum_{\ell \in \mathcal{C}} \sqrt{\frac{P_{\ell,k}}{P_u} G_{\ell,k}} \mathbf{h}_{\ell,k}, \ k = 0, \ldots, K-1, \tag{6.14}$$

[4]The number of coherence tiles per fading block or also termed as the number of single-carrier symbols per block denoted by $N_{\mathsf{c}} = BT_{\mathsf{c}}$, where B is the bandwidth and T_{c} is the channel coherence time. If the fading blocks are IID, then T_{c} coincides with the coherence time of a stationary fading process, which leads to $N_{\mathsf{c}} = \left\lceil \frac{B}{2\nu} \right\rceil$ with ν is the velocity. Note that the expressions of the number of coherence tiles hold if the bandwidth is not too large [62, Chapter 3].

Thereby, the LMMSE channel estimate is given

$$\hat{\mathbf{h}}_k = \frac{\frac{P_k}{P_u}\mathsf{SNR}_k^u}{1+\frac{P_k}{P_u}\mathsf{SNR}_k^u+\sum_{\ell\in\mathcal{C}}\frac{P_{\ell,k}}{P_u}\mathsf{SNR}_{\ell,k}^u}\left(\mathbf{h}_k+\sum_{\ell\in\mathcal{C}}\sqrt{\frac{\frac{P_{\ell,k}}{P_u}\mathsf{SNR}_{\ell,k}^u}{\frac{P_k}{P_u}\mathsf{SNR}_k^u}}\mathbf{h}_{\ell,k}+\mathbf{v}_k^{'}\right), \tag{6.15}$$

and the variance of the LMMSE channel estimation error $\tilde{\mathbf{h}}_k$ becomes

$$\mathsf{MMSE}_k = \frac{1+\sum_{\ell\in\mathcal{C}}\frac{P_{\ell,k}}{P_u}\mathsf{SNR}_{\ell,k}^u}{1+\frac{P_k}{P_u}\mathsf{SNR}_k^u+\sum_{\ell\in\mathcal{C}}\frac{P_{\ell,k}}{P_u}\mathsf{SNR}_{\ell,k}^u}. \tag{6.16}$$

Proof. The proof is given in Appendix D.1. □

6.3.2 Data Transmission

By decomposing the interference into inter-cell and intra-cell components and applying the linear receive filter $\mathbf{w}_k^*$ at the k-th user ($y_{q,k}^u = \mathbf{w}_k^*\mathbf{y}_q^u$), the received signal at the BS of interest of the k-th user is given by (6.17).

$$\begin{aligned} y_{q,k}^u = &\underbrace{\alpha_u\sqrt{G_kP_k}\mathbf{w}_k^*\hat{\mathbf{h}}_ks_k}_{\text{Desired Signal}}+\underbrace{\alpha_u\sqrt{G_kP_k}\mathbf{w}_k^*\tilde{\mathbf{h}}_ks_k}_{\text{Channel Estimation Error}}+\underbrace{\alpha_u\sum_{\mathrm{k}=0}^{K-1}\sqrt{G_kP_{\mathrm{k}}}\mathbf{w}_k^*\left(\hat{\mathbf{h}}_k+\tilde{\mathbf{h}}_k\right)s_{\mathrm{k}}}_{\text{Intra-Cell Interference}} \\ &+\underbrace{\alpha_u\sum_{\ell\neq 0}\sum_{\mathrm{k}=0}^{K_\ell-1}\sqrt{G_{\ell,k}P_{\ell,\mathrm{k}}}\mathbf{w}_k^*\mathbf{h}_{\ell,k}s_{\ell,\mathrm{k}}}_{\text{Inter-Cell Interference}}+\underbrace{\alpha_u\alpha_d\sqrt{P_{\mathsf{SI}}}\sum_{\mathrm{k}=0}^{K-1}\mathbf{w}_k^*\mathbf{H}_{\mathsf{SI}}\mathbf{f}_{\mathrm{k}}s_{\mathrm{k}}^d}_{\text{Self-Interference due to Full-Duplexing}} \\ &+\underbrace{\alpha_u\sqrt{P_{\mathsf{SI}}}\mathbf{w}_k^*\mathbf{H}_{\mathsf{SI}}\mathbf{q}_d+\mathbf{w}_k^*\mathbf{q}_u}_{\text{Aggregate AQNM}}+\underbrace{\alpha_u\mathbf{w}_k^*\mathbf{v}}_{\text{Filtered Noise}} \end{aligned} \tag{6.17}$$

To distinguish pilot contamination from other sources of interference, we decompose the sources of inter-cell interference which results in the expression of the received signal (6.18).

$$
\begin{aligned}
y_{q,k}^{u} = & \underbrace{\alpha_u \sqrt{G_k P_k} \mathbf{w}_k^* \hat{\mathbf{h}}_k s_k}_{\text{Desired Signal}} + \underbrace{\alpha_u \sqrt{G_k P_k} \mathbf{w}_k^* \tilde{\mathbf{h}}_k s_k}_{\text{Channel Estimation Error}} + \underbrace{\alpha_u \sum_{\mathrm{k} \neq k} \sqrt{G_k P_{\mathrm{k}}} \mathbf{w}_{\mathrm{k}}^* \left(\hat{\mathbf{h}}_k + \tilde{\mathbf{h}}_k \right) s_{\mathrm{k}}}_{\text{Intra-Cell Interference}} \\
& + \underbrace{\alpha_u \sum_{\substack{\ell \neq 0 \\ \ell \notin \mathcal{C}}} \sum_{\mathrm{k}=0}^{K_\ell - 1} \sqrt{G_{\ell,k} P_{\ell,\mathrm{k}}} \mathbf{w}_{\ell,\mathrm{k}}^* \mathbf{h}_{\ell,k} s_{\ell,\mathrm{k}} + \alpha_u \sum_{\ell \in \mathcal{C}} \sum_{\substack{\mathrm{k}=0 \\ \mathrm{k} \neq k}}^{K_\ell - 1} \sqrt{G_{\ell,k} P_{\ell,\mathrm{k}}} \mathbf{w}_{\ell,\mathrm{k}}^* \mathbf{h}_{\ell,k} s_{\ell,\mathrm{k}}}_{\text{Inter-Cell Interference}} \\
& + \underbrace{\alpha_u \alpha_d \sqrt{P_{\mathsf{SI}}} \sum_{\mathrm{k}=0}^{K-1} \mathbf{w}_k^* \mathbf{H}_{\mathsf{SI}} \mathbf{f}_{\mathrm{k}} s_{\mathrm{k}}^d}_{\text{Self-Interference due to Full-Duplexing}} + \underbrace{\alpha_u \sum_{\ell \in \mathcal{C}} \sqrt{G_{\ell,k} P_{\ell,k}} \mathbf{w}_{\ell,k}^* \mathbf{h}_{\ell,k} s_{\ell,k}}_{\text{Pilot Contamination}} \\
& + \underbrace{\alpha_u \sqrt{P_{\mathsf{SI}}} \mathbf{w}_k^* \mathbf{H}_{\mathsf{SI}} \mathbf{q}_d + \mathbf{w}_k^* \mathbf{q}_u}_{\text{Aggregate AQNM}} + \underbrace{\alpha_u \mathbf{w}_k^* \mathbf{v}}_{\text{Filtered Noise}}
\end{aligned}
\tag{6.18}
$$

Theorem 6. For LMMSE channel estimation, the output SQINR of the k-th uplink user is given by (6.19).

$$
\mathsf{sqinr}_k = \frac{\alpha_u^2 \frac{P_k}{P_u} \mathsf{SNR}_k^u |\mathbf{w}_k^* \hat{\mathbf{h}}_k|^2}{\mathsf{den}_u}, \tag{6.19}
$$

where den_u is given by (6.20).

$$
\begin{aligned}
\mathsf{den}_u = & \alpha_u^2 \left(1 + \sum_{\mathrm{k} \neq k} \frac{P_{\mathrm{k}}}{P_u} \mathsf{SNR}_{\mathrm{k}}^u \mathsf{MMSE}_{\mathrm{k}} + \sum_{\substack{\ell \neq 0 \\ \ell \notin \mathcal{C}}} \frac{P_{\ell,\mathrm{k}}}{P_u} \mathsf{SNR}_{\ell,\mathrm{k}}^u + \sum_{\ell \in \mathcal{C}} \sum_{\substack{\mathrm{k}=0 \\ \mathrm{k} \neq k}}^{K_\ell - 1} \frac{P_{\ell,\mathrm{k}}}{P_u} \mathsf{SNR}_{\ell,\mathrm{k}}^u \right) \|\mathbf{w}_k\|^2 \\
& + \alpha_u^2 \sum_{\mathrm{k} \neq k} \frac{P_{\mathrm{k}}}{P_u} \mathsf{SNR}_k^u \left| \mathbf{w}_k^* \hat{\mathbf{h}}_{\mathrm{k}} \right|^2 + \alpha_u^2 \sum_{\ell \in \mathcal{C}} \frac{P_{\ell,k}}{P_u} \mathsf{SNR}_{\ell,k}^u \mathbf{w}_k^* \mathbb{E} \left[\mathbf{h}_{\ell,k} \mathbf{h}_{\ell,k}^* | \mathbf{w}_k \right] \mathbf{w}_k \\
& + \frac{\alpha_u^2 \alpha_d^2}{\sigma^2} P_{\mathsf{SI}} \sum_{\mathrm{k}=0}^{K-1} |\mathbf{w}_k^* \mathbf{H}_{\mathsf{SI}} \mathbf{f}_{\mathrm{k}}|^2 + \frac{\alpha_u^2}{\sigma^2} P_{\mathsf{SI}} |\mathbf{w}_k^* \mathbf{H}_{\mathsf{SI}} \mathbf{q}_d|^2 + \frac{1}{\sigma^2} |\mathbf{w}_k^* \mathbf{q}_u|^2 .
\end{aligned}
\tag{6.20}
$$

Proof. The proof is given in Appendix 6. □

If the channel estimation is perfect, the pilot contamination is negligible and inter-cell interference is subsumed within the noise.

Proposition 2. With perfect CSI, without full-duplexing ($\mathbf{H}_{\mathsf{SI}} = \mathbf{0}$) and without pilot contamination, we retrieve the same SQINR expression for reverse link derived by [34].

Averaging over the channel realization $\hat{\mathbf{h}}_k$ and hence $\mathbf{w}_k$, the reverse link user spectral efficiency is provided by

$$\frac{\mathcal{I}_k}{B} = \mathbb{E}\left[\log\left(1 + \mathsf{sqinr}_k\right)\right], \ k = 0, \ldots, K-1, \tag{6.21}$$

If we introduce the pilot overhead, we would need to aggregate the reverse and forward spectral efficiencies or, in its place, a partition of the overhead between the reverse and forward links. Thereby, the effective reverse link spectral efficiency becomes

$$\frac{\mathcal{I}_k^{\mathsf{eff}}}{B} = \left(1 - \beta\frac{N_{\mathsf{p}}}{N_{\mathsf{c}}}\right)\mathbb{E}\left[\log\left(1 + \mathsf{sqinr}_k\right)\right], \ k = 0, \ldots, K-1. \tag{6.22}$$

where $\beta \in [0, 1]$ is the fraction of the pilot overhead ascribed to the reverse link.

6.3.3 Channel Hardening

One of the benefits of having massive number of antennas is the hardening of the filtered signals. Suppose that, rather than $\mathbf{w}_k^*\hat{\mathbf{h}}_k$ (where $\hat{\mathbf{h}}$ is the estimate of $\mathbf{h}$), the decoder regards $\mathbb{E}[\mathbf{w}_k^*\mathbf{h}_k]$ as the filtered channel. The receiver can compute this value from the channel statistics while the fluctuation of the filtered signal around the mean can be treated as SI. Thereby, (6.18) becomes (6.23).

$$y_{q,k}^{u} = \underbrace{\alpha_u \sqrt{G_k P_k}\mathbb{E}[\mathbf{w}_k^* \mathbf{h}_k] s_k}_{\text{Desired Signal}} + \underbrace{\alpha_u \sum_{\mathrm{k}\neq k} \sqrt{G_k P_{\mathrm{k}}} \mathbf{w}_k^* \mathbf{h}_k s_{\mathrm{k}}}_{\text{Intra-Cell Interference}} + \underbrace{\alpha_u \sum_{\ell\neq 0} \sum_{\mathrm{k}=0}^{K_\ell - 1} \sqrt{G_{\ell,k} P_{\ell,\mathrm{k}}} \mathbf{w}_k^* \mathbf{h}_{\ell,k} s_{\ell,\mathrm{k}}}_{\text{Inter-Cell Interference}}$$
$$\overbrace{+ \underbrace{\alpha_u \sqrt{G_k P_k}\left(\mathbf{w}_k^* \mathbf{h}_k - \mathbb{E}[\mathbf{w}_k^* \mathbf{h}_k]\right) s_k}_{\text{Channel Estimation Error}} + \underbrace{\alpha_u \alpha_d \sqrt{P_{\mathsf{SI}}} \sum_{\mathrm{k}=0}^{K-1} \mathbf{w}_k^* \mathbf{H}_{\mathsf{SI}} \mathbf{f}_{\mathrm{k}} s_{\mathrm{k}}^d}_{\text{Self-Interference due to Full-Duplexing}}}^{\text{Aggregate Self-Interference}}$$
$$+ \underbrace{\alpha_u \sqrt{P_{\mathsf{SI}}} \mathbf{w}_k^* \mathbf{H}_{\mathsf{SI}} \mathbf{q}_d + \mathbf{w}_k^* \mathbf{q}_u}_{\text{Aggregate AQNM}} \underbrace{\alpha_u \mathbf{w}_k^* \mathbf{v}}_{\text{Filtered Noise}} \tag{6.23}$$

When considering pilot contamination, the received signal of the k-th user can be reformulated as (6.24).

$$y_{q,k}^{u} = \underbrace{\alpha_u \sqrt{G_k P_k}\mathbb{E}[\mathbf{w}_k^* \mathbf{h}_k] s_k}_{\text{Desired Signal}} + \underbrace{\alpha_u \sqrt{G_k P_k}\left(\mathbf{w}_k^* \mathbf{h}_k - \mathbb{E}[\mathbf{w}_k^* \mathbf{h}_k]\right) s_k}_{\text{Channel Estimation Error}} + \underbrace{\alpha_u \sum_{\mathrm{k}\neq k} \sqrt{G_k P_{\mathrm{k}}} \mathbf{w}_k^* \mathbf{h}_k s_{\mathrm{k}}}_{\text{Intra-Cell Interference}}$$
$$+ \underbrace{\alpha_u \sum_{\ell\in\mathcal{C}} \sqrt{G_{\ell,k} P_{\ell,k}} \mathbf{w}_k^* \mathbf{h}_{\ell,k} s_{\ell,k}}_{\text{Pilot Contamination}} + \underbrace{\alpha_u \alpha_d \sqrt{P_{\mathsf{SI}}} \sum_{\mathrm{k}=0}^{K-1} \mathbf{w}_k^* \mathbf{H}_{\mathsf{SI}} \mathbf{f}_{\mathrm{k}} s_{\mathrm{k}}^d}_{\text{Self-Interference due to Full-Duplexing}}$$
$$\underbrace{+ \alpha_u \sum_{\substack{\ell\neq 0 \\ \ell\notin\mathcal{C}}} \sum_{\mathrm{k}=0}^{K_\ell - 1} \sqrt{G_{\ell,k} P_{\ell,\mathrm{k}}} \mathbf{w}_k^* \mathbf{h}_{\ell,k} s_{\ell,\mathrm{k}} + \alpha_u \sum_{\ell\in\mathcal{C}} \sum_{\substack{\mathrm{k}=0 \\ \mathrm{k}\neq k}}^{K_\ell - 1} \sqrt{G_{\ell,k} P_{\ell,\mathrm{k}}} \mathbf{w}_k^* \mathbf{h}_{\ell,k} s_{\ell,\mathrm{k}}}_{\text{Inter-Cell Interference}}$$
$$+ \underbrace{\alpha_u \sqrt{P_{\mathsf{SI}}} \mathbf{w}_k^* \mathbf{H}_{\mathsf{SI}} \mathbf{q}_d + \mathbf{w}_k^* \mathbf{q}_u}_{\text{Aggregate AQNM}} + \underbrace{\alpha_u \mathbf{w}_k^* \mathbf{v}}_{\text{Filtered Noise}} \tag{6.24}$$

Theorem 7. For channel hardening, the output SQINR of the k-th uplink user is given by

$$\overline{\mathsf{sqinr}}_k = \frac{\alpha_u^2 \frac{P_k}{P_u} \mathsf{SNR}_k^u \left|\mathbb{E}\left[\mathbf{w}_k^* \mathbf{h}_k\right]\right|^2}{\overline{\mathsf{den}}_u}, \tag{6.25}$$

where $\overline{\mathsf{den}}_u$ is given by (6.26).

$$\begin{aligned}\overline{\mathsf{den}}_u =&\alpha_u^2 \frac{P_k}{P_u}\mathsf{SNR}_k^u \mathsf{var}\left[\mathbf{w}_k^* \mathbf{h}_k\right] + \alpha_u^2 \sum_{\mathrm{k}\neq k} \frac{P_{\mathrm{k}}}{P_u}\mathsf{SNR}_{\mathrm{k}}^u \mathbb{E}\left[|\mathbf{w}_k^* \mathbf{h}_{\mathrm{k}}|^2\right] + \alpha_u^2 \sum_{\ell\in\mathcal{C}} \frac{P_{\ell,k}}{P_u}\mathsf{SNR}_{\ell,k}^u \mathbb{E}\left[|\mathbf{w}_k^* \mathbf{h}_{\ell,\mathrm{k}}|^2\right] \\ &+ \alpha_u^2 \left(1 + \sum_{\substack{\ell\neq 0 \\ \ell\notin\mathcal{C}}} \sum_{\mathrm{k}=0}^{K_\ell - 1} \frac{P_{\ell,\mathrm{k}}}{P_u}\mathsf{SNR}_{\ell,k}^u + \sum_{\ell\in\mathcal{C}} \sum_{\substack{\mathrm{k}=0 \\ \mathrm{k}\neq k}}^{K_\ell - 1} \frac{P_{\ell,\mathrm{k}}}{P_u}\mathsf{SNR}_{\ell,\mathrm{k}}^u\right) \mathbb{E}\left[\|\mathbf{w}_k\|^2\right] \\ &+ \frac{\alpha_u^2}{\sigma^2} P_{\mathsf{SI}} \mathbb{E}\left[|\mathbf{w}_k^* \mathbf{H}_{\mathsf{SI}} \mathbf{q}_d|^2\right] + \frac{\alpha_d^2 \alpha_u^2}{\sigma^2} P_{\mathsf{SI}} \sum_{\mathrm{k}=0}^{K-1} \mathbb{E}[|\mathbf{w}_k^* \mathbf{H}_{\mathsf{SI}} \mathbf{f}_{\mathrm{k}}|^2] + \frac{\alpha_u^2}{\sigma^2} \mathbb{E}[|\mathbf{w}_k^* \mathbf{q}_u|^2].\end{aligned} \tag{6.26}$$

With $\overline{\mathsf{sqinr}}_k,\ k = 0, \ldots K-1$ being locally stable, the evaluation of the gross spectral efficiencies do not require averaging over the fading realizations, but rather it is directly computed by

$$\frac{\bar{\mathcal{I}}_k}{B} = \log\left(1 + \overline{\mathsf{sqinr}}_k\right),\ k = 0, \ldots, K-1. \tag{6.27}$$

6.3.4 Matched Filter Receiver

A matched filter for user k satisfies $\mathbf{w}_k^{\mathsf{MF}} \propto \hat{\mathbf{h}}_k$. This entails the following expression as [62, Eq. (10.48)]

$$\mathbf{w}_k^{\mathsf{MF}} = \sqrt{\frac{\frac{P_k}{P_u}\mathsf{SNR}_k^u}{1 + \frac{P_k}{P_u}\mathsf{SNR}_k^u + \sum_{\ell\in\mathcal{C}} \frac{P_{\ell,k}}{P_u}\mathsf{SNR}_{\ell,k}^u}} \left(\mathbf{h}_k + \sum_{\ell\in\mathcal{C}} \sqrt{\frac{\frac{P_{\ell,k}}{P_u}\mathsf{SNR}_{\ell,k}^u}{\frac{P_k}{P_u}\mathsf{SNR}_k^u}} \mathbf{h}_{\ell,k} + \mathbf{v}_k'\right). \tag{6.28}$$

In above equation, the scaling is important to operate the decoder, but immaterial otherwise because it equally affects the received signal as well as the noise and interference. The scaling satisfies $\mathbb{E}\left[\|\mathbf{w}_k^{\mathsf{MF}}\|^2\right] = N_{\mathsf{a}}$ and the entries of $\mathbf{v}_k'$ have power of $1/\left(\frac{P_k}{P_u}\mathsf{SNR}_k^u\right)$ as discussed in [62, Section 10.3.2]. The pilots are assumed to be regular and aligned at every cell.

Corollary 1. If $\mathbf{x}$ and $\mathbf{y}$ are jointly Gaussian, i.e.,

$$\begin{bmatrix}\mathbf{y}\\ \mathbf{x}\end{bmatrix} \sim \mathcal{N}_{\mathbb{C}}\left(\begin{bmatrix}\mu_{\mathbf{y}}\\ \mu_{\mathbf{x}}\end{bmatrix}, \begin{bmatrix}\mathbf{R}_{\mathbf{y}} & \mathbf{R}_{\mathbf{yx}}\\ \mathbf{R}_{\mathbf{xy}} & \mathbf{R}_{\mathbf{x}}\end{bmatrix}\right) \tag{6.29}$$

The random variable $\mathbf{y}|\mathbf{x} = \mathsf{x}$ is complex Gaussian with mean

$$\mu = \mathbf{R}_{\mathbf{yx}}\mathbf{R}_{\mathbf{x}}^{-1}\mathsf{x} \tag{6.30}$$

and covariance

$$\mathbf{R} = \mathbf{R}_{\mathbf{y}} - \mathbf{R}_{\mathbf{yx}}\mathbf{R}_{\mathbf{x}}^{-1}\mathbf{R}_{\mathbf{xy}}. \tag{6.31}$$

We will use Corollary 1 later to prove the results of Theorem 8.

6.3.4.1 LMMSE Channel Estimation

In this part, we will derive the output SQINR of the k-th uplink user under LMMSE channel estimation and with a matched filter receiver.

Theorem 8. For LMMSE channel estimation and with a matched filter receiver, the output SQINR of the k-th uplink user is given by (6.32).

$$\mathsf{sqinr}_k^{\mathsf{MF}} = \frac{\alpha_u^2 \frac{P_k}{P_u}\mathsf{SNR}_k^u |\mathbf{w}_k^{\mathsf{MF}*}\hat{\mathbf{h}}_k|^2}{\mathsf{den}_u^{\mathsf{MF}}} \tag{6.32}$$

where $\mathsf{den}_u^{\mathsf{MF}}$ is given by (6.33).

$$\begin{aligned}\mathsf{den}_u^{\mathsf{MF}} =& \alpha_u^2 \sum_{\mathrm{k}\neq k} \frac{P_{\mathrm{k}}}{P_u}\mathsf{SNR}_{\mathrm{k}}^u |\mathbf{w}_k^{\mathsf{MF}*}\hat{\mathbf{h}}_{\mathrm{k}}|^2 + \alpha_u^2 \left(1 + \sum_{\mathrm{k}=0}^{K-1} \frac{P_{\mathrm{k}}}{P_u}\mathsf{SNR}_{\mathrm{k}}^u \mathsf{MMSE}_{\mathrm{k}} + \sum_{\ell\neq 0}\sum_{\mathrm{k}=0}^{K-1} \frac{P_{\ell,\mathrm{k}}}{P_u}\mathsf{SNR}_{\ell,\mathrm{k}}^u\right) \left\|\mathbf{w}_k^{\mathsf{MF}}\right\|^2 \\ &+ \alpha_u^2 \frac{\sum_{\ell\in\mathcal{C}} \left(\frac{P_{\ell,k}}{P_u}\mathsf{SNR}_{\ell,k}\right)^2}{1 + \frac{P_k}{P_u}\mathsf{SNR}_k^u + \sum_{\ell\in\mathcal{C}} \frac{P_{\ell,k}}{P_u}\mathsf{SNR}_{\ell,k}^u} \left(\left\|\mathbf{w}_k^{\mathsf{MF}}\right\|^4 - \left\|\mathbf{w}_k^{\mathsf{MF}}\right\|^2\right) + \frac{\alpha_u^2\alpha_d^2}{\sigma^2} P_{\mathsf{SI}} \sum_{\mathrm{k}=0}^{K-1} \left|\mathbf{w}_k^{\mathsf{MF}*}\mathbf{H}_{\mathsf{SI}}\mathbf{f}_{\mathrm{k}}\right|^2 \\ &+ \frac{\alpha_u^2}{\sigma^2} P_{\mathsf{SI}} \left|\mathbf{w}_k^{\mathsf{MF}*}\mathbf{H}_{\mathsf{SI}}\mathbf{q}_d\right|^2 + \frac{1}{\sigma^2}\left|\mathbf{w}_k^{\mathsf{MF}*}\mathbf{q}_u\right|^2\end{aligned} \tag{6.33}$$

Proof. The proof of Theorem 8 is given by Appendix D.3. □

Proposition 3. With LMMSE channel estimation, without full-duplexing, with full-resolution ($\alpha_u = \alpha_d = 1$) and with a matched filter receiver, we exactly retrieve the same output SINR of the k-th uplink user given by [62, Eq. (10.50)].

6.3.4.2 Channel Hardening

We adopt the matched filter receiver to design the combiner $\mathbf{w}_k,\ k = 0, \ldots, K^u - 1$.

Corollary 2. The matched filter receiver $\mathbf{w}_k^{\mathsf{MF}}$ (transmitter $\mathbf{f}_k^{\mathsf{MF}}$) has the following properties [53, 40]

1. $\mathbb{E}\left[\|\mathbf{w}_k^{\mathsf{MF}}\|^2\right] = \mathbb{E}\left[\|\mathbf{f}_k^{\mathsf{MF}}\|^2\right] = N_{\mathsf{a}}$.
2. $\mathbb{E}\left[\|\mathbf{w}_k^{\mathsf{MF}}\|^4\right] = \mathbb{E}\left[\|\mathbf{f}_k^{\mathsf{MF}}\|^4\right] = N_{\mathsf{a}}^2 + N_{\mathsf{a}}$.
3. $\mathbb{E}\left[\left|\mathbf{w}_k^{\mathsf{MF}*}\mathbf{h}_{\mathrm{k}}\right|^2\right] = \mathbb{E}\left[\left|\mathbf{h}_{\mathrm{k}}^*\mathbf{f}_k^{\mathsf{MF}}\right|^2\right] = N_{\mathsf{a}}$.

Theorem 9. For channel hardening and a matched filter receiver, the output SQINR of the k-th uplink user is given by (6.34).

$$\overline{\mathsf{sqinr}}_k^{\mathsf{MF}} = \frac{\alpha_u^2 \left(\frac{P_k}{P_u}\mathsf{SNR}_k^u\right)^2 N_{\mathsf{a}}^2}{\left(1 + \frac{P_k}{P_u}\mathsf{SNR}_k^u + \sum_{\ell \in \mathcal{C}} \frac{P_{\ell,k}}{P_u}\mathsf{SNR}_{\ell,k}^u\right)\overline{\mathsf{den}}_u^{\mathsf{MF}}} \tag{6.34}$$

where $\overline{\mathsf{den}}_u^{\mathsf{MF}}$ is given by (6.35).

$$\begin{aligned}\overline{\mathsf{den}}_u^{\mathsf{MF}} =& \alpha_u^2 N_{\mathsf{a}} \left(1 + \sum_{\ell} \sum_{\mathrm{k}=0}^{K_\ell^u - 1} \frac{P_{\ell,\mathrm{k}}}{P_u}\mathsf{SNR}_{\ell,\mathrm{k}}^u\right) + \alpha_u^2 N_{\mathsf{a}}^2 \frac{\sum_{\ell \in \mathcal{C}} \left(\frac{P_{\ell,k}}{P_u}\mathsf{SNR}_{\ell,k}^u\right)^2}{1 + \frac{P_k}{P_u}\mathsf{SNR}_k^u + \sum_{\ell \in \mathcal{C}} \frac{P_{\ell,k}}{P_u}\mathsf{SNR}_{\ell,k}^u} \\ &+ \alpha_u^2 \alpha_d (1 - \alpha_d) K^d N_{\mathsf{a}}^2 \mathsf{INR} + \alpha_u^2 \alpha_d^2 K^d N_{\mathsf{a}}^2 \mathsf{INR} \\ &+ N_{\mathsf{a}} \alpha_u (1 - \alpha_u) \left[2\frac{P_k}{P_u}\mathsf{SNR}_k^u + \sum_{\mathrm{k} \neq k} \frac{P_{\mathrm{k}}}{P_u}\mathsf{SNR}_{\mathrm{k}}^u + \sum_{\ell \neq 0} \sum_{\mathrm{k}} \frac{P_{\ell,\mathrm{k}}}{P_u}\mathsf{SNR}_{\ell,\mathrm{k}}^u + \alpha_d N_{\mathsf{a}} \mathsf{INR} + 1\right].\end{aligned} \tag{6.35}$$

Here, $\mathsf{INR} = P_{\mathsf{SI}}\mu_{\mathsf{SI}}^2/\sigma^2$.

Proof. The proof of Theorem 9 is provided in Appendix D.4 □

Corollary 3. To further characterize the spectral efficiency, we derive a new bound using the following formula [26, Eq. (35)]. Assuming statistical independence between x and y, we have

$$\mathbb{E}\left[\log\left(1+\frac{x}{y}\right)\right] \cong \log\left(1+\frac{\mathbb{E}[x]}{\mathbb{E}[y]}\right). \tag{6.36}$$

Lemma 2. Assuming perfect CSI, and applying Corollary 3, the output SQINR of the k-th uplink user (6.34) becomes

$$\overline{\mathsf{sqinr}}_k^{\mathsf{MF}} = \frac{\left(\frac{P_k}{P_u}\mathsf{SNR}_k^u\right)^2 (N_{\mathsf{a}}^2+N_{\mathsf{a}})}{\left(1+\frac{P_k}{P_u}\mathsf{SNR}_k^u+\sum_{\ell\in\mathcal{C}}\frac{P_{\ell,k}}{P_u}\mathsf{SNR}_{\ell,k}^u\right)\overline{\mathsf{den}}_u^{\mathsf{MF}}}. \tag{6.37}$$

In the proof of Theorem 9 in Appendix D.4, the terms in (6.35) related to the channel estimation error and pilot contamination vanish because the CSI is perfect.

Proposition 4. Considering a single-cell multiuser system (without any inter-cell interference) with perfect CSI, Corollary 3 entails the results for the reverse link in [40].

Proposition 5. With channel hardening, without full-duplexing, with full-resolution and with a matched filter receiver, the output SINR of the k-th uplink user is given by (6.38).

$$\overline{\mathsf{sinr}}_k^{\mathsf{MF}} = \frac{\frac{N_{\mathsf{a}}}{1+\frac{P_k}{P_u}\mathsf{SNR}_k^u+\sum_{\ell\in\mathcal{C}}\frac{P_{\ell,k}}{P_u}\mathsf{SNR}_{\ell,k}^u}\left(\frac{P_k}{P_u}\mathsf{SNR}_k^u\right)^2}{1+\sum_{\ell}\sum_{\mathrm{k}=0}^{K_\ell^u-1}\frac{P_{\ell,\mathrm{k}}}{P_u}\mathsf{SNR}_{\ell,\mathrm{k}}^u+\frac{N_{\mathsf{a}}}{1+\frac{P_k}{P_u}\mathsf{SNR}_k^u+\sum_{\ell\in\mathcal{C}}\frac{P_{\ell,k}}{P_u}\mathsf{SNR}_{\ell,k}^u}\sum_{\ell\in\mathcal{C}}\left(\frac{P_{\ell,k}}{P_u}\mathsf{SNR}_{\ell,k}^u\right)^2}. \tag{6.38}$$

Remark 13. Note that Proposition 5 entails the same result for reverse link derived in [62, Eq. (10.63)].

Lemma 3. When the power (SNR_k^u) of the k-th uplink user goes to infinity, the output SINR (6.38) converges to N_{a}.

This SINR limit, caused by the channel estimation error, is incurred by the users with favorable conditions, i.e., having small shadowing and short distances from the associated BS. However, this limit is irreducible and cannot be overtaken by a matched filter receiver reliant on channel hardening.

Neglecting pilot contamination, the output SINR expression (6.38) can be reduced to

$$\overline{\mathsf{sinr}}_k^{\mathsf{MF}} \approx \frac{N_{\mathsf{a}} \left(\frac{P_k}{P_u}\mathsf{SNR}_k^u\right)^2}{\left(1+\frac{P_k}{P_u}\mathsf{SNR}_k^u\right)\left(1+\sum_{\ell}\sum_{\mathrm{k}=0}^{K_\ell^u-1}\frac{P_{\ell,\mathrm{k}}}{P_u}\mathsf{SNR}_{\ell,\mathrm{k}}^u\right)}. \tag{6.39}$$

6.3.5 Fractional Power Control

In an outdoor environment, the received power is highly degraded by pathloss and shadowing; hence, we adopt a slow power control regime such as fractional power control to compensate pathloss. Such a power adaptation technique is characterized by a parameter $\vartheta \in [0,1]$ to control the received power of the UEs. Formally, $\frac{P_{\ell,0}}{P_u}, \ldots, \frac{P_{\ell,K_\ell^u-1}}{P_u}$ must be optimized at each cell ℓ on the basis of that cell's weighted sum spectral efficiency. Consequently, the power control factor is

$$\frac{P_{\ell,k}}{P_u} \propto \frac{1}{G_{\ell,(\ell,k)}^{\vartheta}},\ k=0,\ldots,K_\ell^u-1. \tag{6.40}$$

By saying $\frac{P_{\ell,k}}{P_u} \leq 1,\ k=0,\ldots,K_\ell^u-1$, we mean the reverse link transmit power must not exceed its maximum value. If $\vartheta = 0$, all UEs have the same transmit power and no power control regime is adopted. When $\vartheta = 1$, the pathloss represented by the pathloss exponent is completely compensated.

6.4 Forward Link Analysis

The signal transmitted by the ℓ-th BS is

$$\mathbf{x}_\ell = \sum_{k=0}^{K_\ell^d-1} \sqrt{\frac{P_{\ell,k}}{N_{\mathsf{a}}}}\mathbf{f}_{\ell,k}s_{\ell,k}, \tag{6.41}$$

where $P_{\ell,k}$ is the power allocated to the data symbol $s_{\ell,k} \sim \mathcal{N}_{\mathbb{C}}(0,1)$, which is precoded by $\mathbf{f}_{\ell,k}$ and intended for its k-th user. The power allocation satisfies

$$\sum_{k=0}^{K_\ell^d-1} P_{\ell,k} = P_d, \tag{6.42}$$

where P_d is the forward link power per cell. Since the BS operates in FD mode, the reverse link users are only corrupted by the SI while the forward link users are SI-free. But since the reverse link users users are sending simultaneously when the forward link users users are receiving, the latter are vulnerable to the IUI caused by the reverse link users.

Upon data transmission from the BS of interest, the k-th user observes the following quantized received signal from the BS of interest as

$$\begin{aligned} y_{q,k}^d =& \alpha_d \sum_{\ell} \sum_{\mathrm{k}=0}^{K_\ell^d-1} \sqrt{\frac{G_{\ell,k} P_{\ell,\mathrm{k}}}{N_{\mathsf{a}}}} \mathbf{h}_{\ell,k}^* \mathbf{f}_{\ell,\mathrm{k}} s_{\ell,\mathrm{k}} + \sum_{\ell} \sum_{\mathrm{k}=0}^{K_\ell^d-1} \sqrt{\frac{G_{\ell,k} P_{\ell,\mathrm{k}}}{N_{\mathsf{a}}}} \mathbf{h}_{\ell,k}^* \mathbf{q}_{d,\ell} \\ &+ \sum_{\ell} \sum_{\mathrm{k}=0}^{K_\ell^u-1} \sqrt{T_{(\ell,\mathrm{k}),k} P_{\ell,\mathrm{k}}^u} \mathbf{g}_{(\ell,\mathrm{k}),k} s_{\ell,\mathrm{k}}^u + v_k. \end{aligned} \tag{6.43}$$

In the reverse link, the LMMSE channel estimates are available at the BSs from the corresponding pilot observations. Therefore, exploiting the channel reciprocity in TDD, we can skip the channel estimation at the UEs. Nevertheless, the channel estimation at the UEs can be carried out by sending precoded forward pilots, using at least one precoded pilot per UE and per coherence time (block of samples).

In the rest of this section, we focus on the analysis of channel-hardening reliant receivers.

6.4.1 Channel Hardening

Since we consider receivers taking advantage of channel hardening, the k-th user served by the BS of interest regards $\mathbb{E}[\mathbf{h}_k^* \mathbf{f}_k]$ as its precoded channel wherein the small-scale fading is averaged. The variation of the actual precoded channel around the mean incurs SI, such that (6.43) can be formulated as (6.44).

$$
\begin{aligned}
y_{q,k}^{d} = & \underbrace{\alpha_d \sqrt{\frac{G_k P_k}{N_{\mathsf{a}}}} \mathbb{E}[\mathbf{h}_k^* \mathbf{f}_k] s_k}_{\text{Desired Signal}} + \underbrace{\alpha_d \sqrt{\frac{G_k P_k}{N_{\mathsf{a}}}} \left(\mathbf{h}_k^* \mathbf{f}_k - \mathbb{E}[\mathbf{h}_k^* \mathbf{f}_k]\right) s_k}_{\text{Channel Estimation Error}} + \underbrace{\alpha_d \sum_{\mathrm{k} \neq k} \sqrt{\frac{G_k P_{\mathrm{k}}}{N_{\mathsf{a}}}} \mathbf{h}_k^* \mathbf{f}_{\mathrm{k}} s_{\mathrm{k}}}_{\text{Intra-Cell Interference}} \\
& + \underbrace{\sum_{\ell} \sum_{\mathrm{k}=0}^{K_\ell^d - 1} \sqrt{\frac{G_{\ell,k} P_{\ell,\mathrm{k}}}{N_{\mathsf{a}}}} \mathbf{h}_{\ell,k}^* \mathbf{q}_\ell}_{\text{Aggregate AQNM}} + \underbrace{\alpha_d \sum_{\ell \neq 0} \sum_{\mathrm{k}=0}^{K_\ell^d - 1} \sqrt{\frac{G_{\ell,k} P_{\ell,\mathrm{k}}}{N_{\mathsf{a}}}} \mathbf{h}_{\ell,k}^* \mathbf{f}_{\ell,\mathrm{k}} s_{\ell,\mathrm{k}}}_{\text{Inter-Cell Interference}} \\
& + \underbrace{\sum_{\mathrm{k} \neq k} \sqrt{T_{\mathrm{k},k} P_{\ell,\mathrm{k}}^u} \mathbf{g}_{\mathrm{k},k} s_{\mathrm{k},u}}_{\text{Same Cell Inter-User Interference}} + \underbrace{\sum_{\ell \neq 0} \sum_{\mathrm{k}=0}^{K_\ell^u - 1} \sqrt{T_{(\ell,\mathrm{k}),k} P_{\ell,\mathrm{k}}^u} \mathbf{g}_{(\ell,\mathrm{k}),k} s_{\ell,\mathrm{k},u}}_{\text{Other Cells Inter-User Interference}} + \underbrace{v_k}_{\text{Noise}}
\end{aligned}
\tag{6.44}
$$

Theorem 10. For channel hardening, the output SQINR of the k-th downlink user is given by (6.45).

$$
\overline{\mathsf{sqinr}}_k = \frac{\alpha_d^2 \frac{P_k}{P_d N_{\mathsf{a}}} \mathsf{SNR}_k^d \left| \mathbb{E}\left[\mathbf{h}_k^* \mathbf{f}_k\right] \right|^2}{\overline{\mathsf{den}}_d} \tag{6.45}
$$

Here, $\overline{\mathsf{den}}_d$ is expressed by (6.46).

$$
\begin{aligned}
\overline{\mathsf{den}}_d = & \alpha_d^2 \frac{P_k}{P_d N_{\mathsf{a}}} \mathsf{SNR}_k^d \mathsf{var}\left[\mathbf{h}_k^* \mathbf{f}_k\right] + \alpha_d^2 \sum_{\mathrm{k} \neq k} \frac{P_{\mathrm{k}}}{P_d N_{\mathsf{a}}} \mathsf{SNR}_k^d \mathbb{E}\left[\left|\mathbf{h}_k^* \mathbf{f}_{\mathrm{k}}\right|^2\right] + \alpha_d^2 \sum_{\ell \neq 0} \sum_{\mathrm{k}=0}^{K_\ell^d - 1} \frac{P_{\ell,\mathrm{k}}}{P_d N_{\mathsf{a}}} \mathsf{SNR}_{\ell,k}^d \mathbb{E}\left[\left|\mathbf{h}_{\ell,k}^* \mathbf{f}_{\ell,\mathrm{k}}\right|^2\right] \\
& + \sum_{\ell} \sum_{\mathrm{k}=0}^{K_\ell^u - 1} \frac{P_{\ell,\mathrm{k}}^u}{P_u} \mathsf{SNR}_{(\ell,\mathrm{k}),k}^{\mathsf{iui}} \mathbb{E}\left[\left|\mathbf{g}_{(\ell,\mathrm{k}),k}\right|^2\right] + \sum_{\ell} \frac{P_{\ell,k}}{P_d N_{\mathsf{a}}} \mathsf{SNR}_{\ell,k}^d \mathbb{E}\left[\left|\mathbf{h}_{\ell,k}^* \mathbf{q}_{d,\ell}\right|^2\right] + 1.
\end{aligned}
\tag{6.46}
$$

where $\mathsf{SNR}_{(\ell,\mathrm{k}),k}^{\mathsf{iui}} = P_u T_{(\ell,\mathrm{k}),k} / \sigma^2$.

Proof. The proof is straightforward by evaluating the expected value of the power of each term. The expected value of the power of channel estimation error is nothing but the variance of the precoded channel. The derivation cannot go further because this result is considered for any given BS precoder. Later in Thereom 11, we will specify the BS precoder and hence the derivation will be more intricate. □

6.4.2 Matched Filter Precoder

The ℓ-th BS gathers channel estimates $\hat{\mathbf{h}}_{\ell,(\ell,0)}, \ldots, \hat{\mathbf{h}}_{\ell,(\ell,K_\ell^d-1)}$ from the reverse link pilots transmitted by its own users. With a matched filter transmitter, the precoders at cell ℓ are given by

$$\mathbf{f}_{\ell,k}^{\mathsf{MF}} = \sqrt{N_{\mathsf{a}}} \frac{\hat{\mathbf{h}}_{\ell,(\ell,k)}}{\sqrt{\mathbb{E}\left[\left\|\hat{\mathbf{h}}_{\ell,(\ell,k)}\right\|^2\right]}}, \; k = 0, \ldots, K_\ell^d - 1, \tag{6.47}$$

where the precoders share the same properties as the matched filter receiver indicated by Corollary 2.

Recall the expression of the reverse link channel estimate at the cell of interest (6.15), and referring to the analogy with the matched filter receiver, the k-th matched filter precoder at the BS of interest is expressed by

$$\mathbf{f}_k^{\mathsf{MF}} = \sqrt{\frac{\frac{P_k}{P_u}\mathsf{SNR}_k^u}{1 + \frac{P_k}{P_u}\mathsf{SNR}_k^u + \sum_{\ell \in \mathcal{C}} \frac{P_{\ell,k}}{P_u}\mathsf{SNR}_{\ell,k}^u}} \left(\mathbf{h}_k + \sum_{\ell \in \mathcal{C}} \sqrt{\frac{\frac{P_{\ell,k}}{P_u}\mathsf{SNR}_{\ell,k}^u}{\frac{P_k}{P_u}\mathsf{SNR}_k^u}} \mathbf{h}_{\ell,k} + \mathbf{v}_k^{'} \right). \tag{6.48}$$

which exactly matches the reverse link matched filter receiver.

Theorem 11. For channel hardening and with a matched filter precoder, the output SQINR of the k-th downlink user is expressed by (6.49).

$$\overline{\mathsf{sqinr}}_k^{\mathsf{MF}} = \frac{\frac{P_k}{P_u}\mathsf{SNR}_k^u \frac{P_k}{P_d}\mathsf{SNR}_k^d N_{\mathsf{a}}}{\left(1 + \frac{P_k}{P_u}\mathsf{SNR}_k^u + \sum_{\ell \in \mathcal{C}} \frac{P_{\ell,k}}{P_u}\mathsf{SNR}_{\ell,k}^u\right) \overline{\mathsf{den}}_d^{\mathsf{MF}}} \tag{6.49}$$

Remark 14. The fractions $\frac{P_{\ell,k}}{P_u}$ and $\frac{P_{\ell,k}}{P_d}$ for any ℓ and k, are the fractional power control and power allocation coefficients, respectively.

While introducing the new term $\varrho = \mathsf{SNR}_{\ell,(l,k)}^d / \mathsf{SNR}_{\ell,(l,k)}^u$ for any ℓ, l and k as the *forward-reverse signal-to-noise ratio (SNR) ratio*, the output SQINR of the k-th downlink UE becomes

$$\overline{\mathsf{sqinr}}_k^{\mathsf{MF}} = \frac{\alpha_d^2 \frac{N_{\mathsf{a}}}{\varrho + \frac{P_k}{P_u}\mathsf{SNR}_k^d + \sum_{\ell \in \mathcal{C}} \frac{P_{\ell,k}}{P_u}\mathsf{SNR}_{\ell,k}^d} \frac{P_k}{P_u} \frac{P_k}{P_d} \left(\mathsf{SNR}_k^d\right)^2}{\overline{\mathsf{den}}_d^{\mathsf{MF}}} \tag{6.50}$$

where $\overline{\mathsf{den}}_d^{\mathsf{MF}}$ is given by (6.51).

$$\begin{aligned}\overline{\mathsf{den}}_d^{\mathsf{MF}} =& 1+\alpha_d^2\sum_{\ell}\mathsf{SNR}_{\ell,k}^d+\alpha_d^2\sum_{\ell\in\mathcal{C}}\frac{N_{\mathsf{a}}}{\varrho+\frac{P_k}{P_u}\mathsf{SNR}_{\ell,k}^d+\sum_{l\in\mathcal{C}}\frac{P_{l,k}}{P_u}\mathsf{SNR}_{\ell,(l,k)}^d}\frac{P_k}{P_u}\frac{P_{\ell,k}}{P_d}\left(\mathsf{SNR}_{\ell,k}^d\right)^2\\ &+\sum_{\ell}\sum_{\mathrm{k}=0}^{K_\ell^u-1}\frac{P_{\ell,\mathrm{k}}^u}{P_u}\mathsf{SNR}_{(\ell,\mathrm{k}),k}^{\mathsf{iui}}+\alpha_d(1-\alpha_d)\sum_{\ell}\frac{P_{\ell,k}}{P_d}\mathsf{SNR}_{\ell,k}^d\left(K_\ell^d+1\right).\end{aligned} \tag{6.51}$$

Proof. The proof of Theorem 11 is provided in Appendix D.5. □

Proposition 6. Considering a single-cell multiuser system (without any inter-cell interference) with perfect CSI, Corollary 3 entails the results for forward link in [40].

Proposition 7. With channel hardening, without full-duplexing (no IUI), with full-resolution and with a matched filter precoder, the output SINR of the k-th downlink user is given by (6.52).

$$\overline{\mathsf{sinr}}_k^{\mathsf{MF}}=\frac{\frac{N_{\mathsf{a}}}{\varrho+\frac{P_k}{P_u}\mathsf{SNR}_k^d+\sum_{\ell\in\mathcal{C}}\frac{P_{\ell,k}}{P_u}\mathsf{SNR}_{\ell,k}^d}\frac{P_k}{P_u}\frac{P_k}{P_d}\left(\mathsf{SNR}_k^d\right)^2}{1+\alpha_d^2\sum_{\ell}\mathsf{SNR}_{\ell,k}^d+\alpha_d^2\sum_{\ell\in\mathcal{C}}\frac{N_{\mathsf{a}}}{\varrho+\frac{P_k}{P_u}\mathsf{SNR}_{\ell,k}^d+\sum_{l\in\mathcal{C}}\frac{P_{l,k}}{P_u}\mathsf{SNR}_{\ell,(l,k)}^d}\frac{P_k}{P_u}\frac{P_{\ell,k}}{P_d}\left(\mathsf{SNR}_{\ell,k}^d\right)^2}. \tag{6.52}$$

Remark 15. Note that Proposition 7 entails the same result for forward link derived in [53].

Neglecting pilot contamination and assuming $\varrho+\frac{P_k}{P_u}\mathsf{SNR}_k^d\approx\frac{P_k}{P_u}\mathsf{SNR}_k^d$, the output SINR of the k-th downlink user (6.52) is reduced to (6.53).

$$\overline{\mathsf{sinr}}_k^{\mathsf{MF}}\approx\frac{\frac{P_k}{P_u}\frac{P_k}{P_d}\left(\mathsf{SNR}_k^d\right)^2N_{\mathsf{a}}}{\left(\varrho+\frac{P_k}{P_u}\mathsf{SNR}_k^d\right)\left(1+\sum_{\ell}\mathsf{SNR}_{\ell,k}^d\right)}. \tag{6.53}$$

Remark 16. Note that the output SINR expression (6.53) admits a duality with its reverse link counterpart (6.39). In addition, the assumption of $\varrho+\frac{P_k}{P_u}\mathsf{SNR}_k^d\approx\frac{P_k}{P_u}\mathsf{SNR}_k^d$

is equivalent to considering a perfect channel estimation and therefore any achievable SINRs in the reverse link can be also achieved in the forward link if the same total power is transmitted.

6.4.3 Tractability

Finding closed-form expressions of the proposed systems is not tractable. However, under special assumptions, tractable expressions of the CDF as well as the spectral efficiency can be derived.

Proposition 8. Without full-duplexing, with full resolution, without pilot contamination, without noise, and with fixed number of users as well as assuming the number of downlink users (K) is the same in all the cells, the CDF and the average spectral efficiency per user under uniform power allocation scheme satisfy (6.54) and (6.55), respectively.

$$\begin{cases} F_{\overline{\mathsf{sir}}_k^{\mathsf{MF}}}(\tau) \cong e^{s^*\left(\frac{N_\mathsf{a}}{\tau K}-1\right)} & 0 \leq \tau < \frac{N_\mathsf{a}/K}{3+\varepsilon} \\ F_{\overline{\mathsf{sir}}_k^{\mathsf{MF}}}(\tau) = 1-\left(\frac{N_\mathsf{a}}{\tau K}-1\right)^{\delta}\mathsf{sinc}(\delta)+\mathsf{B}_\delta\left(\frac{\tau K}{N_\mathsf{a}-2\tau K}\right) & \frac{N_\mathsf{a}/K}{3} \leq \tau < \frac{N_\mathsf{a}/K}{2} \\ F_{\overline{\mathsf{sir}}_k^{\mathsf{MF}}}(\tau) = 1-\left(\frac{N_\mathsf{a}}{\tau K}-1\right)^{\delta}\mathsf{sinc}(\delta) & \frac{N_\mathsf{a}/K}{2} \leq \tau < \frac{N_\mathsf{a}}{K}. \end{cases} \tag{6.54}$$

$$\overline{\mathfrak{I}}_{\overline{\mathsf{sir}}_k^{\mathsf{MF}}} = \log_2(e)\int_0^{+\infty}\frac{1-e^{-zN_\mathsf{a}/K}}{{}_1F_1(1,1-\delta,z)}\frac{dz}{z}, \tag{6.55}$$

Here, the function $\mathsf{B}_\delta(\cdot)$ is defined by

$$\mathsf{B}_\delta(x) = \frac{{}_2F_1\left(1,\delta+1;2\delta+2;-1/x\right)\delta}{x^{1+2\delta}\Gamma\left(2\delta+2\right)\Gamma^2(1-\delta)}, \tag{6.56}$$

Here, ${}_2F_1(\cdot)$ is the Gauss hypergeometric function, ${}_1F_1(\cdot)$ is the confluent hypergeometric or Kumar function, and $\Gamma(\cdot)$ is the Gamma function.

In (6.54), the term $s^* < 0$ is defined as the solution of

$$s^{*\delta}\gamma(-\delta,s^*) = 0. \tag{6.57}$$

where $\gamma(\cdot,\cdot)$ is the incomplete lower Gamma function and $\delta = 2/\eta$. We solve (6.57) to find s* which then determines the values of η and δ in this tractable case. Common values of the parameter s^* for typical pathloss exponents are given by Table 6.2.

Table 6.2: Values for parameter s for typical pathloss exponents η [62, Table 10.1].

η	s
3.5	-0.672
3.6	-0.71
3.7	-0.747
3.8	-0.783
3.9	-0.819
4.0	-0.854

Proof. The proof of the results entailed by Proposition 8 are derived in [53]. □

6.5 Asymptotic Analysis and Power Scaling Laws

In the section, we investigate the effects of the number of quantization bits, number of BS antennas, number of users, and BS and UE power budgets on spectral efficiency for the reverse and forward links. In the next Section, we carry out the analysis for the channel hardening case.

Lemma 4. For a fixed power budget, fixed number of transmit antennas and full-resolution ($b \to \infty$, $\alpha_u = \alpha_d = 1$), the spectral efficiencies for reverse and forward links converge to (6.58) and (6.59), respectively.

$$\frac{\bar{\mathcal{I}}_u^{\mathsf{MF}}}{B} \to \log\left(1 + \frac{\frac{\left(\frac{P_k}{P_u}\mathsf{SNR}_k^u\right)^2 N_{\mathsf{a}}}{1+\frac{P_k}{P_u}\mathsf{SNR}_k^u+\sum_{\ell\in\mathcal{C}}\frac{P_{\ell,k}}{P_u}\mathsf{SNR}_{\ell,k}^u}}{1+\sum_{\ell}\sum_{\mathrm{k}=0}^{K_\ell^u-1}\frac{P_{\ell,\mathrm{k}}}{P_u}\mathsf{SNR}_{\ell,\mathrm{k}}^u + N_{\mathsf{a}}\frac{\sum_{\ell\in\mathcal{C}}\left(\frac{P_{\ell,k}}{P_u}\mathsf{SNR}_{\ell,k}^u\right)^2}{1+\frac{P_k}{P_u}\mathsf{SNR}_k^u+\sum_{\ell\in\mathcal{C}}\frac{P_{\ell,k}}{P_u}\mathsf{SNR}_{\ell,k}^u} + N_{\mathsf{a}}K^d\mathsf{INR}}\right) \tag{6.58}$$

$$\frac{\bar{\mathcal{J}}_d^{\mathsf{MF}}}{B} \rightarrow$$

$$\log\left(1+\frac{\frac{N_{\mathsf{a}}}{\varrho+\frac{P_k}{P_u}\mathsf{SNR}_k^d+\sum_{\ell\in\mathcal{C}}\frac{P_{\ell,k}}{P_u}\mathsf{SNR}_{\ell,k}^d}\frac{P_k}{P_u}\frac{P_k}{P_d}\left(\mathsf{SNR}_k^d\right)^2}{1+\sum_\ell \mathsf{SNR}_{\ell,k}^d+\sum_{\ell\in\mathcal{C}}\frac{N_{\mathsf{a}}}{\varrho+\frac{P_k}{P_u}\mathsf{SNR}_{\ell,k}^d+\sum_{l\in\mathcal{C}}\frac{P_{l,k}}{P_u}\mathsf{SNR}_{\ell,(l,k)}^d}\frac{P_k}{P_u}\frac{P_{\ell,k}}{P_d}\left(\mathsf{SNR}_{\ell,k}^d\right)^2+\sum_\ell\sum_{\mathrm{k}=0}^{K_\ell^u-1}\frac{P_{\ell,\mathrm{k}}^u}{P_u}\mathsf{SNR}_{(\ell,\mathrm{k}),k}^{\mathsf{iui}}}\right) \tag{6.59}$$

In (6.58) and (6.59), the quantization error introduced by finite resolution ADCs and DACs vanishes for full-resolution. When the number of antennas is fixed, spectral efficiency for uplink/downlink users becomes constant. Although increasing ADC/DAC resolution can improve the uplink/downlink spectral efficiency, the latter is limited by pilot contamination, SI, IUI and cellular interference including intra and inter-cell interference.

Lemma 5. For a fixed number of antennas N_{a} and a fixed number of bits b as well as assuming uniform power allocation for the forward link, when $\mathsf{SNR}_k^u, \mathsf{SNR}_k^d \rightarrow \infty$, the spectral efficiency for the reverse and forward links converge to

$$\frac{\bar{\mathcal{J}}_u^{\mathsf{MF}}}{B} \rightarrow \log\left(1+\frac{N_{\mathsf{a}}}{\alpha_u(2-\alpha_u)}\right) \tag{6.60}$$

$$\frac{\bar{\mathcal{J}}_d^{\mathsf{MF}}}{B} \rightarrow \log\left(1+\frac{\alpha_d N_{\mathsf{a}}}{K^d-\alpha_d+1}\right). \tag{6.61}$$

In (6.60) and (6.61), the spectral efficiency for the reverse and forward links depend on the number of antennas N_{a}, number of users K, and the AQNM ADC/DAC resolution parameter α. When the transmit power at the BS and UE in the cell of interest grows large enough, the aggregate interference as well as the pilot contamination are eliminated.

Lemma 6. If the transmit powers of the BS and each user are scaled with the number of antennas N_{a} i.e., $P=\frac{E}{N_{\mathsf{a}}}$ where E is fixed, as $N_{\mathsf{a}} \rightarrow \infty$, the spectral efficiencies for reverse and forward links converge to

$$\frac{\bar{\mathcal{J}}_u^{\mathsf{MF}}}{B} \to \log\left(1+\frac{\alpha_u\left(\frac{E_k}{E_u}\mathsf{SNR}_k^u\right)^2}{1+\alpha_d\left(\alpha_u K^d+1-\alpha_u\right)\mathsf{INR}}\right) \tag{6.62}$$

$$\frac{\bar{\mathcal{J}}_d^{\mathsf{MF}}}{B} \to \log\left(1+\frac{\alpha_d^2}{\varrho}\frac{E_k}{E_u}\frac{E_k}{E_d}\left(\mathsf{SNR}_k^d\right)^2\right). \tag{6.63}$$

In (6.62) and (6.63), we found that using a proper power scaling law and more antennas can eliminate the inter-user, inter-cell and intra-cell interference as well as pilot contamination and noise for both the reverse and forward links. However, the reverse link is still corrupted by the SI.

Lemma 7. If the transmit power and number of users per cell are fixed, the spectral efficiencies for reverse and forward links as $N_{\mathsf{a}}/K \to \infty$ converge to (6.64) and (6.65), respectively.

$$\frac{\bar{\mathcal{J}}_u^{\mathsf{MF}}}{B} \to \log\left(1+\frac{\frac{\alpha_u\left(\frac{P_k}{P_u}\mathsf{SNR}_k^u\right)^2}{1+\frac{P_k}{P_u}\mathsf{SNR}_k^u+\sum_{\ell\in\mathcal{C}}\frac{P_{\ell,k}}{P_u}\mathsf{SNR}_{\ell,k}^u}}{\alpha_u\frac{\sum_{\ell\in\mathcal{C}}\left(\frac{P_{\ell,k}}{P_u}\mathsf{SNR}_{\ell,k}^u\right)^2}{1+\frac{P_k}{P_u}\mathsf{SNR}_k^u+\sum_{\ell\in\mathcal{C}}\frac{P_{\ell,k}}{P_u}\mathsf{SNR}_{\ell,k}^u}+\alpha_d\left(\alpha_u K^d+1-\alpha_u\right)\mathsf{INR}}\right) \tag{6.64}$$

$$\frac{\bar{\mathcal{J}}_d^{\mathsf{MF}}}{B} \to \log\left(1+\frac{\frac{1}{\varrho+\frac{P_k}{P_u}\mathsf{SNR}_k^d+\sum_{\ell\in\mathcal{C}}\frac{P_{\ell,k}}{P_u}\mathsf{SNR}_{\ell,k}^d}\frac{P_k}{P_u}\frac{P_k}{P_d}\left(\mathsf{SNR}_k^d\right)^2}{\sum_{\ell\in\mathcal{C}}\frac{1}{\varrho+\frac{P_k}{P_u}\mathsf{SNR}_{\ell,k}^d+\sum_{l\in\mathcal{C}}\frac{P_{l,k}}{P_u}\mathsf{SNR}_{\ell,(l,k)}^d}\frac{P_k}{P_u}\frac{P_{\ell,k}}{P_d}\left(\mathsf{SNR}_{\ell,k}^d\right)^2}\right). \tag{6.65}$$

Equations (6.64) and (6.65) corroborate the fact that increasing the ratio (N_{a}/K) leads to pilot contamination dominance which imposes a limit on the SQINR. The reverse link performance is also saturated by the SI in addition to the pilot contamination.

6.6 Extension to Millimeter Wave Bands

Up to this point, we have been focusing on sub-7 GHz LTE bands. In this section, we provide an extension of the previous analysis to the mmWave spectrum

from 30 to 300 GHz[5] whereas most users operate at a carrier frequency below 7 GHz. The major benefits of operating in mmWave frequencies is the availability of larger bandwidths and unlicensed spectrum. For example, channels with 2 GHz of bandwidth are common for systems operating at 60 GHz unlicensed mmWave bands. Larger bandwidth channels mean higher data rates.

6.6.1 Channel Model

Radio channel properties depend on the carrier frequency. Electromagnetic waves propagating at low/medium frequency can travel for long distances due to low penetration loss, small pathloss, and rich scattering paths. A good channel model to describe such a phenomenon is the Complex Gaussian or Rayleigh fading. For mmWave bands, electromagnetic waves travel short ranges due to high penetration loss, large pathloss, and limited scattering paths. In other words, mmWave channels are generally sparse wherein the number of rays is small and grouped in a small clusters. A good common channel model that can capture these properties is the 3D geometric channel, a.k.a. the *Saleh-Valenzuela* model, expressed as

$$\mathbf{H} = \sqrt{\frac{N_{\mathsf{RX}} N_{\mathsf{TX}}}{C R_c}} \sum_{c=0}^{C-1} \sum_{r_c=0}^{R_c-1} \alpha_{r_c} \mathbf{a}_{\mathsf{RX}}(\theta_{r_c}) \mathbf{a}_{\mathsf{TX}}^{*}(\phi_{r_c}), \tag{6.66}$$

where N_{RX} and N_{TX} are the numbers of antennas at RX and TX, respectively. C is the number of clusters, R_c is the number of rays per cluster, and θ_{r_c} and ϕ_{r_c} are the AoA and AoD of the r_c-th ray, respectively. Each ray has a complex path gain α_{r_c}. Also, $\mathbf{a}_{\mathsf{RX}}(\theta)$ and $\mathbf{a}_{\mathsf{TX}}(\phi)$ are the RX and TX antenna array response vectors, respectively. We adopt a uniform linear array wherein the array response vector is given by

$$\mathbf{a}_{\mathsf{RX}}(\theta) = \frac{1}{\sqrt{N_{\mathsf{RX}}}} \left[1, \mathsf{e}^{i\frac{2\pi r}{\lambda}\sin(\theta)}, \ldots, \mathsf{e}^{i\frac{2\pi r}{\lambda}(N_{\mathsf{RX}}-1)\sin(\theta)}\right]^{T}. \tag{6.67}$$

where r and λ are the antenna spacing and signal wavelength, respectively.

[5]Although a rigorous definition of mmWave frequencies would place them between 30 and 300 GHz, industry has loosely defined them to include the spectrum from 10 to 300 GHz.

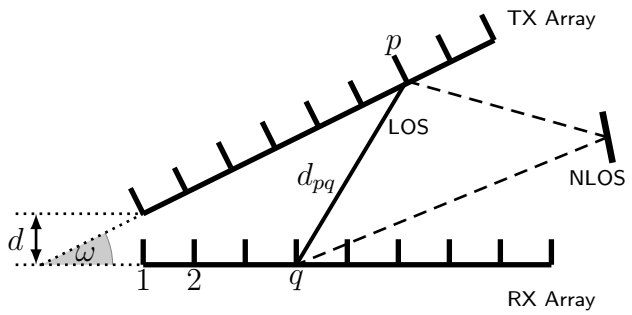

Figure 6.4: Relative position of TX and RX arrays at BS. Given that the TX and RX arrays are collocated, the far-field assumption that the signal impinges on the antenna array as a planar wave does not hold. Instead, for FD transceivers, it is more suitable to assume that the signal impinges on the array as a spherical wave for the near-field LOS channel.

6.6.2 Self-Interference Channel Model

Per Fig. 6.4, the SI leakage at the BS is modeled by the channel matrix $\mathbf{H}_{\mathsf{s}}$. The separation, or transceiver gap, between TX and RX arrays is defined by distance d while the transceiver incline is determined by ω. The SI channel is decomposed into a static LOS channel modeled by $\mathbf{H}_{\mathsf{LOS}}$, which is derived from the geometry of the transceiver, and a NLOS channel described by $\mathbf{H}_{\mathsf{NLOS}}$ which follows the geometric channel model defined by (6.66). The (q,p)-th entry of the LOS SI leakage matrix can be written as

$$[\mathbf{H}_{\mathsf{LOS}}]_{qp} = \frac{1}{d_{pq}} \mathsf{e}^{-i2\pi \frac{d_{pq}}{\lambda}}, \tag{6.68}$$

where d_{pq} is the distance between the p-th antenna in the TX array and q-th antenna in the RX array at BS given by (6.70). The aggregate SI channel matrix can be obtained by

$$\mathbf{H}_{\mathsf{s}} = \underbrace{\sqrt{\frac{\kappa}{\kappa+1}}\mathbf{H}_{\mathsf{LOS}}}_{\text{Near-Field}} + \underbrace{\sqrt{\frac{1}{\kappa+1}}\mathbf{H}_{\mathsf{NLOS}}}_{\text{Far-Field}}, \tag{6.69}$$

where κ is the Rician factor.

$$d_{pq} = \sqrt{\left(\frac{d}{\tan(\omega)} + (q-1)\frac{\lambda}{2}\right)^2 + \left(\frac{d}{\sin(\omega)} + (p-1)\frac{\lambda}{2}\right)^2 - 2\left(\frac{d}{\tan(\omega)} + (q-1)\frac{\lambda}{2}\right)\left(\frac{d}{\sin(\omega)} + (p-1)\frac{\lambda}{2}\right)\cos(\omega)}, \tag{6.70}$$

6.6.3 Signal Processing Perspective

Communicating at mmWave bands is not simply a matter of just switching the frequency band to be higher. Migrating to mmWave completely changes the assumptions that underlie prior developments in signal processing for communications. The RF hardware introduces constraints that have significant effects on the beamforming, precoding, power consumption, etc. Unlike UMTS and LTE, devices operating at mmWave frequencies are power hungry; e.g., the ADC/DAC consumes hefty power because higher sampling rates are needed for the larger bandwidths in mmWave communications.

Adopting a full-digital architecture for the large antenna arrays needed for mmWave LTE communications becomes impractical. In fact, for the full-digital architecture, an RF chain is dedicated for each antenna, but due to the higher power consumption of each RF chain at mmWave bands, the full-digital solution for mmWave communications is not feasible. To reduce the power consumption, adopting a hybrid A/D architecture, wherein the number of RF chains is reduced and each RF chain is connected to the entire array of antennas as illustrated by Fig. 2.4, may solve this shortcoming. Although such a solution reduces the number of RF chains and hence sacrifices degrees of freedom leading to reduction in spectral efficiency, the reduction in the total power consumption can lead to a practical implementation. For comparison, the full-digital architecture of the FD BS is illustrated by Fig. 6.3 and the hybrid A/D architecture of the FD BS by Fig. 6.5.

The full-digital precoder or combiner designed in the previous sections for the reverse and forward links is neither energy-efficient nor feasible for mmWave; however, the designs may serve as benchmarking tools to measure the efficacy of the hybrid

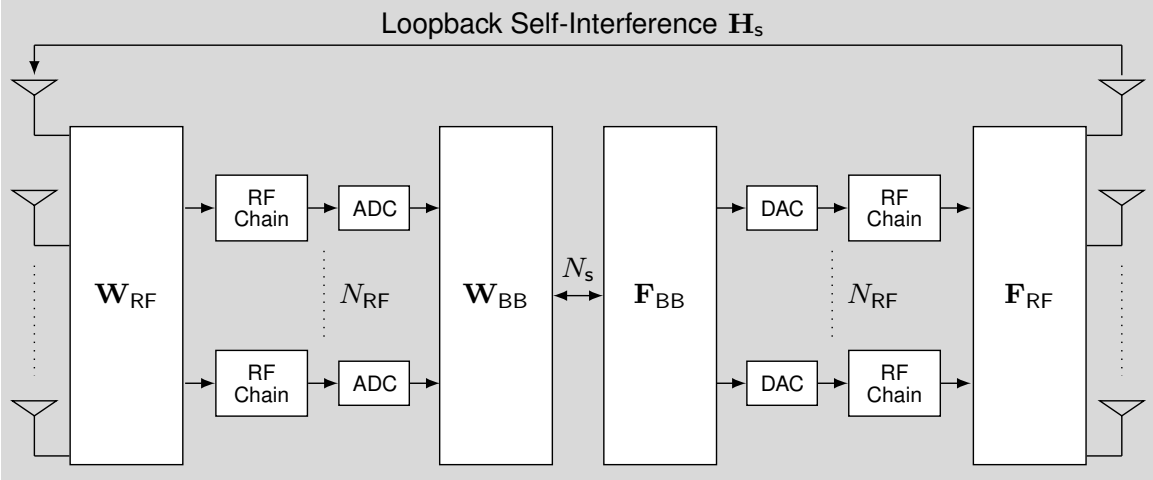

Figure 6.5: Basic abstraction of the hybrid analog/digital architecture of the FD BS. $\mathbf{W}_{\mathsf{RF}}$ and $\mathbf{W}_{\mathsf{BB}}$ are the analog and digital combiners at the BS, respectively. $\mathbf{F}_{\mathsf{RF}}$ and $\mathbf{F}_{\mathsf{BB}}$ are the analog and digital precoders at the BS, respectively. The number of streams that the BS can sustain is denoted by N_{s} while the number of RF chains is denoted by N_{RF}. We further illustrate the loopback SI from the transmit to receive arrays of the BS and we denote by $\mathbf{H}_{\mathsf{s}}$ the aggregated SI channel.

beamforming design in Fig. 6.5. In proceeding with mmWave analysis, we decompose the full-digital solution into the equivalent analog and digital components. Without loss of generality, we conduct the analysis for a given optimal full-digital precoder denoted by $\mathbf{F}_{\mathsf{opt}}$.

In this subsection, we aim at decomposing the optimal precoder $\mathbf{F}_{\mathsf{opt}}$ into the equivalent digital $\mathbf{F}_{\mathsf{BB}}$ and analog $\mathbf{F}_{\mathsf{RF}}$ solutions. The hybrid A/D decomposition problem $\mathscr{P}_1$ can be stated as

$$\begin{aligned} \mathscr{P}_1 : \min_{\mathbf{F}_{\mathsf{BB}},\mathbf{F}_{\mathsf{RF}}} \; & \|\mathbf{F}_{\mathsf{opt}} - \mathbf{F}_{\mathsf{RF}}\mathbf{F}_{\mathsf{BB}}\|_F^2 \\ \text{s.t. } & \mathbf{F}_{\mathsf{RF}} \in \mathcal{F}_{\mathsf{RF}} \\ & \|\mathbf{F}_{\mathsf{RF}}\mathbf{F}_{\mathsf{BB}}\|_F^2 = N_{\mathsf{s}}, \end{aligned} \tag{6.71}$$

where $\mathcal{F}_{\mathsf{RF}}$ is the set of feasible RF precoders which correspond to a hybrid architecture based on phase shifters, i.e., the set of matrices with constant-magnitude entries.

6.6.4 Implementation of Millimeter Wave Solutions

The main objective of this subsection is to illustrate the implementation of the mmWave hybrid A/D solutions following these steps:

1. Find full-digital combiner $\mathbf{W} = [\mathbf{w}_0, \mathbf{w}_1, \ldots, \mathbf{w}_{K^u-1}]$ and precoder $\mathbf{F} = [\mathbf{f}_0, \mathbf{f}_1, \ldots, \mathbf{f}_{K^d-1}]$ at the FD BS of interest. Such solutions could be the matched filter as proposed for LTE bands or other solutions such as ZF or MMSE.

2. Decompose full-digital combiner and precoder at the FD BS into the equivalent analog and digital solutions as $\mathbf{W} = \mathbf{W}_{\mathsf{RF}}\mathbf{W}_{\mathsf{BB}}$ and $\mathbf{F} = \mathbf{F}_{\mathsf{RF}}\mathbf{F}_{\mathsf{BB}}$.

For the forward link, each user receives a single spatial stream from the BS and hence we assume that the total number of allowable spatial streams is $N_{\mathsf{s}} = K$. In addition, we assume that the maximum number of served users is equal to the number of RF chains at the BS, i.e., $K \leq N_{\mathsf{RF}}$. This is motivated by the spatial multiplexing gain of the proposed MU-MIMO hybrid precoding system, which is restricted by $\min(N_{\mathsf{RF}}, K)$ for $N_{\mathsf{a}} > N_{\mathsf{RF}}$. For simplicity, the BS uses K out of the N_{RF} available RF chains to serve the K users. In the digital domain, the BS applies a $K \times K$ digital precoder $\mathbf{F}_{\mathsf{BB}}$ followed by an $N_{\mathsf{a}} \times N_{\mathsf{RF}}$ analog precoder $\mathbf{F}_{\mathsf{RF}}$. Since the analog precoder is implemented using analog phase shifters, it has the constant amplitude constraint, i.e., $\left|[\mathbf{F}_{\mathsf{RF}}]_{m,n}\right|^2 = \frac{1}{N_{\mathsf{a}}}$. Further, we assume that the angles of the analog phase shifters are quantized and have a finite set of possible values. With these assumptions, the analog precoder entries takes the following form $[\mathbf{F}_{\mathsf{RF}}]_{mn} = \frac{1}{\sqrt{N_{\mathsf{a}}}}\mathsf{e}^{i\theta_{mn}}$ where θ_{mn} is the quantized angle at the (m,n)-th entry of the analog precoder. The total power is constrained by normalizing the digital precoder such that $\|\mathbf{F}_{\mathsf{RF}}\mathbf{F}_{\mathsf{BB}}\|_F^2 = N_{\mathsf{s}}$.

For the reverse link, we adopt the same assumptions in terms of the number of spatial streams and RF chains as the forward link. To process the received spatial streams of each user, the BS applies an $N_{\mathsf{a}} \times N_{\mathsf{RF}}$ analog combiner $\mathbf{W}_{\mathsf{RF}}$ followed by a $K \times K$ digital combiner $\mathbf{W}_{\mathsf{BB}}$. Like the analog precoder, the analog combiner is implemented using analog phase shifters and satisfies $\left|[\mathbf{W}_{\mathsf{RF}}]_{m,n}\right|^2 = \frac{1}{N_{\mathsf{a}}}$. Given

that the analog phase shifters are quantized and have finite set of feasible values, the analog combiner entries satisfies $[\mathbf{W}_{\mathsf{RF}}]_{mn} = \frac{1}{\sqrt{N_{\mathsf{a}}}}\mathsf{e}^{i\phi_{mn}}$ where ϕ_{mn} is the quantized angle at the (m,n)-th entry of the analog combiner.

We start by designing the digital precoder $\mathbf{F}_{\mathsf{BB}}$ by using the LS routine as

$$\mathbf{F}_{\mathsf{BB}} = \mathbf{F}_{\mathsf{RF}}^{\dagger}\mathbf{F}_{\mathsf{opt}}, \tag{6.72}$$

To satisfy the power constraint in (6.71), we normalize the digital precoder $\mathbf{F}_{\mathsf{BB}}$ by a factor of $\frac{N_{\mathsf{s}}}{\|\mathbf{F}_{\mathsf{RF}}\mathbf{F}_{\mathsf{BB}}\|_F}$.

To design the analog precoder $\mathbf{F}_{\mathsf{RF}}$, we proceed by alternating optimization; i.e., we fix the digital precoder $\mathbf{F}_{\mathsf{BB}}$ and seek the analog precoder that optimizes the following problem

$$\begin{aligned} \mathscr{P}_2 : & \min_{\mathbf{F}_{\mathsf{BB}},\mathbf{F}_{\mathsf{RF}}} \|\mathbf{F}_{\mathsf{opt}} - \mathbf{F}_{\mathsf{RF}}\mathbf{F}_{\mathsf{BB}}\|_F^2 \\ & \mathsf{s.t.}\ \mathbf{F}_{\mathsf{RF}} \in \mathcal{F}_{\mathsf{RF}}. \end{aligned} \tag{6.73}$$

It is important to note that decomposing the optimal solution into a hybrid A/D solution is not straightforward due to the non-convex unit modulus constraints. There is no general method to optimally solve (6.73). To solve this problem, we adopt the approach used by [161] to offer a near-optimal solution of (6.73). The authors apply the Conjugate Gradient Algorithm for analog precoding based on Manifold Optimization [161]. More details about Manifold Optimization can be found in [116]. The hybrid precoding design is summarized by Algorithm 7.

Algorithm 7 Hybrid Beamforming Design

1: **Input** $\mathbf{F}_{\mathsf{opt}}$
2: Construct $\mathbf{F}_{\mathsf{RF}}^{(0)}$ with random phases and set $n = 0$
3: **repeat**
4: Fix $\mathbf{F}_{\mathsf{RF}}^{(n)}$ and $\mathbf{F}_{\mathsf{BB}}^{(n)} = \mathbf{F}_{\mathsf{RF}}^{(n)\dagger}\mathbf{F}_{\mathsf{opt}}$ Optimize $\mathbf{F}_{\mathsf{RF}}^{(n+1)}$ using [161, Algorithm 1] when $\mathbf{F}_{\mathsf{BB}}^{(n)}$ is fixed.
5: $n \leftarrow n+1$.
6: **until** a stopping criterion triggers
7: For the digital precoder at the transmit side, normalize $\mathbf{F}_{\mathsf{BB}} \leftarrow \frac{\sqrt{N_{\mathsf{s}}}}{\|\mathbf{F}_{\mathsf{RF}}\mathbf{F}_{\mathsf{BB}}\|_F}\mathbf{F}_{\mathsf{BB}}$

6.6.5 Upper Bound on Spectral Efficiency

For the interference-free case, the optimal beamformers diagonalize the channel. By applying the SVD on the channel, we retrieve the singular values and extract the first N_{s} modes associated with the spatial streams. The upper bound for uplink or downlink is given by

$$\mathcal{I}_{\mathsf{Bound}} = \sum_{\ell=0}^{N_{\mathsf{s}}-1} \log\left(1 + \sigma_{\ell}\left(\mathbf{H}\right)^{2} \mathsf{SNR}\right). \tag{6.74}$$

6.7 Energy Efficiency and Outage Probability

6.7.1 Energy Efficiency

The energy efficiency, expressed in bits/s/Watt or bits/Joule, is defined as the ratio between the spectral efficiency $\mathcal{I}(\mathsf{sqinr})$ and total power consumption ρ_{Total}. It is expressed as

$$\mathcal{J}(\mathsf{sqinr}) = \frac{\mathcal{I}(\mathsf{sqinr})}{\rho_{\mathsf{Total}}}. \tag{6.75}$$

In this work, we define the energy efficiency with respect to reverse link since the receiver (BS) is equipped with multiple antennas. For full-digital BS combiner as illustrated by Fig. 6.6, the total power consumption model is defined by

$$\rho_{\mathsf{Total}}^{\mathsf{DC}} = N_{\mathsf{a}}\left(\rho_{\mathsf{LNA}} + \rho_{\mathsf{RF}} + 2\rho_{\mathsf{ADC}}\right), \tag{6.76}$$

where ρ_{RF} is the power consumption per RF chain which is defined by

$$\rho_{\mathsf{RF}} = \rho_{\mathsf{M}} + \rho_{\mathsf{LO}} + \rho_{\mathsf{LPF}} + \rho_{\mathsf{BB}_{\mathsf{amp}}}. \tag{6.77}$$

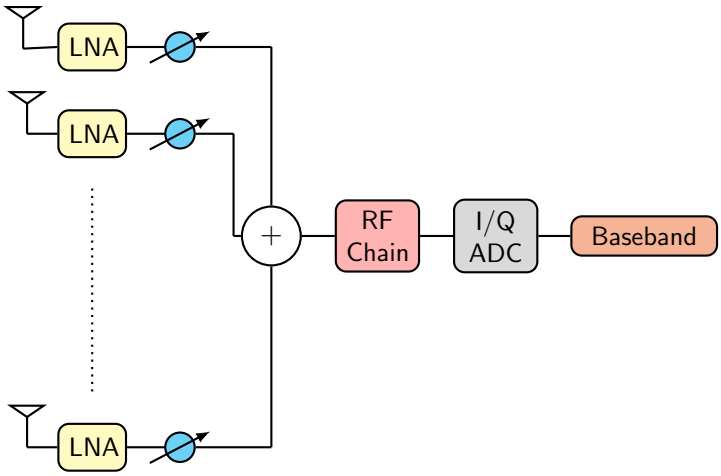

Figure 6.7: Basic abstraction of an analog combiner (AC).

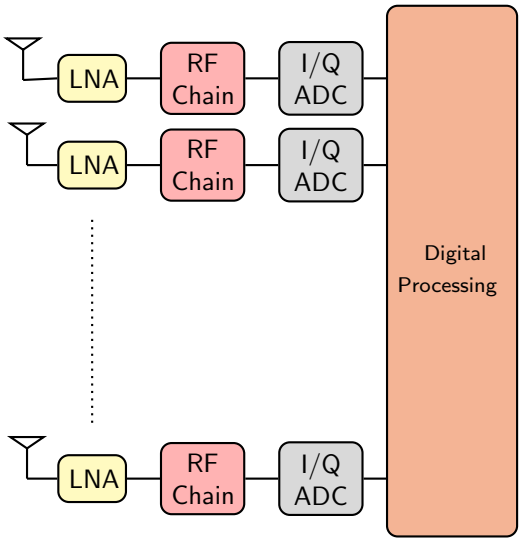

Figure 6.6: Basic abstraction of a digital combiner (DC).

For analog architecture as illustrated by Fig. 6.7, the total power consumption can be expressed as

$$\rho_{\mathsf{Total}}^{\mathsf{AC}} = N_{\mathsf{a}} \left(\rho_{\mathsf{LNA}} + \rho_{\mathsf{PS}}\right) + \rho_{\mathsf{RF}} + \rho_{\mathsf{C}} + 2\rho_{\mathsf{ADC}}. \tag{6.78}$$

For hybrid A/D architecture as illustrated by Fig. 6.8, the total power con-

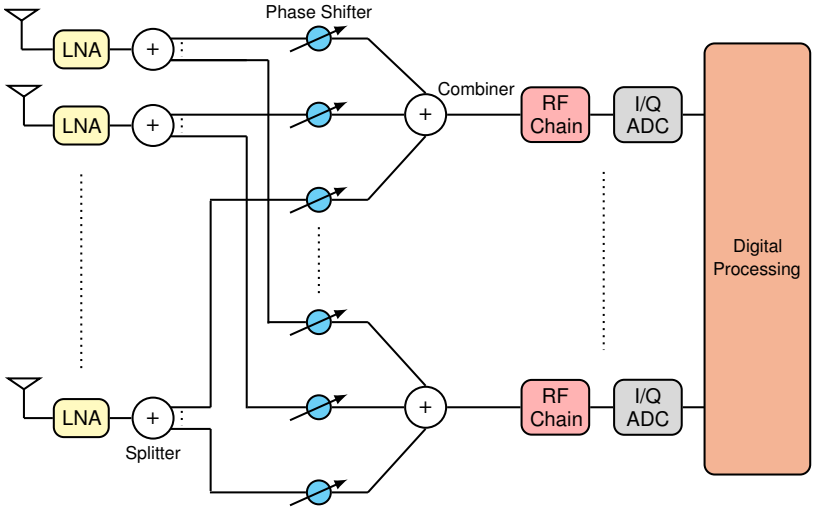

Figure 6.8: Basic abstraction of a hybrid analog/digital combiner.

sumption by the mmWave hybrid receiver is expressed by

$$\rho_{\mathsf{Total}}^{\mathsf{HC}} = N_{\mathsf{a}} \left(\rho_{\mathsf{LNA}} + \rho_{\mathsf{SP}} + N_{\mathsf{RF}} \rho_{\mathsf{PS}} \right) + N_{\mathsf{RF}} \left(\rho_{\mathsf{RF}} + \rho_{\mathsf{C}} + 2\rho_{\mathsf{ADC}} \right). \tag{6.79}$$

Examples of the power consumption of each device is presented in Table 6.3. The power consumption of all components except the ADC is independent of the bandwidth B and number of bits b, whereas ρ_{ADC} grows exponentially with b and linearly with B and with Walden's figure of merit for ADCs c, which is the energy consumption per conversion step per Hz. Common values of c are given in Table 6.4.

In this work, we selected three reasonable component power consumption models that we approximately identify with current and future generations of technology. The Walden figures of merit c for these ADCs are detailed in Table 6.4.

- The HPADC model is based on an existing device that supports sampling at Gs/s and has been cited in related literature such as [115]. In order to give phase shifters appropriate power consumption values, we pair the existing ADC model with an existing phase shifter model with $\rho_{\mathsf{ADC}} = 2\mathsf{mW}$ in [77].

Table 6.3: Power Consumption of Each Device [3].

Device	Notation	Value
Low Noise Amplifier	ρ_{LNA}	39 mW
Splitter	ρ_{SP}	19.5 mW
Combiner	ρ_{C}	19.5 mW
Phase Shifter	ρ_{PS}	2 mW
Mixer	ρ_{Mixer}	16.8 mW
Local Oscillator	ρ_{LO}	5 mW
Low Pass Filter	ρ_{LPF}	14 mW
Baseband Amplifier	$\rho_{\mathsf{BB_{amp}}}$	5 mW
ADC	ρ_{ADC}	$cB2^b$

Table 6.4: ADC Power Consumption Per Sample Per Level, c [3].

Scenario	Value	Generation
LPADC	5 fJ/step/Hz	Low Power (ideal future value)
IPADC	65 fJ/step/Hz	Intermediate Power
HPADC	494 fJ/step/Hz	High Power (state of the art)

- The LPADC model considers a likely future best-case scenario deduced from the hardware survey [105]. Likewise, we pair this "best case scenario" with a best case phase shifter model, with negligible power consumption $\sim 0\mathsf{mW}$ in [88].

- The ADC power values are rapidly changing, and we consider the extreme cases of well-established HPADC [115] and future LPADC [105]. Very recently a new IPADC has been proposed in [108]. Given this dynamic situation, we complement our study by using the method and associated Web visualization tool in [2] to enable researchers include advances in ADC technology.

6.7.2 Outage Probability

Once a transmission strategy is specified, the corresponding CDF or outage probability for rate R (bits/s/Hz) is then

$$P_{\mathsf{out}}(\mathsf{sqinr}, R) = \mathbb{P}[\mathcal{I}(\mathsf{sqinr}) < R], \tag{6.80}$$

With available powerful channel codes, the probability of error when there is no outage is very small and hence the outage probability is an accurate approximation for the actual block error probability [95]. As justified in the literature, radio systems such as UMTS and LTE operate at a target error probability [95]. Therefore, the primary communications performance measure is the maximum rate[6], at each sqinr, such that this threshold ϵ is not overtaken, i.e.,

$$R_{\epsilon}(\mathsf{sqinr}) = \max_{\zeta} \left\{ \zeta : P_{\mathsf{out}}(\mathsf{sqinr}, \zeta) \leq \epsilon \right\}. \tag{6.81}$$

6.8 Numerical Results

In this section, we discuss numerical results of the system performance. Unless otherwise stated, Table 6.5 presents the values of the system parameters[7]. We assume uniform power allocation for the forward links as well as a two-tier hexagonal network.

For hexagonal and square grids, we draw the geometry of the cells wherein a BS is dropped at the center of each cell (square or hexagonal) and users are uniformly distributed in each cell. For PPP tessellations, we draw the Voronoi network wherein

[6] In this work, we define the notion of rate with outage as the average data rate that is correctly received/decoded at the receiver which is equivalent to the throughput. In other standards in the literature, the rate with outage is often synonymous with the transmit data rate. If we consider the rate with outage as the throughput, we would account for the probability of bursts (outage) by multiplying by the term $(1 - \epsilon)$, while for the transmit data rate, the term $(1 - \epsilon)$ would not be accounted for.

[7] It is important to note here that these values for the parameters are selected from [111, 53, 40] subject to the standards to prove the validity of the obtained results. For all cases, 10^5 realizations of the random variables were generated to perform the Monte Carlo simulation in MATLAB.

Table 6.5: System Parameters [111, 53, 40, 21].

Parameter	**Symbol**	**Default Value**
Bandwidth (LTE)	B	20 MHz
Base station antenna gain		30 dB
Fraction of pilot overhead	β	0.5
Distance between adjacent hexagonal cells		$\sqrt{3}$ km
Fractional frequency reuse	Δ	1
Length of cell side	D_{cell}	1 km
Pathloss exponent	η	4
Pathloss offset		-128 dB
Number of forward/reverse link users per cell	K_ℓ	10
BS density	λ_{BS}	0.1 BS/km^2
UE density	λ_{UE}	0.5 UE/km^2
Number of antennas	N_{a}	100
Number of fading coherence tiles	N_{c}	20,000 (Pedestrians)
Number of pilots per cell	N_{p}	$3K_\ell$
Noise figure		3 dB
Forward link transmit power		40 W
SI channel power	μ_{SI}	10 dB
SI power	P_{SI}	40 W
Reverse link transmit power		200 mW
Shadowing	σ_{dB}	8 dB
Thermal noise spectral density		-174 dBm/Hz
Reverse fractional power control	ϑ	0.7
Forward power allocation	ϑ	0.0 (uniform)
Carrier frequency (mmWave)		28 GHz
Bandwidth (mmWave)		850 MHz
Number of clusters	C	6
Number of rays per cluster	R	8
AoA/AoD angular spread		20°
Transceivers gap	d	2λ
Transceivers incline	ω	$\frac{\pi}{6}$
Rician factor	κ	5 dB

a BS is dropped in each Voronoi cell and the BS locations are generated using PPP with rate λ_{BS} while user locations are generated using PPP with rate λ_{UE}.

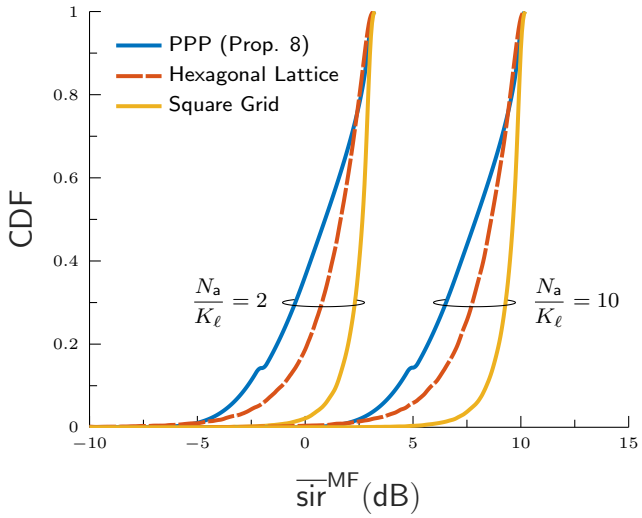

Figure 6.9: Forward link results: Large-scale distributions of $\overline{\text{sir}}^{\text{MF}}$ of an interference-limited network with uniform power allocation, where the number of pilots per cell $N_{\text{p}} \longrightarrow \infty$. Comparison between the analytical solution in Proposition 8 and the simulation-based results for a hexagonal with 2-tier (19 cells) and a square (25 cells) lattice networks.

The comparison of the analytical solution stated by Proposition 8 with the simulation-based results is illustrated by Fig. 6.9. The gap between the analytical results (which are asymptotic in the shadowing standard deviation and number of cells) and simulation results (with only 19 hexagonal and 25 square grid cells) is always less than 2 dB. As the strength of the shadowing and number of cells increases, the gap shrinks as the simulation curves converge to their analytical counterparts. Likewise, if the BS locations cease to conform to a lattice and adopt a more irregular layout, the simulation curves would shift left of the analytical ones based on a regular layout.

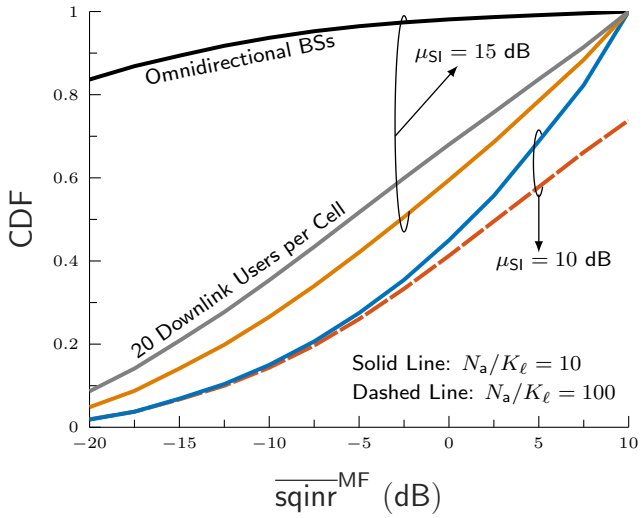

Figure 6.10: Reverse link results: Effects of antenna gain, SI channel power and number of downlink UEs on the CDF of the SQINR. Unless otherwise stated, the number of downlink UEs per cell is 10 users and the antenna array gain is 30 dB. The difference between red and blue curves is the value of the ratio N_{a}/K_ℓ. The difference between the gray and orange curves is the number of downlink users per cell, i.e., 20 vs. 10. The black curve is simulated using the default values except antenna gain is 0 dB.

Fig. 6.10 illustrates the CDF of the average reverse link SQINR. When the number of downlink users is large (20 users per cell) and hence there is significant SI power, the CDF performance worsens, and vice-versa. In addition, by increasing the ratio N_{a}/K_ℓ, the user beams become exceedingly narrow which allows the desired signal to dominate the noise and rejects a large amount of interference. In addition, by increasing the SI channel power from 10 to 15 dB, the SI power increases and hence the CDF worsens. Furthermore, antenna array directivity plays an important role in compensating pathloss and suppressing interference. This is confirmed when employing omnidirectional BSs, the CDF performance degrades, and vice versa.

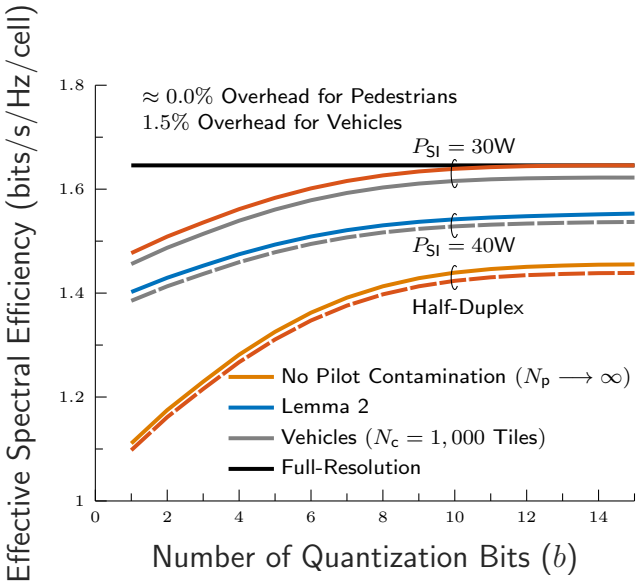

Figure 6.11: Reverse link results: Effects of SI power, overhead, ADC/DAC resolution, duplexing mode and pilot contamination on spectral efficiency. The dashed red curve is simulated for HD and accounts for pilot contamination unlike the solid yellow curve. The dashed gray curve is simulated using the default values in Table 6.5. A hexagonal grid is assumed for this simulation. The solid red curve is considered for pedestrians unlike the solid gray curve which is considered for vehicles.

Fig. 6.11 plots the effective spectral efficiency vs. number of ADC/DAC quantization bits (b). Spectral efficiency increases with b and converges to a ceiling defined by the full-resolution case. The rate decreases when adopting low-resolution ADC/DACs (i.e. having a small number of bits b). In addition, spectral efficiency noticeably degrades for 40W vs. 30W of SI power. Although FD is vulnerable to loopback SI, FD outperforms HD mode which is one of the goals of this work. We evaluate a low mobility case (pedestrians) and a high mobility case (vehicles). Since the pedestrian model features a large fading coherence tile and hence low overhead, better effective spectral efficiency is achieved compared to the vehicular case that features a small fading coherence tile and hence higher overhead.

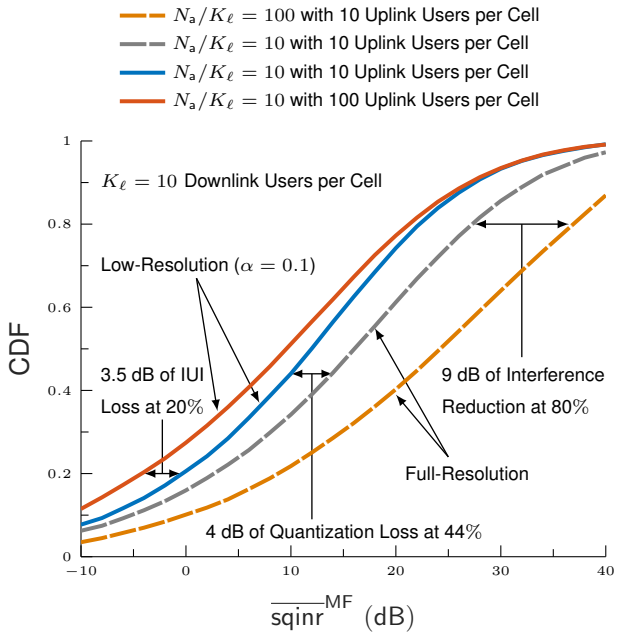

Figure 6.12: Forward link results: Effects of full-duplexing, ADC/DAC quantization error, and the ratio N_a/K_ℓ on the CDF of the SQINR. The dashed gray and solid blue curves are simulated for full and low resolution DAC, respectively.

Fig. 6.12 plots the CDF, or outage probability, of the average forward link SQINR. When the number of reverse link users is large (e.g. 100 users per cell) and hence IUI is large, the CDF performance worsens, and vice versa. In addition, the performance improves with increasing ADC/DAC resolution. By significantly increasing the ratio N_a/K_ℓ, the user beams become exceedingly narrow, and the desired signal dominates the noise and interference. This factor, for example, rejects about 9 dB of interference at a CDF of 80%. Although the increase of this factor is important, the SINR is limited by the pilot contamination which is corroborated by (6.52).

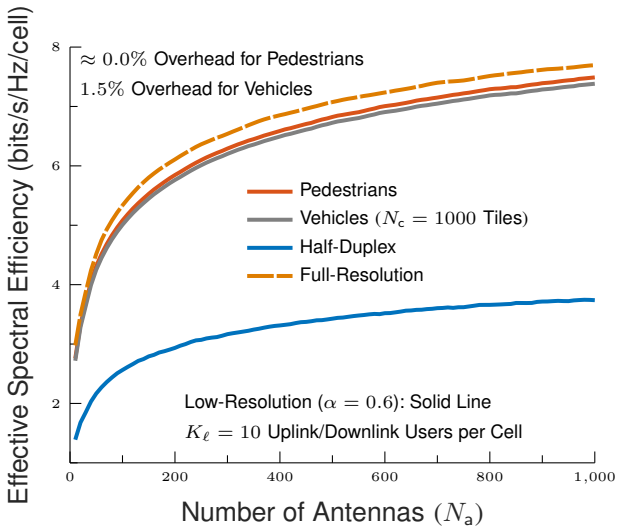

Figure 6.13: Forward link results: Effects of SI power, overhead, DAC resolution, duplexing mode and pilot contamination on the spectral efficiency. Dashed yellow curve stands for full-resolution, pedestrians and FD. Solid red and gray curves stand for low-resolution and FD. Solid blue curve stands for low-resolution DAC, HD and pedestrians scenario.

Fig. 6.13 shows the forward link spectral efficiency vs. number of BS antennas for low and full DAC resolution. Since the pedestrian mobility features a large fading coherence tile and hence low overhead, better spectral efficiency is achieved vs. vehicular mobility that features a small fading coherence tile and hence higher overhead. In addition, we observe that the proposed system outperforms HD mode, which shows the feasibility of FD in cellular networks.

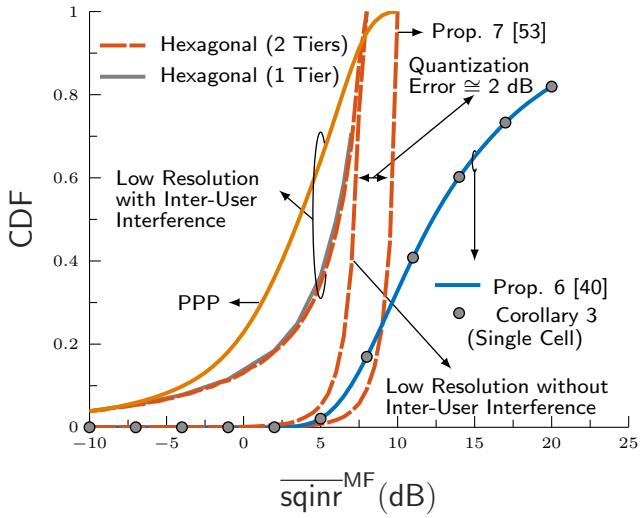

Figure 6.14: Forward link results: Effects of full-duplexing, quantization error, and network cell shapes on outage probability (CDF) with quantizer gains $\alpha_u = \alpha_d = 0.6$. The results are simulated without accounting for pilot contamination.

Fig. 6.14 plots the CDF, or outage probability, vs. forward link SQINR. In the CDF, the PPP tessellation exceeds the hexagonal lattice except for a small range of 5–8 dB of forward link SNR. In addition, the performance decreases with increasing inter-user interference incurred by FD operation of the BS and uplink UEs transmission. The plot shows the loss incurred by the low-resolution ADC/DAC is about 2 dB when the CDF saturates.

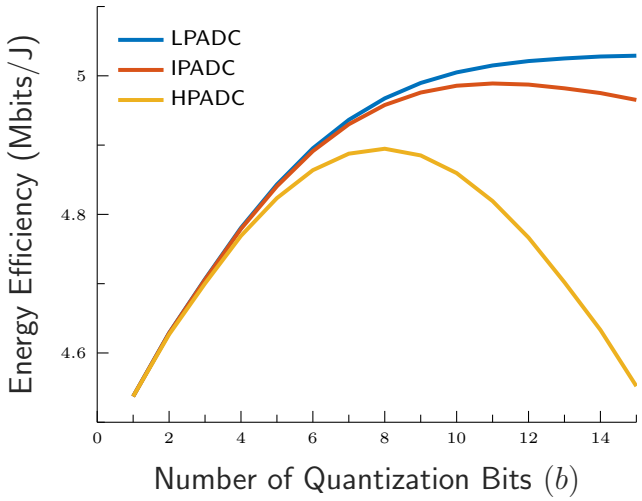

Figure 6.15: Reverse link results: Energy efficiency vs. number of quantization bits for three ADC generations using values of Walden's figure of merit c given in Table 6.4.

Fig. 6.15 plots the energy efficiency vs. number of quantization bits b for three ADC generations. Each generation shows the number of ADC bits that gives maximum energy efficiency, e.g. 8 bits for HPADC, 11 bits for IPADC and 15 bits for LPDAC described in Section 6.7.1, with energy efficiency increasing for b lower than this value and decreasing for b greater than this value. The optimal point is influenced by both the saturation of the spectral efficiency as b increases, which depends on SNR, and by the ADC power consumption model, which increases with b. Comparing ADC generations, the power consumption of the legacy LPADC model increases at a higher rate vs. b than for either IPADC or HPADC models.

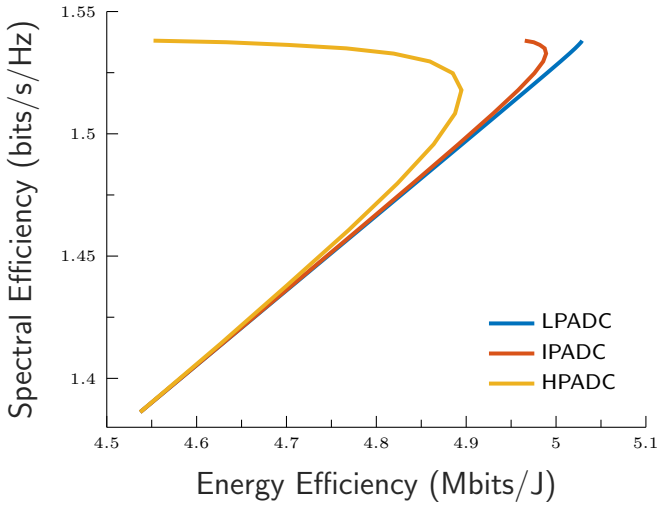

Figure 6.16: Reverse link results: Spectral efficiency vs. energy efficiency for three ADC generations using values of Walden's figure of merit c given in Table 6.4.

Fig. 6.16 plots the spectral vs. energy efficiency for three ADC generations. In the chart, we notice curves that evolve as the number of bits b is increased, reaching upward and right up to a point where they wrap around themselves and energy efficiency returns to the top left corner. Each curve can be interpreted as an "operating region" where the BS receiver can be implemented. The more extended the area covered by a receiver, the more versatile the corresponding design; the closer a curve to the top-right corner, the better the corresponding architecture. We observe that the energy efficiency only increases up to a certain number of bits due to the fact that for a smaller number of bits b, the spectral efficiency increases more than the power, and the energy efficiency increases. However, for a larger number of bits b, the power consumption increases faster than the spectral efficiency, thereby resulting in a decrease of the energy efficiency while the spectral efficiency still increases. This occurs due to the fact that the power consumption of ADC increases exponentially, whereas the spectral efficiency increases sub-linearly, with an increase in the number of ADC bits.

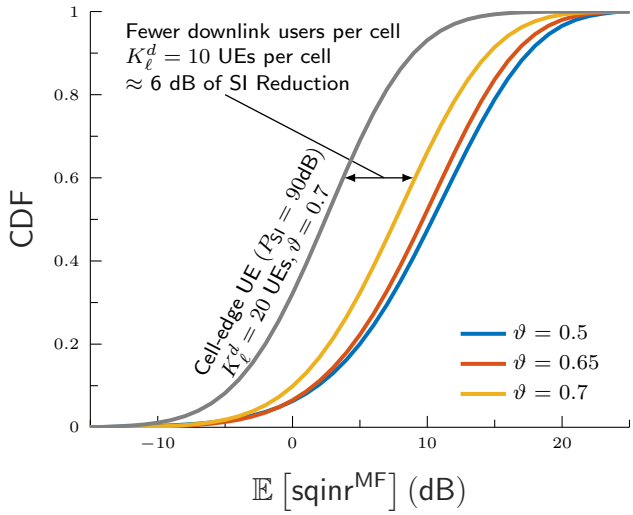

Figure 6.17: Large-scale distribution of $\mathbb{E}\left[\mathsf{sqinr}^{\mathsf{MF}}\right]$ based LMMSE estimation in the reverse link of a two-tier hexagonal network with fractional power control (ϑ) and SI power (P_{SI}). A cell-edge user is considered for the simulation with 3 bits of ADC resolution at the BS. The gray and yellow curves are simulated for the same power control ($\vartheta = 0.7$) but with a different number of downlink users per cell. The blue, red and yellow curves correspond to the same simulation parameters including the same number of downlink UEs = 10, but with different power control coefficients (ϑ).

Fig. 6.17 plots the CDF of the SQINR based on LMMSE channel estimation for different fractional power control values as well as SI power. The primary motivations for a fractional power control policy in the cellular reverse link are to provide beneficial coverage enhancements for the lowest-percentile users, who are typically at the cell-edge, and manage the average transmit power of battery-powered UE devices. In practical cellular systems such as LTE and New Radio (NR), fractional power control policy is network-specific and not user-specific; thus, there needs to be some optimization carried out to select parameters that can provide acceptable performance for the majority of users and bestow a high overall system capacity. For $\vartheta = 0$, the fractional power control policy reverts to a fixed-power transmission. For $\vartheta > 0$, conversely, it compresses the dynamic range of the received power by a factor ϑ. At high SNR, the use of larger values ϑ affects the CDF since the users closest to their serving BSs greatly decrease their transmit power relative to the users at the

cell-edge. Exponent values for ϑ in the range of 0.5 to 0.7 have been identified as providing a satisfactory balance between cell-edge and aggregate performance [62]. In addition, the cell-edge features high SI power of around 90 dB. When the number of forward link UEs decreases, the forward link transmit power at the BSs decreases resulting in lowering the SI power by approximately 6 dB and hence improving the CDF.

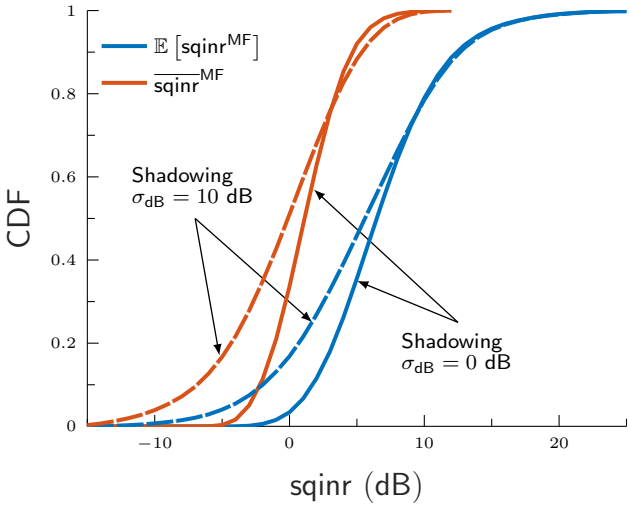

Figure 6.18: Large-scale distribution of $\mathbb{E}\left[\mathsf{sqinr}^{\mathsf{MF}}\right]$ based LMMSE estimation and $\overline{\mathsf{sqinr}}^{\mathsf{MF}}$ based channel hardening in the reverse link of a two-tier hexagonal network without power control. For ADC resolution, $b = 3$ bits is assumed.

Fig. 6.18 plots the CDF of the large-scale distribution for LMMSE channel estimation and channel hardening as well as different values of the shadowing standard deviation. We observe that $\overline{\mathsf{sqinr}}^{\mathsf{MF}}$ (channel hardening) tracks $\mathbb{E}\left[\mathsf{sqinr}^{\mathsf{MF}}\right]$ (LMMSE channel estimation) most of the way with a gap of roughly 7 dB. Certainly, $\overline{\mathsf{sqinr}}_k^{\mathsf{MF}} \leq \mathbb{E}\left[\mathsf{sqinr}_k^{\mathsf{MF}}\right], k = 0, \ldots, K-1$ because to evaluate $\overline{\mathsf{sqinr}}_1^{\mathsf{MF}}, \ldots, \overline{\mathsf{sqinr}}_{K-1}^{\mathsf{MF}}$, we have unconditioned on $\hat{\mathbf{h}}_0, \ldots, \hat{\mathbf{h}}_{K-1}$ and $\mathbf{w}_k$, thereby depriving the receiver of information. However, the performance of a channel hardening-based receiver is less complex to compute, and deep into the massive MIMO regime; it is hardly inferior but instead serves as a tight lower bound and convenient analytical tool. We further

observe that the shadowing strength raises the lower tail of the SQINR distribution at the expense of a slight reduction in the upper tail of the CDF near saturation.

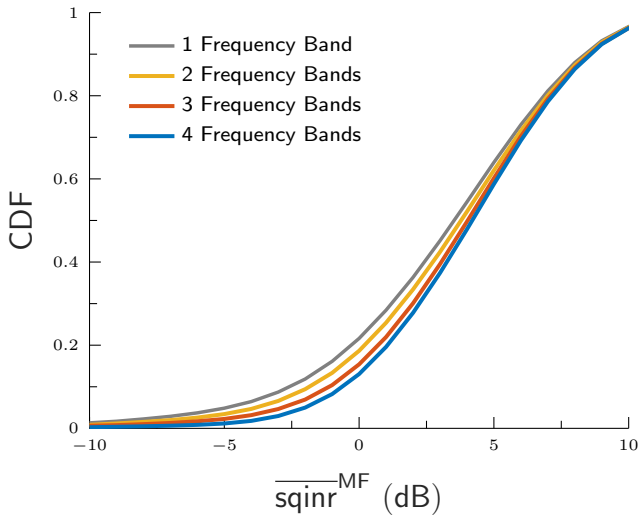

Figure 6.19: Large-scale CDF vs. $\overline{\text{sqinr}}^{\text{MF}}$ based channel hardening in the forward link for a PPP network for four different numbers of frequency bands, Δ. For ADC resolution, $b = 3$ bits is assumed.

Cellular network service providers must guarantee a minimum QoS for their customers such as rate and coverage probability. Commercial cellular network designers must find a way to increase and maintain a satisfied coverage probability. For the case where the network is interference-limited, a robust way to improve the coverage is to decrease the number of interfering BSs. This can be carried out using fractional frequency reuse policy wherein $\Delta \geq 1$ is the reuse factor that determines the number of various frequency bands exploited by the network, where one band is used per cell. From the independent thinning Theorem of PPP [56, Theorem 2.36], it follows that the interfering BSs that transmit in the same frequency band are a thinned version of the original PPP and have a density $\lambda_{\text{BS}}/\Delta$. Note that the thinned version of a PPP is also a PPP. Increasing the frequency reuse factor leads to minimizing the interference and hence improving the outage probability (CDF) as shown by Fig. 6.19. When $\Delta \longrightarrow \infty$, cellular interference is completely eliminated and hence the network

becomes noise-limited.

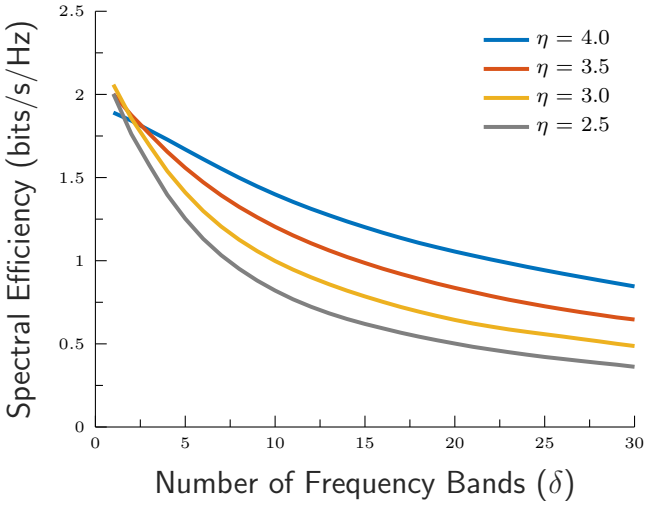

Figure 6.20: Spectral efficiency vs. number of frequency bands for the large-scale $\overline{\mathsf{sqinr}}^{\mathsf{MF}}$ based channel hardening in the reverse link for a PPP network. Simulations are considered for different values of the pathloss (η) as well as 3 bits of ADC resolution.

The desirable increase in coverage with increasing Δ has to be balanced against the fact that each cell can only exploit $1/\Delta$-th of the available frequencies. Fig. (6.20) shows the optimal fractional frequency reuse Δ from the average spectral efficiency perspective is in fact $\Delta = 1$; i.e., any increase in coverage from frequency reuse is paid for by decreasing the sum spectral efficiency in the network. Therefore, increasing the number of frequency bands can lead to non-efficient use of the spectrum and hence degrade the spectral efficiency. We also observe spectral efficiency improves with increasing pathloss. In fact, this is explained by the fact that since the network is interference-limited, the higher pathloss exponent would also reduce the power of the interfering signals, thereby leading to the spectral efficiency improvement.

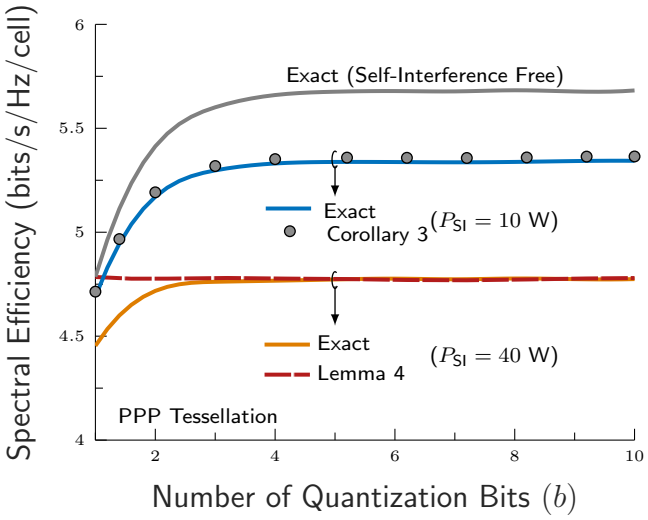

Figure 6.21: Spectral efficiency vs. number of quantization bits for large-scale distribution $\overline{\mathsf{sqinr}}^{\mathsf{MF}}$ in the reverse link for a PPP network. We assume $N_{\mathsf{a}} = 1000$ antennas at the BS.

Fig. 6.21 simulates the reverse link spectral efficiency vs. number of quantization bits (b) for a PPP tessellation network. Spectral efficiency increases with b and converges to a ceiling derived by (6.58) in Lemma 4; the rate decreases when adopting low-resolution ADCs and DACs (low b). Spectral efficiency degrades for 10W and 40W of SI power vs. the SI-free case.

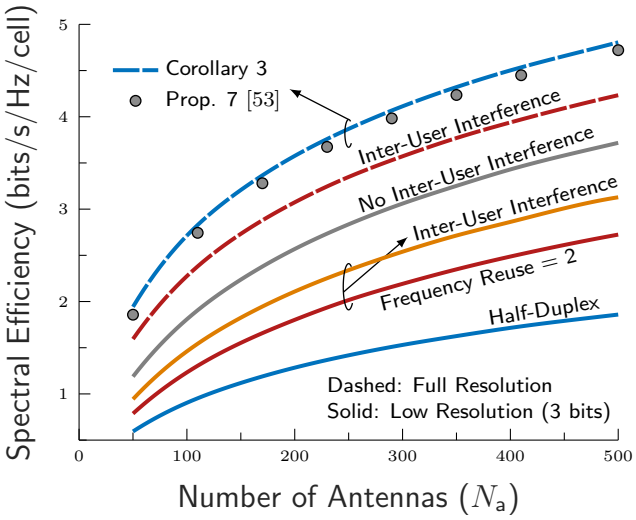

Figure 6.22: Spectral efficiency vs. number of antennas for large-scale distribution $\overline{\mathsf{sqinr}}^{\mathsf{MF}}$ in the forward link for a PPP network. The default value of frequency reuse factor is 1.

Fig. 6.22 shows the forward link spectral efficiency increasing with the number of quantization bits b and BS antennas for a PPP tessellation. When considering low and full resolution data converters, spectral efficiency converges to a fixed ceiling with enough antennas, which agrees with (6.65) in Lemma 7.

Fig. 6.23 illustrates the performance of the reverse link spectral efficiency vs. average SNR. We observe that the proposed hybrid beamforming FD design achieves better spectral efficiency than the HD mode, and the relative gap increases with average SNR. Moreover, there are losses in spectral efficiency between the proposed design in comparison with the benchmarks of the all-digital case (wherein an RF chain is dedicated to each antenna element) and the upper bound. These losses are incurred by the unit modulus constraint as well as the limited number of RF chains in the hybrid architecture which itself is a loss in the DoF.

Fig. 6.24 shows the performance of the forward link spectral efficiency vs. average SNR. We notice that the performance improves with the number of RF chains at the BS and approaches the all-digital performance with 8 RF chains. In fact,

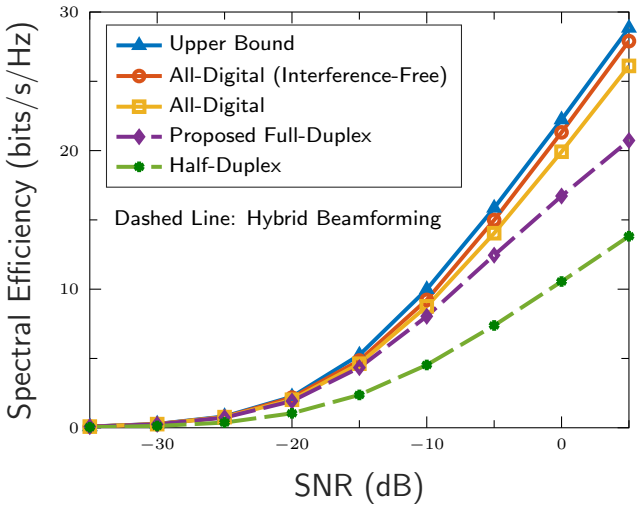

Figure 6.23: Reverse link spectral efficiency results for single cell, multiuser scenario: Comparison of the proposed FD hybrid beamforming algorithm with the HD case, all-digital beamforming, and upper bound. 5 users are uniformly dropped in the cell.

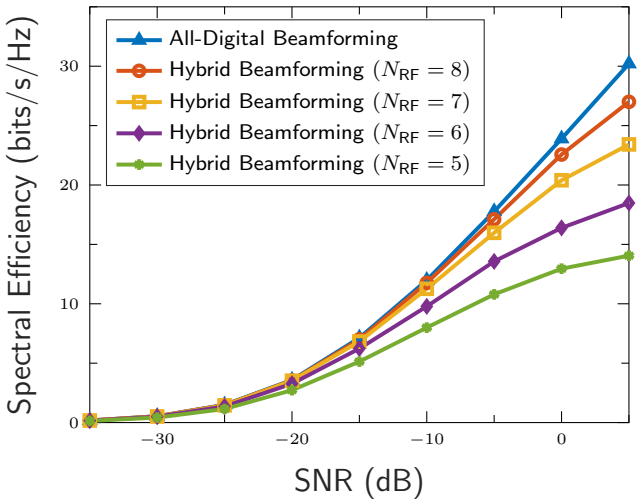

Figure 6.24: Forward link spectral efficiency results for single cell, multiuser scenario. Comparison between all-digital and hybrid beamforming for different numbers of RF chains at the BS. 5 users are uniformly placed in the cell.

increasing the number of RF chains is equivalent to providing more DoF to cancel the interference and achieve a spatial multiplexing gain, thereby resulting in good spectral efficiency.

6.9 Conclusion

In this chapter, we provided a unified framework for full-duplex cellular networks with low resolution ADCs/DACs. Using the framework, we developed analytical expressions for the SQINR and spectral efficiency and for forward and reverse links under pilot contamination, LMMSE channel estimation and channel hardening. The proposed modeling accounts for pilot overhead, self-interference, and network geometry such as hexagonal lattice, square grid and PPP tessellation. Matched filter receivers and precoders are applied at the receive and transmit arrays of the BSs, respectively, to further reduce complexity.

Further, we derived special cases, asymptotic results and power scaling laws to unpack several engineering insights of the proposed model. First, if the number of antennas N_{a} and number of resolution bits b are held fixed and the power goes to infinity, the spectral efficiency for the reverse and forward links are saturated by a ceiling determined by the number of antennas and the ADC/DAC resolution gains. Second, if the power scales with the number of antennas and the latter becomes massive, cellular interference including pilot contamination, inter-cell interference, and intra-cell interference vanishes except for the SI power. Third, if the ratio of the number of antennas N_{a} and the number of users per cell K_ℓ goes to infinity, cellular interference is rejected but pilot contamination and SI power remain. We also observe spectral efficiency improves with increasing pathloss. In fact, this is explained by the fact that since the network is interference-limited, the higher pathloss exponent would also reduce the the interfering signals power, thereby leading to the spectral efficiency improvement.

Furthermore, we extended the analysis of sub-7 GHz LTE bands to support

mmWave bands. In the analysis, we introduced a signal processing perspective on hybrid A/D beamforming, a problem formulation of the hybrid beamforming design and benchmarking tools such as the impractical all-digital beamforming approach and an upper bound on the spectral efficiency.

We also analyzed power consumption and investigated the effects of ADC/DAC power, Walden's figure merit for ADCs/DACs, and the number of quantization bits on energy efficiency. In addition, the overall system performance is quantified in terms of effective spectral efficiency and outage probability (i.e. cumulative distribution function of the large-scale distribution of the SQINR). Using a proper scaling ratio of the number of antennas N_{a} over number of users per cell K_ℓ, a large amount of interference can be rejected as previously mentioned; this justifies the use of matched filter beamforming which is less complex than MMSE and ZF filters. Although the SQINR is limited by pilot contamination for a massive number of antennas, this effect is not pronounced.

Simulation results show the quantization error, SI, and IUI incur rate losses; however, the rate loss can be compensated by employing a large number of BS antennas as well as high resolution ADCs/DACs in the UEs. The hefty power consumption in the BSs due to having a large number of antennas can be reduced by employing low resolution ADCs/DACs. The simulation results also corroborated the robustness of the proposed FD mode compared to the HD mode, which is one of the goals of this work to demonstrate the feasibility of the FD in cellular networks.

Finally, analytical expressions derived for matched filters are widely applicable, as corroborated by a multitude of examples. This wide applicability of the proposed reverse and forward link analysis makes its extension to other low-complex and yet resilient transmit and receive strategies, power allocation, user association policies and even channel conditions, highly attractive.

Chapter 7: Conclusions

This chapter concludes the dissertation with a summary of contributions in Section 7.1 and potential future directions in Section 7.2

7.1 Summary

This dissertation has explored advanced signal processing techniques for enabling FD communication in mmWave systems for different scenarios. The research contributions presented have proposed beamforming-based solutions that allow mmWave communication systems to simultaneously transmit and receive over the same resource block, facilitating efficient FD operation.

- Contribution I: I investigated a point-to-point system in which two FD nodes communicate over bidirectional links at the mmWave band. In this work, I developed a hybrid A/D beamforming design that addresses several key practical considerations. The design employs convex optimization techniques to spatially minimize SI power to levels sufficiently low to prevent the saturation of critical receiver chain components, such as LNAs and ADCs. Simulation results demonstrate that the proposed design achieves significant SI reduction in the analog domain, averaging approximately 67 dB, while also improving the sum spectral efficiency. From an industrial perspective, the design can be practically implemented using 128 antennas and 32 RF chains, yielding a spectral efficiency of 20.8642 bits/s/Hz and a computational complexity of approximately 2.8071 MFLOPS. Additionally, the design achieves substantial SI suppression of around 70.3621 dB. This high level of SI suppression could enable the use of lower-resolution ADCs by reducing the dynamic range requirements, thereby decreasing the power consumption of the ADCs.

- Contribution II: I investigated a single-cell, single-user communication scenario where both single uplink and single downlink transmissions are facilitated by a FD BS. I developed a hybrid A/D beamforming design that addresses several key constraints, including minimizing SI and inter-user interference, while adhering to unit modulus and semi-unitary constraints. The primary objective was to design a low-complexity, yet robust, hybrid beamforming solution that effectively mitigates interference and converges within a few iterations. Additionally, I examined factors that influence the algorithm's convergence, such as the regularization of the interference covariance matrix and the normalization of beamforming both pre- and post-convergence. The performance of the algorithm was evaluated using critical metrics, including SI reduction, computational complexity, convergence rate, and stability. Simulation results demonstrate the robustness of the proposed design, achieving substantial improvements in interference suppression and spectral efficiency compared to existing methods. The proposed design offers a significant enhancement in uplink spectral efficiency, with improvements of up to 70%, while achieving interference suppression below the -50 dB threshold in the analog domain to prevent ADC saturation. Notably, increasing the number of BS antennas further reduces effective SI to -130 dB, while enhancing uplink spectral efficiency to 14 bits/s/Hz. The approach skillfully leverages the available degrees of freedom to balance interference suppression and spectral efficiency optimization. A key advantage of the algorithm is its rapid convergence, typically within $5-10$ iterations, which is essential for minimizing latency and reducing the overhead associated with beamforming configuration. This efficiency in convergence highlights the time savings achieved by the method. Furthermore, the proposed strategy outperforms existing hybrid beamforming approaches and half-duplex methodologies, underscoring the transformative potential of FD mmWave technology in cellular networks.
- Contribution III: I explored the IAB system in which the IAB node receives data

from the gNB donor via the backhaul link and transmits it to the user over the access channel. Operating in FD mode, the IAB node experiences significant self-interference (SI), which adversely affects the backhaul channel. To mitigate this issue, I formulated an optimization problem aimed at minimizing the SI power at the IAB node. Utilizing a similar approach as in the first contribution, I designed the analog beamformers for the IAB node and derived regularized zero-forcing beamformers for the gNB donor and MMSE beamformers for the user. The computational cost of designing the hybrid beamformers was found to be relatively efficient compared to existing methods. By tracking SI reduction in both the analog and digital domains, the proposed algorithm demonstrated rapid convergence, typically within $3-5$ iterations, effectively reducing SI to a lower level. Moreover, simulation results revealed that the proposed hybrid A/D beamforming design outperforms half-duplex systems in terms of spectral efficiency and offers superior performance compared to other related approaches, thus highlighting the practicality and feasibility of the proposed design for real-world applications.

- Contribution IV: Building upon the second contribution, I extended the research to encompass wideband mmWave multiuser uplink and downlink communications. In this setup, the user devices employ a fully digital architecture, while the BS adopts a hybrid A/D architecture. To reduce power consumption, the phase shifters at the BS are quantized, and the transmit/receive arrays utilize a partially connected structure. I formulated the per-subcarrier sum spectral efficiency for both uplink and downlink users, focusing on minimizing SI, inter-user interference (uplink interference with downlink users), and multiuser interference (interference among uplink or downlink users). Given the stringent constraints of the hybrid architecture—such as the absence of amplitude control in the phase shifters and the challenge of finite-resolution phase shifters—I demonstrated the feasibility of incorporating these limitations into the design

while achieving significant interference reduction in the analog domain to prevent ADC saturation. Specifically, the proposed analog beamformers effectively suppress wideband SI through the implementation of multiple frequency nulls. Simultaneously, the baseband beamformers are carefully optimized to enhance beamformed signal power and minimize residual SI and multiuser interference, as shown by the improved beam patterns. In addition, I employed a partially connected array structure in the hybrid architecture to improve energy efficiency. The proposed approach outperforms existing hybrid beamforming techniques and HD methods, demonstrating the transformative potential of FD mmWave technology in cellular networks and integrated sensing and communication systems.

- Contribution V: In this work, I extended the previous contribution to a massive MIMO multicell, multiuser scenario, where BSs operate in FD mode and are equipped with a large number of antennas. I developed a unified analytical framework to address both uplink (reverse) and downlink (forward) communications, applicable to both LTE and mmWave bands, while incorporating low-resolution data converters. The analysis accounts for various system imperfections, including low-resolution quantization noise, pilot contamination, network irregularities, imperfect CSI, user mobility, cellular interference, and SI. A key performance metric, the SQINR, was derived, enabling an in-depth investigation of the system's effective spectral and energy efficiency. Furthermore, I derived special cases, asymptotic results, and power scaling laws to provide critical engineering insights into the proposed model. Specifically, I examined the effect of the ratio between the number of antennas and the number of users on pilot contamination, cellular interference, and self-interference. The analysis was also extended from sub-7 GHz LTE bands to mmWave bands, incorporating hybrid A/D beamforming and formulating the beamforming design problem. Benchmarking tools, such as the impractical all-digital beamforming

approach and upper bounds on spectral efficiency, were also introduced. Additionally, I analyzed power consumption and explored the impact of ADC/DAC power, Walden's figure of merit for ADCs/DACs, and quantization resolution on energy efficiency. The overall system performance was quantified using metrics such as effective spectral efficiency and outage probability, represented by the cumulative distribution function of the large-scale distribution of the SQINR. By maintaining a suitable scaling ratio of antennas to users per cell, a significant portion of interference can be mitigated, justifying the use of matched filter beamforming, which offers lower complexity compared to MMSE and ZF filters. Although the SQINR is theoretically limited by pilot contamination in massive antenna arrays, this effect was shown to be minimal. Simulation results demonstrate that quantization errors, self-interference, and inter-user interference lead to rate degradation; however, this loss can be compensated by increasing the number of BS antennas and employing high-resolution ADCs/DACs at the UE. The high power consumption at the BS, due to the large number of antennas, can be reduced by using low-resolution ADCs/DACs. Simulation results further confirmed the robustness of the proposed FD mode in comparison to half-duplex operation, validating the feasibility of FD technology in cellular networks. Finally, the analytical expressions derived for matched filters are widely applicable, as supported by numerous examples. This versatility makes the proposed reverse and forward links analysis highly attractive for extension to other low-complexity, resilient transmission and reception strategies, power allocation schemes, user association policies, and various channel conditions.

7.2 Future Directions

This dissertation concludes by detailing directions for future research that can capitalize on the progress made herein.

7.2.1 Full-Duplex in Integrated Sensing and Communication Systems

Integrated Sensing and Communication (ISAC) is becoming a key component of emerging applications such as autonomous vehicles, industrial IoT, and smart cities, where systems must communicate while simultaneously sensing their environment. FD technology enables simultaneous transmission and reception, allowing ISAC systems to perform both tasks concurrently. However, managing interference between the communication and sensing functions remains a significant challenge. Research could explore new beamforming and interference mitigation techniques to ensure that both communication and sensing are carried out efficiently. In a smart city scenario, for instance, FD ISAC systems could enable autonomous vehicles to simultaneously communicate with traffic management systems while using radar to detect nearby obstacles. The FD system would allow vehicles to send real-time updates about their location, speed, and traffic conditions, while also using sensors to monitor the surrounding environment for potential hazards. This would greatly improve safety and efficiency, particularly in high-traffic areas, where quick decision-making is critical. The challenge lies in ensuring that communication and sensing tasks do not interfere with each other, which requires sophisticated interference management and beamforming strategies.

7.2.2 Full-Duplex in Cooperative and Relay Networks

In cooperative communication systems, where nodes assist in forwarding data between users, FD relays can significantly boost network throughput by enabling simultaneous transmission and reception. This has the potential to double the effective data rate compared to half-duplex relays. However, implementing FD in relay systems introduces additional interference, particularly from the transmitted signals to the received signals. Advanced SI cancellation techniques need to be developed for relay scenarios to ensure reliable data forwarding without degradation in performance. Research could also focus on optimizing the relay protocols to manage the increased

complexity introduced by FD.

Consider a healthcare scenario in a remote village where FD relays are used to extend connectivity from a main hospital to a smaller clinic. These relays would enable simultaneous transmission of medical data from the clinic to the hospital and reception of patient records or consultations from the hospital. The relay could forward critical patient data in real-time, improving the quality of healthcare by allowing instant communication between doctors and patients. The ability to double the data rate without doubling the infrastructure is particularly valuable in rural areas, where building new infrastructure can be costly and time-consuming.

7.2.3 Machine Learning for Full-Duplex Resource Management

Managing the complexity of FD systems, especially in multiuser and massive MIMO settings, requires intelligent resource management strategies. ML algorithms could be used to dynamically allocate resources such as power, bandwidth, and beamforming configurations in real time. ML models can learn from network conditions and optimize interference mitigation and resource usage based on real-time data. This would be particularly useful in environments with highly variable interference and traffic loads, such as smart cities or industrial IoT networks.

In a smart city like San Diego, where network demand fluctuates throughout the day, ML algorithms could predict periods of high traffic and optimize FD BS resources accordingly. For example, during rush hour, the algorithms could allocate more resources to areas with higher data demand, such as public transportation hubs, while minimizing interference in adjacent areas. This real-time optimization would ensure a smooth communication experience for users while maximizing the efficiency of the FD system, reducing power consumption, and mitigating interference.

7.2.4 Security in Full-Duplex Systems

FD systems, while offering performance gains, also introduce new security challenges, such as the risk of eavesdropping on SI channels or vulnerability to jamming attacks. Physical-layer security techniques could be developed to protect FD systems from these threats. For example, artificial noise could be generated to mask sensitive communications, or cooperative jamming could be used to disrupt potential eavesdroppers. Research could focus on developing security protocols that leverage FD technology to provide robust protection against these new types of attacks.

In a high-security environment, such as financial institutions in downtown Austin, FD systems with enhanced security features could ensure that sensitive data, such as financial transactions, remain secure even in the presence of potential eavesdroppers. By using artificial noise generation to mask communication signals, FD systems could prevent unauthorized interception of data. This would be particularly important in environments where privacy and security are critical, and traditional security mechanisms may be insufficient.

7.2.5 Full-Duplex for Quantum Communication Networks

As quantum communication networks become a reality, ensuring the efficient transmission and reception of quantum information will be critical. FD technology could potentially play a role in quantum communication networks by allowing quantum bits (qubits) to be transmitted and received simultaneously, improving the overall efficiency of quantum data transfer. However, integrating FD with quantum communication presents unique challenges, particularly in managing the delicate nature of quantum states and ensuring that interference does not degrade quantum entanglement or coherence.

Research could explore how FD techniques can be adapted to quantum communication, focusing on minimizing quantum noise and maintaining the integrity of qubits during transmission and reception. For example, in a quantum key distribu-

tion system, FD could enable faster and more secure transmission of quantum keys by allowing simultaneous exchange of quantum information between two parties, improving the speed and security of encryption.

Appendix A: Proofs of Chapter 2

A.1 Proof of Theorem 1

The objective is to minimize the cost function (effective interference power) in (2.5), while preserving the rank of the effective channel. We express the Lagrangian function given by

$$\mathcal{L}\left(\mathbf{W}_n^{\mathsf{RX}}, x\right) = \mathbf{W}_n^{\mathsf{RF}*}\mathbf{R}_n\mathbf{W}_n^{\mathsf{RF}} + x\left(\mathbf{W}_n^{\mathsf{RF}*}\mathbf{H}_{nm}\mathbf{F}_m^{\mathsf{RF}} - \mathbf{I}_{N_{\mathsf{RF}}}\right) \tag{A.1}$$

The Lagrangian conditions for this problem are expressed by

$$\nabla_{\mathbf{W}_n^{\mathsf{RF}*}}\mathcal{L} = 0 \tag{A.2}$$

$$x^{\star}\left(\mathbf{W}_n^{\mathsf{RF}*}\mathbf{H}_{nm}\mathbf{F}_n^{\mathsf{RF}} - \mathbf{I}_{N_{\mathsf{RF}}}\right) = 0 \tag{A.3}$$

Then, (A.2) can be reformulated as

$$\nabla_{\mathbf{W}_n^{\mathsf{RF}*}}\mathrm{Tr}\left(\mathbf{W}_n^{\mathsf{RF}*}\mathbf{R}_n\mathbf{W}_n^{\mathsf{RF}}\right) + x^{\star}\nabla_{\mathbf{W}_n^{\mathsf{RF}*}}\left(\mathbf{W}_n^{\mathsf{RF}*}\mathbf{H}_{nm}\mathbf{F}_m^{\mathsf{RF}} - \mathbf{I}_{N_{\mathsf{RF}}}\right) = 0 \tag{A.4}$$

where ∇ is the gradient operator and $x^{\star}$ is the Lagrange multiplier. Differentiating (A.4) with respect to $\mathbf{W}_{\mathsf{BS}}^{*}$, we obtain

$$\mathbf{R}_n\mathbf{W}_n^{\mathsf{RF}} + x\mathbf{H}_{nm}\mathbf{F}_n^{\mathsf{RF}} = 0 \tag{A.5}$$

$$\mathbf{W}_n^{\mathsf{RF}} = -\mathbf{R}_n^{-1}\mathbf{H}_{nm}\mathbf{F}_m^{\mathsf{RF}}x \tag{A.6}$$

Then substituting the expression of $\mathbf{W}_n^{\mathsf{RF}}$ in (A.3), we get

$$\left(-\mathbf{R}_n^{-1}\mathbf{H}_{nm}\mathbf{F}_m^{\mathsf{RF}}x\right)^{*}\mathbf{H}_{nm}\mathbf{F}_m^{\mathsf{RF}} = \alpha\mathbf{I}_{N_{\mathsf{RF}}} \tag{A.7}$$

$$x = -\alpha\left(\mathbf{F}_m^{\mathsf{RF}*}\mathbf{H}_{nm}^{*}\mathbf{R}_n^{-1}\mathbf{H}_{nm}\mathbf{F}_m^{\mathsf{RF}}\right)^{-1} \tag{A.8}$$

Thereby

$$\mathbf{W}_n^{\mathsf{RF}} = \alpha\mathbf{R}_n^{-1}\mathbf{H}_{nm}\mathbf{F}_m^{\mathsf{RF}}\left(\mathbf{F}_m^{\mathsf{RF}*}\mathbf{H}_{nm}^{*}\mathbf{R}_n^{-1}\mathbf{H}_{nm}\mathbf{F}_m^{\mathsf{RF}}\right)^{-1} \tag{A.9}$$

The proof of the analog precoder ($\mathbf{F}_n^{\mathsf{RF}}$) follows the same derivation steps as $\mathbf{W}_n^{\mathsf{RF}}$.

A.2 Proof of Theorem 2

For a given $\mathbf{X}_n^{\mathsf{RF}}$, consider the SVD $\mathbf{X}_n^{\mathsf{RF}} = \mathbf{U}_n^{\mathsf{RF}}\mathbf{S}_n^{\mathsf{RF}}\mathbf{V}_n^{\mathsf{RF}*}$, and let $\mathbf{Q} = \mathbf{S}_n^{\mathsf{RF}}\mathbf{V}_n^{\mathsf{RF}*}\mathbf{X}_n^{\mathsf{BB}} \in \mathbb{C}^{L\times N}$. Then $\mathbf{X}_n^{\mathsf{RF}}\mathbf{X}_n^{\mathsf{BB}} = \mathbf{U}_n^{\mathsf{RF}}\mathbf{Q}$ so that $\mathbf{X}_n^{\mathsf{BB}*}\mathbf{X}_n^{\mathsf{RF}*}\mathbf{X}_n^{\mathsf{RF}}\mathbf{X}_n^{\mathsf{BB}} = \mathbf{Q}^*\mathbf{U}_n^{\mathsf{RF}*}\mathbf{U}_n^{\mathsf{RF}}\mathbf{Q} = \mathbf{Q}^*\mathbf{Q}$. The generic form of the spectral efficiency in (2.3) is expressed in terms of $\mathbf{Q}$ as

$$\max_{\mathbf{Q}^*\mathbf{Q}=\mathbf{I}_N} \log\det\left(\mathbf{I} + \rho\mathbf{Q}^*\mathbf{U}_n^{\mathsf{RF}*}\mathbf{A}_n\mathbf{A}_n^*\mathbf{U}_n^{\mathsf{RF}}\mathbf{Q}\right) \tag{A.10}$$

Solution $\mathbf{Q}_\star$ is given by the N dominant left singular vectors of $\mathbf{U}_n^{\mathsf{RF}}\mathbf{A}_n$. By changing variables, we solve $\mathbf{X}_n^{\mathsf{BB}} = \mathbf{V}_n^{\mathsf{RF}}(\mathbf{S}_n^{\mathsf{RF}})^{-1}\mathbf{Q}_\star$. For $\mathbf{Q} = \mathbf{Q}_\star$, the objective function becomes

$$\log\det\left(\mathbf{I} + \rho\mathbf{Q}^*\mathbf{U}_n^{\mathsf{RF}*}\mathbf{A}_n\mathbf{A}_n^*\mathbf{U}_n^{\mathsf{RF}}\mathbf{Q}\right) \leq \log\det\left(\mathbf{I} + \rho\mathbf{A}_n^*\mathbf{A}_n\right) \tag{A.11}$$

with the bound in (A.11) applying to any semi-unitary $\mathbf{U}_n^{\mathsf{RF}}$. This bound holds with equality if the columns of $\mathbf{U}_n^{\mathsf{RF}}$ are taken as the L dominant left singular vectors of $\mathbf{A}_n$.

Appendix B: Proofs of Chapter 3

B.1 Proof of Theorem 3

The objective is to minimize the cost function (effective interference power) in (3.16), while preserving the rank of the effective channel. We express the Lagrangian function given by

$$\mathcal{L}\left(\mathbf{W}_{\mathsf{BS}}, x\right) = \mathbf{W}_{\mathsf{BS}}^{*}\mathbf{R}_{1}\mathbf{W}_{\mathsf{BS}} + x\left(\mathbf{W}_{\mathsf{BS}}^{*}\mathbf{H}_{\mathsf{u}}\mathbf{F}_{\mathsf{UE}} - \mathbf{I}_{N_{\mathsf{s}}}\right) \tag{B.1}$$

The Lagrangian conditions for this problem are expressed by

$$\nabla_{\mathbf{W}_{\mathsf{BS}}^{*}}\mathcal{L} = 0 \tag{B.2}$$

$$x^{\star}\left(\mathbf{W}_{\mathsf{BS}}^{*}\mathbf{H}_{\mathsf{u}}\mathbf{F}_{\mathsf{UE}} - \mathbf{I}_{N_{\mathsf{s}}}\right) = 0 \tag{B.3}$$

Then, (B.2) can be reformulated as

$$\nabla_{\mathbf{W}_{\mathsf{BS}}^{*}}\mathrm{Tr}\left(\mathbf{W}_{\mathsf{BS}}^{*}\mathbf{R}_{1}\mathbf{W}_{\mathsf{BS}}\right) + x^{\star}\nabla_{\mathbf{W}_{\mathsf{BS}}^{*}}\left(\mathbf{W}_{\mathsf{BS}}^{*}\mathbf{H}_{\mathsf{u}}\mathbf{F}_{\mathsf{UE}} - \mathbf{I}_{N_{\mathsf{s}}}\right) = 0 \tag{B.4}$$

where ∇ is the gradient operator and $x^{\star}$ is the Lagrange multiplier. Differentiating (B.4) with respect to $\mathbf{W}_{\mathsf{BS}}^{*}$, we obtain

$$\mathbf{R}_{1}\mathbf{W}_{\mathsf{BS}} + x\mathbf{H}_{\mathsf{u}}\mathbf{F}_{\mathsf{UE}} = 0 \tag{B.5}$$

$$\mathbf{W}_{\mathsf{BS}} = -\mathbf{R}_{1}^{-1}\mathbf{H}_{\mathsf{u}}\mathbf{F}_{\mathsf{UE}}x \tag{B.6}$$

Then substituting the expression of $\mathbf{W}_{\mathsf{BS}}$ in (B.3), we get

$$\left(-\mathbf{R}_{1}^{-1}\mathbf{H}_{\mathsf{u}}\mathbf{F}_{\mathsf{UE}}x\right)^{*}\mathbf{H}_{\mathsf{u}}\mathbf{F}_{\mathsf{UE}} = \alpha\mathbf{I}_{N_{\mathsf{s}}} \tag{B.7}$$

$$x = -\alpha\left(\mathbf{F}_{\mathsf{UE}}^{*}\mathbf{H}_{\mathsf{u}}^{*}\mathbf{R}_{1}^{-1}\mathbf{H}_{\mathsf{u}}\mathbf{F}_{\mathsf{UE}}\right)^{-1} \tag{B.8}$$

Thereby

$$\mathbf{W}_{\mathsf{BS}} = \alpha\mathbf{R}_{1}^{-1}\mathbf{H}_{\mathsf{u}}\mathbf{F}_{\mathsf{UE}}\left(\mathbf{F}_{\mathsf{UE}}^{*}\mathbf{H}_{\mathsf{u}}^{*}\mathbf{R}_{1}^{-1}\mathbf{H}_{\mathsf{u}}\mathbf{F}_{\mathsf{UE}}\right)^{-1} \tag{B.9}$$

The proof of the all-digital BS precoder ($\mathbf{F}_{\mathsf{BS}}$) and the all-digital precoder ($\mathbf{F}_{\mathsf{UE}}$) and combiner ($\mathbf{W}_{\mathsf{UE}}$) at UEs follow the same derivation steps as $\mathbf{W}_{\mathsf{BS}}$. In a similar way, we reproduce the same routine to solve for the analog beamformers.

Appendix C: Proofs of Chapter 4

C.1 Proof of Theorem 4

The objective is to minimize the equality in (4.9), while preserving the signal dimensions. We begin by expressing the Lagrangian function given by

$$\mathcal{L}\left(\mathbf{W}_{\mathsf{IAB}}^{\mathsf{RF}}, x\right) = \mathbf{W}_{\mathsf{IAB}}^{\mathsf{RF}*}\mathbf{R}_{\mathsf{IAB}}\mathbf{W}_{\mathsf{IAB}}^{\mathsf{RF}} + x\left(\mathbf{W}_{\mathsf{IAB}}^{\mathsf{RF}*}\mathbf{H}_{\mathsf{b}}\mathbf{F}_{\mathsf{gNB}}^{\mathsf{RF}} - \mathbf{I}_{N_{\mathsf{RF}}}\right) \tag{C.1}$$

The Lagrangian conditions for this problem are

$$\nabla_{\mathbf{W}_{\mathsf{IAB}}^{\mathsf{RF}*}}\mathcal{L} = 0 \tag{C.2}$$

$$x^{\star}\left(\mathbf{W}_{\mathsf{IAB}}^{\mathsf{RF}*}\mathbf{H}_{\mathsf{b}}\mathbf{F}_{\mathsf{gNB}}^{\mathsf{RF}} - \mathbf{I}_{N_{\mathsf{RF}}}\right) = 0 \tag{C.3}$$

Eq. (A.2) can be reformulated as

$$\nabla_{\mathbf{W}_{\mathsf{IAB}}^{\mathsf{RF}*}}\mathrm{Tr}\left(\mathbf{W}_{\mathsf{IAB}}^{\mathsf{RF}*}\mathbf{R}_{\mathsf{IAB}}\mathbf{W}_{\mathsf{IAB}}^{\mathsf{RF}}\right) + x^{\star}\nabla_{\mathbf{W}_{\mathsf{IAB}}^{\mathsf{RF}*}}\left(\mathbf{W}_{\mathsf{IAB}}^{\mathsf{RF}*}\mathbf{H}_{\mathsf{b}}\mathbf{F}_{\mathsf{gNB}}^{\mathsf{RF}} - \mathbf{I}_{N_{\mathsf{RF}}}\right) = 0 \tag{C.4}$$

Where ∇ is the gradient operator and $x^{\star}$ is the Lagrangian multiplier. Differentiating (C.4) with respect to $\mathbf{W}_{\mathsf{IAB}}^{\mathsf{RF}*}$, we get

$$\mathbf{R}_{\mathsf{IAB}}\mathbf{W}_{\mathsf{IAB}}^{\mathsf{RF}} + x\mathbf{H}_{\mathsf{b}}\mathbf{F}_{\mathsf{gNB}}^{\mathsf{RF}} = 0 \tag{C.5}$$

$$\mathbf{W}_{\mathsf{IAB}}^{\mathsf{RF}} = -\mathbf{R}_{\mathsf{IAB}}^{-1}\mathbf{H}_{\mathsf{b}}\mathbf{F}_{\mathsf{gNB}}^{\mathsf{RF}}x \tag{C.6}$$

Then substituting the expression of $(\mathbf{W}_{\mathsf{IAB}}^{\mathsf{RF}})$ in (A.3), we obtain

$$\left(-\mathbf{R}_{\mathsf{IAB}}^{-1}\mathbf{H}_{\mathsf{b}}\mathbf{F}_{\mathsf{gNB}}^{\mathsf{RF}}x\right)^{*}\mathbf{H}_{\mathsf{b}}\mathbf{F}_{\mathsf{gNB}}^{\mathsf{RF}} = \alpha\mathbf{I}_{N_{\mathsf{RF}}} \tag{C.7}$$

$$x = -\alpha\left(\mathbf{F}_{\mathsf{gNB}}^{\mathsf{RF}*}\mathbf{H}_{\mathsf{b}}^{*}\mathbf{R}_{\mathsf{IAB}}^{-1}\mathbf{H}_{\mathsf{b}}\mathbf{F}_{\mathsf{gNB}}^{\mathsf{RF}}\right)^{-1} \tag{C.8}$$

Thereby

$$\mathbf{W}_{\mathsf{IAB}}^{\mathsf{RF}} = \alpha\mathbf{R}_{\mathsf{IAB}}^{-1}\mathbf{H}_{\mathsf{b}}\mathbf{F}_{\mathsf{gNB}}^{\mathsf{RF}}\left(\mathbf{F}_{\mathsf{gNB}}^{\mathsf{RF}*}\mathbf{H}_{\mathsf{b}}^{*}\mathbf{R}_{\mathsf{IAB}}^{-1}\mathbf{H}_{\mathsf{b}}\mathbf{F}_{\mathsf{gNB}}^{\mathsf{RF}}\right)^{-1} \tag{C.9}$$

The proof of the analog precoder at the IAB node $(\mathbf{F}_{\mathsf{IAB}}^{\mathsf{RF}})$ follows the same derivation steps as $(\mathbf{W}_{\mathsf{IAB}}^{\mathsf{RF}})$.

C.2 Proof of Theorem 5

For $\mathbf{X}_{\mathsf{RF}}$ given Consider the SVD $\mathbf{X}_{\mathsf{RF}} = \mathbf{U}_{\mathsf{RF}}\mathbf{S}_{\mathsf{RF}}\mathbf{V}_{\mathsf{RF}}^{*}$, and let $\mathbf{Q} = \mathbf{S}_{\mathsf{RF}}\mathbf{V}_{\mathsf{RF}}^{*}\mathbf{X}_{\mathsf{BB}} \in \mathbb{C}^{L\times N}$. Then $\mathbf{X}_{\mathsf{RF}}\mathbf{X}_{\mathsf{BB}} = \mathbf{U}_{\mathsf{RF}}\mathbf{Q}$ so that $\mathbf{X}_{\mathsf{BB}}^{*}\mathbf{X}_{\mathsf{RF}}^{*}\mathbf{X}_{\mathsf{RF}}\mathbf{X}_{\mathsf{BB}} = \mathbf{Q}^{*}\mathbf{U}_{\mathsf{RF}}^{*}\mathbf{U}_{\mathsf{RF}}\mathbf{Q} = \mathbf{Q}^{*}\mathbf{Q}$. The generic form of the spectral efficiency in (4.18) and (4.19) is expressed in terms of $\mathbf{Q}$ as

$$\max_{\mathbf{Q}^{*}\mathbf{Q}=\mathbf{I}_{N}} \log\det\left(\mathbf{I}_{N} + \rho\mathbf{Q}^{*}\mathbf{U}_{\mathsf{RF}}^{*}\mathbf{A}\mathbf{A}^{*}\mathbf{U}_{\mathsf{RF}}\mathbf{Q}\right) \tag{C.10}$$

Solution $\mathbf{Q}_{\star}$ is given by the N dominant left singular vectors of $\mathbf{U}_{\mathsf{RF}}\mathbf{A}$. By changing variables, we solve $\mathbf{X}_{\mathsf{BB}} = \mathbf{V}_{\mathsf{RF}}\mathbf{S}_{\mathsf{RF}}^{-1}\mathbf{Q}_{\star}$. For $\mathbf{Q} = \mathbf{Q}_{\star}$, the objective function becomes

$$\log\det\left(\mathbf{I}_{N} + \rho\mathbf{Q}^{*}\mathbf{U}_{\mathsf{RF}}^{*}\mathbf{A}\mathbf{A}^{*}\mathbf{U}_{\mathsf{RF}}\mathbf{Q}\right) \leq \log\det\left(\mathbf{I}_{N} + \rho\mathbf{A}^{*}\mathbf{A}\right) \tag{C.11}$$

with the bound in (C.11) applying to any semi-unitary $\mathbf{U}_{\mathsf{RF}}$. This bound holds with equality if the columns of $\mathbf{U}_{\mathsf{RF}}$ are taken as the L dominant left singular vectors of $\mathbf{A}$.

Appendix D: Proofs of Chapter 6

D.1 Proof of the LMMSE Channel Estimate

During channel estimation in the reverse link, the BSs switch to operate in HD mode and full-resolution so that the received signal at the BS of interest becomes

$$\mathbf{y}_k = \sqrt{G_k P_k}\mathbf{h}_k + \sum_{\ell \in \mathcal{C}} \sqrt{G_{\ell,k} P_{\ell,k}}\mathbf{h}_{\ell,k} + \mathbf{v}_k. \tag{D.1}$$

The LMMSE equalizer is

$$\mathbf{w}^{\mathsf{MMSE}} = \left(G_k P_k + \sum_{\ell \in \mathcal{C}} G_{\ell,k} P_{\ell,k} + \sigma^2 \right)^{-1} \sqrt{G_k P_k}\mathbf{I}. \tag{D.2}$$

Therefore, the LMMSE channel estimate ($\hat{\mathbf{h}}_k = \mathbf{w}^{\mathsf{MMSE}}\mathbf{y}_k$) is

$$\hat{\mathbf{h}}_k = \frac{G_k P_k}{G_k P_k + \sum_{\ell \in \mathcal{C}} G_{\ell,k} P_{\ell,k} + \sigma^2} \left(\mathbf{h}_k + \sum_{\ell, \in \mathcal{C}} \sqrt{\frac{G_{\ell,k} P_{\ell,k}}{G_k P_k}}\mathbf{k}_{\ell,k} + \frac{v_k}{\sqrt{G_k P_k}} \right). \tag{D.3}$$

By properly scaling the numerator and denominator by the noise power, we have

$$\hat{\mathbf{h}}_k = \frac{\frac{G_k P_k}{\sigma^2}}{\frac{G_k P_k + \sum_{\ell \in \mathcal{C}} G_{\ell,k} P_{\ell,k} + \sigma^2}{\sigma^2}} \left(\mathbf{h}_k + \sum_{\ell \in \mathcal{C}} \sqrt{\frac{\frac{G_{k,\ell} P_{\ell,k}}{G_k P_k}}{\sigma^2}}\mathbf{h}_{\ell,k} + \frac{\mathbf{v}_k}{\sqrt{G_k P_k}} \right), \tag{D.4}$$

which leads to the result in (6.15) with $\mathbf{v}'_k = \mathbf{v}_k / \sqrt{G_k P_k}$ and

$$\frac{1}{N_{\mathsf{a}}} \mathbb{E}\left[\|\mathbf{v}'_k\|^2 \right] = \frac{1}{N_{\mathsf{a}}} N_{\mathsf{a}} \frac{|\mathbf{v}_{k,i}|^2}{G_k P_k} = \frac{\sigma^2}{G_k P_k} = \frac{1}{\frac{P_k}{P_u}\mathsf{SNR}_k^u}. \tag{D.5}$$

The estimation error is $\tilde{\mathbf{h}}_k = \mathbf{h}_k - \hat{\mathbf{h}}_k$, which is

$$\begin{aligned} \tilde{\mathbf{h}}_k =& \frac{1 + \sum_{\ell \in \mathcal{C}} \frac{P_{\ell,k}}{P_u}\mathsf{SNR}_{\ell,k}^u}{1 + \frac{P_k}{P_u}\mathsf{SNR}_k^u + \sum_{\ell \in \mathcal{C}} \frac{P_{\ell,k}}{P_u}\mathsf{SNR}_{\ell,k}^u}\mathbf{h}_k \\ & - \frac{\frac{P_k}{P_u}\mathsf{SNR}_k^u}{1 + \frac{P_k}{P_u}\mathsf{SNR}_k^u + \sum_{\ell \in \mathcal{C}} \frac{P_{\ell,k}}{P_u}\mathsf{SNR}_{\ell,k}^u} \sum_{\ell \in \mathcal{C}} \sqrt{\frac{\frac{P_{\ell,k}\mathsf{SNR}_{\ell,k}^u}{P_u}}{\frac{P_k \mathsf{SNR}_k^u}{P_u}}}\mathbf{h}_{\ell,k} \\ & - \frac{\frac{P_k}{P_u}\mathsf{SNR}_k^u}{1 + \frac{P_k}{P_u}\mathsf{SNR}_k^u + \sum_{\ell \in \mathcal{C}} \frac{P_{\ell,k}}{P_u}\mathsf{SNR}_{\ell,k}^u}\mathbf{v}'_k. \end{aligned} \tag{D.6}$$

While the variance of the estimation error is calculated as

$$\mathsf{MMSE}_k = \frac{1 + \sum_{\ell \in \mathcal{C}} \frac{P_{\ell,k}}{P_u} \mathsf{SNR}^u_{\ell,k}}{1 + \frac{P_k}{P_u} \mathsf{SNR}^u_k + \sum_{\ell \in \mathcal{C}} \frac{P_{\ell,k}}{P_u} \mathsf{SNR}^u_{\ell,k}}. \tag{D.7}$$

D.2 Proof of Theorem 6

The derivations of the terms related to SI and aggregate AQNM in the denominator of (6.19) are straightforward. We will focus on deriving the remaining terms.

The desired signal is the component projected onto what the receiver regards as the true channel for the k-th uplink user, $\hat{\mathbf{h}}_k$, while the projection onto the estimation error $\tilde{\mathbf{h}}_k$ is treated as additional Gaussian noise (filtered by $\mathbf{w}_k$). The inter-cell interference, included within the noise, is made explicit in this formulation, but also treated as Gaussian noise (filtered by $\mathbf{h}_k$). Conditioned on $\hat{\mathbf{h}}_0, \ldots, \hat{\mathbf{h}}_{K-1}$ and $\mathbf{w}_k$, which the BS of interest is privy to, the output SQINR for user k equals to (6.19) where we have capitalized on the independence between $\mathbf{w}_k$ and $\tilde{\mathbf{h}}_{\mathrm{k}}$, for $\mathrm{k} = 0, \ldots, K-1$, to develop

$$\begin{aligned}
\mathbb{E}\left[\left|\mathbf{w}_k^* \mathbf{h}_{\mathrm{k}}\right|^2 | \mathbf{w}_k\right] &= \mathbb{E}\left[\mathbf{w}_k^* \tilde{\mathbf{h}}_{\mathrm{k}} \tilde{\mathbf{h}}_{\mathrm{k}}^* \mathbf{w}_k | \mathbf{w}_k\right] \\
&= \mathbf{w}_k^* \mathbb{E}\left[\tilde{\mathbf{h}}_{\mathrm{k}} \tilde{\mathbf{h}}_{\mathrm{k}}^*\right] \mathbf{w}_k \\
&= \mathbf{w}_k^* \left(\mathsf{MMSE}_{\mathrm{k}} \cdot \mathbf{I}\right) \mathbf{w}_k \\
&= \mathsf{MMSE}_{\mathrm{k}} \|\mathbf{w}_k\|^2.
\end{aligned} \tag{D.8}$$

As far as the inter-cell interference goes, the term $\mathbb{E}\left[|\mathbf{h}_k^* \mathbf{h}_{\ell,\mathrm{k}}|^2 | \mathbf{w}_k\right] = \mathbf{w}_k^* \mathbb{E}\left[\mathbf{h}_{\ell,\mathrm{k}} \mathbf{h}_{\ell,\mathrm{k}}^* | \mathbf{w}_k\right] \mathbf{w}_k$ cannot be further elaborated in complete generality for copilot interferers, i.e., for $\ell \in \mathcal{C}$ and $\mathrm{k} = k$, because $\mathbf{w}_k$ is contaminated by, and therefore it is not independent of, $\mathbf{h}_{\ell,k}$ whenever $\ell \in \mathcal{C}$. For noncopilot interferers, though, $\mathbf{w}_k$ and $\mathbf{h}_{\ell,\mathrm{k}}$ do exhibit independence and thus

$$\mathbf{w}_k^* \mathbb{E}\left[\mathbf{h}_{\ell,\mathrm{k}} \mathbf{h}_{\ell,\mathrm{k}}^* | \mathbf{w}_k\right] \mathbf{w}_k = \mathbf{w}_k^* \mathbb{E}\left[\mathbf{h}_{\ell,\mathrm{k}} \mathbf{h}_{\ell,\mathrm{k}}^*\right] \mathbf{w}_k = \|\mathbf{w}_k\|^2. \tag{D.9}$$

Therefore, we obtain the expression (6.19) in Theorem 6.

D.3 Proof of Theorem 8

The derivation of the terms in (6.33) are straightforward except for the term $\mathbb{E}\left[\mathbf{h}_{\ell,k}\mathbf{h}_{\ell,k}^{*}|\mathbf{w}_{k}^{\mathsf{MF}}\right]$. For a matched filter receiver $\mathbf{w}_{k}^{\mathsf{MF}}$, using the results of Corollary 1 and after some mathematical manipulations, the conditional covariance of the copilot interference can be evaluated as

$$\mathbb{E}\left[\mathbf{h}_{\ell,k}\mathbf{h}_{\ell,k}^{*}|\mathbf{w}_{k}^{\mathsf{MF}}\right]=\mathbf{I}+\frac{\frac{P_{\ell,k}}{P_{u}}\mathsf{SNR}_{\ell,k}^{u}}{1+\frac{P_{k}}{P_{u}}\mathsf{SNR}_{k}^{u}+\sum_{l\in\mathcal{C}}\frac{P_{k,l}}{P_{u}}\mathsf{SNR}_{l,k}^{u}}\left(\mathbf{w}_{k}^{\mathsf{MF}}\mathbf{w}_{k}^{\mathsf{MF}*}-\mathbf{I}\right). \tag{D.10}$$

After substituting (D.10) in (6.32), we prove the results of Theorem 8.

D.4 Proof of Theorem 9

From the expression of the SQINR (6.34), $\overline{\mathsf{den}}_{u}^{\mathsf{MF}}$ can be written as (D.11).

$$\begin{aligned}\overline{\mathsf{den}}_{u}^{\mathsf{MF}}=&\alpha_{u}^{2}\frac{P_{k}}{P_{u}}\mathsf{SNR}_{k}^{u}\mathsf{var}\left[\mathbf{w}_{k}^{\mathsf{MF}*}\mathbf{h}_{k}\right]+\alpha_{u}^{2}\sum_{\mathrm{k}\neq k}\frac{P_{\mathrm{k}}}{P_{u}}\mathsf{SNR}_{\mathrm{k}}^{u}\mathbb{E}\left[\left|\mathbf{w}_{k}^{\mathsf{MF}*}\mathbf{h}_{\mathrm{k}}\right|^{2}\right]+\alpha_{u}^{2}\sum_{\ell\in\mathcal{C}}\frac{P_{\ell,k}}{P_{u}}\mathsf{SNR}_{\ell,k}^{u}\mathbb{E}\left[\left|\mathbf{w}_{k}^{\mathsf{MF}*}\mathbf{h}_{\ell,k}\right|^{2}\right]\\&+\alpha_{u}^{2}N_{\mathsf{a}}\left(1+\sum_{\substack{\ell\neq 0\\ \ell\notin\mathcal{C}}}\sum_{\mathrm{k}=0}^{K_{\ell}^{u}-1}\frac{P_{\ell,\mathrm{k}}}{P_{u}}\mathsf{SNR}_{\ell,\mathrm{k}}^{u}+\sum_{\ell\in\mathcal{C}}\sum_{\mathrm{k}\neq k}\frac{P_{\ell,\mathrm{k}}}{P_{u}}\mathsf{SNR}_{\ell,\mathrm{k}}^{u}\right)+\frac{\alpha_{u}^{2}}{\sigma^{2}}P_{\mathsf{SI}}\mathbb{E}\left[|\mathbf{w}_{k}^{\mathsf{MF}*}\mathbf{H}_{\mathsf{SI}}\mathbf{q}_{d}|^{2}\right]\\&+\frac{\alpha_{d}^{2}\alpha_{u}^{2}}{\sigma^{2}}P_{\mathsf{SI}}\sum_{\mathrm{k}=0}^{K-1}\mathbb{E}\left[|\mathbf{w}_{k}^{\mathsf{MF}*}\mathbf{H}_{\mathsf{SI}}\mathbf{f}_{\mathrm{k}}|^{2}\right]+\frac{1}{\sigma^{2}}\mathbb{E}\left[|\mathbf{w}_{k}^{\mathsf{MF}*}\mathbf{q}_{u}^{2}|\right].\end{aligned} \tag{D.11}$$

Using Corollary 2, we derive the terms of (D.11) as

$$\begin{aligned}\mathsf{var}\left[\left|\mathbf{w}_{k}^{\mathsf{MF}*}\mathbf{h}_{k}\right|^{2}\right]&=\mathbb{E}\left[\left|\mathbf{w}_{k}^{\mathsf{MF}*}\mathbf{h}_{k}\right|^{2}\right]-\frac{\frac{P_{k}}{P_{u}}\mathsf{SNR}_{k}^{u}}{1+\frac{P_{k}}{P_{u}}\mathsf{SNR}_{k}^{u}+\sum_{\ell\in\mathcal{C}}\frac{P_{\ell,k}}{P_{u}}\mathsf{SNR}_{\ell,k}^{u}}N_{\mathsf{a}}^{2}\\&=N_{\mathsf{a}}.\end{aligned} \tag{D.12}$$

Since $\mathbf{w}_k^{\mathsf{MF}}$ and $\mathbf{h}_{\mathrm{k}}$ are independent for $\mathrm{k} \neq k$

$$\begin{aligned}\mathbb{E}\left[\left|\mathbf{w}_k^{\mathsf{MF}*}\mathbf{h}_{\mathrm{k}}\right|^2\right] &= \mathbb{E}\left[\mathbf{w}_k^{\mathsf{MF}*}\overbrace{\mathbb{E}\left[\mathbf{h}_{\mathrm{k}}\mathbf{h}_{\mathrm{k}}^*\right]}^{\mathbf{I}}\mathbf{w}_k^{\mathsf{MF}}\right] \\ &= \mathbb{E}\left[\left\|\mathbf{w}_k^{\mathsf{MF}}\right\|^2\right] \\ &= N_{\mathsf{a}}.\end{aligned} \tag{D.13}$$

The unconditional copilot interference power equals to

$$\mathbb{E}\left[\left|\mathbf{w}_k^{\mathsf{MF}*}\mathbf{h}_{\ell,k}\right|^2\right] = N_{\mathsf{a}} + \frac{\frac{P_{\ell,k}}{P_u}\mathsf{SNR}_{\ell,k}^u}{1+\frac{P_k}{P_u}\mathsf{SNR}_k^u + \sum_{l\in\mathcal{C}}\frac{P_{l,k}}{P_u}\mathsf{SNR}_{\ell,k}^u}N_{\mathsf{a}}^2. \tag{D.14}$$

Since $\mathbf{w}_k^{\mathsf{MF}}, \mathbf{H}_{\mathsf{SI}}$ and $\mathbf{q}_d$ are mutually independent

$$\begin{aligned}\mathbb{E}\left[\left|\mathbf{w}_k^{\mathsf{MF}*}\mathbf{H}_{\mathsf{SI}}\mathbf{q}_d\right|^2\right] &= \mathbb{E}\left[\mathbf{w}_k^{\mathsf{MF}*}\mathbb{E}\left[\mathbf{H}_{\mathsf{SI}}\mathbf{H}_{\mathsf{SI}}^*\right]\left[\mathbf{q}_d\mathbf{q}_d^*\right]\mathbf{w}_k^{\mathsf{MF}}\right] \\ &= \alpha_d(1-\alpha_d)K^d\mu_{\mathsf{SI}}^2N_{\mathsf{a}}^2\end{aligned} \tag{D.15}$$

In addition, the mutual independence of $\mathbf{w}_k^{\mathsf{MF}}, \mathbf{H}_{\mathsf{SI}}$ and $\mathbf{f}_{\mathrm{k}}^{\mathsf{MF}}$ yields

$$\sum_{\mathrm{k}=0}^{K^d-1}\mathbb{E}\left[\left|\mathbf{w}_k^{\mathsf{MF}*}\mathbf{H}_{\mathsf{SI}}\mathbf{f}_{\mathrm{k}}^{\mathsf{MF}}\right|^2\right] = \mu_{\mathsf{SI}}^2K^dN_{\mathsf{a}}^2. \tag{D.16}$$

Using [40, Appendix A], the last term of (D.11) is given by (D.17)

$$\frac{1}{\sigma^2}\mathbb{E}\left[\left|\mathbf{w}_k^{\mathsf{MF}*}\mathbf{q}_u\right|^2\right] = N_{\mathsf{a}}\alpha_u(1-\alpha_u)\left[2\frac{P_k}{P_u}\mathsf{SNR}_k^u + \sum_{\mathrm{k}\neq k}\frac{P_{\mathrm{k}}}{P_u}\mathsf{SNR}_{\mathrm{k}}^u + \sum_{\ell\neq 0}\sum_{\mathrm{k}}\frac{P_{\ell,\mathrm{k}}}{P_u}\mathsf{SNR}_{\ell,\mathrm{k}}^u + \alpha_dN_{\mathsf{a}}\mathsf{INR} + 1\right]. \tag{D.17}$$

where $\mathsf{INR} = P_{\mathsf{SI}}\mu_{\mathsf{SI}}^2/\sigma^2$. The derivation of the above terms leads to the results of Theorem 9.

D.5 Proof of Theorem 11

In Theorem 11, initially the denominator $\overline{\mathsf{den}}_d^{\mathsf{MF}}$ of the output SQINR is expressed by (D.18).

$$\begin{aligned}\overline{\mathsf{den}}_d^{\mathsf{MF}} =&\alpha_d^2\frac{P_k}{P_dN_{\mathsf{a}}}\mathsf{SNR}_k^d\mathsf{var}\left[\mathbf{h}_k^*\mathbf{f}_k^{\mathsf{MF}}\right]+\alpha_d^2\sum_{\mathrm{k}\neq k}\frac{P_{\mathrm{k}}}{P_dN_{\mathsf{a}}}\mathsf{SNR}_k^d\mathbb{E}\left[\left|\mathbf{h}_k^*\mathbf{f}_{\mathrm{k}}^{\mathsf{MF}}\right|^2\right]+\alpha_d^2\sum_{\ell\in\mathcal{C}}\frac{P_{\ell,k}}{P_dN_{\mathsf{a}}}\mathsf{SNR}_{\ell,k}^d\mathbb{E}\left[\left|\mathbf{h}_{\ell,k}^*\mathbf{f}_{\ell,k}^{\mathsf{MF}}\right|^2\right]\\&+\alpha_d^2\sum_{\substack{\ell\neq 0\\ \ell\notin\mathcal{C}}}\sum_{\mathrm{k}=0}^{K_\ell^u-1}\frac{P_{\ell,\mathrm{k}}}{P_dN_{\mathsf{a}}}\mathsf{SNR}_{\ell,k}^d\mathbb{E}\left[\left|\mathbf{h}_{\ell,k}^*\mathbf{f}_{\ell,\mathrm{k}}^{\mathsf{MF}}\right|^2\right]+\alpha_d^2\sum_{\ell\in\mathcal{C}}\sum_{\mathrm{k}\neq k}\frac{P_{\ell,\mathrm{k}}}{P_dN_{\mathsf{a}}}\mathsf{SNR}_{\ell,\mathrm{k}}^d\mathbb{E}\left[\left|\mathbf{h}_{\ell,k}^*\mathbf{f}_{\ell,\mathrm{k}}^{\mathsf{MF}}\right|^2\right]\\&+\sum_{\ell}\sum_{\mathrm{k}=0}^{K_\ell^u-1}\frac{P_{\ell,\mathrm{k}}^u}{P_u}\mathsf{SNR}_{(\ell,\mathrm{k}),k}^{\mathsf{iui}}\mathbb{E}\left[\left|\mathbf{g}_{(\ell,\mathrm{k}),k}\right|^2\right]+\sum_{\ell}\frac{P_{\ell,k}^d}{P_dN_{\mathsf{a}}}\mathsf{SNR}_{\ell,k}^d\mathbb{E}\left[\left|\mathbf{h}_{\ell,k}^*\mathbf{q}_{d,\ell}\right|^2\right]+1\end{aligned}\tag{D.18}$$

Using [40, Appendix A], the 7-th term of (D.18) can be simplified as follows:

$$\sum_{\ell}\frac{P_{\ell,k}}{P_dN_{\mathsf{a}}}\mathsf{SNR}_{\ell,k}^d\mathbb{E}\left[\left|\mathbf{h}_{\ell,k}^*\mathbf{q}_{d,\ell}\right|^2\right]=\alpha_d(1-\alpha_d)\sum_{\ell}\frac{P_{\ell,k}}{P_d}\mathsf{SNR}_{\ell,k}^d\left(K_\ell^d+1\right).\tag{D.19}$$

The first 5 terms of (D.18) can be derived using results from the reverse link analysis (D.12)-(D.14) as well as Corollary 2. After mathematical manipulations, (D.18) can be simplified as (D.20).

$$\begin{aligned}\overline{\mathsf{den}}_d^{\mathsf{MF}} =&1+\alpha_d^2\sum_{\ell}\mathsf{SNR}_{\ell,k}^d+\alpha_d^2N_{\mathsf{a}}\sum_{\ell\in\mathcal{C}}\frac{\frac{P_k}{P_u}\mathsf{SNR}_{\ell,k}^u}{1+\frac{P_k}{P_u}\mathsf{SNR}_{\ell,k}^u+\sum_{l\in\mathcal{C}}\frac{P_{l,k}}{P_u}\mathsf{SNR}_{\ell,(l,k)}^u}\frac{P_{\ell,k}}{P_d}\mathsf{SNR}_{\ell,k}^d\\&+\sum_{\ell}\sum_{\mathrm{k}=0}^{K_\ell^u-1}\frac{P_{\ell,\mathrm{k}}^u}{P_u}\mathsf{SNR}_{(\ell,\mathrm{k}),k}^{\mathsf{iui}}+\alpha_d(1-\alpha_d)\sum_{\ell}\frac{P_{\ell,k}}{P_d}\mathsf{SNR}_{\ell,k}^d\left(K_\ell^d+1\right).\end{aligned}\tag{D.20}$$

While introducing the new term $\varrho=\mathsf{SNR}_{\ell,(l,k)}^d/\mathsf{SNR}_{\ell,(l,k)}^u$ for any ℓ,l and k as the *forward-reverse SNR ratio*, (D.20) can be reduced to (6.51) and hence Theorem 11 is proved.

Works Cited

[1] The 5g evolution: 3gpp rel. 16-17. `https://www.5gamericas.org/wp-content/uploads/2020/01/5G-Evolution-3GPP-R16-R17-FINAL.pdf`, 2020.

[2] W. B. Abbas, F. Gomez-Cuba, and M. Zorzi. mmWave receiver beamforming comparison tool. *http://enigma.det.uvigo.es/ fgomez/mmWaveADCwebviewer/*.

[3] W. B. Abbas, F. Gomez-Cuba, and M. Zorzi. Millimeter Wave Receiver Efficiency: A Comprehensive Comparison of Beamforming Schemes With Low Resolution ADCs. *IEEE Trans. Wireless Commun.*, 16(12):8131–8146, 2017. doi: 10.1109/TWC.2017.2757919.

[4] Elsayed Ahmed and Ahmed M. Eltawil. All-digital self-interference cancellation technique for full-duplex systems. *IEEE Transactions on Wireless Communications*, 14(7):3519–3532, 2015. doi: 10.1109/TWC.2015.2407876.

[5] Mustafa Riza Akdeniz, Yuanpeng Liu, Mathew K. Samimi, Shu Sun, Sundeep Rangan, Theodore S. Rappaport, and Elza Erkip. Millimeter wave channel modeling and cellular capacity evaluation. *IEEE J. Sel. Areas in Commun.*, 32(6):1164–1179, 2014. doi: 10.1109/JSAC.2014.2328154.

[6] George C. Alexandropoulos, Md Atiqul Islam, and Besma Smida. Full duplex hybrid a/d beamforming with reduced complexity multi-tap analog cancellation. In *IEEE International Work. on Signal Process. Adv. in Wireless Commun.*, pages 1–5, 2020. doi: 10.1109/SPAWC48557.2020.9154241.

[7] Ahmed Alkhateeb, Omar El Ayach, Geert Leus, and Robert W. Heath. Channel estimation and hybrid precoding for millimeter wave cellular systems. *IEEE J. Selected Topics in Signal Processing*, 8(5):831–846, 2014. doi: 10.1109/JSTSP.2014.2334278.

[8] Sylvain Almonacil, Fabien Boitier, and Patricia Layec. Performance model and design rules for optical systems employing low-resolution dac/adc. *Journal of Lightwave Technology*, 38(11):3007–3014, 2020. doi: 10.1109/JLT.2020.2984924.

[9] J. G. Andrews, F. Baccelli, and R. K. Ganti. A tractable approach to coverage and rate in cellular networks. *IEEE Trans. Commun.*, 59(11):3122–3134, November 2011. ISSN 1558-0857. doi: 10.1109/TCOMM.2011.100411.100541.

[10] Prince Anokye, Roger Kwao Ahiadormey, Han-Shin Jo, Changick Song, and Kyoung-Jae Lee. Low-resolution ADC quantized full-duplex massive MIMO-enabled wireless backhaul in heterogeneous networks over Rician channels. *IEEE Trans. Wireless Commun.*, 19(8):5503–5517, 2020. doi: 10.1109/TWC.2020.2994034.

[11] Prince Anokye, Roger K. Ahiadormey, and Kyoung-Jae Lee. Full-duplex cell-free massive MIMO with low-resolution ADCs. *IEEE Trans. Vehicular Technology*, 70(11):12179–12184, 2021. doi: 10.1109/TVT.2021.3112212.

[12] Bridget D. Antwi-Boasiako, Roger K. Ahiadormey, Prince Anokye, and Kyoung-Jae Lee. On the Performance of Massive MIMO Full-Duplex Relaying With Low-Resolution ADCs. *IEEE Communications Letters*, 26(6):1259–1263, 2022. doi: 10.1109/LCOMM.2022.3164466.

[13] Ehsan Aryafar, M. Khojastepour, K. Sundaresan, S. Rangarajan, and M. Chiang. MIDU: enabling MIMO full duplex. In *Mobicom '12*, 2012.

[14] Omar El Ayach, Sridhar Rajagopal, Shadi Abu-Surra, Zhouyue Pi, and Robert W. Heath. Spatially Sparse Precoding in Millimeter Wave MIMO Systems. *IEEE Trans. Wireless Commun.*, 13(3):1499–1513, 2014. doi: 10.1109/TWC.2014.011714.130846.

[15] Elyes Balti and Brian L. Evans. Hybrid beamforming design for wideband mmwave full-duplex systems. *https://arxiv.org/abs/2107.06166*, 2021.

[16] Elyes Balti and Brian L. Evans. Joint beamforming and interference cancellation in MmWave wideband full-duplex systems, 2021. URL `https://arxiv.org/abs/2110.12266`.

[17] Elyes Balti and Brian L. Evans. Forward link analysis for full-duplex cellular networks with low resolution adc/dac. In *2022 IEEE 23rd International Workshop on Signal Processing Advances in Wireless Communication (SPAWC)*, pages 1–5, 2022. doi: 10.1109/SPAWC51304.2022.9833946.

[18] Elyes Balti and Brian L. Evans. Full-duplex massive mimo cellular networks with low resolution adc/dac. In *GLOBECOM 2022 - 2022 IEEE Global Communications Conference*, pages 1649–1654, 2022. doi: 10.1109/GLOBECOM48099.2022.10001148.

[19] Elyes Balti and Brian L. Evans. Reverse link analysis for full-duplex cellular networks with low resolution adc/dac. In *2022 IEEE 23rd International Workshop on Signal Processing Advances in Wireless Communication (SPAWC)*, pages 1–5, 2022. doi: 10.1109/SPAWC51304.2022.9833977.

[20] Elyes Balti and Brian L. Evans. A unified framework for full-duplex massive mimo cellular networks with low resolution data converters. *IEEE Open Journal of the Communications Society*, 4:1–28, 2023. doi: 10.1109/OJCOMS.2022.3230327.

[21] Elyes Balti and Neji Mensi. Zero-forcing max-power beamforming for hybrid mmwave full-duplex MIMO systems. In *Int. Conf. Adv. Systems and Emergent Technologies*, pages 344–349, 2020. doi: 10.1109/IC_ASET49463.2020.9318295.

[22] Elyes Balti, Chris Dick, and Brian L. Evans. Low Complexity Hybrid Beamforming for mmWave Full-Duplex Integrated Access and Backhaul. In *IEEE Global Commun. Conf.*, pages 1606–1611, 2022. doi: 10.1109/GLOBECOM48099.2022.10001634.

[23] Carlos Baquero Barneto, Taneli Riihonen, Sahan Damith Liyanaarachchi, Mikko Heino, Nuria González-Prelcic, and Mikko Valkama. Beamformer Design and Optimization for Joint Communication and Full-Duplex Sensing at mmWaves. *IEEE Transactions on Communications*, 70(12):8298–8312, 2022. doi: 10.1109/TCOMM.2022.3218623.

[24] Dinesh Bharadia, Emily McMilin, and Sachin Katti. Full duplex radios. *SIGCOMM Comput. Commun. Rev.*, 43(4):375–386, aug 2013. ISSN 0146-4833. doi: 10.1145/2534169.2486033. URL `https://doi.org/10.1145/2534169.2486033`.

[25] Mathew Biedka, Yuanxun Ethan Wang, Qiang Mark Xu, and Yuexing Li. Full-duplex RF front ends: From antennas and circulators to leakage cancellation. *IEEE Microwave Mag.*, 20(2):44–55, 2019. doi: 10.1109/MMM.2018.2880496.

[26] Emil Bjornson, Michail Matthaiou, and Merouane Debbah. A New Look at Dual-Hop Relaying: Performance Limits with Hardware Impairments. *IEEE Transactions on Communications*, 61(11):4512–4525, 2013. doi: 10.1109/TCOMM.2013.100913.130282.

[27] Pierre Blanche, Arkady S. Bablumian, Ram Voorakaranam, Cory W. Christenson, Wei-Tang Lin, Tao Gu, D. Flores, Peng Wang, Wan-Yun Hsieh, Mohanalingam Kathaperumal, Bartlomej Rachwal, Ozair Siddiqui, Jayan Thomas, Robert A. Norwood, Michiharu Yamamoto, and Nasser Peyghambarian. Holographic three-dimensional telepresence using large-area photorefractive polymer. *Nature*, 468:80–83, 2010. URL `https://api.semanticscholar.org/CorpusID:205222841`.

[28] D. W. Bliss, P. A. Parker, and A. R. Margetts. Simultaneous transmission and reception for improved wireless network performance. In *IEEE Work. Stat. Signal Process.*, pages 478–482, 2007. doi: 10.1109/SSP.2007.4301304.

[29] Bartłomiej Błaszczyszyn, Martin Haenggi, Paul Keeler, and Sayandev Mukherjee. *Stochastic Geometry Analysis of Cellular Networks*. Cambridge University Press, 2018. doi: 10.1017/9781316677339.

[30] Yunlong Cai, Ming-Min Zhao, Kaidi Xu, and Rui Zhang. Intelligent reflecting surface aided full-duplex communication: Passive beamforming and deployment design. *IEEE Trans. Wireless Commun.*, 21(1):383–397, 2022. doi: 10.1109/TWC.2021.3095939.

[31] Fei Chen, Robert Morawski, and Tho Le-Ngoc. Self-interference channel characterization for wideband 2 × 2 mimo full-duplex transceivers using dual-polarized antennas. *IEEE Transactions on Antennas and Propagation*, 66(4): 1967–1976, 2018. doi: 10.1109/TAP.2018.2800521.

[32] Tingjun Chen, Mahmood Baraani Dastjerdi, Harish Krishnaswamy, and Gil Zussman. Wideband full-duplex phased array with joint transmit and receive beamforming: Optimization and rate gains. *IEEE/ACM Trans. Networking*, 29(4):1591–1604, 2021. doi: 10.1109/TNET.2021.3069125.

[33] Yifan Chen and V.K. Dubey. The accuracy of geometric channel modeling methods. In *Fourth International Conference on Information, Communications and Signal Processing, 2003 and the Fourth Pacific Rim Conference on Multimedia. Proceedings of the 2003 Joint*, volume 1, pages 381–385 Vol.1, 2003. doi: 10.1109/ICICS.2003.1292479.

[34] Yunseong Cho, Jinseok Choi, and Brian L. Evans. Coordinated beamforming in quantized massive MIMO systems with per-antenna constraints. In *IEEE Wireless Commun. and Networking Conf.*, April 2022.

[35] J. Choi, M. Jain, K. Srinivasan, P. Levis, and S. Katti. Achieving single channel, full duplex wireless communication. *Int. Conf. Mobile Computing and Networking*, 2010.

[36] Aditya Chopra, Ian P. Roberts, Thomas Novlan, and Jeffrey G. Andrews. 28 ghz phased array-based self-interference measurements for millimeter wave full-duplex. In *2022 IEEE Wireless Communications and Networking Conference (WCNC)*, pages 2583–2588, 2022. doi: 10.1109/WCNC51071.2022.9771589.

[37] Minkeun Chung, Min Soo Sim, Jaeweon Kim, Dong Ku Kim, and Chan-byoung Chae. Prototyping real-time full duplex radios. *IEEE Commun. Mag.*, 53(9): 56–63, 2015. doi: 10.1109/MCOM.2015.7263346.

[38] Mark Cudak, Amitabha Ghosh, Arunabha Ghosh, and Jeffrey Andrews. Integrated access and backhaul: A key enabler for 5g millimeter-wave deployments. *IEEE Communications Magazine*, 59(4):88–94, 2021. doi: 10.1109/MCOM.001.2000690.

[39] José Mairton Barros da Silva, Ashutosh Sabharwal, Gábor Fodor, and Carlo Fischione. 1-bit phase shifters for large-antenna full-duplex mmwave communications. *IEEE Trans. Wireless Commun.*, 19(10):6916–6931, 2020. doi: 10.1109/TWC.2020.3006959.

[40] Jianxin Dai, Juan Liu, Jiangzhou Wang, Junxi Zhao, Chonghu Cheng, and Jin-Yuan Wang. Achievable rates for full-duplex massive MIMO systems with low-resolution ADCs/DACs. *IEEE Access*, 7:24343–24353, 2019. doi: 10.1109/ACCESS.2019.2900273.

[41] Brian P. Day, Adam R. Margetts, Daniel W. Bliss, and Philip Schniter. Full-duplex bidirectional mimo: Achievable rates under limited dynamic range. *IEEE Trans. Signal Processing*, 60(7):3702–3713, 2012. doi: 10.1109/TSP.2012.2192925.

[42] Alpaslan Demir, Tanbir Haque, Erdem Bala, and Patrick Cabrol. Exploring the possibility of full-duplex operations in mmwave 5g systems. In *IEEE Wireless and Microwave Technology Conf.*, pages 1–5, 2016. doi: 10.1109/WAMICON.2016.7483861.

[43] Digi-Capital. AR to Approach $90bn Revenue by 2022. Available: `https://advanced-television.com/2018/01/29/digi-capital-ar-to-approach-90bn-revenue-by2` Accessed: 2024-09-12.

[44] Tolga Dinc, Anandaroop Chakrabarti, and Harish Krishnaswamy. A 60 ghz same-channel full-duplex cmos transceiver and link based on reconfigurable polarization-based antenna cancellation. In *IEEE Radio Frequency Integrated Circuits Symp.*, pages 31–34, 2015. doi: 10.1109/RFIC.2015.7337697.

[45] Qingfeng Ding, Yichong Lian, and Yindi Jing. Performance analysis of full-duplex massive MIMO systems with low-resolution ADCs/DACs over Rician fading channels. *IEEE Trans. Veh. Tech.*, 69(7), 2020. doi: 10.1109/TVT.2020.2991143.

[46] Hesham ElSawy, Ahmed Sultan-Salem, Mohamed-Slim Alouini, and Moe Z. Win. Modeling and analysis of cellular networks using stochastic geometry: A tutorial. *IEEE Commun. Surveys and Tutorials*, 19(1):167–203, 2017. doi: 10.1109/COMST.2016.2624939.

[47] R.B. Ertel and J.H. Reed. Angle and time of arrival statistics for circular and elliptical scattering models. *IEEE Journal on Selected Areas in Communications*, 17(11):1829–1840, 1999. doi: 10.1109/49.806814.

[48] E. Everett, C. Shepard, L. Zhong, and A. Sabharwal. SoftNull: Many-Antenna Full-Duplex Wireless via Digital Beamforming. *IEEE Trans. Wireless Commun.*, 15(12):8077–8092, Dec 2016. ISSN 1558-2248. doi: 10.1109/TWC.2016.2612625.

[49] Evan Everett, Achaleshwar Sahai, and Ashutosh Sabharwal. Passive self-interference suppression for full-duplex infrastructure nodes. *IEEE Trans. Wireless Commun.*, 13(2):680–694, 2014. doi: 10.1109/TWC.2013.010214.130226.

[50] Evan Everett, Clayton Shepard, Lin Zhong, and Ashutosh Sabharwal. Soft-null: Many-antenna full-duplex wireless via digital beamforming. *IEEE Trans. Wireless Commun.*, 15(12):8077–8092, 2016. doi: 10.1109/TWC.2016.2612625.

[51] Li Fan, Shi Jin, Chao-Kai Wen, and Haixia Zhang. Uplink achievable rate for massive MIMO systems with low-resolution ADC. *IEEE Commun. Let.*, 19 (12):2186–2189, 2015. doi: 10.1109/LCOMM.2015.2494600.

[52] Margarita Gapeyenko, Vitaly Petrov, Dmitri Moltchanov, Sergey Andreev, Nageen Himayat, and Yevgeni Koucheryavy. Flexible and reliable UAV-assisted backhaul operation in 5G mmWave cellular networks. *IEEE J. Selected Areas in Commun.*, 36(11):2486–2496, 2018. doi: 10.1109/JSAC.2018.2874145.

[53] Geordie George, Angel Lozano, and Martin Haenggi. Massive MIMO forward link analysis for cellular networks. *IEEE Trans. Wireless Commun.*, 18(6): 2964–2976, Jun 2019. ISSN 1558-2248. doi: 10.1109/twc.2019.2907584.

[54] GrandViewResearch. Digital Twin Market Size Worth $26.07 Billion By 2025 with CAGR 38.2%. Available: `https://www.grandviewresearch.com/press-release/global-digital-twin-market`.

[55] Felipe Gómez-Cuba, Tommaso Zugno, Junseok Kim, Michele Polese, Saewoong Bahk, and Michele Zorzi. Hybrid Beamforming in 5G mmWave Networks: A Full-Stack Perspective. *IEEE Trans. Wireless Commun.*, 21(2):1288–1303, 2022. doi: 10.1109/TWC.2021.3103575.

[56] Martin Haenggi. *Stochastic Geometry for Wireless Networks*. Cambridge University Press, 2012. doi: 10.1017/CBO9781139043816.

[57] Jiang Hao, Zhou Jie, and Hisakazu Kikuchi. Angle and time of arrival statistics for a 3-d pie-cellular-cut scattering channel model. *Wirel. Pers. Commun.*, 78(2):851–865, sep 2014. ISSN 0929-6212. doi: 10.1007/s11277-014-1787-y. URL `https://doi.org/10.1007/s11277-014-1787-y`.

[58] Armen Harutyunyan and Padmanava Sen. In-band full-duplex solutions in the paradigm of integrated sensing and communication. In *2023 IEEE International Conference on Acoustics, Speech, and Signal Processing Workshops (ICASSPW)*, pages 1–5, 2023. doi: 10.1109/ICASSPW59220.2023.10193639.

[59] Yimin He, Hongzhi Zhao, Wenbo Guo, Shihai Shao, and Youxi Tang. Frequency-domain successive cancellation of nonlinear self-interference with reduced complexity for full-duplex radios. *IEEE Trans. Commun.*, pages 1–1, 2022. doi: 10.1109/TCOMM.2022.3148428.

[60] Yongyu He, Xuefeng Yin, and Hong Chen. Spatiotemporal characterization of self-interference channels for 60-ghz full-duplex communication. *IEEE Antennas and Wireless Propagation Letters*, 16:2220–2223, 2017. doi: 10.1109/LAWP.2017.2707318.

[61] R. W. Heath, N. González-Prelcic, S. Rangan, W. Roh, and A. M. Sayeed. An overview of signal processing techniques for millimeter wave MIMO systems. *IEEE Journal of Selected Topics in Signal Processing*, 10(3):436–453, 2016.

[62] Robert W. Heath Jr. and Angel Lozano. *Foundations of MIMO Communication*. Cambridge University Press, 2018. doi: 10.1017/9781139049276.

[63] Mikko Heino, Dani Korpi, Timo Huusari, Emilio Antonio-Rodriguez, Sathya Venkatasubramanian, Taneli Riihonen, Lauri Anttila, Clemens Icheln, Katsuyuki Haneda, Risto Wichman, and Mikko Valkama. Recent advances in antenna design and interference cancellation algorithms for in-band full duplex relays. *IEEE Communications Magazine*, 53(5):91–101, 2015. doi: 10.1109/MCOM.2015.7105647.

[64] Mikko Heino, Dani Korpi, Timo Huusari, Emilio Antonio-Rodriguez, Sathya Venkatasubramanian, Taneli Riihonen, Lauri Anttila, Clemens Icheln, Katsuyuki Haneda, Risto Wichman, and Mikko Valkama. Recent advances in antenna design and interference cancellation algorithms for in-band full duplex relays. *IEEE Commun. Mag.*, 53(5):91–101, 2015. doi: 10.1109/MCOM.2015.7105647.

[65] Sean Huberman and Tho Le-Ngoc. Mimo full-duplex precoding: A joint beamforming and self-interference cancellation structure. *IEEE Trans. Wireless Commun.*, 14(4):2205–2217, 2015. doi: 10.1109/TWC.2014.2382589.

[66] Mordor Intelligence. Global Holographic Display Market - Segmented by Technology. Available: `https://www.mordorintelligence.com/industry-reports/holographic-display-market`. A.

[67] Md Atiqul Islam, George C. Alexandropoulos, and Besma Smida. A unified beamforming and a/d self-interference cancellation design for full duplex mimo radios. In *IEEE International Symp. Personal, Indoor and Mobile Radio Commun.*, pages 1–7, 2019. doi: 10.1109/PIMRC.2019.8904094.

[68] L. Jiang and S.Y. Tan. Simple geometrical-based aoa model for mobile communication systems. *Electronics Letters*, 40:1203–1205(2), September 2004. ISSN 0013-5194. URL `https://digital-library.theiet.org/content/journals/10.1049/el_20045599`.

[69] Mohamad Katanbaf, Kun-Da Chu, Tong Zhang, Chenxin Su, and Jacques C. Rudell. Two-way traffic ahead: Rfanalog self-interference cancellation techniques and the challenges for future integrated full-duplex transceivers. *IEEE Microwave Mag.*, 20(2):22–35, 2019. doi: 10.1109/MMM.2018.2880489.

[70] Mohamad Katanbaf, Kun-Da Chu, Tong Zhang, Chenxin Su, and Jacques Christophe Rudell. Two-Way Traffic Ahead: RF/Analog Self-Interference Cancellation

Techniques and the Challenges for Future Integrated Full-Duplex Transceivers. *IEEE Microwave Magazine*, 20:22–35, 2019.

[71] Tewelgn Kebede, Yihenew Wondie, Johannes Steinbrunn, Hailu Belay Kassa, and Kevin T. Kornegay. Precoding and Beamforming Techniques in mmWave-Massive MIMO: Performance Assessment. *IEEE Access*, 10:16365–16387, 2022. doi: 10.1109/ACCESS.2022.3149301.

[72] Noor M. Khan, Mohammed T. Simsim, and Predrag B. Rapajic. A generalized model for the spatial characteristics of the cellular mobile channel. *IEEE Transactions on Vehicular Technology*, 57(1):22–37, 2008. doi: 10.1109/TVT.2007.904532.

[73] Asil Koc and Tho Le-Ngoc. Full-duplex mmwave massive MIMO systems: A joint hybrid precoding/combining and self-interference cancellation design. *IEEE Open J. Commun. Society*, 2:754–774, 2021. doi: 10.1109/OJCOMS.2021.3069672.

[74] Kenneth E. Kolodziej, Bradley T. Perry, and Jeffrey S. Herd. In-band full-duplex technology: Techniques and systems survey. *IEEE Trans. Microwave Theory and Techniques*, 67(7):3025–3041, 2019. doi: 10.1109/TMTT.2019.2896561.

[75] Kenneth E. Kolodziej, Jonathan P. Doane, Bradley T. Perry, and Jeffrey S. Herd. Adaptive beamforming for multi-function in-band full-duplex applications. *IEEE Wireless Communications*, 28(1):28–35, 2021. doi: 10.1109/MWC.001.2000203.

[76] Chuili Kong, Caijun Zhong, Shi Jin, Sheng Yang, Hai Lin, and Zhaoyang Zhang. Full-duplex massive MIMO relaying systems with low-resolution ADCs. *IEEE Trans. Wireless Commun.*, 16(8):5033–5047, 2017. doi: 10.1109/TWC.2017.2705041.

[77] Lingkai Kong. *Energy-Efficient 60 GHz Phased-Array Design for Multi-Gb/s Communication Systems*. PhD thesis, Dept. EECS, University of California, Berkeley, Dec 2014. URL `http://www2.eecs.berkeley.edu/Pubs/TechRpts/2014/EECS-2014-191.html`.

[78] Dani Korpi, Lauri Anttila, Ville Syrjälä, and Mikko Valkama. Widely linear digital self-interference cancellation in direct-conversion full-duplex transceiver. *IEEE J. Selected Areas in Commun.*, 32(9):1674–1687, 2014. doi: 10.1109/JSAC.2014.2330093.

[79] Nour Kouzayha, Hesham Elsawy, Hayssam Dahrouj, Khlod Alshaikh, Tareq Y. Al-Naffouri, and Mohamed-Slim Alouini. Analysis of large scale aerial terrestrial networks with mmWave backhauling. *IEEE Trans. Wireless Commun.*, 20(12):8362–8380, 2021. doi: 10.1109/TWC.2021.3092293.

[80] Michael Kraemer, Daniela Dragomirescu, and Robert Plana. Design of a very low-power, low-cost 60 GHz receiver front-end implemented in 65 nm CMOS technology. *Intl. J. Microwave and Wireless Technologies*, 3(2):131–138, 2011. doi: 10.1017/S1759078711000067.

[81] Tho Le-Ngoc and Ahmed Masmoudi. *Full-Duplex Wireless Communications Systems: Self-Interference Cancellation*. SpringerLink, 2017.

[82] Byunghwan Lee, Jong-Bu Lim, Chaehee Lim, Byungchul Kim, and Ji-yun Seol. Reflected self-interference channel measurement for mmwave beamformed full-duplex system. In *2015 IEEE Globecom Workshops (GC Wkshps)*, pages 1–6, 2015. doi: 10.1109/GLOCOMW.2015.7414127.

[83] Hongyu Li, Ming Li, and Qian Liu. Hybrid Beamforming With Dynamic Subarrays and Low-Resolution PSs for mmWave MU-MISO Systems. *IEEE Transactions on Communications*, 68(1):602–614, 2020. doi: 10.1109/TCOMM.2019.2950905.

[84] Ruozhu Li, Ahmed Masmoudi, and Tho Le-Ngoc. Self-interference cancellation with nonlinearity and phase-noise suppression in full-duplex systems. *IEEE Transactions on Vehicular Technology*, 67(3):2118–2129, 2018. doi: 10.1109/TVT.2017.2754489.

[85] Wei-Tsung Li, Yun-Chieh Chiang, Jeng-Han Tsai, Hong-Yuan Yang, Jen-Hao Cheng, and Tian-Wei Huang. 60-GHz 5-bit phase shifter with integrated VGA phase-error compensation. *IEEE Trans. Microwave Theory and Techniques*, 61(3):1224–1235, 2013. doi: 10.1109/TMTT.2013.2244226.

[86] Ning Liang and Wenyi Zhang. Mixed-ADC massive MIMO. *IEEE J. Sel. Areas Commun.*, 34(4):983–997, 2016. doi: 10.1109/JSAC.2016.2544604.

[87] J.C. Liberti and T.S. Rappaport. A geometrically based model for line-of-sight multipath radio channels. In *Proceedings of Vehicular Technology Conference - VTC*, volume 2, pages 844–848 vol.2, 1996. doi: 10.1109/VETEC.1996.501430.

[88] Yu-Hsuan Lin and Huei Wang. A low phase and gain error passive phase shifter in 90 nm CMOS for 60 GHz phase array system application. In *IEEE MTT-S Intl. Microwave Symposium*, pages 1–4, 2016. doi: 10.1109/MWSYM.2016.7540372.

[89] Panagiota Lioliou, Mats Viberg, Mikael Coldrey, and Fredrik Athley. Self-interference suppression in full-duplex MIMO relays. In *Asilomar Conference on Signals, Systems and Computers*, pages 658–662, 2010. doi: 10.1109/ACSSC.2010.5757643.

[90] Tianle Liu, Jun Tong, Qinghua Guo, Jiangtao Xi, Yanguang Yu, and Zhitao Xiao. Energy Efficiency of Massive MIMO Systems With Low-Resolution ADCs and Successive Interference Cancellation. *IEEE Transactions on Wireless Communications*, 18(8):3987–4002, 2019. doi: 10.1109/TWC.2019.2920129.

[91] Tianle Liu, Jun Tong, Qinghua Guo, Jiangtao Xi, Yanguang Yu, and Zhitao Xiao. On the Performance of Massive MIMO Systems With Low-Resolution ADCs and MRC Receivers Over Rician Fading Channels. *IEEE Systems Journal*, 15(3):4514–4524, 2021.

[92] Xiao Liu, Zhenyu Xiao, Lin Bai, Jinho Choi, Pengfei Xia, and Xiang-Gen Xia. Beamforming based full-duplex for millimeter-wave communication. *Sensors*, 16(7), Jul 2016.

[93] Yanzhen Liu, Qiyu Hu, Yunlong Cai, Guanding Yu, and Geoffrey Ye Li. Deep-unfolding beamforming for intelligent reflecting surface assisted full-duplex systems. *IEEE Trans. Wireless Commun.*, pages 1–1, 2021. doi: 10.1109/TWC.2021.3133296.

[94] D.J. Love and R.W. Heath. Limited feedback unitary precoding for spatial multiplexing systems. *IEEE Trans. Info. Theory*, 51(8):2967–2976, 2005. doi: 10.1109/TIT.2005.850152.

[95] Angel Lozano and Nihar Jindal. Transmit diversity vs. spatial multiplexing in modern MIMO systems. *IEEE Trans. Wireless Commun.*, 9(1):186–197, 2010. doi: 10.1109/TWC.2010.01.081381.

[96] Roberto López-Valcarce and Marcos Martínez-Cotelo. Full-Duplex mmWave Communication with Hybrid Precoding and Combining. In *2020 28th European Signal Processing Conference (EUSIPCO)*, pages 1752–1756, 2021. doi: 10.23919/Eusipco47968.2020.9287814.

[97] Roberto López-Valcarce and Marcos Martínez-Cotelo. Analog Beamforming for Full-Duplex mmWave Communication with Low-Resolution Phase Shifters. In *ICC 2021 - IEEE International Conference on Communications*, pages 1–6, 2021. doi: 10.1109/ICC42927.2021.9500656.

[98] Roberto López-Valcarce and Marcos Martínez-Cotelo. Full-Duplex mmWave MIMO With Finite-Resolution Phase Shifters. *IEEE Trans. Wireless Commun.*, 21(11):8979–8994, 2022. doi: 10.1109/TWC.2022.3171664.

[99] Mobeen Mahmood, Asil Koc, and Tho Le-Ngoc. Energy-Efficient MU-Massive-MIMO Hybrid Precoder Design: Low-Resolution Phase Shifters and Digital-to-Analog Converters for 2D Antenna Array Structures. *IEEE Open Journal of the Communications Society*, 2:1842–1861, 2021. doi: 10.1109/OJCOMS.2021.3101747.

[100] Jacqueline R. Malayter and David J. Love. A Low-Latency Precoding Strategy for In-Band Full-Duplex MIMO Relay Systems. *IEEE Trans. Wireless Commun.*, pages 1–1, 2023. doi: 10.1109/TWC.2023.3292985.

[101] T. Marzetta. Noncooperative Cellular Wireless with Unlimited Numbers of Base Station Antennas. *IEEE Trans. Wireless Commun.*, 9:3590–3600, 2010.

[102] Amine Mezghani, Josef A. Nossek, and A. Lee Swindlehurst. Low SNR Asymptotic Rates of Vector Channels With One-Bit Outputs. *IEEE Transactions on Information Theory*, 66(12):7615–7634, 2020. doi: 10.1109/TIT.2020.3030855.

[103] M&M. Virtual reality market. Available: `https://www.marketsandmarkets.com/Market-Reports/reality-applications-market-458.html?gclid=CjwKCAjw7-P1BRA2EixTXs0djAhoCKrUQAvD_BwE`.

[104] Mohammadali Mohammadi, Zahra Mobini, Diluka Galappaththige, and Chintha Tellambura. A comprehensive survey on full-duplex communication: Current solutions, future trends, and open issues. *IEEE Communications Surveys & Tutorials*, 25(4):2190–2244, 2023. doi: 10.1109/COMST.2023.3318198.

[105] B. Murmann. Adc performance survey 1997-2016. *http://web.stanford.edu/m̃urmann/adcsurvey.* 2021.

[106] R. Méndez-Rial, C. Rusu, N. González-Prelcic, A. Alkhateeb, and R. W. Heath. Hybrid MIMO Architectures for Millimeter Wave Communications: Phase Shifters or Switches? *IEEE Access*, 4:247–267, 2016. doi: 10.1109/ACCESS.2015.2514261.

[107] Syed Hassan Raza Naqvi and Pin-Han Ho. Achieving 5G NR mmWave indoor coverage under integrated access backhaul. *IEEE Systems Journal*, 15(4):5429–5439, 2021. doi: 10.1109/JSYST.2021.3053550.

[108] Bayan Nasri, Sunit P. Sebastian, Kae-Dyi You, RamKumar RanjithKumar, and Davood Shahrjerdi. A 700 μW 1GS/s 4-bit folding-flash ADC in 65nm CMOS for wideband wireless communications. In *IEEE Intl. Symp. Circuits and Sys.*, pages 1–4, 2017. doi: 10.1109/ISCAS.2017.8050624.

[109] Syed Junaid Nawaz, Bilal Hasan Qureshi, and Noor M. Khan. A generalized 3-d scattering model for a macrocell environment with a directional antenna at the bs. *IEEE Transactions on Vehicular Technology*, 59(7):3193–3204, 2010. doi: 10.1109/TVT.2010.2050015.

[110] Hien Quoc Ngo, Himal A. Suraweera, Michail Matthaiou, and Erik G. Larsson. Multipair full-duplex relaying with massive arrays and linear processing. *IEEE J. Sel. Areas Commun.*, 32(9):1721–1737, 2014. doi: 10.1109/JSAC.2014.2330091.

[111] T. D. Novlan, H. S. Dhillon, and J. G. Andrews. Analytical modeling of uplink cellular networks. *IEEE Trans. Wireless Commun.*, 12(6):2669–2679, June 2013. ISSN 1558-2248. doi: 10.1109/TWC.2013.050613.120325.

[112] Chinaemerem David Nwankwo, L. Zhang, A. Quddus, M. Imran, and R. Tafazolli. A Survey of Self-Interference Management Techniques for Single Frequency Full Duplex Systems. *IEEE Access*, 6:30242–30268, 2018.

[113] A.Y. Olenko, K.T. Wong, and E. Hui-On Ng. Analytically derived toa-doa statistics of uplink/downlink wireless multipaths arisen from scatterers on a hollow-disc around the mobile. *IEEE Antennas and Wireless Propagation Letters*, 2:345–348, 2003. doi: 10.1109/LAWP.2004.824174.

[114] A.Y. Olenko, K.T. Wong, and M. Abdulla. Analytically derived toa-doa distributions of uplink/downlink wireless-cellular multipaths arisen from scatterers with an inverted-parabolic spatial distribution around the mobile. *IEEE Signal Processing Letters*, 12(7):516–519, 2005. doi: 10.1109/LSP.2005.847859.

[115] Oner Orhan, Elza Erkip, and Sundeep Rangan. Low power analog-to-digital conversion in millimeter wave systems: Impact of resolution and bandwidth on performance. In *Info. Theory and Appl. Workshop*, pages 191–198, 2015. doi: 10.1109/ITA.2015.7308988.

[116] R. Sepulchre P.-A. Absil, R. Mahony. *Optimization algorithms on matrix manifolds*. Princeton University Press, 2009.

[117] Joan Palacios, Javier Rodriguez-Fernandez, and Nuria Gonzalez-Prelcic. Hybrid precoding and combining for full-duplex millimeter wave communication. In *IEEE Global Communications Conf.*, pages 1–6, 2019. doi: 10.1109/GLOBECOM38437.2019.9013484.

[118] Joan Palacios, Javier Rodriguez-Fernandez, and Nuria Gonzalez-Prelcic. Hybrid Precoding and Combining for Full-Duplex Millimeter Wave Communication. In *2019 IEEE Global Communications Conference (GLOBECOM)*, pages 1–6, 2019. doi: 10.1109/GLOBECOM38437.2019.9013484.

[119] J.D. Parsons and A.S. Bajwa. Wideband characterisation of fading mobile radio channels. *IEE Proceedings F (Communications, Radar and Signal Processing)*, 129:95–101(6), April 1982. ISSN 0143-7070. URL `https://digital-library.theiet.org/content/journals/10.1049/ip-f-1.1982.0016`.

[120] P. Petrus, J.H. Reed, and T.S. Rappaport. Geometrical-based statistical macrocell channel model for mobile environments. *IEEE Transactions on Communications*, 50(3):495–502, 2002. doi: 10.1109/26.990911.

[121] P. Petrus, J.H. Reed, and T.S. Rappaport. Geometrical-based statistical macrocell channel model for mobile environments. *IEEE Transactions on Communications*, 50(3):495–502, 2002. doi: 10.1109/26.990911.

[122] Michele Polese, Marco Giordani, Tommaso Zugno, Arnab Roy, Sanjay Goyal, Douglas Castor, and Michele Zorzi. Integrated access and backhaul in 5G mmwave networks: Potential and challenges. *IEEE Commun. Mag.*, 58(3): 62–68, 2020. doi: 10.1109/MCOM.001.1900346.

[123] Amr M. Ragheb, Qazi Tareq, Maged. A. Esmail, Habib Fathallah, Saleh A. Alshebeili, and Mohammed Z. M. Khan. Sub-THz Signal Transmission in Harsh Environments Using L-Band Quantum-Dash Laser Source: Experiments and Modeling. *IEEE J. Sel. Topics in Quantum Electronics*, 29(5: Terahertz Photonics):1–9, 2023. doi: 10.1109/JSTQE.2023.3299228.

[124] Sridhar Rajagopal, Rakesh Taori, and Shadi Abu-Surra. Self-interference mitigation for in-band mmwave wireless backhaul. In *IEEE Consumer Commun. and Networking Conf.*, pages 551–556, 2014. doi: 10.1109/CCNC.2014.6866625.

[125] Venkatesh Ramireddy, Marcus Grossmann, Markus Landmann, and Giovanni Del Galdo. Enhancements on Type-II 5G New Radio Codebooks for UE Mobility Scenarios. *IEEE Commun. Standards Magazine*, 6(1):35–40, 2022. doi: 10.1109/MCOMSTD.0001.2100072.

[126] Theodore S Rappaport, (Robert William) Heath, (Robert Clark) Daniels, and (James Nelson) Murdock. *Millimeter wave wireless communications*. Prentice Hall, 2015. ISBN 9780132172288. Includes bibliographical references (pages 585-651) and index.

[127] Muhammad Riaz, Noor M. Khan, and Syed Junaid Nawaz. A generalized 3-d scattering channel model for spatiotemporal statistics in mobile-to-mobile communication environment. *IEEE Transactions on Vehicular Technology*, 64 (10):4399–4410, 2015. doi: 10.1109/TVT.2014.2371531.

[128] T. Riihonen, A. Balakrishnan, K. Haneda, S. Wyne, S. Werner, and R. Wichman. Optimal eigenbeamforming for suppressing self-interference in full-duplex MIMO relays. *Conf. on Info. Sciences and Systems*, pages 1–6, 2011.

[129] Taneli Riihonen, Stefan Werner, and Risto Wichman. Spatial loop interference suppression in full-duplex MIMO relays. In *Asilomar Conf. Signals, Sys. and Computers*, pages 1508–1512, 2009. doi: 10.1109/ACSSC.2009.5470111.

[130] Taneli Riihonen, Stefan Werner, and Risto Wichman. Mitigation of loopback self-interference in full-duplex MIMO relays. *IEEE Trans. Signal Process.*, 59 (12):5983–5993, 2011. doi: 10.1109/TSP.2011.2164910.

[131] Ian P. Roberts and Sriram Vishwanath. Beamforming cancellation design for millimeter-wave full-duplex. In *IEEE Global Communications Conf.*, pages 1–6, 2019. doi: 10.1109/GLOBECOM38437.2019.9013116.

[132] Ian P. Roberts, Hardik B. Jain, and Sriram Vishwanath. Frequency-Selective Beamforming Cancellation Design for Millimeter-Wave Full-Duplex. In *IEEE Int. Conf. Commun.*, pages 1–6, 2020. doi: 10.1109/ICC40277.2020.9149419.

[133] Ian P. Roberts, Jeffrey G. Andrews, Hardik B. Jain, and Sriram Vishwanath. Millimeter-wave full duplex radios: New challenges and techniques. *IEEE Wireless Commun.*, 28(1):36–43, 2021. doi: 10.1109/MWC.001.2000221.

[134] Ian P. Roberts, Jeffrey G. Andrews, and Sriram Vishwanath. Hybrid beamforming for millimeter wave full-duplex under limited receive dynamic range. *IEEE Trans. Wireless Commun.*, 20(12):7758–7772, 2021. doi: 10.1109/TWC.2021.3087417.

[135] Ian P. Roberts, Aditya Chopra, Thomas Novlan, Sriram Vishwanath, and Jeffrey G. Andrews. Beamformed self-interference measurements at 28 ghz: Spatial insights and angular spread. *IEEE Transactions on Wireless Communications*, 21(11):9744–9760, 2022. doi: 10.1109/TWC.2022.3179232.

[136] Ashutosh Sabharwal, Philip Schniter, Dongning Guo, Daniel W. Bliss, Sampath Rangarajan, and Risto Wichman. In-Band Full-Duplex Wireless: Challenges and Opportunities. *IEEE Journal on Selected Areas in Communications*, 32 (9):1637–1652, 2014. doi: 10.1109/JSAC.2014.2330193.

[137] K. Satyanarayana, Mohammed El-Hajjar, Ping-Heng Kuo, Alain Mourad, and Lajos Hanzo. Hybrid beamforming design for full-duplex millimeter wave communication. *IEEE Trans. Veh. Technology*, 68(2):1394–1404, 2019. doi: 10.1109/TVT.2018.2884049.

[138] Damith Senaratne and C. Tellambura. Beamforming for Space Division Duplexing. *IEEE Int. Conf. Commun.*, pages 1–5, 2011.

[139] Chandan Kumar Sheemar, Christo Kurisummoottil Thomas, and Dirk Slock. Practical hybrid beamforming for millimeter wave massive MIMO full duplex with limited dynamic range. *IEEE Open J. Commun. Society*, 3:127–143, 2022. doi: 10.1109/OJCOMS.2022.3140422.

[140] Arman Shojaeifard, Kai-Kit Wong, Marco Di Renzo, Gan Zheng, Khairi Ashour Hamdi, and Jie Tang. Massive MIMO-enabled full-duplex cellular networks. *IEEE Trans. Commun.*, 65(11):4734–4750, 2017. doi: 10.1109/TCOMM.2017.2731768.

[141] Min Soo Sim, MinKeun Chung, Dongkyu Kim, Jaehoon Chung, Dong Ku Kim, and Chan-Byoung Chae. Nonlinear self-interference cancellation for full-duplex radios: From link-level and system-level performance perspectives. *IEEE Communications Magazine*, 55(9):158–167, 2017. doi: 10.1109/MCOM.2017.1600264.

[142] Besma Smida, Ashutosh Sabharwal, Gábor Fodor, George C. Alexandropoulos, Himal A. Suraweera, and Chan-Byoung Chae. Full-Duplex Wireless for 6G: Progress Brings New Opportunities and Challenges. *IEEE J. Sel. Areas in Commun.*, 41(9):2729–2750, 2023.

[143] Besma Smida, Ashutosh Sabharwal, Gábor Fodor, George C. Alexandropoulos, Himal A. Suraweera, and Chan-Byoung Chae. Full-duplex wireless for 6g: Progress brings new opportunities and challenges. *IEEE J. Selected Areas in Commun.*, 41(9):2729–2750, 2023. doi: 10.1109/JSAC.2023.3287612.

[144] T. Snow, C. Fulton, and W. Chappell. Transmit–Receive Duplexing Using Digital Beamforming System to Cancel Self-Interference. *IEEE Trans. Microwave Theory and Tech.*, 59:3494–3503, 2011.

[145] Foad Sohrabi and Wei Yu. Hybrid digital and analog beamforming design for large-scale antenna arrays. *IEEE J. Selected Topics in Signal Processing*, 10 (3):501–513, 2016. doi: 10.1109/JSTSP.2016.2520912.

[146] Lingyang Song, Risto Wichman, Yonghui Li, and Zhu Han. *Full-Duplex Communications and Networks*. Cambridge University Press, 2017. doi: 10.1017/9781316662106.

[147] D. B. Taylor, H. S. Dhillon, T. D. Novlan, and J. G. Andrews. Pairwise interaction processes for modeling cellular network topology. In *IEEE Global Commun. Conf.*, pages 4524–4529, Dec 2012. doi: 10.1109/GLOCOM.2012.6503831.

[148] Orawan Tipmongkolsilp, Said Zaghloul, and Admela Jukan. The evolution of cellular backhaul technologies: Current issues and future trends. *IEEE Commun. Surveys and Tutorials*, 13(1):97–113, 2011. doi: 10.1109/SURV.2011.040610.00039.

[149] Sathya N. Venkatasubramanian, Leo Laughlin, Katsuyuki Haneda, and Mark A. Beach. Wideband self-interference channel modelling for an on-frequency repeater. *2016 10th European Conference on Antennas and Propagation (EuCAP)*, pages 1–5, 2016. URL `https://api.semanticscholar.org/CorpusID:38957515`.

[150] Kun Wang, Ruonan Zhang, Zhimeng Zhong, Xiaomei Zhang, and Xiaoyan Pang. Measurement of self-interference channels for full-duplex relay in an urban scenario. In *2017 IEEE International Conference on Communications Workshops (ICC Workshops)*, pages 1153–1158, 2017. doi: 10.1109/ICCW.2017.7962814.

[151] Siyuan Wang, Yi Liu, Wei Zhang, and Hailin Zhang. Achievable rates of full-duplex massive MIMO relay systems over Rician fading channels. *IEEE Trans. Veh. Technol.*, 66(11):9825–9837, 2017. doi: 10.1109/TVT.2017.2724238.

[152] Zihuan Wang, Ming Li, Qian Liu, and A. Lee Swindlehurst. Hybrid Precoder and Combiner Design With Low-Resolution Phase Shifters in mmWave MIMO Systems. *IEEE Journal of Selected Topics in Signal Processing*, 12(2):256–269, 2018.

[153] Hao Wu. Efficient Allocation of the Amount of Radio Resources in 5G NR to Efficient Allocation of Radio Resources in 5G NR. *IEEE Trans. Wireless Commun.*, 21(5):3321–3332, 2022. doi: 10.1109/TWC.2021.3120271.

[154] Xiangyu Wu, Ying Shen, and Youxi Tang. The power delay profile of the single-antenna full-duplex self-interference channel in indoor environments at 2.6 ghz. *IEEE Antennas and Wireless Propagation Letters*, 13:1561–1564, 2014. doi: 10.1109/LAWP.2014.2345066.

[155] A. D. Wyner. Shannon-theoretic approach to a Gaussian cellular multiple-access channel. *IEEE Trans. Info. Theory*, 40(6):1713–1727, Nov 1994. ISSN 1557-9654. doi: 10.1109/18.340450.

[156] Zhenyu Xiao, Pengfei Xia, and Xiang-Gen Xia. Full-Duplex Millimeter-Wave Communication. *IEEE Wireless Commun.*, 24(6):136–143, 2017. doi: 10.1109/MWC.2017.1700058.

[157] J. Xu, J. Zhang, and J. G. Andrews. On the accuracy of the Wyner model in cellular networks. *IEEE Trans. Wireless Commun.*, 10(9):3098–3109, Sep. 2011. ISSN 1558-2248. doi: 10.1109/TWC.2011.062911.100481.

[158] Kui Xu, Zhexian Shen, Yurong Wang, Xiaochen Xia, and Dongmei Zhang. Hybrid Time-Switching and Power Splitting SWIPT for Full-Duplex Massive MIMO Systems: A Beam-Domain Approach. *IEEE Transactions on Vehicular Technology*, 67(8):7257–7274, 2018. doi: 10.1109/TVT.2018.2831790.

[159] Xuewu Xu, Yuechao Pan, Phyu Phyu Mar Yi Lwin, and Xinan Liang. 3d holographic display and its data transmission requirement. In *2011 International Conference on Information Photonics and Optical Communications*, pages 1–4, 2011. doi: 10.1109/IPOC.2011.6122872.

[160] Danyang Yu, Yi Liu, and Hailin Zhang. Energy-efficient beamforming design for user-centric full-duplex wireless backhaul networks. In *IEEE Global Commun. Conf.*, pages 1–6, 2021. doi: 10.1109/GLOBECOM46510.2021.9685903.

[161] Xianghao Yu, Juei-Chin Shen, Jun Zhang, and Khaled B. Letaief. Alternating Minimization Algorithms for Hybrid Precoding in Millimeter Wave MIMO Systems. *IEEE Journal of Selected Topics in Signal Processing*, 10(3):485–500, 2016. doi: 10.1109/JSTSP.2016.2523903.

[162] Y. Yu, P. G. M. Baltus, A. de Graauw, E. van der Heijden, C. S. Vaucher, and A. H. M. van Roermund. A 60 GHz Phase Shifter Integrated With LNA and PA in 65nm CMOS for Phased Array Systems. *IEEE J. Solid-State Circuits*, 45(9):1697–1709, 2010. doi: 10.1109/JSSC.2010.2051861.

[163] Yu-Hsuan Lin and H. Wang. A low phase and gain error passive phase shifter in 90 nm CMOS for 60 GHz phase array system application. In *IEEE MTT-S Intl. Microwave Symp.*, pages 1–4, 2016. doi: 10.1109/MWSYM.2016.7540372.

[164] S.A. Zekavat and C.R. Nassar. Power-azimuth-spectrum modeling for antenna array systems: a geometric-based approach. *IEEE Transactions on Antennas and Propagation*, 51(12):3292–3294, 2003. doi: 10.1109/TAP.2003.820973.

[165] Deyou Zhang, Ming Xiao, Mikael Skoglund, and H. Vincent Poor. Beamforming Design for Active RIS-Aided Over-the-Air Computation, 2023.

[166] Jiayi Zhang, Linglong Dai, Shengyang Sun, and Zhaocheng Wang. On the spectral efficiency of massive MIMO systems with low-resolution ADCs. *IEEE Commun. Let.*, 20(5):842–845, 2016. doi: 10.1109/LCOMM.2016.2535132.

[167] Jiayi Zhang, Linglong Dai, Ziyan He, Shi Jin, and Xu Li. Performance analysis of Mixed-ADC massive MIMO systems over Rician fading channels. *IEEE J. Sel. Areas in Commun.*, 35(6):1327–1338, 2017. doi: 10.1109/JSAC.2017.2687278.

[168] Jiayi Zhang, Linglong Dai, Ziyan He, Bo Ai, and Octavia A. Dobre. Mixed-ADC/DAC multipair massive MIMO relaying systems: Performance analysis and power optimization. *IEEE Trans. Commun.*, 67(1):140–153, 2019. doi: 10.1109/TCOMM.2018.2869596.

[169] Junkai Zhang, Navneet Garg, Mark Holm, and Tharmalingam Ratnarajah. Design of full duplex millimeter-wave integrated access and backhaul networks. *IEEE Wireless Communications*, 28(1):60–67, 2021. doi: 10.1109/MWC.001.2000199.

[170] Xianyu Zhang, Tao Liang, Kang An, Gan Zheng, and Symeon Chatzinotas. Secure transmission in cell-free massive MIMO with RF impairments and low-

resolution ADCs/DACs. *IEEE Transactions on Vehicular Technology*, 70(9): 8937–8949, 2021. doi: 10.1109/TVT.2021.3098693.

[171] Zhongshan Zhang, Xiaomeng Chai, Keping Long, Athanasios V. Vasilakos, and Lajos Hanzo. Full duplex techniques for 5g networks: self-interference cancellation, protocol design, and relay selection. *IEEE Communications Magazine*, 53(5):128–137, 2015. doi: 10.1109/MCOM.2015.7105651.

[172] Zhongshan Zhang, Keping Long, Athanasios V. Vasilakos, and Lajos Hanzo. Full-duplex wireless communications: Challenges, solutions, and future research directions. *Proceedings of the IEEE*, 104(7):1369–1409, 2016. doi: 10.1109/JPROC.2015.2497203.

[173] Pengcheng Zhu, Zheng Sheng, Jialong Bao, and Jiamin Li. Antenna Selection for Full-Duplex Distributed Massive MIMO via the Elite Preservation Genetic Algorithm. *IEEE Communications Letters*, 26(4):922–926, 2022. doi: 10.1109/LCOMM.2022.3141546.

[174] C. Ziółkowski and J. M. Kelner. Geometry-based statistical model for the temporal, spectral, and spatial characteristics of the land mobile channel. *Wireless Personal Communications*, 83(1):631–652, July 2015.

Vita

Elyes Balti received the B.S. degree in electrical engineering from The École Supérieure des Communications de Tunis (Sup'Com), Aryanah, Tunisia, in 2013, and the M.S. degree in electrical engineering from the University of Idaho, Moscow, ID, USA, in 2018. He is currently working toward the Ph.D. degree in electrical engineering with The University of Texas at Austin, Austin, TX, USA. He is a Member of The Wireless Networking and Communications Group (WNCG) and The 6G@UT Research Center with The University of Texas at Austin. He has held summer internships at Motorola Mobility, Chicago, IL USA, in 2019, Huawei, Bridgewater, NJ, USA, in 2020, and Qualcomm, San Diego, CA, USA, in 2021 and 2022, respectively. His research interests include wireless communications, signal processing, and massive MIMO.

Address: 2303 East Side Drive APT 110
Austin, Texas 78704-5219

This dissertation was typeset with LaTeX[†] by the author.

[†]LaTeX is a document preparation system developed by Leslie Lamport as a special version of Donald Knuth's TeX Program.